Optical properties of subvisual cirrus clouds measured by the OSIRIS instrument

A Thesis

Submitted to the Faculty of Graduate Studies and Research

in Partial Fulfillment of the Requirements

for the Degree of

Doctor of Philosophy

in the Department of Physics and Engineering Physics by

J. Truitt Wiensz

Saskatoon, Saskatchewan

Permission to Use

In presenting this thesis in partial fulfillment of the requirements for a Postgraduate degree from the University of Saskatchewan, the author agrees that the Libraries of this University may make it freely available for inspection. The author further agrees that permission for copying of this thesis in any manner, in whole or in part, for scholarly purposes may be granted by the professor who supervised this thesis work or, in his absence, by the Head of the Department or the Dean of the College in which this thesis work was done. It is understood that any copying or publication or use of this thesis or parts thereof for financial gain shall not be allowed without written approval from the author. It is also understood that due recognition shall be given to the author and to the University of Saskatchewan in any scholarly use which may be made of any material in this thesis.

Requests for permission to copy or to make other use of material in this thesis in whole or in part should be addressed to:

Head of the Department of Physics and Engineering Physics
116 Science Place
University of Saskatchewan
Saskatoon, Saskatchewan
Canada
S7N 5E2

Abstract

Satellite-based measurements with limb viewing geometry give high-quality information about the atmosphere. However, low-altitude measurements are very sensitive to thin clouds, which act as a semi-reflective layer that can screen out the lower atmosphere and the earth's surface. The work described in this thesis demonstrates the ability to retrieve the optical properties of these clouds from observations of scattered sunlight by the OSIRIS instrument.

Retrievals from satellite measurements require a radiative transfer model well-suited to the measurement geometry. For this reason the SASKTRAN model is used, which employs full spherical geometry. Since this model was not initially intended to model cloud-particle scattering, several sources for the light-scattering properties of ice crystals – from both first-principles algorithms and from in-cloud particle measurements – were incorporated. Also, since these properties violate several simplifying assumptions of the model, modifications to the model were required. With the work described in this thesis, SASKTRAN replicates in-cloud radiance measurements with high accuracy across the measured spectrum.

Cloud property retrievals are demonstrated that use SASKTRAN in an iterative retrieval technique. Assuming an effective cloud particle size, cloud particle number densities are retrieved that replicate the spectral measurements with very good accuracy. The effect of cloud properties on ozone and stratospheric aerosol retrievals is investigated. Systematic biases that result from neglecting cloud-particle scattering are discussed. Coincident measurements from another satellite instrument shows very good agreement with OSIRIS cloud properties.

Acknowledgements

I want to extend my sincere thanks to those who made this work possible. First, my thanks go to Doug Degenstein for the opportunity to pursue this work, for his interest in it, and for his helpful comments as this work progressed. As well, my thanks go to the Natural Sciences and Engineering Research Council, the Canadian Space Agency, the University of Saskatchewan, and the Institute of Space and Atmospheric Studies, who each in part provided financial support.

Personally, I would like to thank Nick Lloyd, Adam Bourassa, and Ted Llewellyn for many helpful conversations and much good advice throughout this work. As well, I want to thank Paul Loewen and Chris Roth for being excellent office mates and swimming partners.

Finally, my sincere appreciation goes to my family for their unceasing support and encouragement. In particular, I am grateful for my wife Sabina – without her support this work could not have been completed – and our son Ezra, who has brought much joy and laughter into our life.

To Sabina

השמים מספרים כבוד־אל

ומעשה ידיו מגיד הרקיע

ἡ γάρ ἀποκαραδοκία τῆς κτίσεως τὴν αποκάλυψιν τῶν υἱῶν τοῦ Θεοῦ ἀπεκδέχεται

Contents

List of Figures

List of Tables

List of Abbreviations

CALIOP	Cloud-Aerosol Lidar with Orthogonal Polarization
CALIPSO	Cloud-Aerosol Lidar and Infrared Pathfinder Satellite Observations
DDA	Discrete-dipole approximation
ECMWF	European Centre for Mid-range Weather Forecasting
GCM	Global climate model
GOES	Geostationary Operational Environmental Satellite
IN	Ice nuclei
ITCZ	Inter-tropical convergence zone
LIDAR	LIght Detection And Ranging
LOS	Line of sight
MART	Multiplicative algebraic reconstruction technique
NCEP	National Centers for Environmental Protection
OSIRIS	Optical Spectrograph and InfraRed Imaging System
PSD	Particle Size Distribution
SAGE	Stratospheric Aerosol and Gas Experiment
SVC	Subvisual cirrus clouds
TTL	Tropical tropopause layer
UTLS	Upper troposphere-lower stratosphere
WMO	World Meteorological Organization
WV	Water vapour

Nomenclature

		Units
a	Surface albedo	
D_e	Cloud effective particle size	μm
D_m	Median mass diameter	μm
$\mathbf{E}^{\text{inc}}$	Incident electric field	
$\mathbf{E}^{\text{sca}}$	Scattered electric field	
f	Fraction of light attributed as scattered forward	
g	Asymmetry factor of phase function	
$F(\mathbf{r})$	Irradiance	$\frac{\text{photons}}{\text{cm}^2\,\text{s}}$
$\mathbf{F}(\hat{\mathbf{\Omega}}, \hat{\mathbf{\Omega}}')$	Scattering matrix	
ϕ	Azimuth angle	
$\overline{\overline{\mathsf{G}}}$	Dyadic Green's function	
IWC	Cloud ice water content	g/m^{-3}
IWP	Ice water path	g/m^{-2}
$I(\mathbf{r}, \hat{\mathbf{\Omega}})$	Radiance	$\frac{\text{photons}}{\text{cm}^2\,\text{s steradian nm}}$
$J(\mathbf{r}, \hat{\mathbf{\Omega}})$	Multiple scattering source radiance	$\frac{\text{photons}}{\text{cm}^2\,\text{s steradian nm}}$
k_{abs}	Absorption extinction	cm^{-1} or km^{-1}
k_{sca}	Scattering extinction	cm^{-1} or km^{-1}
k	Total extinction	cm^{-1} or km^{-1}
k_1	Wavenumber of light in free space	radian/m
k_2	Wavenumber of light inside scattering particle	radian/m
κ	Photon conservation scaling factor	
$\mathbf{K}$	Jacobian matrix, weighting function	
L	Maximum dimension of ice crystal	μm
$\mathbf{M}_{mn}$,$\mathbf{N}_{mn}$	Vector spherical wave funtions	
n	Number density	cm^{-3}
$P(\Theta)$	Scattering phase function	steradian^{-1}
RH_i	Relative humidity with respect to ice	%
$\mathbf{r}$	Location of observer	m
$\mathbf{r}_0$	Location of observed position	m
σ_{abs}	Absorption cross section	cm^2
σ_{sca}	Scattering cross section	cm^2
σ_{ext}	Extinction cross section	cm^2
s	Distance from observer along line of sight	m
$\mathbf{S}$	Scattering amplitude matrix	
$\mathbf{S}$	Poynting vector	

		Units
τ	Optical depth	
τ_c	Cloud optical thickness	
$\Delta\tau_z$	Segment optical depth along vertical direction	
$\Delta\tau_s$	Segment optical depth along a ray	
θ	Zenith angle in local coordinate system	
Θ	Scattering angle	
Θ_0	Solar scattering angle	
$\Theta(h)$	Potential temperature	
W	Power measured by a photosensitive detector	
x	Scattering size parameter	
$\mathbf{x}$	State vector	
$\mathbf{y}$	Measurement vector	
$\mathbf{Z}(\hat{\mathbf{\Omega}}, \hat{\mathbf{\Omega}}')$	Phase matrix	
$\tilde{\omega}$	Single scattering albedo	
Ω	Solid angle	sterad
$\hat{\mathbf{\Omega}}$	Direction of observation	
$\hat{\mathbf{\Omega}}_0$, (θ_0, ϕ_0)	Solar direction; solar (zenith,azimuth) angle	
$\hat{\mathbf{\Omega}}^{\text{inc}}$	Direction of light incident on object	
$\hat{\mathbf{\Omega}}^{\text{sca}}$	Direction of light scattering	

Chapter 1

Introduction

Satellite-based measurements of the earth provide a wealth of information about its many systems from a global perspective. The last fifty years has seen an explosion in the number of earth-oriented satellite missions that gather information about large-scale processes of the oceans, land surface, and atmosphere. A wide range of techniques have been developed to probe the composition and dynamics of the atmosphere using a range of active and passive techniques at wavelengths across the electromagnetic spectrum. One very commonly-used technique to study the atmosphere is to make spectral measurements of sunlight that has been scattered from the atmosphere and the surface of the earth.

Several viewing geometries have been applied to measurements of scattered sunlight. The most mature geometry used in satellites is nadir-viewing, in which the instrument looks directly below the satellite and scans its field of view perpendicular to the satellite's direction of motion and thus measures in a zig-zag pattern as it progresses in its orbit. This geometry provides high horizontal resolution but is quite limited in providing details of vertical structure. The other geometry most currently in use is solar occultation, in which the instrument looks directly at the sun during a satellite sunrise (or sunset) and measures the increase (decrease) in brightness due to the varying transmission over the range of altitudes sampled (*McCormick*, 1987). Accordingly, solar occultation measurements provide very high vertical resolution but are limited in their horizontal coverage due to having only two measurements per

orbit.

Another viewing geometry has been developed over the past twenty-five years that attempts to capture elements of both techniques. In limb-viewing geometry, the instrument looks at the edge of the atmosphere, typically forward along its direction of travel. In this geometry the instrument field of view is typically moved to perform a vertical scan of the atmospheric limb (from the Latin *limbus*, literally 'edge' or 'fringe'). This technique is able to capture some of the vertical resolution achieved by solar occultation instruments, however it has the advantage of being able to take measurements throughout the daylight segment of the orbit. The OSIRIS instrument on the Odin satellite (*Llewellyn et al.*, 2004), launched in 2001 and still in operation at time of writing, measures scattered sunlight from a limb-viewing geometry.

Properties of the atmosphere can be inferred from such measurements by first using the laboratory-measured absorption properties of gases to model differences in the spectral characteristics of scattered sunlight from that of the incident sunlight. Mathematical modeling of the interaction of sunlight with the molecules and particulate matter in the atmosphere is performed to interpret these spectral differences. However, the equations that describe these interactions are integro-differential equations whose solutions must be performed over the entire illuminated atmosphere, and moreover these equations have no analytic solutions of practical interest. Because of this, software models are needed to simulate the interactions in order to interpret the measurements. Since the simplifying assumptions for solving the necessary equations vary, depending upon the viewing geometry, a range of such model types exist.

The presence of clouds in remote-sensing measurements typically acts as a source of measurement uncertainty. In addition, since clouds form a partially-reflective surface that obscures the atmosphere below, the presence of significant cloud amounts is sufficient to set a lower bound on the altitudes that can be probed by satellites that use visible and near-IR wavelengths. The amount of numerical work that is involved in accounting for the interactions of cloud particles with sunlight presents a significant challenge to many models used in satellite measurements – in particular those used in limb-viewing geometry.

While one aspect of clouds' importance is as a significant source of measurement uncertainty, clouds can play a significant – though still uncertain – role in a number of climate systems. The representation of cloud processes in models of global climate is the single largest source of uncertainty in current predictions of future climate. While this will continue to be the case for any numerical model that attempts to replicate global-scale processes without the ability to model cloud microphysics, understanding the microphysical and optical properties of observed clouds is a necessary component to improving our ability to represent them in climate models.

In this work, we consider observations of extremely thin clouds made from a limb-viewing satellite platform. It is demonstrated that it is possible to characterize the radiative effects of observed clouds in terms of a characteristic thickness and an effective particle size that are found through an automated retrieval algorithm. This task is done by extending the capabilities of a radiative transfer software model to allow simulations of limb-viewing satellite observations when thin cirrus clouds are present.

In general, retrievals of atmospheric properties from remote-sensing measurements are described by two processes. First, by assuming a suitable choice of values for the properties of interest, the model must accurately simulate the measurements. When this is achieved, the model is used in an iterative sense to move the assumed values toward a set that, ideally, exactly replicates the actual measurement to within experimental uncertainty. These two processes are referred to as *forward modeling* and *retrieval* by the remote sensing community. The work in this thesis focuses primarily on the forward-modeling problem in a cirrus cloud environment, and concludes by demonstrating the ability to retrieve cloud parameters from satellite measurements using the tools developed.

Chapter 2 provides background information relevant to the study of subvisual cirrus clouds. A summary of the geophysical significance of subvisual cirrus clouds is followed by a brief survey of measurements of their physical and optical properties from ground-based and remote-sensing instruments. Further, this chapter introduces the OSIRIS instrument on the Odin satellite and introduces the reader to detections

of cirrus clouds that have been made with OSIRIS.

Chapters 3 through 6 focus on forward modeling of satellite measurements in the presence of thin cirrus clouds. In Chapter 3, the necessary discussion of radiative transfer theory is given for describing simulations of OSIRIS observations of thin cirrus clouds. Radiometric quantities relevant to this work are first discussed. The discrete ordinates and successive-orders of scatter model types are summarized. This chapter concludes with a discussion of the SASKTRAN radiative transfer model, on which this work is based. Illustrative simulations of OSIRIS clear-sky measurements are given.

In its previous operational mode, the SASKTRAN model accounted for the light-scattering properties of key molecular constituents of the atmosphere and of stratospheric sulphate aerosols, but did not account for the light-scattering properties of ice crystals in cirrus clouds. The physical basis for computing these properties is introduced in Chapter 4. After a brief discussion of the scattering theory pertinent to modeling the interaction of sunlight with ice crystals, this chapter discusses two numerical algorithms used in this work. The T-matrix and Discrete Dipole Approximation methods are described, followed by the introduction of a measurement-based database of ice crystal light-scattering properties.

The scattering properties of ice crystals in cirrus clouds violate several simplifying assumptions in the previous operational distribution of SASKTRAN. Chapter 5 describes a novel photon conservation technique that is used to diagnose and treat these numerical inaccuracies. The usefulness of this technique is illustrated in relation to the simulation of OSIRIS measurements in cloud scenes. Chapter 6 discusses modifications and configurations that are necessary to use SASKTRAN for simulating in-cloud measurements made by OSIRIS. It is shown that this work is able to simulate in-cloud spectra to a high degree of accuracy.

The inverse problem of estimating cloud properties from satellite observations is initiated in Chapter 7. First, a brief survey is given of retrieval techniques that are commonly used in related problems. A measurement vector is defined that captures well the sensitivity of OSIRIS observations to cirrus cloud properties and a retrieval

algorithm is used to retrieve the height distribution of the cloud particle number density. The ability to retrieve cloud properties from OSIRIS observations is demonstrated. The sensitivity of the retrieval to auxiliary model parameters the effects of this work on trace gas retrievals are discussed. Preliminary comparisons of retrieved cloud properties with coincident measurements are shown. Chapter 8 summarizes the main findings of this work and discusses directions that could be taken to further use and extend this work.

Chapter 2

Background

Cirrus clouds are familiar from everyday experience as tenuous high-altitude clouds. They reside in the upper troposphere with typical mid-cloud temperatures between $-40°$C and $-70°$C (*Sassen and Cho*, 1992). While composed of ice crystals with sizes up to 1 mm, the particle densities of these clouds are quite low, typically on the order of 25 mg/m^3. A typical cirrus cloud is 1.5 km thick and can extend from tens to hundreds of kilometres horizontally.

2.1 Subvisual Cirrus Clouds

Subvisual cirrus (SVC) are extremely thin clouds (typically 500 m) whose name derives from the fact that they are not visible from the ground but contain sufficient ice concentrations to be detected by a range of remote-sensing instruments. They are typically much colder (below $-80°$C) and contain much smaller particles (1-100 μm) than typical cirrus clouds. As well, SVC can extend over hundreds of kilometres horizontally, and can persist for up to several days.

2.1.1 Significance of subvisual cirrus clouds

Despite their very low particle numbers, cirrus clouds play a role in several feedback mechanisms that regulate the earth's climate. Any process on the surface of earth

that involves feedbacks with solar radiation and water vapour will also feed back on cloud processes. For example, decreased surface albedo from melting of pack ice in the Arctic results in increased solar radiation absorbed by the northern ocean. This net warming of the seawater leads to increased evaporation of vater vapour, which reinforces the warming since water vapour is a strong absorber at infrared wavelengths. Increased water vapour can also lead to increased cloud formation, which may result in a net atmospheric warming or cooling, depending on the cloud altitude and thermodynamic state of the cloud particles.

This coupled nature of cloud processes to other earth-system processes is a major source of uncertainty in current predictions of future climate using global climate models (GCMs). Equally important is the inherent difficulty of representing sub-micron cloud particle formation processes in GCMs, whose grid cells currently are near 100 km horizontally. This gap in scale ensures that the representation of cloud processes and their feedbacks will remain the single largest source of uncertainty in GCM predictions. A great amount of work has been done in the development of Cloud Resolving Models (CRM, *Tao and Moncrieff* (2009)) to bridge this scale gap, but many parameterizations are still necessary to represent cloud processes. The anthropogenic sources of climate change described by the Intergovernmental Panel on Climate Change (IPCC) Summary for Policymakers (*Alley et al.*, 2007) lists cloud-related effects, described in terms of the aerosol direct and indirect effects, as the greatest source of uncertainty in the climate system models.

Subvisual cirrus clouds play three key roles in processes that regulate the earth's climate system. SVC have a definite radiative effect on the heat balance of the atmosphere due to their interactions with incoming solar radiation and outbound infrared radiation. Also, the efficiency of cloud particle formation processes heavily impacts the amount of water vapour that reaches the upper atmosphere, which also affects the radiative balance. Third, cloud-forming particles – a number of which are due to human activities – may be chemically modified by natural cloud processes.

First, SVC can affect the radiative balance of the atmosphere. An increase in earth surface temperature in response to increased anthropogenic 'greenhouse-gas'

emissions will increase the evaporation of water from the earth's surface, primarily through surface evaporation and transpiration through stomata of tree leaves (evapotranspiration). Since water vapour is a more efficient greenhouse gas than carbon dioxide or methane, the initial temperature increase from CO_2 can trigger a larger response in this positive feedback. The changes in water vapour can also change the cloud amount in the atmosphere. The net effect of any cloud is a balance between the opposing albedo and greenhouse effects: either clouds will more dominantly scatter solar radiation back to space and consequently cool the surface, or they will tend to absorb and re-radiate infrared radiation in all directions, causing a net warming of the atmosphere. For cirrus clouds, the greenhouse effect tends to dominate due to the transparency of ice at solar wavelengths and absorptivity at infrared wavelengths. Subvisual cirrus can then be considered as a positive radiative forcing to the climate system.

Second, changes to the cloud amounts can affect the amount of stratospheric water vapour. Increases in stratospheric water vapour (WV) act to cool the stratosphere but to warm the troposphere, and the reverse is true for stratospheric WV decreases (*Solomon et al.*, 2010). Water vapour that has been lofted to the tropopause from the boundary layer by convectively unstable regions preferentially enters the stratosphere in the tropics by slow upwelling through the extremely cold tropical tropopause. As a result, air in the tropical tropopause layer (TTL) is very dry, with typical volume mixing ratios of 3-4 ppmv. It is thought that upper tropospheric air is 'freeze-dried', or dehydrated through this slow ascent to the saturation vapour pressure of ice at the cold point tropopause temperature, which occurs by removing water by ice crystal sedimentation.

According to this hypothesis, there should be a ubiquitous thick cirrus layer below the tropical tropopause, which is not observed (*Holton et al.*, 1995). As well, a number of recent in-situ measurements have shown high in-cloud ice supersaturation, as high as 200%, which could only be explained on this basis by limited nucleation on the surface of ice particles (*Jensen et al.*, 2008). In spite of this, there is very good evidence that the amount of water vapour that enters the stratosphere is sig-

nificantly modulated by the TTL temperature, causing a well-documented seasonal change in WV entering the stratosphere, termed the 'tape-recorder' effect (*Mote et al.*, 1996). In northern hemisphere winter the temperature of the tropopause above the western Pacific warm pool (the Indonesian maritime continent) – which dominates troposphere-to-stratosphere transport in the tropics – is seasonally colder by 3°C, and the water vapour amount entering the stratosphere during this time is 1 ppm lower, in phase with the low temperature (*Fueglistaler et al.*, 2009). In addition to the 'tape recorder' signal (the temperature-WV correlation), the 'tape' speed – the mean ascent rate across the TTL – varies in phase with the low tropopause temperatures, varying from 0.3 mm/s between June and August up to 0.6 mm/s between December and February. Both of these factors influence, and in turn are influenced by, persistent cirrus near the tropical tropopause.

Third, atmospheric particulates are processed by ice clouds. All cloud formation in the atmosphere depends upon the presence of condensation nuclei. In the atmosphere, these take the form of *aerosols*, a catch-all term to denote any non-molecular particle in the atmosphere, which typically are sub-micron in size. Aerosols that act as ice nuclei are dust, sea spray, industrial pollutants, meteoric remnants, and solution droplets formed from volcanic eruptions. The chemical composition of these aerosols can be changed by a cloud through the process of vapour deposition on the aerosol, chemical re-combination during cloud particle formation, and sublimation after particles sediment through a cloud layer.

Lastly, in addition to their importance to climate processes, thin cirrus clouds have the effect of significantly contributing to measurement uncertainty in satellite-based remote-sensing measurements. The presence of a thin cloud layer that efficiently scatters light can significantly impact the retrieval of trace gas amounts from a satellite platform (*Koelemeijer and Stammes*, 1999). Obtaining occurrence distributions and light-scattering properties of these clouds is thus a key element of reducing this uncertainty.

2.1.2 Formation of cirrus clouds

In a rough sense, cirrus clouds form when a moist parcel of air that contains a sufficient number of effective nucleating particles is sufficiently cooled. Any cloud consists of an ongoing competition between particle formation/growth and sedimentation/sublimation. Cooling of air layers to form ice clouds generally occurs through several mechanisms: detrainment outflow from deep convection, slow ascent from adiabatic cooling in the TTL, lifting from synoptic-scale weather systems, and wave-induced updrafts.

Subvisual cirrus are thought to form predominantly by slow, in-situ lofting. For this type of formation a three-layer conceptual model works quite well to describe cirrus formation and persistence, and agrees well with in-cloud measurements of ice crystal sizes and shapes. As illustrated in Figure 2.1, most ice crystal formation occurs near the cloud top in the *nucleation layer*, which has the highest relative humidities and coldest in-cloud temperatures. This layer is typically supersaturated with respect to ice. In the thicker *aggregation* or *growth layer*, particles sediment

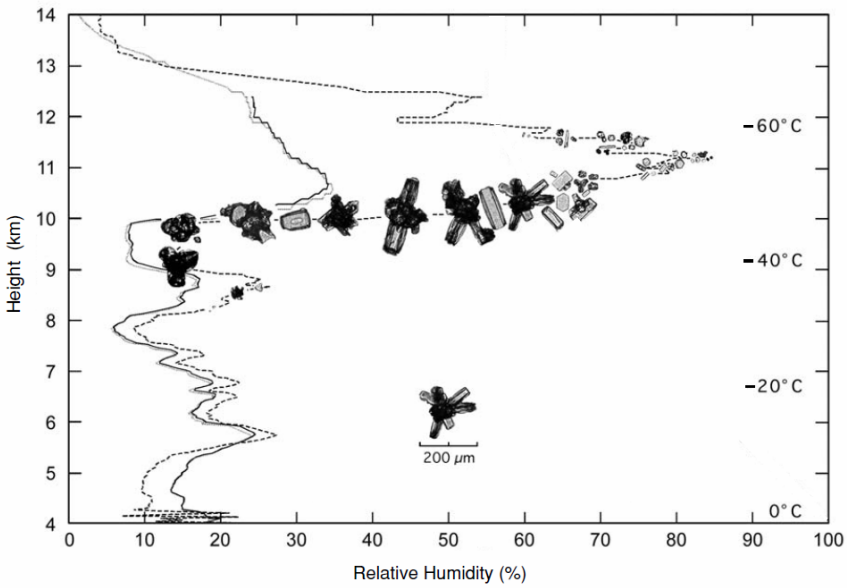

Figure 2.1: Height profile of cirrus ice crystal sizes and shapes with respect to relative humidity and temperature (*Liou*, 2002).

and grow mainly by vapour diffusion onto solid particle surfaces. Near cloud bottom,

the *sublimation layer* is vertically thinner and is composed of more rounded crystals, where sublimation in the subsaturated region results in gradual decay and eventual disappearance of the crystals. In the most common situation due to conditions in which a typical value of the Reynolds number is 10^{-3}, ice crystals throughout a cirrus cloud are randomly-oriented due to eddy shedding during sedimentation. Clouds that form in-situ just below the tropopause are typically 'capped' from above since the temperature begins to increase several hundred metres above. Occasional overshooting of humid layers from extremely strong convection events can inject ice crystals above the local tropopause, although this is relatively rare (*Fueglistaler et al.*, 2009).

There is a large range of ice crystal shapes and sizes encountered within a typical cirrus cloud. Figure 2.2 shows in-situ images of cloud ice crystals form an aircraft-mounted Cloud Particle Imager (CPI) probe, which is described in the next section. As seen from several images in this figure, crystals with hexagonal symmetries are

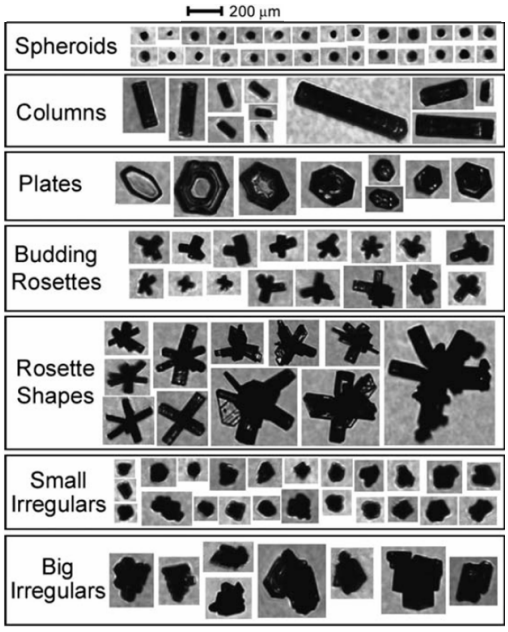

Figure 2.2: In-situ Cloud Particle Imager (CPI) images of various cirrus ice crystals shapes (*Lawson et al.*, 2006).

very common, with hexagonal plates and columns, together with rosettes, comprising the bulk of cirrus cloud ice. The conditions in which cirrus clouds form significantly affect the shape (called the crystal 'habit') and potential sizes of the ice crystals.

Within deep convective cores, updraft speeds on the order of metres per second are not uncommon (*Jensen et al.*, 1994), which results in very fast ice crystal growth by deposition and aggregation. In slowly ascending and radiatively cooled layers, ascent rates are on the order of centimetres per second (*Starr and Cox*, 1985) and crystal growth rates are much smaller, which tends to produce more pristine crystals. These aspects, in turn, affect the radiative properties of the cloud. The dependence of nucleation rate on updraft speeds has been studied extensively in microphysical models, the physical basis of which will be briefly discussed. Recent *in situ* studies (*Lawson et al.*, 2008) have shown subvisual cirrus clouds containing unusually large (100 μm) ice crystals near the tropical tropopause in the absence of convective activity, suggesting additional formation of subvisual cirrus from gravity wave perturbations to the temperature and updraft speed profiles.

Nucleation processes in ice clouds are classified by the thermodynamic phase in which crystal growth occurs. In *homogeneous nucleation*, an ice crystal forms spontaneously from a droplet of supercooled liquid water, and the molecules in the droplet must overcome the activation energy for diffusion across the water-ice boundary. The energy of formation of a 'critical embryo' – typically modeled as a spherical cap, must first be overcome – which is assumed to occur through sufficient fluctuations in the mother phase (*Pruppacher and Klett*, 1997). Homogeneous nucleation requires very high ice supersaturations and very low temperatures – typically above 140% and below -40°C. Water droplets at cirrus altitudes can also contain dissolved salts, which further lower the temperature for homogeneous ice nucleation. The presence of these and other aerosol particles affect nucleation rates, depending on their solubility in water. Frequently, homogeneous nucleation results in several preferential growth sites in the outward direction from a frozen droplet. Ice pillars that grow outward from these sites form the large 'rosette'-type crystals seen in Figure 2.2.

Heterogeneous nucleation of ice occurs on the surface of insoluble ice nuclei (IN), which are typically organic substances, mineral dust, or metals (*DeMott et al.*, 1998). This mechanism is thought to occur through several possible pathways. In vapour deposition, molecules in supersaturated conditions are adsorbed onto the IN surface.

In condensation freezing, the soluble liquid component of a mixed particle causes condensation, while the insoluble component acts as a catalyst for freezing. In contact freezing, a solid particle initiates freezing upon collision with a supercooled water droplet. Lastly, supercooled water droplets can be deposited onto a dry sulphate particle. Microphysical modeling of heterogeneous nucleation is less mature due in part to the difficulty involved in determining the surface reaction properties for the large number of materials that can act as ice nuclei.

The relative importance of homogeneous and heterogeneous nucleation is currently highly disputed. In strong updrafts with rapid cooling – as in deep convection in the inter-tropical convergence zone (ITCZ) – homogeneous nucleation is thought to dominate, whereas heterogeneous nucleation is expected dominant in synoptic-scale lifting, where cooling rates are much smaller. In the TTL there are a large number of available ice nuclei, in the range of $n \sim 1 - 10^2$ cm^{-3} depending on type and volcanic activity, but the activation efficiency of many of these is very low, with typically only 1 in 10^3 particles becoming activated to form an ice crystal. Model studies into the effects of heterogeneous ice nuclei against a control scheme of homogeneous-only nucleation (*Kärcher*, 2004) show that the dehydration potential of heterogeneous nuclei is 0.3 ppmv WV compared to 1.3 ppmv for homogeneous nucleation, but that cloud occurrence frequency increases significantly with heterogeneous ice nuclei concentration for IN amounts as low as $n = 0.01$ L^{-1}.

The classification of ice nuclei aerosol type is a key element in attributing any changes to cloud properties that result from the addition of anthropogenic aerosols. Recent in-situ mass spectrometry of ice crystals and interstitial aerosols showed ice nuclei rich in oxidized organic matter (*Froyd et al.*, 2010). *Murray et al.* (2010) showed in a cloud simulation chamber that heterogeneous nucleation onto typical 'glassy' aerosols are consistent with high in-cloud humidity and typical ice number densities. Rather than the formation of smaller, more numerous particles that would accompany homogeneous nucleation, heterogeneous nucleation was seen on fewer, larger glassy aerosols that could explain several campaigns that have measured low numbers of ice crystals and high in-cloud humidity (*Jensen et al.* (2008), *Kärcher*

(2002)).

2.2 Measurements of subvisual cirrus clouds

The first observations of subvisual cirrus clouds were made by World War II fighter pilots, who reported a thin layer of cirrus several hundred feet above them. As they ascended, the thin layer of cirrus appeared to still be above them, earning them the nickname 'cirrus evadus'. Due to their very low detection thresholds, subvisual cirrus were not remotely observed until the development of sufficiently sensitive lidar, solar occultation, and limb-viewing instruments.

The first in-situ samplings of SVC were measured in the mid-1970's by *Heymsfield* (1986), in which high-altitude aircraft were flown through clouds first identified by ground-based lidar measurements. An extremely cold cloud (-83°C) at altitudes above 16.5 km was sampled in the western Pacific warm pool with particle sizes much smaller than typical cirrus. Modal peaks in the size distribution were near 10 μm and maximum dimensions were 50 μm based on sizing measurements with a forward scattering spectrometer probe (FSSP) and a formvar replicator. The replicator probe measurements showed the cloud to be composed of roughly equal parts trigonal or hexagonal plates and columnar crystals with some bullet rosettes, without the larger aggregates typically found in cirrus.

The first space-based observations of subvisual cirrus were made by solar occultation measurements. In this measurement geometry, in which the satellite instrument observes the rising and setting of the sun through the atmosphere, the transmission at a range of wavelengths through the atmosphere is used to infer the composition of absorbing and scattering atmospheric constituents. Measurements are also typically made outside any significant amount of atmosphere for ongoing calibration purposes. In such a geometry the instrument has a long observation path length through the atmosphere, and as such is sensitive to thin cloud layers with good height resolution. A global climatology of subvisual cirrus was reported from the SAGE II solar occultation instrument by *Wang et al.* (1996). This provided a long-term global record of

the distributions and optical thicknesses of SVC from 1985 to 2005. This climatology indicated occurrence frequencies near 50% in key areas in the tropics, as well as a negative correlation between high-altitude cloud occurrence and lower stratospheric WV mixing ratio. SAGE II observations also suggested that the overall effect of subvisual cirrus clouds is a net positive radiative forcing of 0.5-1 W/m^2 in the tropics.

Active measurements have detected the presence of SVC for the longest period of time. Lidar measurements, which measure the attenuated backscatter signal from a gated polarized laser beam, provide high-resolution measurements of cloud backscatter. The current definition of SVC was established by *Sassen and Cho* (1992), who operated a ground-based polarized 694 nm lidar together with an all-sky camera to characterize mid-latitude cirrus clouds (Salt Lake City, 40°N, 111°W). The *optical thickness* τ_c of SVC, a dimensionless parameter that will be defined in Chapter 3, was measured with lidar backscatter to lie below a threshold value of $\tau_c = 0.03$ using concurrent all-sky images. Cloud linear depolarization measurements were made using the incident polarized laser, with typical depolarization values of 0.3-0.4, and in-cloud temperatures of between $-40°$ and -55°C.

The first space-based lidar cirrus detections were made from the LITE instrument on space shuttle STS-64 (*Winker and Trepte*, 1998), and determined the typical vertical thickness of these clouds to lie between several hundred metres and one kilometre, and showed horizontal extents from several hundred up to over a thousand kilometres. This study also showed several occurrences of subvisual cirrus above the tropical tropopause. Lidar measurements from the CALIPSO satellite (*Sassen et al.* (2008), *Martins et al.* (2011)), launched in 2006, provide global coverage and high vertical resolution (60 m) with the ability to monitor multilayered clouds. Their results have confirmed previous measurements that showed the highest occurrences within and surrounding the ITCZ, where the highest occurrences are concentrated over the western Pacific warm pool and near the Congo and Amazon basins. Despite the very good spatial resolution, CALIPSO detections of SVC are limited to clouds with optical thicknesses $\tau_c > 10^{-3}$ due to their relatively low signal-to-noise ratio.

Recent in-situ measurements of SVC have given a more clear picture of the micro-

physical properties of these clouds. Using cloud particle imaging equipment mounted on high-altitude aircraft, *Lawson et al.* (2008) and *Jensen et al.* (2008) indicated the presence of large ice crystal sizes in SVC, with maximum dimensions of up to 100 μm, compared with 50 μm or less from earlier measurements (*Heymsfield*, 1986). Cloud particles of this size are quite unexpected near the TTL since sedimentation rates for such large particles would preclude cloud lifetimes longer than an hour, even for strong wave activity and particle aspect ratios above 10:1. These measurements were made with independent imaging and sizing instruments. The Cloud Particle Imager (CPI) probe takes stunning images of cloud particles with 2.3 μm pixels with an imaging laser triggered by a particle-detection beam. The CPI images shown in Figure 2.3, which were taken inside a subvisual cirrus cloud, show thin plates with hexagonal and trigonal symmetries. Complementary sizing measurements in this

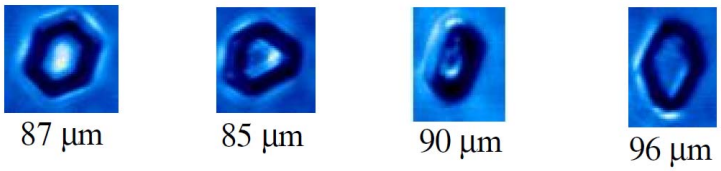

Figure 2.3: In-situ CPI images of subvisual cirrus ice crystals (*Jensen et al.*, 2008).

campaign were made with a 2D-S stereo probe that forms two separate, diffraction-corrected images of ice crystals from orthogonally-placed linear pixel arrays that are both perpendicular to the direction of aircraft motion. The crystal habit distributions reported in this study also display more tendency toward quasi-spherical and hexagonal plate geometry, in contrast with the hexagonal columns, plates, and bullet rosettes reported earlier.

Insight into the composition of ice nuclei from evaporated ice crystals was gained during the same campaign from in-situ mass spectrometry measurements (*Froyd et al.*, 2010). These measurements indicated that the dominant nuclei were mixed sulphate aerosols and organic material. Ice nuclei composed of mineral dust showed evidence of organic and sulphate coatings, which would lower their effectiveness as heterogeneous ice nuclei. This study also showed that, in contrast with similar measurements of cumulonimbus anvil cirrus whose nuclei were primarily mineral dust and

sea salt (*Cziczo et al.*, 2004), SVC predominantly form on sulphate-organic aerosols, with a small contribution from mineral dust.

Recent work at CERN (*Kirkby et al.*, 2011) that simulated galactic cosmic rays (GCRs) in the Cosmics Leaving OUtdoor Droplets (CLOUD) experiment has attracted significant interest from their novel studies on the role of GCRs on sulphuric acid nucleation rates, particularly as a non-anthropogenic climate forcing from solar-induced changes in natural GCR flux. During periods of low solar activity, it has been hypothesized that increased GCR flux can increase the rates of cloud condensation nuclei formation, which could induce a change in the cloud albedo effect. *Kirkby et al.* (2011) found that the presence of ammonia vapour inhibits evaporation of very small (< 1 nm) sulphuric acid droplets, allowing these to grow to sufficient size (500 nm) to form condensation nuclei for homogeneous freezing. This effect was enhanced in the presence of the simulated GCR flux. While this experiment has shed significant light on early particle formation processes, the ammonia concentrations and changes to GCR flux were much greater than those encountered in the atmosphere (*Pierce*, 2011).

Moving from the microphysical scale to global scales, the two current global climatologies of SVC currently available do not agree well with each other. Occurrence frequencies from SAGE II (*Wang et al.*, 1996), which measured from 1985-2005, and CALIPSO (*Fu et al.*, 2007), which was launched in 2006 and continues operation, are different by a factor of more than two in the tropics (*Fueglistaler et al.*, 2009). This is partly due to CALIPSO's limited SVC detection range, as noted above. The cloud occurrence frequency, as well as the cloud optical depth and effective particle size, are essential inputs to GCMs and are required constraints in CRMs. Further study of the occurrence and optical properties of these clouds is certainly needed. We now turn to the limb measurement geometry, which is the platform used in this work.

2.3 Limb Scatter Measurements

2.3.1 Technique

A number of space-based measurements have used scattered sunlight for retrieving atmospheric constituents. Long-term monitoring of ozone has been done by the NASA Total Ozone Mapping Spectrometer (TOMS) and Solar Backscatter Ultraviolet instrument (SBUV), which both observed in a nadir direction. By scanning the instrument field of view across the satellite track and measuring the backscattered UV brightness, these instruments are able to measure the quantity of absorption by ozone and provide total (column) amounts of ozone with high horizontal resolution. As well, some vertical information of the distribution of absorbing species can be inferred from the use of several wavelengths that have differing absorbtion strengths, but this method is quite limited at altitudes below the peak ozone number densities in the stratosphere.

The limb-scattering method is a relatively new remote sensing technique that measures scattered sunlight from the atmospheric limb, that is, the glowing edge of the atmosphere. In this measurement geometry, the instrument line of sight is pointed toward the atmospheric limb and vertically scanned to obtain the spectral brightness at a set of tangent altitudes. In addition, and array of sensors can be mounted to make continuous profile measurements. From either measurement, the variation of the scattered brightness at selected wavelengths can provide height-dependent absorbing and scattering properties for the measured volume. The basic measurement geometry for a limb-scanning instrument is shown in Figure 2.4. In this figure, shown as a vertical cross section in a plane that contains the instrument line of sight, the sun is far out of plane, and the instrument line of sight – defined by the observer 'look' direction, $\hat{\mathbf{\Omega}}$ – passes most near to the surface at the tangent height, h_t. The location of the sun in this measurement geometry is typically defined by several angles specified at the line of sight tangent point. The *solar zenith angle*, θ_0, the angular distance of the solar direction from the local zenith; the *solar scattering angle*, Θ_0, defined as the angle through which solar radiation is deflected by scattering directly

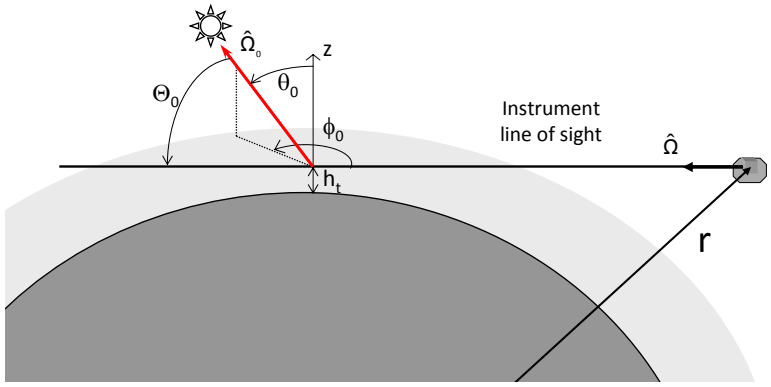

Figure 2.4: Limb scatter geometry, showing the definitions of solar zenith angle (θ_0), solar azimuth angle (ϕ_0), and solar scattering angle (Θ_0).

into the instrument line of sight, $\cos\Theta_0 = \hat{\mathbf{\Omega}}_0 \cdot \hat{\mathbf{\Omega}}$; and the *solar azimuth angle*, ϕ_0, as measured counterclockwise from the instrument line of sight.

The limb-scattering technique provides two advantages. First, since the satellite instrument is measuring scattered sunlight, it can make continuous measurements throughout the daylight portion of the orbit, and thus can make many profile measurements per orbit in contrast with solar occultation's sunrise and sunset. Second, this technique provides good height resolution, as multiple height measurements are made as the line of sight scans the height of the atmosphere. These advantages come at the expense of increased difficulty in modeling and retrieval of parameters from the measurements. Since the observer line of sight passes through very long segments of atmosphere near the tangent point, horizontal homogeneity is required in retrievals from such an instrument, although tomographic retrievals can be done with fast enough sampling.

The first instrument to use this geometry was the Solar Mesosphere Explorer (SME, *Barth et al.* (1983)), which measured limb brightness at solar wavelengths. Lower-altitude limb-scattering measurements required the use of radiative transfer computations employing a spherical geometry that accounts for multiple scattering and improved instrument pointing. This was investigated with the Shuttle Ozone Limb Sounding Experiment (SOLSE) and Limb Ozone Retrieval Experiment (LORE), flown as proofs of concept on space shuttle flight STS-87 in 1997, which

measured ozone profiles at 3 km vertical resolution for altitudes between 15 and 40 km (*McPeters et al.*, 2000).

Most recently, three instruments have been employed in limb-scattering measurements of ozone, other trace gases, and stratospheric aerosols. The Scanning Imaging Absorption Spectrometer for Atmospheric ChartographY (SCIAMACHY) instrument, which was launched on the European Space Agency's ENVISAT satellite in March, 2002, and which recently ceased operations, made spectral measurements from 220 nm to 2380 nm with 3 km vertical resolution (*Bovensmann et al.*, 1999). The Ozone Mapper and Profile Suite (OMPS) instrument on NASA's Suomi National Polar-orbiting Partnership satellite (NPP), which was launched in October of 2011, measures ozone and stratospheric aerosols in both nadir and limb-viewing geometries. The Canadian Optical Spectrograph and InfraRed Imaging System (OSIRIS), launched in February, 2001, and in operation at time of writing, is the only other instrument currently making limb-scatter measurements, and is the subject of this work.

Several techniques have been developed for retrieval of atmospheric trace gases from limb-scattered spectra, including spectral analysis methods (*Flittner et al.* (2000), *Von Savigny et al.* (2003)), Differential Optical Absorption Spectroscopy (DOAS, *Haley et al.* (2004), *Rault* (2005)), and a Multiplicative Algebraic Reconstruction Technique (MART, *Degenstein et al.* (2009)) for trace gases and stratospheric aerosols.

Some work in retrieval of cloud properties in a limb geometry has been done with the Microwave Limb Sounder (MLS) radiometer (*Wu et al.*, 2006), which measures emissions at millimetre and submillimetre wavelengths. Retrieval of cloud optical properties from a limb-scattering satellite platform, however, has not been done before, and is of significant interest, in particular considering the previously-mentioned discrepancy between standard SVC optical property climatologies from SAGE II and CALIPSO and their importance as GCM inputs.

2.3.2 OSIRIS on Odin

The Canadian OSIRIS instrument (*Llewellyn et al.*, 2004) is on the Swedish-led satellite Odin (*Murtagh et al.*, 2002), whose designed purpose was to measure molecular emissions and scattered sunlight in the atmospheric limb. Odin was launched into a retrograde sun-synchronous orbit, inclined at 97.8° to the equatorial plane, on February 20, 2001. The ascending node of Odin is at 1800 local solar time. Since the OSIRIS field of view is pointed at the limb in the along-track direction, the latitudinal coverage is from 82°S to 82°N. The 96 minute orbit period gives longitudinal coverage of the earth over one day, with each successive ascending node track displaced 24° to the west. During the equatorial and mid-latitude portions of the ascending and descending nodes, the local time remains quite constant, and Odin sweeps quickly through local noon and midnight at high latitudes.

Cloud detections and retrieval of cloud properties with OSIRIS can only be done during the sunlit portion of the orbit ($\theta_0 < 90°$), which varies in latitude throughout the year due to orbit precession. The variation of the mean tangent-point solar zenith angle throughout 2002 is shown for reference in Figure 2.5. In this figure it is seen

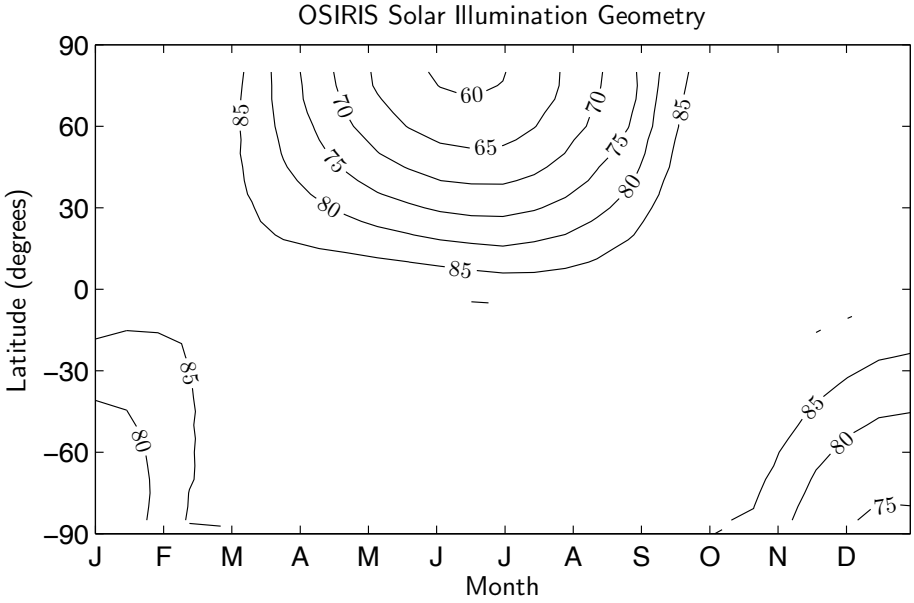

Figure 2.5: Latitudinal variation of OSIRIS tangent point solar zenith angle throughout the year.

that solar zenith angle in the tropics (30°N to 30°S), which is the region of primary interest in SVC studies, is always greater than 75°. As well, during the ascending and descending node equatorial crossings, the sun is near the horizon, or $\theta_0 \approx 90°$, due to the near-terminator orbit. The solar zenith angles remain quite close to 90° at all latitudes during the terminator days in late February and early October, where the orbit plane is oriented directly toward the sun.

Since retrieving cloud properties requires modeling the scattering of sunlight by cloud ice particles, it is necessary to consider the variation in solar scattering angle, Θ_0, in the dominant SVC region over the course of the year. The variation in the scattering angle from the sun directly into the instrument line of sight at the tangent point for low-latitude measurements is shown in Figure 2.6. Due to the changing ori-

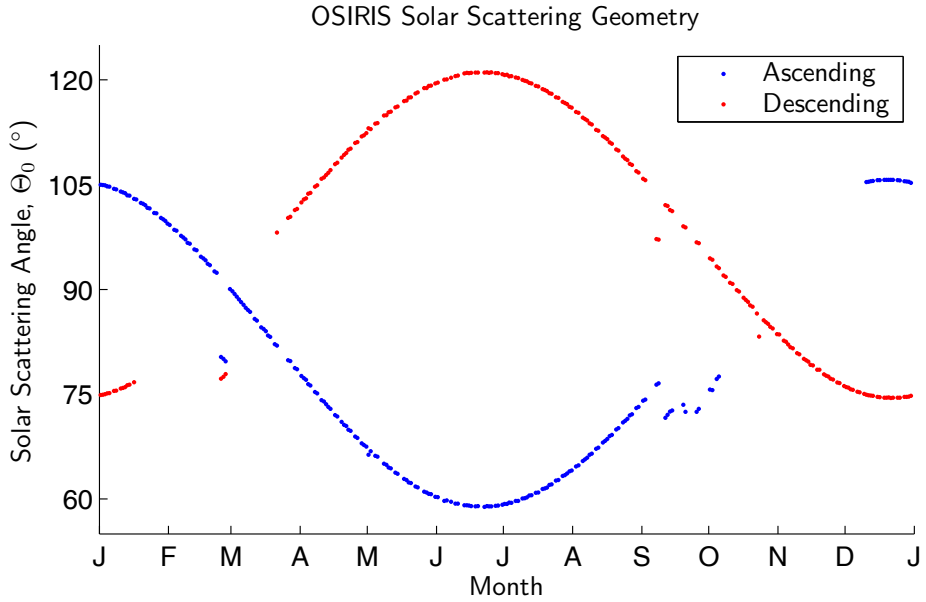

Figure 2.6: Mean solar scattering angle for ascending- and descending-node measurements at latitudes between 15° S and 15° N.

entation of the orbit plane with respect to the sunward direction from its precession, the scattering angles at the ascending and descending nodes vary throughout the year between 60° and 120°. Between March and October in this figure, Odin moves toward the sun on the ascending node, and scattering is in a slightly forward-scattering direction, $60 \leq \Theta_0 < 90°$. On the descending node during these months, Odin

moves away from the sun, and the geometry is oriented slightly towards backscatter, $90 \leq \Theta_0 < 120°$. During the other months of the year this scattering geometry is reversed due to precession of Odin's orbit. This variation in scattering angle can be used to infer information about the scattering properties of a volume sampled first on the ascending node and later on the descending node, assuming that the constituents of the volume have not changed significantly during that time.

The OSIRIS instrument itself consists of two subsystems, an Optical Spectrograph (OS) that measures scattered sunlight between 280 and 810 nm with approximately 1 nm resolution, and an InfraRed Imaging System (IRIS) that measures excited O_2 and OH emissions at 1.26, 1.27, and 1.53 μm. The optical axes of the two subsystems are coaligned and point on-track, in the direction of travel, at the atmospheric limb. The Odin satellite itself nods to scan the horizontally-oriented OS entrance slit over tangent heights between 10 and 60 km to obtain height profiles of the scattered brightness across the UV-visible-near IR spectrum. Each OS scan takes approximately 90 seconds, allowing for roughly 60 scans per orbit. At typical exposure rates, successive exposures in OS scans are separated by 1.5-2 km in tangent altitude. The pointing accuracy from the on-board control system is approximately $\pm$15 arcseconds, or $\pm$200 m vertically at the tangent point.

A typical limb spectrum is shown in Figure 2.7, where the spectral radiance is shown as a function of tangent altitude and wavelength. The *radiance*, which is defined in the following chapter, has units of photons per square centimetre per second per steradian per nanometre, and is an indication of the power measured per detector surface area for a given instrument field of view and spectral resolution. At most wavelengths in Figure 2.7, the measured radiance is seen to increase at a near-exponential rate together with the molecular number density in the atmosphere. Several molecular absorption features are visible in this figure, such as the Chappuis band of ozone between 530 and 700 nm, as well as the molecular oxygen A-band near 762 nm. The data missing between 475 and 535 nm result from the use of a spectral order sorter with the diffraction grating, where measurements from this area are not used.

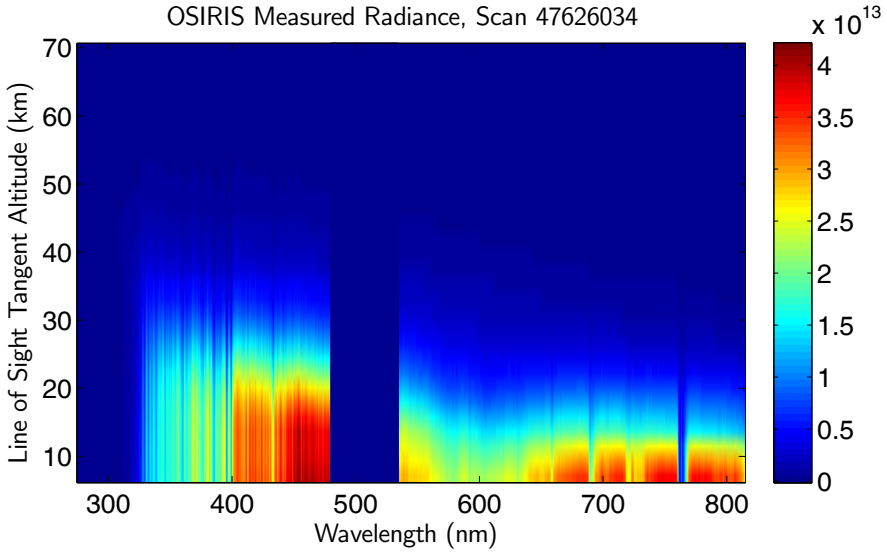

Figure 2.7: Typical measured limb-scattered radiance from OSIRIS.

Frequently, at the lowest tangent altitudes, significant enhancements to the Rayleigh-scattered signal are seen that correspond well in location and frequency of occurrence to cirrus clouds. An example of such an enhancement is shown in Figure 2.8a, where the measured radiances at tangent altitudes below 30 km are shown at left as a function of wavelength. In this figure, since the measured signal is brightest at low

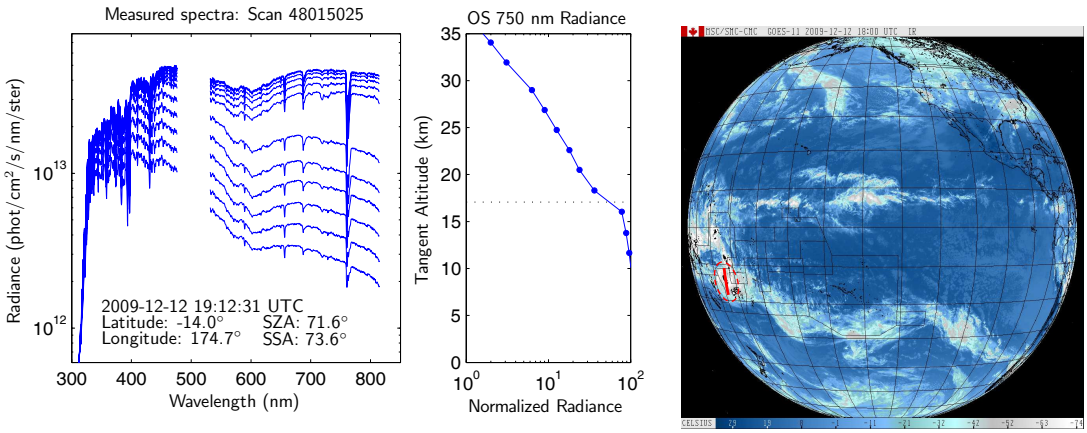

(a) OSIRIS scan 48015025 (b) Concurrent GOES-11 image

Figure 2.8: Upper-tropospheric enhancement to limb brightness at 750 nm.

altitudes where the molecular number density is the highest, the brightest spectra

are recorded at the lowest tangent altitudes.

The height profile of the 750 nm radiance, shown with respect to the radiance at a cloud- and aerosol-free altitude of 37.5 km, is shown in the middle panel of this figure. In general, the 750 nm radiance profile follows the exponentially-increasing number density profile, but a clear enhancement above this trend occurs at 16 km altitude, below which the signal remains very bright. For reference, the dotted line in this figure indicates the height of the thermal lapse rate tropopause at the scan location, as determined from NCEP (National Centers for Environmental Prediction) 6-hour reanalysis data.

A concurrent GOES full-disk image of 10.7 μm brightness temperature is shown in Figure 2.8b, where the approximate scattering volume of the OSIRIS scan is indicated by the solid red line. It is clear that this OSIRIS scan directly observed the middle of a widely-distributed deep convective system over the south Pacific Ocean, where the brightness temperature near the top of the outflow anvil was below -75°C. The spectral signature of this cloud system shows a distinct increase in the long-wavelength (500-810 nm) portion of the measured spectrum that is characteristic of in-cloud multiple scattering.

Many OSIRIS scans indicate a similar enhancement to the limb radiance near the tropopause, but the radiance profile suggest the presence of a very thin scattering layer. Figure 2.9a shows a scan in which the radiance profile increases significantly just below the tropopause but maintains a near-Rayleigh scattering-dominated profile below. The spectral dependence of the enhanced radiance in this figure also shows the characteristic increase in long-wavelength radiance that was evident in Figure 2.8a. However, in contrast with the previous scan, there is no visible cloud present in the concurrent GOES image despite the existence of a significant enhancement to the measured spectra just below the tropopause. Such measurements are suggestive of the presence of clouds characterized by geometrically thin and horizontally broad regions that contain strongly-scattering particles.

A direct comparison of in-cloud and clear-sky radiances at identical tangent altitudes is shown in Figure 2.10. Even for a very thin cloud, such as shown in Figure

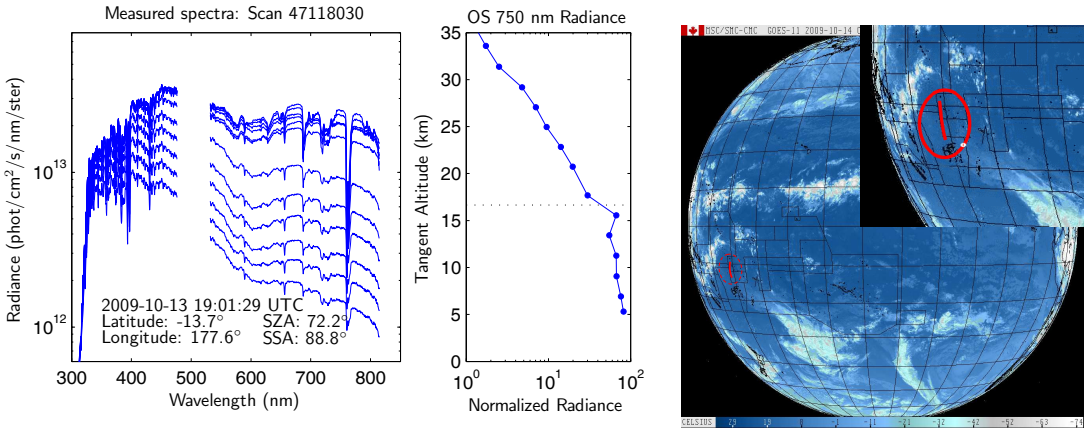

(a) OSIRIS scan 47118030 (b) Concurrent GOES-11 image

Figure 2.9: OSIRIS observation of subvisual cirrus cloud.

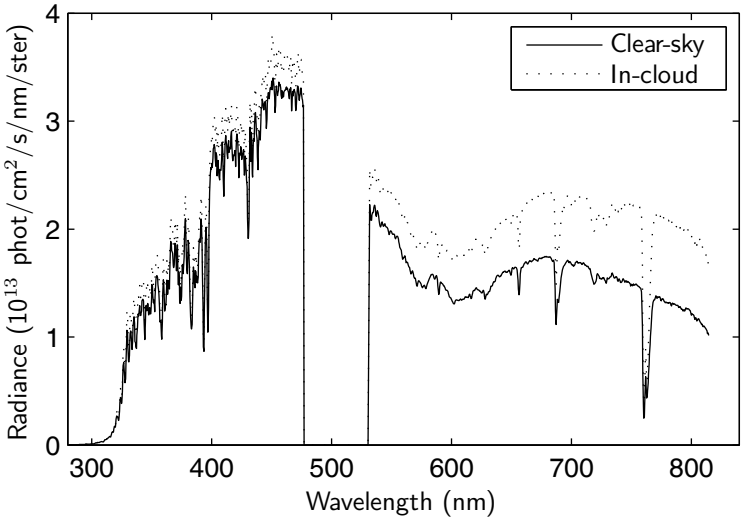

Figure 2.10: OSIRIS in-cloud radiance and clear-sky radiances at the same altitude.

2.10, the enhancement to the measured spectrum at wavelengths above the spectral order sorter is significant. As well, it is characteristic that this increase is largely restricted to wavelengths above 400 nm, and that the in-cloud spectrum exhibits 'whitening', that is, increased enhancement at longer wavelengths.

The difference between the radiance profiles seen in Figures 2.9a and 2.8a relate to the scattering properties of the measured volume, and the characterization of these enhancements by assuming known ice crystal scattering properties is, in large

part, the subject of this work. The presence of such enhancements to the radiance measured at 750 nm is used as a detection criterion for cirrus clouds, which is now discussed.

2.4 OSIRIS Cirrus Detections

2.4.1 Cloud-top detection algorithm

OSIRIS measurements at the lowest tangent altitudes are made over very long path lengths through the upper troposphere. As such, the presence of thin cirrus clouds is clearly indicated as has been suggested. In the limb-viewing geometry used by OSIRIS, the measured brightness is closely related to the scattering properties near the tangent point, since the instrument line of sight passes through a long horizontal region with relatively high number densities. Although the formal presentation of radiative transfer theory is presented in the next chapter, a simple cloud-top detection algorithm is formed using a solution to the equation of radiative transfer, namely equation (3.43).

The purpose of this detection algorithm is to detect the presence of the significant upper-tropospheric enhancement to the 750 nm radiance profile seen in Figures 2.8a and 2.9a. If all of the measured signal brightness at a given tangent altitude, $I(h)$, is assumed to come from the region immediately surrounding the tangent point, then it can be assumed that the brightness is expressed as

$$I(h) = [\sigma_m \, n_m(h) + \sigma_c \, n_c(h)] I_0 \, \Delta s. \tag{2.1}$$

In this expression, it is assumed for present purposes that the scattering behaviours of molecular constituents and ice crystals do not differ significantly for the scattering geometry of interest. In this expression, $n_m(h)$ and $n_c(h)$ are the molecular and cloud particle concentrations, respectively, and σ_m and σ_c are the molecular and cloud scattering cross sections, which are discussed in detail in Chapter 4. The incident brightness is denoted by I_0 and the path length through the scattering region by Δs.

If the ratio of the brightness from two heights is taken, then the brightness ratio, $\tilde{I} = \frac{I(h_1)}{I(h_2)}$, relative to the molecular number density ratio, $\tilde{n} = \frac{n_m(h_1)}{n_m(h_2)}$, at these heights is

$$\frac{\tilde{I}}{\tilde{n}} = \frac{\sigma_m\, n_m(h_1) + \sigma_c\, n_c(h_1)}{\sigma_m\, n_m(h_2) + \sigma_c\, n_c(h_2)} \frac{n_m(h_2)}{n_m(h_1)} \frac{\sigma_m}{\sigma_m}, \tag{2.2}$$

If the reference height h_2 is taken above any aerosol or cloud particles, typically above 37 km, then $n_c(h_2) = 0$ so that

$$\frac{\tilde{I}}{\tilde{n}} = 1 + \frac{\sigma_c}{\sigma_m} \frac{n_c(h_1)}{n_m(h_1)}, \tag{2.3}$$

which is rewritten in terms of the quantity $k_{m1} = \sigma_m\, n_m(h_1)$ and $k_{c1} = \sigma_c\, n_c(h_1)$ as

$$k_{c1} = \left(\frac{\tilde{I}}{\tilde{n}} - 1 \right) k_{m1}. \tag{2.4}$$

Within this very simple detection scheme, the quantities k_{c1} and k_{m1} roughly correspond to cloud and molecular *extinctions*, which will be defined in Chapter 3. For the purposes of these detections, the quantity $k_{n1} = n(h)\sigma_n$ and the number density ratio, $\tilde{n}$, are evaluated using the ECMWF (European Centre for Medium-Range Weather Forecasts) number density profile $n(h)$ at the measurement location and the molecular-scattering cross sections, σ_n, which are be evaluated analytically.

Equation (2.4) forms a threshold condition to detect the presence of large upper-tropospheric enhancements. By using the criteria applied by *Wang et al.* (1996) to solar occultation measurements of subvisual cirrus clouds, we find that when the quantity k_{c1} has passed a threshold value of 2×10^{-4} km^{-1}, it is said that the OS has observed a cloud. Two such detection vectors are shown in Figure 2.11, where the effect of cirrus clouds on the detection vector for OSIRIS scan 47626029 is shown as a function of tangent altitude. The maximum value of the detection vector due to cirrus clouds typically lies between 4×10^{-4} and 1×10^{-3}, and the vector typically has a sharp peak from the cloud geometry. The smaller-magnitude, more vertically extended enhancements in the detection vector seen above the tropopause are due to stratospheric sulphate aerosols, which have a lower optical depth than cirrus cloud

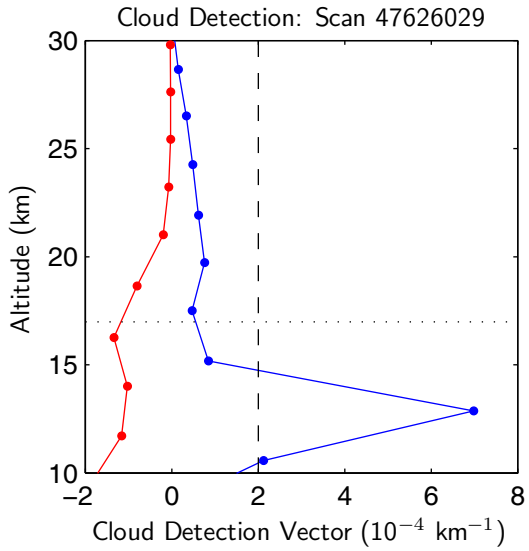

Figure 2.11: OS cloud detection vector, $k_c(h)$ for cloud-free and in-cloud conditions.

particles. Because OSIRIS measures the extinction of these aerosols, this effect can be accounted for within the cloud detections.

The preliminary detections of cirrus made with this algorithm, discussed below, capture well the features seen in existing cirrus climatologies (*Wang et al.*, 1996). Note that the detections shown in this section are for cirrus clouds of all thicknesses, not strictly for SVC.

2.4.2 OSIRIS Cirrus Distributions

Cirrus detections are shown in this section for the measurement period 2001-2007 due to the absence of significant volcanic activity during this time. A world map of cirrus occurrence frequency for all OSIRIS scans is shown in Figure 2.12. In this figure, all cirrus cloud detections that were made with the criterion (2.4) have been placed in 2.5° latitude and longitude bins, and polar stratospheric clouds observed with this technique have been removed. The features in this map have excellent agreement with CALIPSO cirrus measurements (*Sassen et al.*, 2008). Cirrus occur most persistently near areas of intense convection – surrounding the Indonesian maritime continent and the western Pacific warm pool, the Congo basin of Africa, the Amazon basin of South America, and throughout the belt of the ITCZ – as expected from detrainment by

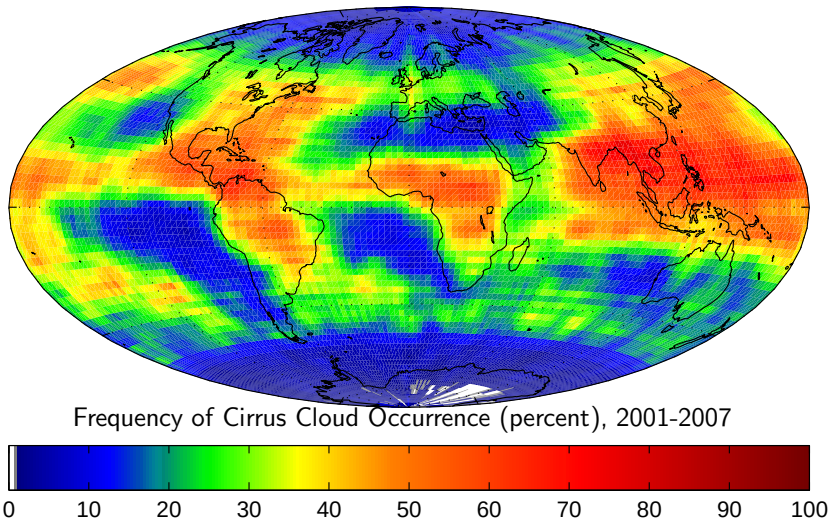

Figure 2.12: World map of cirrus cloud occurrence frequency, 2001-2007.

deep-convective cumulonimbus in these regions. In the sub-tropics, cirrus are rarely observed within the descending regions of the Hadley circulation, which injects dry air into the earth's main desert regions. At midlatitudes, higher cirrus occurrences are seen in the presence of warm ocean currents, for example near the Gulf Stream and the Brazil current.

The meridional distribution of cirrus occurrence frequency is shown in Figure 2.13, where the dotted lines indicate the meridional average tropopause height for each zone. Note the three equatorial convection centres previously mentioned, and as well the high cirrus occurrences seen in the region of the Indian monsoon (15-30°N, 60-120°E). Here the clouds are 2 km higher than at any other location, which likely occurs due to intense convection during the summer Asian monsoon season and orographic lifting caused by the Himalayan mountain range. Though not shown here, this feature appears most strongly in the northern hemisphere summer. The zonal occurrence frequency of cirrus is shown in Figure 2.14. The slightly northern bias of the ITCZ is seen clearly, as are persistent cirrus related to synoptic lifting in midlatitudes, whose heights largely lie 1-2 km below the mean tropopause height,

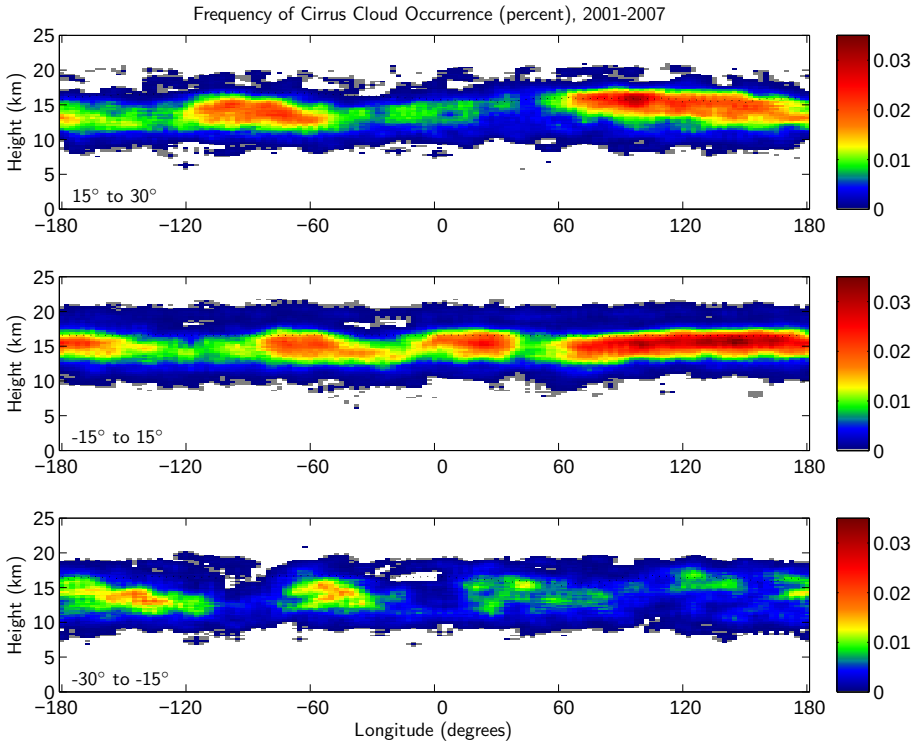

Figure 2.13: OSIRIS meridional occurrence frequencies for cirrus clouds, 2001-2007.

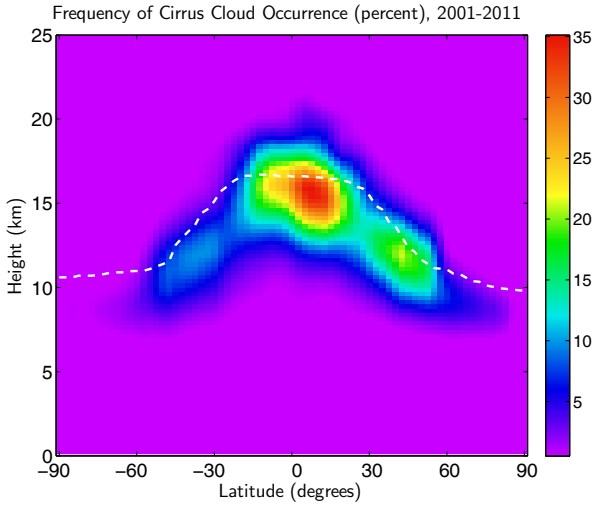

Figure 2.14: OSIRIS zonal average occurrence frequency for cirrus clouds, 2001-2011.

which is shown as a dashed line in the plot.

The cirrus detections from OSIRIS provide a wealth of information on the locations and properties of these clouds. A range of potential studies – of the differences

in clouds between ascending- and descending-node detections that are indicative of diurnal change, seasonal changes in response to global temperature and water vapour trends like El Niño-Southern Oscillation (ENSO) – are possible with this data. These studies require the characterization of these cloud detections in terms of the optical properties of the cirrus ice crystals. The bulk of this work is concerned with enabling this characterization.

Chapter 3

Radiative Transfer Modeling

Radiative transfer theory forms the physical basis for inferences about atmospheric composition from remote sensing measurements. The equation of radiative transfer describes the transportation of radiation through a region as a function of the light-absorbing and scattering properties of the constituents for a given wavelength. The physical basis of radiative transfer theory was given its most complete expression in the work of *Chandrasekhar* (1960), from which most atmospheric and astrophysical models originate. This chapter presents a sufficient amount of the theory to introduce a model that is used to simulate OSIRIS measurements for inferring subvisual cirrus cloud properties.

3.1 Background

The viewing geometry for a satellite instrument that measures limb-scattered sunlight, such as OSIRIS, is shown in Figure 3.1. In the geometry shown, the sun is out of the plane of the figure and the satellite instrument is shown at right. Light is scattered into the instrument's field of view by a combination of many possible processes. Light can be singly scattered toward the observer by a molecule or cloud particle, as shown in path (a). Light can also be scattered into the line of sight after multiple scatters from atmospheric constituents, as shown for three scatters in path (c). Alternatively, light can scatter toward the observer after reflection from the

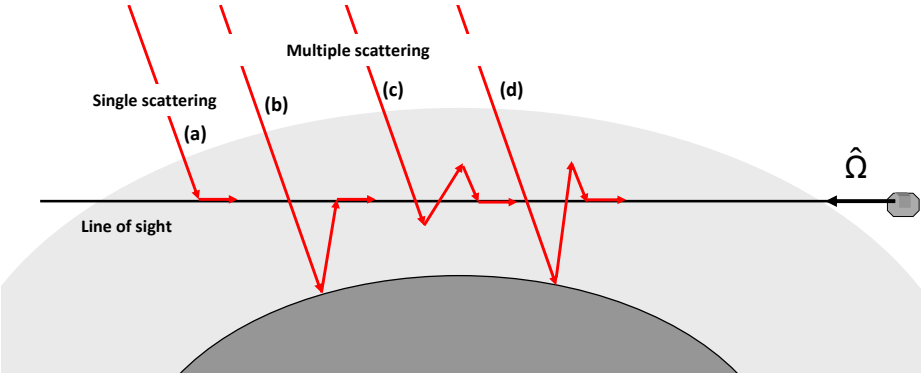

Figure 3.1: Geometry of several possible processes for scattering of sunlight into the line of sight for an observer with a limb-viewing geometry.

ground and several atmospheric scatters, as shown in (b) and (d). The goal of any radiative transfer model is to estimate the amount of light absorbed by the medium, as well as the amount scattered into the observer line of sight through a combination of these many scattering processes.

3.2 Radiative Transfer Theory

The fundamental quantity recorded by a light-sensitive instrument on a satellite platform is the electromagnetic power within its range of wavelength sensitivity that enters its field of view. In this work, the source is the wavelength-dependent brightness of sunlight that has been scattered and attenuated by the atmosphere, as viewed in the atmospheric limb. Before the radiative transfer equation is developed, we define several quantities necessary for the discussion.

3.2.1 Radiometric Quantities

To describe the radiation measured in this work, as well as its relation to other quantities required for radiative transfer modeling, we follow a similar development to that given by *McCartney* (1976).

The most fundamental radiometric quantity is the *radiant energy*, Q, from a source. This and other spectral radiometric quantities are commonly expressed in terms of the number of photons instead of energy units. The radiant energy of a

source, or equivalently, the number of photons emanating from the source, is Q. Since the energy from most sources is strongly wavelength-dependent, this energy is typically expressed as the spectral radiant energy,

$$Q_\lambda = \frac{\mathrm{d}Q}{\mathrm{d}\lambda}, \tag{3.1}$$

such that, as the spectral interval is made indefinitely small, this quantity reaches a definite value. Thus the radiant energy over a spectral interval is found by integration,

$$Q = \int_{\lambda_1}^{\lambda_2} Q_\lambda(\lambda)\,\mathrm{d}\lambda, \tag{3.2}$$

which then is the total energy emitted when the limits are extended to zero and infinity. The spectral *radiant power*, $\Phi_\lambda(\Omega, \hat{\mathbf{\Omega}})$, is the power flowing into a solid angle Ω about a direction $\hat{\mathbf{\Omega}}$, and has units of watts per nanometre, or $\Phi_{\lambda,q}(\hat{\mathbf{\Omega}})$ in units of photons per second per nanometre.

The spectral *radiant intensity*, $R_\lambda(\hat{\mathbf{\Omega}})$, is the radiant power emitted in a given direction, $\hat{\mathbf{\Omega}}$, by a source or an element of the source in the solid angle $\mathrm{d}\Omega$ about the direction $\hat{\mathbf{\Omega}}$,

$$R_\lambda(\hat{\mathbf{\Omega}}) = \frac{\mathrm{d}\Phi_\lambda(\Omega, \hat{\mathbf{\Omega}})}{\mathrm{d}\Omega}. \tag{3.3}$$

As the solid angle about the direction $\hat{\mathbf{\Omega}}$ is made indefinitely small, the radiant intensity takes on a limiting value. The spectral radiant power past a given point in the direction $\hat{\mathbf{\Omega}}$ with infinitesimal solid angle $\mathrm{d}\Omega$ is then $\mathrm{d}\Phi_\lambda(\hat{\mathbf{\Omega}})\,\mathrm{d}\Omega$.

To relate these quantities to remote-sensing measurements, it is necessary to describe the radiant power in terms of its measurement by a surface. The spectral *irradiance* is the amount of radiant power incident from all upward directions on an element of surface divided by the area of the element,

$$F_\lambda = \frac{\mathrm{d}\Phi_\lambda}{\mathrm{d}A}. \tag{3.4}$$

An analogous definition applies for the radiant power that leaves a surface either by

emission or by reflection. The units of irradiance, F_λ, are watts per square metre per nanometre or photons per square centimetre per second per nanometre. The irradiance corresponds to the radiant power per unit cross-sectional area of a light beam. This area may refer either to a virtual surface in space normal to the axis of the beam, or it may refer to a material surface. In this work, radiant energy from the sun is described as an irradiance.

The radiant intensity – considered earlier as the radiant power that originates from a source in a certain direction $\hat{\mathbf{\Omega}}$ – can also be applied to an elemental area of an extended source. In general, the radiant intensity of an elemental area that is measured in a particular direction will vary upon the angle between the surface normal and the viewing direction, $\hat{\mathbf{\Omega}}$. Quite often, if the emission or reflection characteristics of a surface are not well known, the surface is assumed to be a *Lambertian* reflector, in which case the radiant intensity measured by an observer is the same regardless of the observer's angle of view relative to the surface normal. Since the projection of a finite surface area, A, onto a direction $\hat{\mathbf{\Omega}}$ at an angle θ relative to its normal, $\hat{\mathbf{n}}$, is $A\cos\theta = (A\,\hat{\mathbf{n}})\cdot\hat{\mathbf{\Omega}}$, the radiant intensity (3.3) at an angle to the normal is expressed as

$$R_{\lambda,\theta} = \frac{\mathrm{d}\Phi_{\lambda,\hat{\mathbf{n}}}\cos\theta}{\mathrm{d}\Omega}, \tag{3.5}$$

where $\Phi_{\lambda,\hat{\mathbf{n}}}$ is the intensity in the normal direction.

The spectral *radiance* can be defined for an extended surface in a fashion similar to the radiant intensity (3.3). The radiance of a surface, measured at an angle θ, is defined as the ratio of the radiant power leaving a surface element to the product of the projected area and solid angle,

$$I_{\lambda,\theta} = \frac{\mathrm{d}^2\Phi_\lambda}{(\mathrm{d}A\,\cos\theta)\mathrm{d}\Omega} = \frac{\mathrm{d}R_{\lambda,\theta}}{\mathrm{d}A\,\cos\theta}, \tag{3.6}$$

in the limit that $\mathrm{d}A$ and $\mathrm{d}\Omega$ become very small. The second expression is obtained through the definition of radiant intensity, (3.3), and indicates that the radiance in a given direction is the radiant intensity per unit projected area in that direction. Then, for a Lambertian surface and for any viewing direction, the radiance (3.6) can

be written as

$$I_{\lambda,\theta} = \frac{\mathrm{d}R_{\lambda,\hat{\mathbf{n}}}\cos\theta}{\mathrm{d}A\cos\theta} = \frac{\mathrm{d}R_{\lambda,\hat{\mathbf{n}}}}{\mathrm{d}A}, \tag{3.7}$$

and so the radiance of a Lambertian surface is independent of the observation direction. To consider this definition of radiance in the context of measuring scattered light from the atmosphere, we define the radiance in terms of a reference plane normal to the observation direction. In this case, assuming for the moment no attenuation by the medium, the radiance measured by a satellite instrument is then

$$I_\lambda = \frac{\mathrm{d}^2\Phi_\lambda}{\mathrm{d}A'\,\mathrm{d}\Omega'} = \frac{\mathrm{d}F_\lambda}{\mathrm{d}\Omega'}. \tag{3.8}$$

In this case, I_λ is the source radiance, Φ_λ is the radiant power at the normal receiving surface, $\mathrm{d}A'$ is an area element of this surface, $\mathrm{d}\Omega'$ is the solid angle subtended at the observing surface by an area element of the source, and F_λ is the source irradiance. The formulations (3.6) and (3.8) define radiance in terms of the receiving and sending ends, respectively. By comparison of these two equations, we can say that the radiance measured by a satellite instrument is then the radiant power incident per unit area of receiving surface per steradian of sky, which is the quantity used in this work to describe the measured spectral brightness from OSIRIS.

We consider briefly the relation between the irradiance incident on a partially-reflecting surface and the radiance measured at an angle relative to the surface normal. This relation is necessary for modeling the radiance due to scattering that occurs at the surface of the earth. The *albedo* of a surface, a_λ, is the ratio of the reflected and incident irradiance to a surface,

$$a_\lambda = \frac{F_{\lambda,\mathrm{reflected}}}{F_{\lambda,\mathrm{incident}}}, \tag{3.9}$$

and expresses the wavelength-dependent bulk reflective properties of the surface. Equation (3.6) can be used to express the differential radiant power emanating from the surface as

$$\mathrm{d}^2\Phi_{\lambda,\mathrm{reflected}} = I_{\lambda,\theta}\,\mathrm{d}\Omega\,\mathrm{d}A\cos\theta. \tag{3.10}$$

If the incident and reflected radiant power to the area element are expressed as irradiances and related by the albedo through equation (3.9), then the outbound radiance is related to the radiant power incident on $\mathrm{d}A$ through

$$\mathrm{d}^2\Phi_{\lambda,\text{incident}} = a_\lambda \, I_{\lambda,\theta} \, \mathrm{d}\Omega \, \mathrm{d}A \cos\theta. \tag{3.11}$$

If both sides of (3.11) are integrated over the hemisphere above the surface $\mathrm{d}A$, and recalling that the radiance from a Lambertian surface is independent of viewing angle, then we find that

$$\begin{aligned} \mathrm{d}\Phi_{\lambda,\text{incident}} &= \mathrm{d}A \int_{2\pi} \cos\theta \, a_\lambda \, I_{\lambda,\text{reflected}} \, \mathrm{d}\Omega \\ &= \mathrm{d}A \, 2\pi \, a_\lambda \, I_{\lambda,\text{reflected}} \int_0^{\pi/2} \cos\theta \sin\theta \, \mathrm{d}\theta \\ \mathrm{d}\Phi_{\lambda,\text{incident}} &= \mathrm{d}A \, \pi \, a_\lambda \, I_{\lambda,\text{reflected}}. \end{aligned} \tag{3.12}$$

Then, from the definition of irradiance (3.4), we find that the radiance emanating from the surface element is related to the incident irradiance as

$$F_{\lambda,\text{incident}} = \pi \, a_\lambda \, I_{\lambda,\text{reflected}}. \tag{3.13}$$

For subsequent derivations in this chapter, the subscript λ that denotes spectral units is assumed and will be suppressed for clarity.

3.2.2 Observation Geometry

Modeling the multi-dimensional radiance field measured by an observer requires the specification of an appropriate set of coordinates. The geometrical specification of an *observer*, located at $\mathbf{r}$, with a photosensitive surface oriented with unit normal or *look direction*, $\hat{\mathbf{\Omega}}$, is shown in Figure 3.2. In this figure, the primed system of coordinates has its axis z' parallel to $\mathbf{r}$, with spherical coordinates in this system, (θ, ϕ), that define the look direction, $\hat{\mathbf{\Omega}}$. The radiation field is then specified as a function of five spatial coordinates.

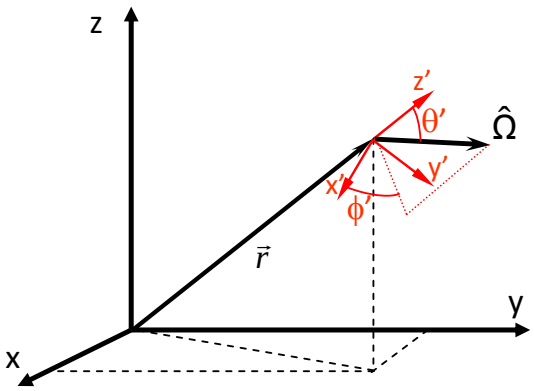

Figure 3.2: Specification of observer, $\mathbf{r}$, and look direction, $\hat{\mathbf{\Omega}}$, geometry.

In the general sense, the radiance measured by an observer is expressed as a Stokes vector,

$$\mathbf{I} = \begin{bmatrix} I \\ Q \\ U \\ V \end{bmatrix}, \tag{3.14}$$

whose four components have units of radiance and describe the polarization state and rate of energy transfer of a beam of electromagnetic radiation. Components Q and U describe the linear polarization with respect to a reference plane that contains the direction of wave propagation, V describes the state of circular polarization, and I is the total value.

3.2.3 Heuristic Derivation for Randomly-Polarized Light

Consider the change in radiance of a beam of radiation as it passes through a thin region containing scattering and absorbing particles, as shown schematically in Figure 3.3. The region, of thickness ds, is characterized by an *extinction*, $k(s)$. For an isotropic medium, the extinction expresses the fraction of photons removed per unit length of the medium traversed, typically expressed in units of cm^{-1}. For a single chemical species or type of interacting particle, the extinction is proportional to the

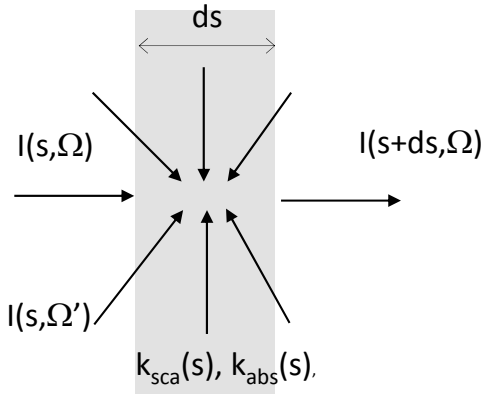

Figure 3.3: Characterization of a region containing absorbing and scattering particles by diffuse radiance $I(s, \hat{\mathbf{\Omega}}')$ and extinction $k(s)$.

particle number density, n_i,

$$k_i = n_i \, \sigma_{i,ext}, \tag{3.15}$$

where the proportionality constant is the *extinction cross section*, $\sigma_{i,\text{ext}}$. The cross section, which expresses the probability of interaction of the particles with the radiation as a geometric area, is proportional to the average area A of the particle projected onto a surface normal to $\hat{\mathbf{\Omega}}$,

$$\sigma_{i,ext} = Q_{i,ext} \, A_i. \tag{3.16}$$

The *extinction efficiency*, Q_{ext}, in this expression is a function of the particle size relative to the wavelength of radiation and the optical characteristics of the particle. Note that in these and subsequent equations, the position and wavelength dependence of all quantities is assumed.

When the medium through which the radiation passes contains several types of interacting particles for the wavelength of interest, the total extinction is given by the weighted sum of all extinction cross sections,

$$k = \sum_i k_i = \sum_i n_i \sigma_{i,ext}. \tag{3.17}$$

Since the extinction specifies the total amount of radiation removed per unit length, the extinction (3.17) is the total energy removed in the region through absorption and scattering processes, and so is expressed as

$$k = k_{abs} + k_{sca}. \tag{3.18}$$

For a single type of interacting particle, the extinction cross section is the sum of the *absorption cross section* and the *scattering cross section*,

$$\sigma_{i,ext} = \sigma_{i,abs} + \sigma_{i,sca}, \tag{3.19}$$

which are the respective probabilities of absorption and scattering expressed as geometric areas. Both have associated efficiencies, Q_{abs} and Q_{sca}, related to the interaction characteristics of the particles with the incident radiation. For scattering by the diatomic molecules that are the dominant constituents of the atmosphere, the *Rayleigh-scattering*, or dipole-scattering, cross section is used, which has a wavelength dependence of

$$\sigma_{sca,Rayl} = \frac{8\pi^3}{3}\frac{1}{\lambda^4}|\alpha|^2, \tag{3.20}$$

where α is the molecular polarizability. The most noteworthy aspect of the Rayleigh-scattering cross section at this point is its dependence on wavelength, which causes the cross section to become large for smaller wavelengths. The physical descriptions of the scattering and extinction cross sections will be discussed in more detail in Section 4.1.3 of the following chapter.

When computing the radiance in the direction $\hat{\mathbf{\Omega}}$, there exists – in addition to the radiance in this direction – a *diffuse radiance* field within the region, specified at point s in all directions, $\hat{\mathbf{\Omega}}'$, as $I(s, \hat{\mathbf{\Omega}}')$. The change in the radiance, $\mathrm{d}I(s, \hat{\mathbf{\Omega}}) = I(s + \mathrm{d}s, \hat{\mathbf{\Omega}}) - I(s, \hat{\mathbf{\Omega}})$, of a cone of radiation in the direction $\hat{\mathbf{\Omega}}$ is considered as it passes through an infinitesimal thickness, $\mathrm{d}s$, of the absorbing and scattering region.

The reduction in radiance is proportional to both the incident radiance and the

extinction,

$$\mathrm{d}I_{abs}(s,\hat{\mathbf{\Omega}}) = -\left(k_{abs}(s) + k_{sca}(s)\right) I(s,\hat{\mathbf{\Omega}})\,\mathrm{d}s. \tag{3.21}$$

Since in this work we are concerned with wavelengths between 280 and 810 nm, any contributions to the radiance from thermal emissions are negligible.

The change in radiance due to scattering within the volume must consider the contributions of scattering from radiance all directions, and so is

$$\mathrm{d}I_{sca}(s,\hat{\mathbf{\Omega}}) = k_{sca}(s)\left[\int_{4\pi} \bar{P}(\hat{\mathbf{\Omega}},\hat{\mathbf{\Omega}}')I(s,\hat{\mathbf{\Omega}}')\mathrm{d}\Omega'\right]\mathrm{d}s. \tag{3.22}$$

The function $\bar{P}(\hat{\mathbf{\Omega}},\hat{\mathbf{\Omega}}')$ is the differential scattering cross section,

$$\bar{P}(\hat{\mathbf{\Omega}},\hat{\mathbf{\Omega}}') = \frac{1}{\sigma_{sca}}\frac{\mathrm{d}\sigma_{sca}}{\mathrm{d}\Omega}, \tag{3.23}$$

which for historical reasons in astronomy and remote sensing is called the *phase function*, and expresses the angular dependence of scattering for the particles in the volume. The overbar in the scattering phase function denotes the scattering extinction-weighted mean over all scattering particle types. The phase function as expressed in equation (3.22) is normalized for each type of scattering particle, i, such that

$$\int_{4\pi} P_i(\hat{\mathbf{\Omega}},\hat{\mathbf{\Omega}}')\,\mathrm{d}\Omega' = 1, \tag{3.24}$$

where P has units of steradian^{-1}. A related parameter is the *asymmetry factor*,

$$g = \langle\cos\Theta\rangle = \int_{4\pi} P(\Theta)\cos\Theta\,\mathrm{d}\Omega, \tag{3.25}$$

which is a measure of the asymmetry of scattering. The value of g varies between $g = -1$ for pure backward scattering, zero for isotropic scattering, and $g = +1$ for pure forward scattering. Note that the change in radiance due to scattering, equation (3.22), can be positive or negative.

We combine the scattering and absorption terms for the total change in radiance

due to passage through the thin layer,

$$\mathrm{d}I(s,\hat{\mathbf{\Omega}}) = \left[-\left[k_{abs}(s) + k_{sca}(s)\right] I(s,\hat{\mathbf{\Omega}}) + k_{sca}(s) \int_{4\pi} \bar{P}(\hat{\mathbf{\Omega}},\hat{\mathbf{\Omega}}') I(s,\hat{\mathbf{\Omega}}') \mathrm{d}\Omega' \right] \mathrm{d}s. \tag{3.26}$$

The unitless *optical depth* is defined as

$$\mathrm{d}\tau = -k(s)\,\mathrm{d}s, \tag{3.27}$$

and is proportional to the number of interacting particles along a path. We note that although this definition for optical depth is used presently, one may define the elemental optical depth as either $\mathrm{d}\tau = \pm k(s)\mathrm{d}s$, depending on the geometry for the chosen method of solution.

For a single interacting particle type, the *single-scattering albedo* is defined as the fraction of removed photons that are removed by scattering,

$$\tilde{\omega}_i = \frac{k_{i,sca}}{k_i} = \frac{k_{i,sca}}{k_{i,abs} + k_{i,sca}}. \tag{3.28}$$

The single-scattering albedo can be defined analogously for the composite extinction due to scattering, k_{sca}, and the composite extinction, k, for all types of interacting particles in the media. When this composite single-scatter albedo, $\tilde{\omega} = \frac{k_{sca}}{k_{abs}+k_{sca}}$, is substituted into (3.26) together with the differential optical depth (3.27), we obtain the equation of radiative transfer,

$$\frac{\mathrm{d}I(s,\hat{\mathbf{\Omega}})}{\mathrm{d}\tau} = I(s,\hat{\mathbf{\Omega}}) - J(s,\hat{\mathbf{\Omega}}). \tag{3.29}$$

This equation expresses the change in the randomly-polarized component of the Stokes vector, I, due to its interaction with a collection of scattering and absorbing particles. The second term on the right-hand side of this equation,

$$J(s,\hat{\mathbf{\Omega}}) = \tilde{\omega} \int_{4\pi} \bar{P}(\hat{\mathbf{\Omega}},\hat{\mathbf{\Omega}}') I(s,\hat{\mathbf{\Omega}}') \mathrm{d}\Omega', \tag{3.30}$$

expresses the contribution to the radiance from scattering at location s to the radiance I, and is typically called the *multiple-scattering source term*, or simply the source term. In a more general form of coordinates, the radiative transfer equation is typically expressed as

$$\hat{\mathbf{\Omega}} \cdot \nabla I(\mathbf{r}, \hat{\mathbf{\Omega}}) = -k(\mathbf{r})\, I(\mathbf{r}, \hat{\mathbf{\Omega}}) + k_{sca}(\mathbf{r}) \int_{4\pi} I(\mathbf{r}, \hat{\mathbf{\Omega}})\, \bar{P}(\mathbf{r}, \hat{\mathbf{\Omega}}, \hat{\mathbf{\Omega}}')\, \mathrm{d}\Omega'. \tag{3.31}$$

3.2.4 Vector Radiative Transfer Equation

The preceding derivation was done for the total radiance without reference to its polarization state. Although this work is primarily concerned with modeling the randomly-polarized component of radiance measured by OSIRIS, we present briefly the polarized (vector) radiative transfer equation. If the complete Stokes vector is considered for the change in polarized radiance as a result of interaction with an absorbing and scattering medium, an analogous vector integro-differential equation exists for polarized radiance, $\mathbf{I}$.

The scattering operation when polarization is considered involves the *phase matrix*, $\mathbf{Z}(\Theta)$, that transforms the incident field polarization to the scattered field based on the particle's size, shape, and orientation,

$$\mathbf{I}_{sca}(\hat{\mathbf{\Omega}}^{\mathrm{sca}}) \equiv \mathbf{Z}(\hat{\mathbf{\Omega}}^{\mathrm{sca}}, \hat{\mathbf{\Omega}}^{\mathrm{inc}})\, \mathbf{I}_{inc}(\hat{\mathbf{\Omega}}^{\mathrm{inc}}). \tag{3.32}$$

In this expression the Stokes vectors are defined relative to their respective meridional (reference) planes. A related quantity is the *scattering matrix*, $\mathbf{F}(\hat{\mathbf{\Omega}}^{\mathrm{sca}}, \hat{\mathbf{\Omega}}^{\mathrm{inc}})$, which expresses the light-scattering properties of a particle in the reference frame of the particle itself. To perform the scattering operation, the Stokes vector must be transformed by rotation into the particle reference frame and back into the original reference frame. This rotation on the surface of the unit sphere is illustrated in Figure 3.4. The relation between the phase matrix $\mathbf{Z}$ and the scattering matrix, $\mathbf{F}$, is then

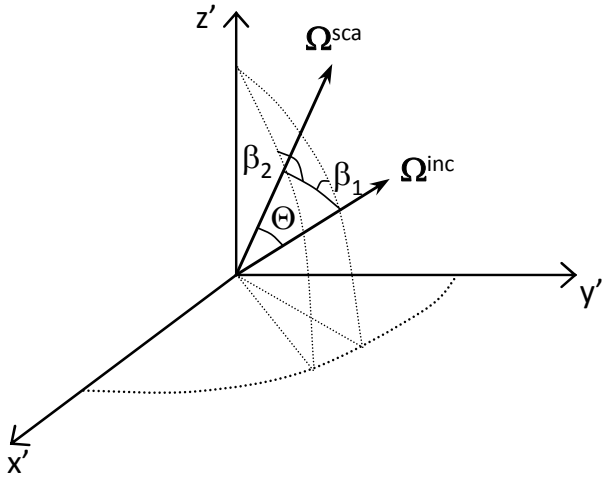

Figure 3.4: Rotation of Stokes vector reference plane into and out of the scattering plane.

through the rotations β_1 and β_2 as

$$\mathbf{Z}(\hat{\mathbf{\Omega}}^{\text{sca}}, \hat{\mathbf{\Omega}}^{\text{inc}}) = \mathbf{L}(\beta_2)\, \mathbf{F}(\hat{\mathbf{\Omega}}^{\text{sca}}, \hat{\mathbf{\Omega}}^{\text{inc}})\, \mathbf{L}(\beta_1). \tag{3.33}$$

The rotation matrix $\mathbf{L}(\beta)$ transforms the linear polarization components through an angle 2β counterclockwise about the direction of propagation. The scattering matrix, $\mathbf{F}$, relates the Stokes parameters of the incident and scattered beams defined with respect to the *scattering plane*, that is, the plane defined by $\hat{\mathbf{\Omega}}^{\text{inc}}$ and $\hat{\mathbf{\Omega}}^{\text{sca}}$. In this plane, the *scattering angle*, Θ, measures the angular distance of the scattered light direction, $\hat{\mathbf{\Omega}} = \hat{\mathbf{\Omega}}^{\text{sca}}$, from the incident direction, $\hat{\mathbf{\Omega}}' = \hat{\mathbf{\Omega}}^{\text{inc}}$, and so $\cos\Theta = \hat{\mathbf{\Omega}}^{\text{inc}} \cdot \hat{\mathbf{\Omega}}^{\text{sca}}$. Since the phase matrix relates the Stokes vectors in the 'observer' frame of reference, the radiative transfer equation (3.29) becomes

$$\frac{\mathrm{d}\mathbf{I}(s, \hat{\mathbf{\Omega}})}{\mathrm{d}\tau} = \mathbf{K}(s)\mathbf{I}(s, \hat{\mathbf{\Omega}}) - \tilde{\omega} \int_{4\pi} \mathbf{Z}(s, \hat{\mathbf{\Omega}}, \hat{\mathbf{\Omega}}')\, \mathbf{I}(s, \hat{\mathbf{\Omega}}')\, \mathrm{d}\Omega', \tag{3.34}$$

where the *extinction matrix*, $\mathbf{K}$, and the *phase matrix*, $\mathbf{Z}$, are clearly generalizations of the extinction, k, and the phase function, $P(\Theta)$.

Equations (3.29) and (3.34), as integro-differential equations, require the simulta-

neous solution of the equation at all relevant points in the atmosphere to obtain the observed radiance in the direction $\hat{\mathbf{\Omega}}$. A range of solution types have been applied to this problem and have reached a high level of sophistication. We now discuss the two solutions most relevant to the problem of simulating the radiance scattered by a collection of cirrus cloud particles.

3.3 Methods of Solution

3.3.1 Discrete Ordinates

One of the first solutions proposed to the equation of transfer is the discrete ordinates method (*Chandrasekhar*, 1960), which uses a semi-analytical solution to the radiative transfer equation. This method is frequently used for radiative transfer modeling with cloudy scenes due to its basic architecture. As well, this model type has significant heritage in nadir-based measurements (*Stamnes et al.*, 1988).

If a plane-parallel geometry is assumed, as shown in Figure 3.5, the coordinates in which the radiance field is defined are the optical depth τ, cosine of the zenith direction $\mu = \cos\theta$, and azimuth ϕ with respect to the solar direction, ϕ_0. The

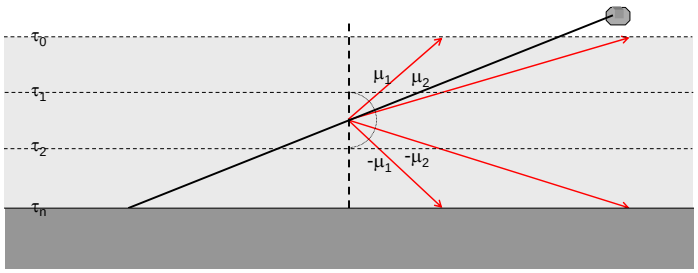

Figure 3.5: Distribution of rays in a discrete-ordinates model.

phase function $P(\tau, \cos\theta)$ is expanded in a series of $2N$ Legendre polynomials and the diffuse radiance is expanded in a Fourier cosine series,

$$I(\tau, \mu, \phi) = \sum_{m=0}^{2N-1} I^m(\tau, \mu) \cos\left[m(\phi_0 - \phi)\right]. \tag{3.35}$$

The equation of radiative transfer (3.29) is then to be solved for each cosine component of (3.35) as

$$\mu \frac{\mathrm{d}I^m(\tau,\mu)}{\mathrm{d}\tau} = I^m(\tau,\mu) - \int_{-1}^{+1} D^m(\tau,\mu,\mu')I^m(\tau,\mu')\,\mathrm{d}\mu' - Q^m(\tau,\mu), \tag{3.36}$$

for $m = 0, 1, \ldots, 2N-1$, where the phase function is internally expanded as

$$D^m(\tau,\mu,\mu') = \frac{\tilde{\omega}(\tau)}{2} \sum_{l=m}^{2N-1} (2l+1) g_l^m(\tau) P_l^m(\mu) P_l^m(\mu'), \tag{3.37}$$

and the direct component of incident radiation is given by

$$Q^m(\tau,\mu) = \frac{\tilde{\omega}(\tau) I_0}{4\pi}(2-\delta_{m0}) \sum_{l=}^{2N-1} (-1)^{l+m}(2l+1) g_l^m(\tau) P_l^m(\mu) P_l^m(\mu_0)\, \exp(-\tau/\mu_0). \tag{3.38}$$

Here δ_{ml} is the Kronecker delta, the coordinates (μ_0, ϕ_0) indicate the source direction, and the weights $g_l^m(\tau) = g_l(\tau)\frac{(l-m)!}{(l+m)!}$ are found from the Legendre moments of the phase function, $g_l(\tau) = \int_{-1}^{+1} P(\tau, \cos\theta) P_l(\cos\theta)\,\mathrm{d}(\cos\theta)$. In this formulation, equation (3.36) is expressed as a Gaussian quadrature such that the quadrature points, $\mu_i,\ i = \pm 1, \ldots, \pm N$, define the zeniths at which radiances are computed, called the 'N-stream' approximation, with their corresponding weights w_j,

$$\mu_i \frac{\mathrm{d}I^m(\tau,\mu_i)}{\mathrm{d}\tau} = I^m(\tau,\mu_i) - \sum_{\substack{j=-N \\ j\neq 0}}^{N} w_j D^m(\tau,\mu_i,\mu_j) I^m(\tau,\mu_j) - Q^m(\tau,\mu_i). \tag{3.39}$$

This form allows the RTE to be solved as a set of simultaneous first-order linear equations that are solved at each discrete optical depth layer, $\tau_k,\ k = 1 \ldots L$, which turns (3.36) into a system of $(2N \times L) \times (2N \times L)$ linear equations. The solution is performed by propagating the radiances at the upper boundary, $I(\tau_0, \mu, \phi)$, through the atmosphere; applying the absorptive or reflective properties of the bottom surface; and iterating this process towards convergence.

In the typical implementation of the discrete-ordinates method, the computation time is relatively independent of cloud optical thickness since the solutions are

closed-form analytic functions of the τ coordinate. Depending on the desired height resolution, computation time increases linearly with the number of discrete optical depths, τ_k, that are required to simulate vertical structure.

The computational load becomes quite heavy, by contrast, when high angular resolution is desired. The computation time tends roughly as the third power of the number of 'streams', $2N$, and so high angular resolution is very costly (*Stamnes et al.*, 1988). A major drawback of this method – particularly salient for modeling limb-scattered radiances – is the fundamental plane-parallel assumption. Since the model atmosphere is assumed to consist of infinite horizontal slabs, the radiance solution asymptotically becomes undefined at zeniths approaching 90° from above and below with a sharp discontinuity.

3.3.2 Successive Orders of Scatter

In the method of successive orders of scatter, the radiance is computed individually for photons scattered once, twice, three times, and so on, so that the total radiance is the sum of each of these terms. The basis of the method is the evaluation of light that has been scattered N times from light that has been scattered $N-1$ times. The *order* of scatter denotes the number of times light has been scattered. In this solution, solar irradiance is propagated through the atmosphere and scattered at a set of points in the atmosphere and on the ground, which forms the *first-order* radiance. The first-order radiance is scattered into a set of discrete directions at each of these points and propagated to all other points in the model atmosphere, at which point it is scattered again to form the *second-order* radiance, and so forth. In principle, this process is repeated to arbitrarily-high orders of scatter to obtain the total radiance in the atmosphere.

The successive-orders of scatter solution is most easily represented through a particular solution to the radiative transfer equation (3.29). Consider an observer at a location $\mathbf{r}$ with an instrument oriented to measure radiance incident in the direction $\hat{\mathbf{\Omega}}$, as shown in Figure 3.6. The relative positions of the observer and the observed location, $\mathbf{r}_0$, can be parameterized as $\mathbf{r}_0 = \mathbf{r} + s\hat{\mathbf{\Omega}}$, such that s increases in the

direction $(-\hat{\mathbf{\Omega}})$. In this geometry it is convenient to write the equation of transfer

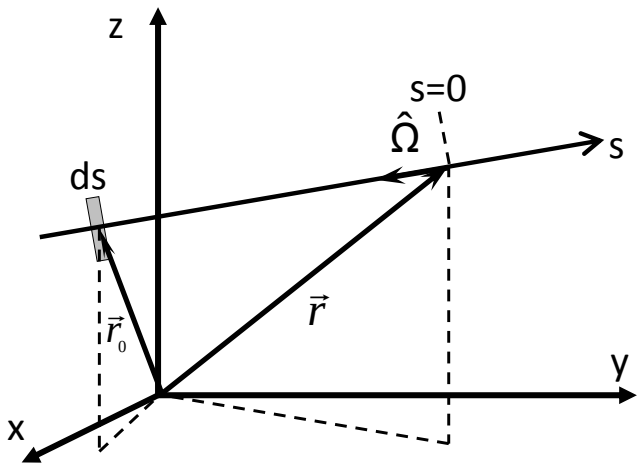

Figure 3.6: Observer geometry for successive-orders solution.

(3.29) as

$$\frac{\mathrm{d}I(\tau,\hat{\mathbf{\Omega}})}{\mathrm{d}\tau} - I(\tau,\hat{\mathbf{\Omega}}) = -J(\tau,\hat{\mathbf{\Omega}}). \tag{3.40}$$

If the left hand side is expressed as $\frac{\mathrm{d}}{\mathrm{d}\tau}\left(I(\tau,\hat{\mathbf{\Omega}})e^{-\tau}\right)$, then equation (3.40) can be integrated from a reference point τ_0 to arbitrary optical depth τ,

$$\int_{\tau_0}^{\tau} \frac{\mathrm{d}}{\mathrm{d}\tau'}\left(I(\tau',\hat{\mathbf{\Omega}})e^{-\tau'}\right)\mathrm{d}\tau' = -\int_{\tau_0}^{\tau} J(\tau',\hat{\mathbf{\Omega}})e^{-\tau'}\mathrm{d}\tau', \tag{3.41}$$

and so

$$I(\tau,\hat{\mathbf{\Omega}})e^{-\tau} - I(\tau_0,\hat{\mathbf{\Omega}})e^{-\tau_0} = -\int_{\tau_0}^{\tau} J(\tau,\hat{\mathbf{\Omega}})\mathrm{d}\tau'. \tag{3.42}$$

If the reference point, τ_0, is taken to be the observation point, $\mathbf{r}$, then by changing variables to the path coordinate, s, we obtain a solution

$$I(0,\hat{\mathbf{\Omega}}) = \tilde{I}(s_1,\hat{\mathbf{\Omega}})e^{-\tau(s_1,0)} + \int_{s_1}^{0} J(s,\hat{\mathbf{\Omega}})e^{-\tau(s,0)}k(s)\,\mathrm{d}s. \tag{3.43}$$

In this expression the first term corresponds to the radiance at the end of the observer line of sight. For example, if the observer line of sight (LOS) intersects the ground, there will be an upwelling radiance component $\tilde{I}(s_1,\hat{\mathbf{\Omega}})$ that is attenuated back to

the observer. If the observer LOS does not intersect any source of radiation, such as the earth's surface or the solar direction, then this first term is zero. The second term in this expression corresponds to the integrated source function $J(s, \hat{\mathbf{\Omega}})$, where the contributions from each point s in the region are attenuated back to the observer.

In the successive-orders of scatter solution, the terms $\tilde{I}(s_1, \hat{\mathbf{\Omega}})$ and $J(s, \hat{\mathbf{\Omega}})$ in equation (3.43) are computed iteratively for each order of scatter, such that the solution is expressed as

$$\begin{aligned} I(0, \hat{\mathbf{\Omega}}) = \int_{s_1}^{0} \left[J_1(s, \hat{\mathbf{\Omega}}) + J_2(s, \hat{\mathbf{\Omega}}) + \sum_{i=3}^{\infty} J_i(s, \hat{\mathbf{\Omega}}) \right] e^{-\tau(s,0)} k(s) \, \mathrm{d}s \\ + \left[\tilde{I}_1(s_1, \hat{\mathbf{\Omega}}) + \tilde{I}_2(s_1, \hat{\mathbf{\Omega}}) + \sum_{i=3}^{\infty} \tilde{I}_i(s_1, \hat{\mathbf{\Omega}}) \right] e^{-\tau_0}, \end{aligned} \tag{3.44}$$

where the subscript i indicates the order of scatter. Here $\tilde{I}_i(s_1, \hat{\mathbf{\Omega}})$ is the radiance of light that has been scattered exactly i times, with the last scatter being a reflection from the surface. The terms $J_i(s, \hat{\mathbf{\Omega}})$ result from i scattering events, with the last scatter occurring from a particle in the atmosphere. The fundamental relation for the successive-orders of scatter solution is the computation of the next-order source term radiance from the previous-order radiance,

$$J_{i+1}(s, \hat{\mathbf{\Omega}}) = \tilde{\omega} \int_{4\pi} \left[I_i(s, \hat{\mathbf{\Omega}}') \right] P(s, \hat{\mathbf{\Omega}}, \hat{\mathbf{\Omega}}') \, \mathrm{d}\Omega' \,. \tag{3.45}$$

This method is initialized by attenuating solar irradiance to all points in the atmosphere and on the ground, scattering into all directions to compute $\tilde{I}_i(s_1, \hat{\mathbf{\Omega}})$ and $J_{i+1}(s, \hat{\mathbf{\Omega}})$ for as many scattering orders as are desired, and finding the resulting contributions into the observer line of sight through the summation of orders in equation (3.44).

In limb-viewing geometries, the contribution of multiply-scattered radiance to the measured signal is significant. This is illustrated in Figure (3.44), as in *Bourassa et al.* (2008), where the contributions to the measured radiance at 25 km tangent altitude from the first six orders of scatter are shown as a function of wavelength for

a surface albedo of 0.8. In this figure, the contributions from scattering events by the

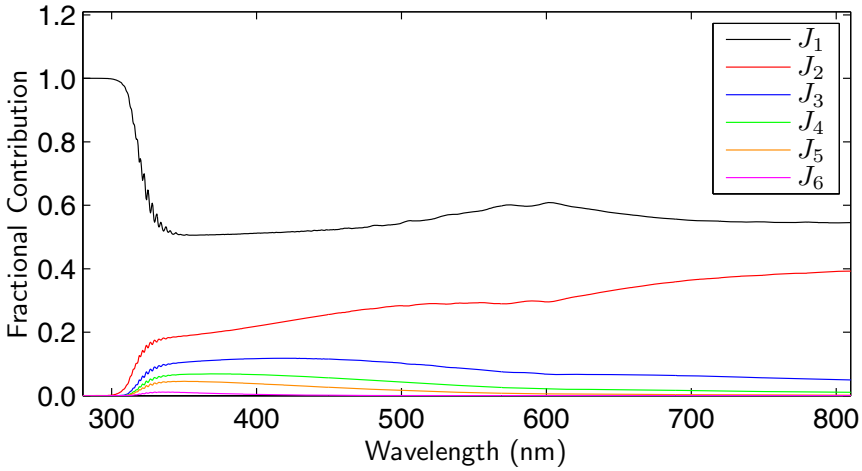

Figure 3.7: Fractional contributions to 25 km tangent altitude measurement as in *Bourassa et al.* (2008).

atmosphere and ground are included in the source terms, J_i. In UV wavelengths, in particular at high altitudes, single-scatter contributions are of primary importance due to strong ozone absorption. This contribution is also seen to be slightly higher between 525 and 650 nm within the Chappuis band of ozone. Radiance contributions from second-order scattering becomes quite significant at wavelengths above the Hartley-Huggins region, and grows at longer wavelengths due to the decreasing value of the dominant Rayleigh-scattering cross section (3.20) of the molecular atmosphere at longer wavelengths. It is noteworthy in this figure that the first- and second-order sources form the most significant contribution to the limb radiance.

The successive-orders of scatter method provides a robust solution that provides an intuitive solution to the equation of radiative transfer, and is one whose accuracy is checked easily through using sufficiently high orders of scatter to ensure convergence. A disadvantage of this method, in contrast with the discrete ordinates method, is the large amount of resources required to model high in-cloud optical depths.

3.4 The SASKTRAN Radiative Transfer Model

The SASKTRAN model (*Bourassa et al.*, 2008), which is employed in this work, is based on the successive-orders of scattering method and traces rays in a fully spherical model of the atmosphere. It was developed at the University of Saskatchewan to perform fast and accurate retrievals of atmospheric trace gases from limb-scattered spectral radiances. SASKTRAN is written in the C++ programming language and uses the inheritance and polymorphism features of object-oriented programming to allow flexibility and customization to user needs. As well, SASKTRAN employs multithreading algorithms to perform retrievals on a standard desktop computer.

3.4.1 Successive-Orders Solution

The fundamental unit of the SASKTRAN model is a traced ray that originates at location $\mathbf{r}$, has 'look' direction $\hat{\mathbf{\Omega}}$, and whose radiance at $\mathbf{r}$ is gathered according to equation (3.44). In the terminology of the model, this ray is called a line of sight (LOS). It is helpful to separate scattering orders within the model into four groups: light that has scattered once from the atmosphere, light that has scattered once from the ground, multiply-scattered light that has its last scatter by the atmosphere, and multiply-scattered light that has its last scatter from the ground. In the expressions that follow, the radiances are always those measured by an 'observer', that is, the radiance measured at the ray origin.

First, light scattered once by the atmosphere is calculated directly through source points chosen along the observer line of sight. As shown schematically for an observer inside the atmosphere in Figure 3.8, solar irradiance is attenuated by a factor $e^{-\tau(\text{sun},s)}$ to the line of sight, scattered into the observer line of sight, and attenuated back to the observer. This radiance contribution is calculated as

$$I_{1,a}(0,\hat{\mathbf{\Omega}}) = \tilde{\omega}\, F_0 \int_{s_1}^{0} e^{-\tau(\text{sun},s)} P(s,\hat{\mathbf{\Omega}},\hat{\mathbf{\Omega}}_0) e^{-\tau(s,0)} k(s)\, \mathrm{d}s \tag{3.46}$$

The source term in this equation results from solar irradiance that has been scattered

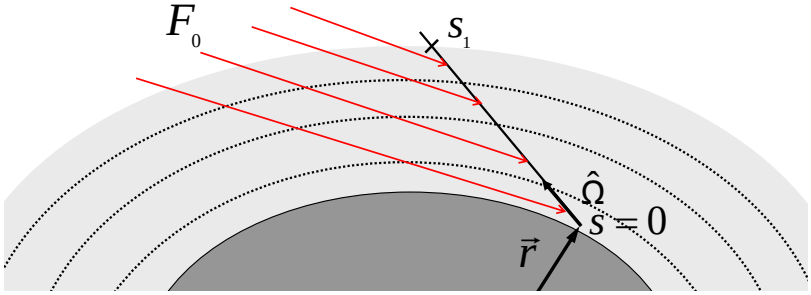

Figure 3.8: Geometry for computing radiance scattered once from points in the atmosphere.

from the solar direction, $\hat{\mathbf{\Omega}}_0$, into the the observer line of sight, $\hat{\mathbf{\Omega}}$.

For an observer line of sight that intersects the ground, as illustrated in Figure 3.9, the ground radiance $\tilde{I}$ in equation (3.43) is computed through attenuating the solar irradiance to the surface, scattering it at the ground, and attenuating the result back to the observer at $s = 0$. Since the surface in SASKTRAN is assumed to be a

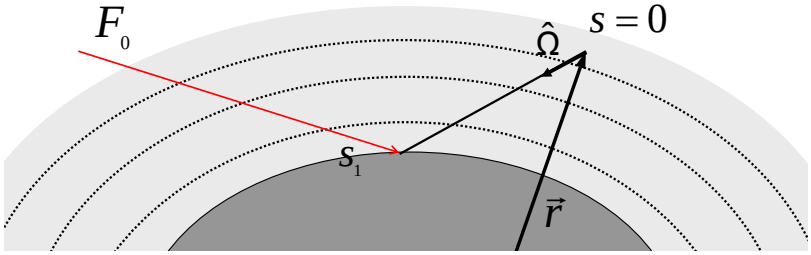

Figure 3.9: Geometry for computing radiance scattered by the ground at the end of an observer line of sight.

Lambertian scatterer with an albedo a, the radiance at the observer is

$$I_{1,g}(0, \hat{\mathbf{\Omega}}) = \frac{a}{\pi} e^{-\tau(\text{sun}, s_1)} F_0 \cos\theta_0 \, e^{-\tau(s_1, 0)}. \tag{3.47}$$

The second-order atmospheric source term is computed at source points along the LOS through gathering the first-order atmosphere (3.46) and ground (3.47) radiances from all directions $\hat{\mathbf{\Omega}}'$ into the scattering integral (3.30),

$$J_{2,a}(s, \hat{\mathbf{\Omega}}) = \tilde{\omega} \int_{4\pi} P(s, \hat{\mathbf{\Omega}}, \hat{\mathbf{\Omega}}_0) \left[I_{1,a}(s, \hat{\mathbf{\Omega}}') + I_{1,g}(s, \hat{\mathbf{\Omega}}') \right] \mathrm{d}\Omega'. \tag{3.48}$$

This process is shown schematically in Figure 3.10, where rays (the green lines of sight) have been distributed from one of the LOS source points into all directions, $\hat{\mathbf{\Omega}}'$. For each of the rays sent out from the source point, the single-scatter source

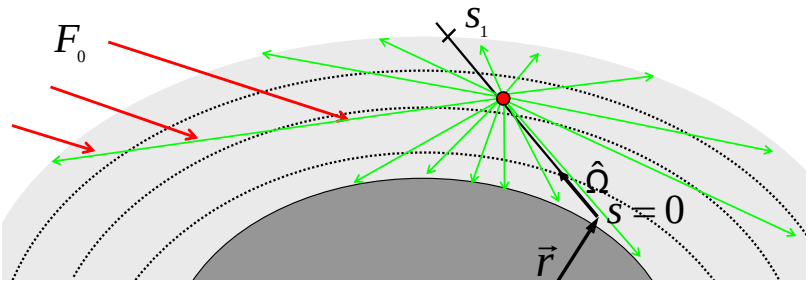

Figure 3.10: Geometry for computing source function, $J_{2,a}(s, \hat{\mathbf{\Omega}})$, due to multiply-scattered light from atmospheric scatterers.

term is evaluated at a large set of secondary source points along each of the lines of sight. This process is illustrated schematically by the intersections of the three red rays with the lines of sight, although in the actual implementation there are tens of thousands of these source points per instrument LOS source point. The second-order atmosphere-scattered radiance is then the integral of these source terms along the line of sight,

$$I_{2,a}(0, \hat{\mathbf{\Omega}}) = \int_{s_1}^{0} J_{2,a}(s, \hat{\mathbf{\Omega}}) e^{-\tau(s)} k(s)\, \mathrm{d}s. \tag{3.49}$$

The radiance scattered twice from the ground is obtained by integrating the first-order atmosphere-scattered radiance over all directions within the upward-facing hemisphere,

$$I_{2,g}(s, \hat{\mathbf{\Omega}}) = \frac{a}{\pi} e^{-\tau(s_1, s)} \int_{2\pi} I_{1,a}(s_1, \hat{\mathbf{\Omega}}') \cos\theta'\, \mathrm{d}\Omega', \tag{3.50}$$

which provides this component of the radiance as illustrated in Figure 3.11. As in the previous figure, only three scattering interactions along the secondary lines of sight are shown for clarity.

In general, the source functions, J, for each order of scattering, $(i+1)$, are computed by scattering the previous-order radiance, as in equation (3.45), through

$$J_{i+1,a}(s, \hat{\mathbf{\Omega}}) = \tilde{\omega} \int_{4\pi} P(s, \hat{\mathbf{\Omega}}, \hat{\mathbf{\Omega}}_0) \left[I_{i,a}(s, \hat{\mathbf{\Omega}}') + I_{i,g}(s, \hat{\mathbf{\Omega}}') \right] \mathrm{d}\Omega', \tag{3.51}$$

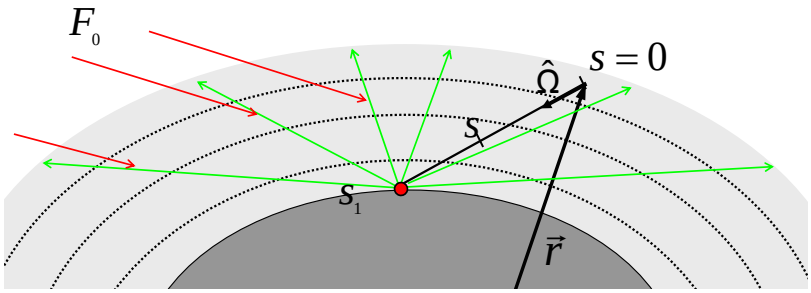

Figure 3.11: Geometry for computing radiance multiply-scattered from the ground along a line of sight.

and evaluating the radiance at the observer location by

$$I_{i+1,a}(0,\hat{\mathbf{\Omega}}) = \int_{s_1}^{0} J_{i+1,a}(s,\hat{\mathbf{\Omega}}) e^{-\tau(s)} k(s)\,\mathrm{d}s. \tag{3.52}$$

The same order of scattering from the ground can be generalized as

$$I_{i+1,g}(s_1,\hat{\mathbf{\Omega}}) = \frac{a}{\pi} e^{-\tau(s_1,s)} \int_{2\pi} I_{i,a}(s_1,\hat{\mathbf{\Omega}}') \cos\theta'\,\mathrm{d}\Omega', \tag{3.53}$$

and the total radiance contribution at the observer is evaluated using the sum of atmosphere and ground scatter terms, (3.52) and (3.53), through the sum-of-orders expression, equation (3.44). In that expression, the second-order atmosphere and ground terms are expressed as separate from higher-order terms to signify that these terms are evaluated without approximation. It was shown in Figure 3.7 that the first- and second-order terms form the most important contribution to a typical limb-scattering measurement scenario. For this reason, the source functions in SASKTRAN for the first- and second-order terms are evaluated explicitly by sending rays out from each source point along the observer line of sight.

The successive-orders solution is performed in SASKTRAN in a stepwise manner by scattering solar irradiance into successively higher orders in the manner described. Since the magnitude of scattered radiance decreases as the order of scattering increases, the solution to the radiative transfer equation in this architecture is carried out by recursively computing the radiance field until additional contributions to the

observed radiance (3.52) from higher-order terms become negligible. The details of the spatial distribution of discrete source function evaluation points and the angular distributions of rays are now discussed.

3.4.2 Geometry Configuration

The optical properties of scattering and absorbing particles are assumed to be constant within spherical cells for the implementation of SASKTRAN used in this work. The observer location, $\mathbf{r}$, is defined in SASKTRAN with respect to the centre of an *osculating sphere* that best fits the radius of the oblate spheroid of the earth along the local meridian at a reference point. The location of this reference point is typically the tangent point of the observer line of sight. In the current implementation the model ignores ray curvature due to atmospheric refraction and traces rays using straight-line propagation.

The nomenclature used in discussing the ray-tracing geometry is that the intersection points of a ray through concentric spherical *shells* are used to define the ray path lengths through homogeneous *cells* that lie between them.

In a model atmosphere that consists of optical properties specified in homogeneous spherical cells, the diffuse radiance field is symmetric with respect to solar azimuth angle, which reduces by one the number of coordinates for which the radiative transfer equation must be solved. With reference to the specified geometry in Figure 3.2, the radiance field is then fully specified by two spatial coordinates and two directional coordinates. To exploit this symmetry, it is convenient to define a spherical coordinate system with the z axis oriented toward the sun, in which case the solar zenith angle, θ_0, is the colatitude, as illustrated in Figure 3.12. In this figure an observer line of sight is shown that passes through the atmosphere without intersecting the ground, and where the segment that passes through the atmosphere is shown in red. Since it has been shown that the diffuse radiance varies slowly with solar zenith angle (*Herman et al.* (1994), *McLinden et al.* (2002)), well-defined solutions can be constructed using a set of discretized solar zenith angles in the model atmosphere.

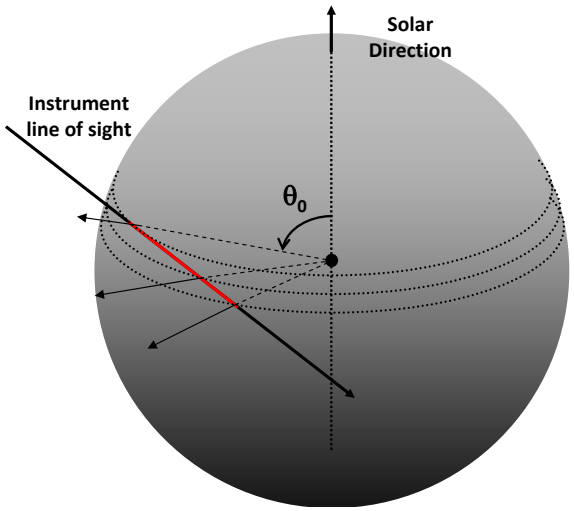

Figure 3.12: Instrument line of sight in SASKTRAN solar coordinate system.

At each of the set of solar zenith angles, a set of *diffuse points* is distributed in altitude to span the region of interest. Each height profile of diffuse points at a given zenith angle is called a *diffuse profile*. A set of diffuse points is illustrated in Figure 3.13. As illustrated in this figure, each diffuse point contains a set of *incoming rays*

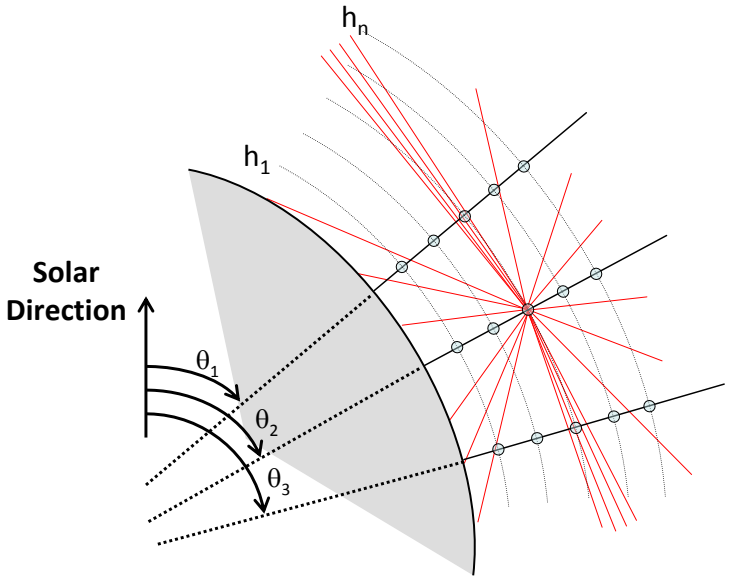

Figure 3.13: Distribution of diffuse points in solar zenith angle and altitude.

that are used to evaluate the multiple-scatter source terms $J_{i+1,a}(s, \hat{\mathbf{\Omega}})$ as in equation

(3.51), which in the figure are shown in red. The incoming ray directions are specified in the diffuse point's local zenith and azimuth coordinates, with the azimuth defined with respect to the direction of the sun. In Figure 3.13, only the rays for the sunward and anti-sunward azimuth angles are shown.

The angular distribution of incoming rays is configured to capture best the distribution of the diffuse scattered sunlight in the atmosphere. A typical distribution of the ray locations, in local zenith and azimuth coordinates, is shown in Figure 3.14. At a given point in the atmosphere, the upwelling radiance from lower altitudes and

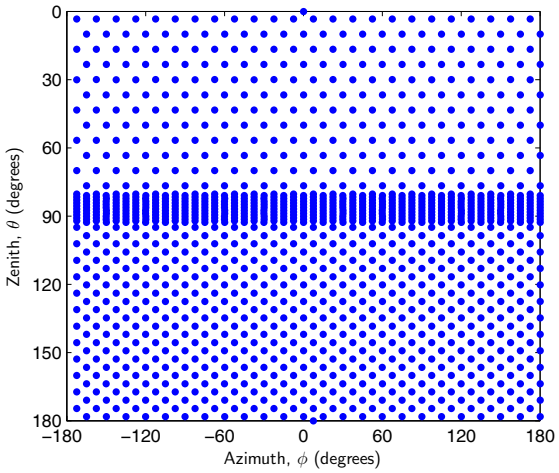

Figure 3.14: Angular distribution of incoming directions, $\hat{\mathbf{\Omega}}'_j$, in local zenith and azimuth angle.

from the ground is both greater than, and also varies more than the radiance from higher altitudes. Thus rays are more densely distributed for downward zeniths. Rays are most densely-packed at zeniths between the local horizon and 90° since both the brightest radiances and the most sharp change in radiance occur here from scattering within the same layer. Rays are evenly distributed in azimuth angle.

The set of incoming directions, $\hat{\mathbf{\Omega}}'_j$, defines the points at which the scattering integral (3.51) is evaluated at each diffuse point. The incoming radiances are scattered into a set of *outbound directions* $\hat{\mathbf{\Omega}}_k$, for which the source functions $J_{i+1,a}(s, \hat{\mathbf{\Omega}}_k)$ from each scattering order are specified. The outbound, or source function, directions are specified according to a minimum-energy (i.e. Thompson problem) distribution

of equally-charged points on the surface of the unit sphere (*Sloan and Womersley*, 2004).

The first-order incoming and second-order outbound radiances are shown on the surface of the unit sphere, along with the incoming and outbound ray distributions, for a diffuse point at 38.5 km altitude and solar zenith angle 72° in Figure 3.15. In this figure all radiances are normalized to unity. Incoming radiances are specified on a grid of 24 azimuths and 28 zeniths, and outbound radiances at 324 directions. The

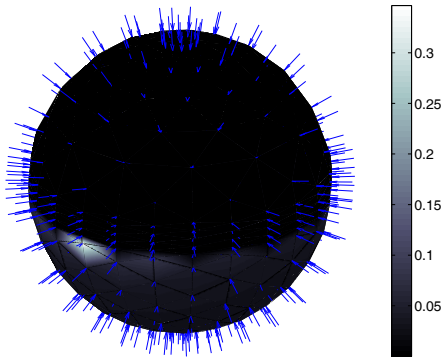

(a) Incoming radiance, $I_0(s, \hat{\mathbf{\Omega}}'_j)$

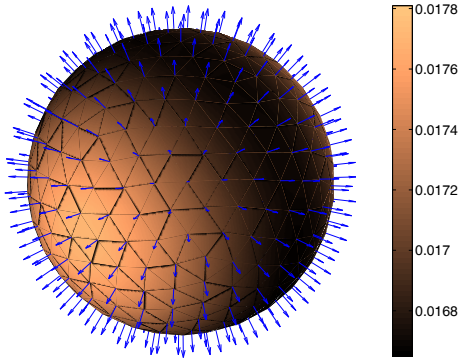

(b) Outbound radiance, $J_{1,a}(s, \hat{\mathbf{\Omega}}_k)$

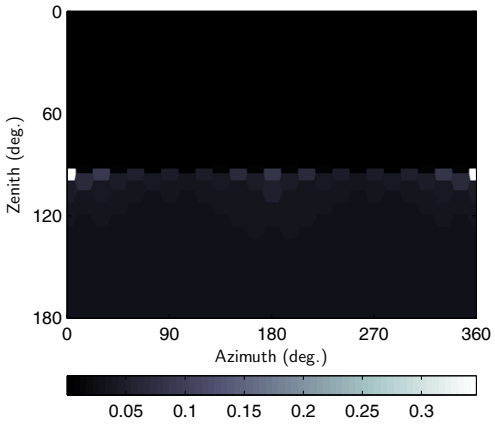

(c) Incoming radiance, $I_0(s, \theta', \phi')$

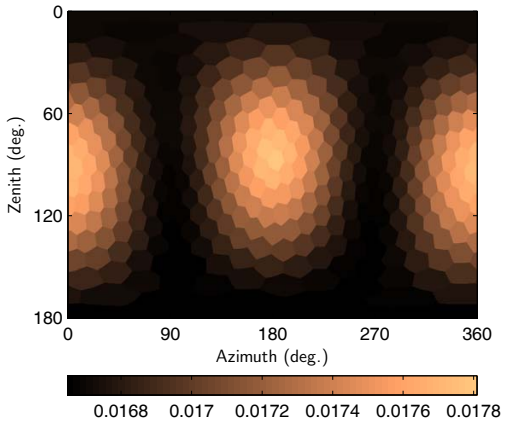

(d) Outbound radiance, $J_{1,a}(s, \theta, \phi)$

Figure 3.15: Distributions of incoming and outbound directions and radiances for a diffuse point at altitude 38.5 km.

first-order radiance, $I_{1,a}(s, \hat{\mathbf{\Omega}}'_j) + I_{1,g}(s, \hat{\mathbf{\Omega}}'_j)$, includes contributions from atmospheric

single scatter and ground scatter with a surface albedo of 0.3. As expected, the upwelling radiance ($90^\circ < \theta \leq 180^\circ$) exceeds the down-welling ($0 \leq \theta \leq 90$) radiance. The highest incoming radiances occur between the horizontal direction ($\theta = 90^\circ$) and the limb ray – at those zeniths that have the longest path length through the greatest number of scattering particles ($\theta \simeq 94^\circ$). For the incoming radiances in Figures 3.15a and 3.15c, as one moves from zenith angles $\theta > 90^\circ$ through the horizon to $\theta < 90^\circ$, the incoming radiances move from contributions from the bright ground and very bright lower atmosphere to those from the very thin atmosphere above. In the outbound radiances in Figures 3.15b and 3.15d, the smooth forward and backward-scattering peaks from Rayleigh scattering are evident. For computing the radiances reflected from the ground, the integral of the upward hemisphere in equation (3.53) is performed using similar distributions of rays over its domain.

As mentioned in the previous section, the first- and second-order source terms are evaluated exactly through tracing of rays from a set of source term points along the observer line of sight. For higher-order scattering, the source terms $J_{i,a}(s, \hat{\mathbf{\Omega}}),\ i \geq 3$ are evaluated at each point along the line of sight by identifying those diffuse points with the nearest altitudes and solar zenith angles. These surrounding diffuse points are translated in solar azimuth angle to the observer LOS and are linearly interpolated in altitude, solar zenith angle, and outbound direction to obtain the source radiance in the direction $\hat{\mathbf{\Omega}}$. The nearest three vertices of the outbound directions, $\hat{\mathbf{\Omega}}_k$, are used for interpolation on the surface of each unit sphere. Diffuse points are typically distributed in altitude such that they lie directly between successive shell boundaries, that is, in the middle of the spherical 'cells'. Optical properties are typically specified at and exactly between the shell boundary heights.

The integral (3.52) of the source functions $J(s, \hat{\mathbf{\Omega}})$ along the observer LOS is made discrete by considering individually the integral along path length segments through the homogeneous cells. The integral along each path length segment is computed using Gaussian quadrature with a user-configurable number of points within the interval. For cells in which a LOS is tangent and has a very long path length, Δs, the number of evaluation points can be made quite large. The source functions at

each of these points are interpolated in height from the surrounding diffuse points.

The properties of limb-scattered radiances are predominantly related to the solar conditions at the tangent point, but the varying illumination conditions at other locations along the line of sight must be accounted for when computing the diffuse field. This is done in SASKTRAN by using a range of diffuse profiles that span the solar zenith angles encountered throughout the instrument line of sight. These are typically spaced by $\Delta\theta_0 = 1^\circ$. Depending on the choice needed between accuracy and computational speed, diffuse profiles can be placed as closely or as sparsely as needed.

With the use of these discretizations, the integrals to compute the source terms (3.51) and radiances, (3.52) and (3.53), become summations. These summations are rewritten as sparse matrices such that the order-$(i+1)$ source functions are a linear combination of the previous-order radiances. The matrix elements are simply functions of the optical properties of the atmosphere and the scattering geometry, which are independent of scattering order. These matrix elements are then computed in an initialization step and can be applied repeatedly to perform the successive-scattering operation.

3.4.3 Clear-Sky Modeled Radiances

The use of SASKTRAN to compute clear-sky radiances for an OSIRIS scan is briefly illustrated here, where the importance of multiple scattering contributions to the measured limb-scattered radiance is highlighted.

In SASKTRAN, the observer geometry is easily configured to model the radiance observed for a given OSIRIS scan. In addition, the optical properties of the model atmosphere can be configured with the retrieved trace gas amounts from OSIRIS, which have been described elsewhere: O_3 (*Degenstein et al.* (2009) and *Roth et al.* (2007)), NO_2 (*Bourassa et al.*, 2011), and stratospheric aerosol (*Bourassa et al.*, 2007). The surface albedo is also estimated from OSIRIS measurements. The modeled radiances for a cloud-free scan configured in this way are compared with the OSIRIS measured radiances, following *Bourassa et al.* (2008), in Figure 3.16. In this figure, the limb

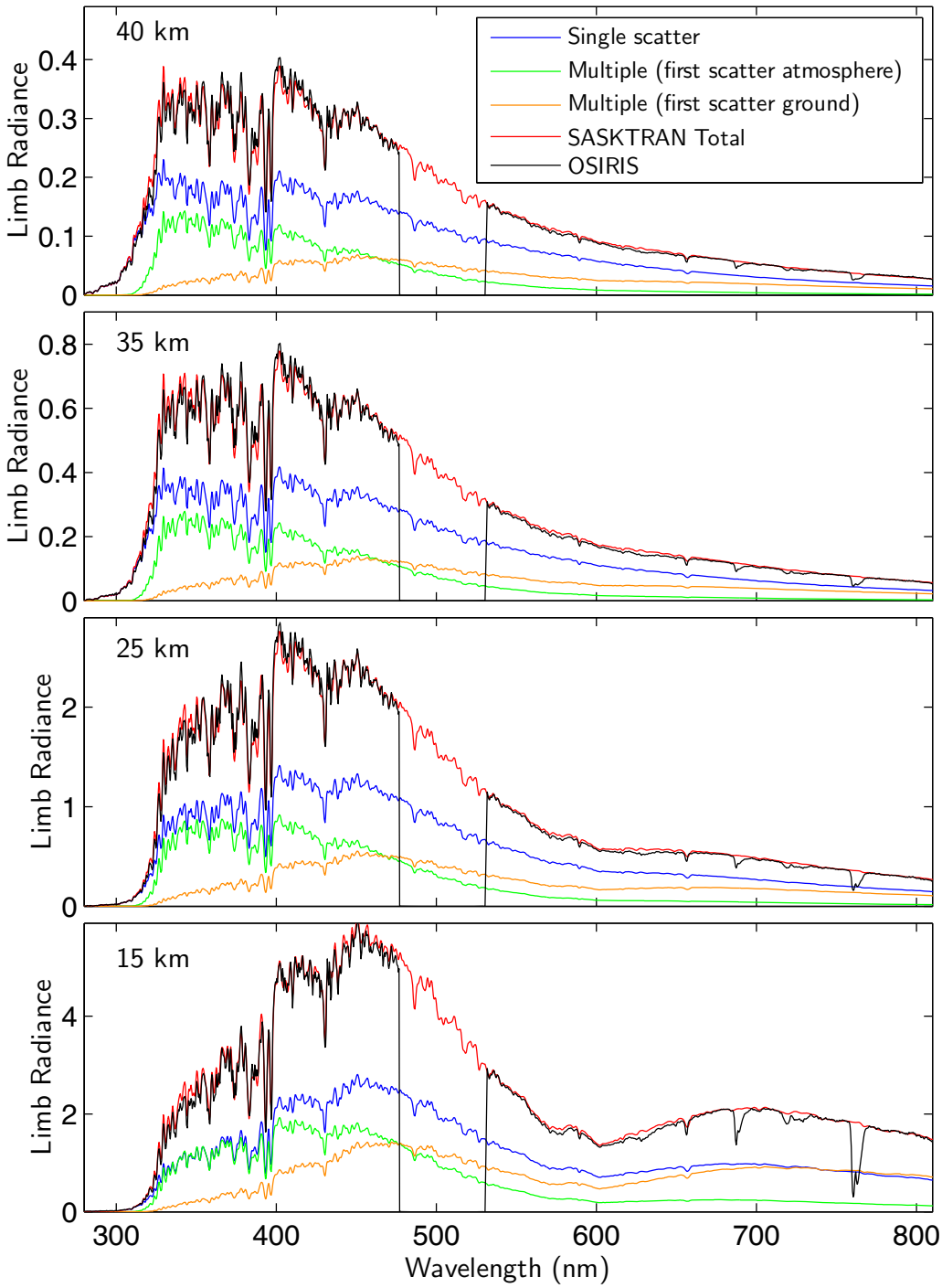

Figure 3.16: Modeled spectral radiance (in units of 10^{13} phot/s/cm^2/nm/sr) at selected tangent altitudes for OSIRIS scan 6432019 as in *Bourassa et al.* (2008).

radiances modeled by SASKTRAN are shown at selected tangent altitudes. The contributions from single and multiple scattering are shown separately. Further, the multiple-scattering contributions are subdivided according to the original scattering source: atmosphere or ground. For this scan, a retrieved (wavelength-independent) surface albedo of 0.84 was used. This scan was made at 82°N, 38°E, with a solar zenith angle of 68°.

As illustrated by this figure, the successive-orders of scatter solution applied to a cloud-free atmosphere yields a highly accurate solution. The numerical evaluation of the integral (3.45) for cloud-free scans is very accurate since the phase functions are smooth and since the incoming ray distribution captures well the incoming radiance field. When the phase functions are sufficiently smooth, it is a good approximation to use the value of the phase function at the mean scattering angle, namely $\bar{\Theta} = \langle \arccos(\hat{\mathbf{\Omega}} \cdot \hat{\mathbf{\Omega}}') \rangle$.

However, when computations are to be performed in the presence of ice crystals or large aerosol or dust particles, using the value of the phase function at the mean scattering angle $\bar{\Theta}$ is clearly insufficient. A necessary approach must incorporate the mean value of the phase function over the scattering angles defined by the incoming direction's associated solid angle, $\bar{P}(\hat{\mathbf{\Omega}}, \hat{\mathbf{\Omega}}') = \bar{P}(\Theta)$. This work is investigated in Chapter 5, with diagnostics performed using a novel photon-conserving technique. First, we investigate several source of scattering properties for ice crystals in cirrus clouds.

Chapter 4

Light-Scattering Properties of Cirrus Cloud Particles

Retrievals of cloud particle number density and effective size require efficient computations of the light-scattering properties of cloud particles. The range of ice crystal sizes encountered in a typical subvisual cirrus cloud, between 1 and 100 μm, obviates the use of geometric optics for visible and near-IR wavelengths at all but the largest ice crystal sizes. It is useful to define the size parameter $x = kr = \frac{2\pi r}{\lambda}$, the ratio of the circumference of an equivalent-volume sphere to the wavelength of light scattered. The majority of computations must be done in the resonance region where the wavelength is on the order of the particle size. This chapter describes the fundamental aspects of light scattering from ice crystals and describes the sources of scattering properties used in this work.

4.1 Light Scattering by Ice Crystals

Computing the scattering properties of ice crystals requires solving the Maxwell equations for the boundary conditions determined by the particle shapes, which can take a wide range of hexagonal-based crystal habits within a given cloud, the most common of which in subvisual cirrus are hexagonal plates and columns. Long columns tend to fall with their long axes horizontal, and plate crystals tend to fall with their major

axes parallel to the ground. Near terminal velocity, the axes of these crystals show a spread about these orientations and are frequently randomly oriented. However, a cloud with relatively pristine shapes and with certain dynamical conditions – such as a persistent horizontal wind – can create alignments, forming the halos and arcs more commonly seen at high latitudes. Although specific and random particle orientations must in general be considered, the case of scattering from randomly-oriented crystals, treated through ensemble orientation averaging, is assumed in this work.

4.1.1 Light Scattering by Spherical Particles

Lorenz-Mie theory provides an exact solution for the scattering and absorption of light from dielectric spheres. In this method an incident monochromatic plane wave is expanded in vector spherical wave functions, and boundary conditions match the incident and scattered waves according to the material properties of the scattering sphere. The scattering and extinction cross sections and phase matrix elements are expressed as power series expansions in $\cos\Theta$, with the associated Legendre functions as basis functions. Typically the series expansions converge when the number of terms $N \sim x$, necessitating efficient codes for large size parameters. Such codes have been developed (*Wiscombe*, 1980) to efficiently compute the series expansions of the associated Legendre and spherical Bessel functions to great accuracy. We now turn to a generalization of the Lorenz-Mie theory's mathematical framework applied to light scattering from nonspherical particles.

4.1.2 Light Scattering by Arbitrary-Shaped Particles

The geometry involved in the scattering of a plane wave by an arbitrarily-shaped particle is shown schematically in Figure 4.1. The plane wave is incident in the direction $\hat{\mathbf{\Omega}}^{inc}$, with incident electric field $\mathbf{E}^{\text{inc}}$. Light scattered by the particle is represented here by outbound spherical waves, specified here in the direction $\hat{\mathbf{\Omega}}^{sca}$ with scattered electric field vector $\mathbf{E}^{\text{sca}}$. In this geometry, $k_2 = k_1 m = k_1(m_r + im_i)$ is the wavenumber within the scattering object, having a generally complex index of

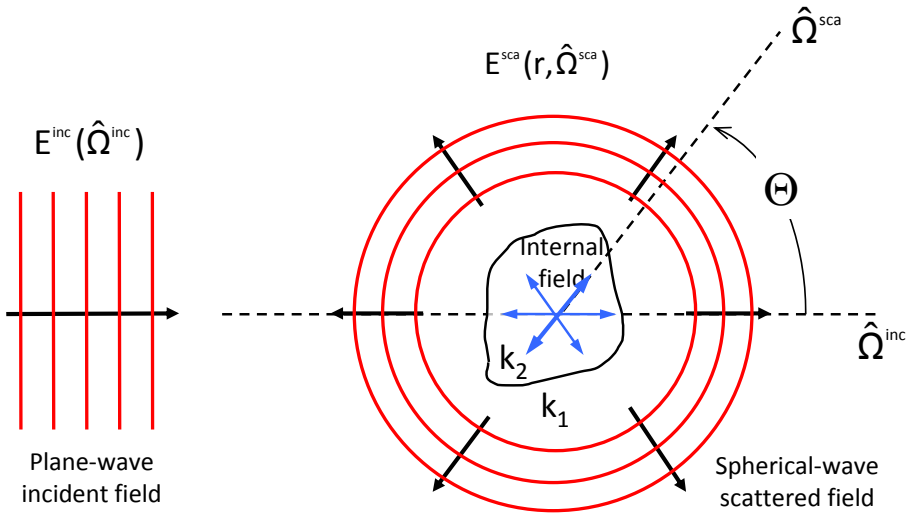

Figure 4.1: Scattering of a plane wave from an arbitrarily-shaped particle.

refraction m, and k_1 is the wavenumber in the surrounding medium. In this section, the development of light-scattering properties is similar to the treatments given by *Bohren and Huffman* (1983) and *Mishchenko et al.* (2002).

To compute the scattered electric field $\mathbf{E}^{\text{sca}}$ from a finite nonspherical scattering object, consider the monochromatic Maxwell equations for the electric field inside and outside of the scattering object,

$$\nabla \times \nabla \times \mathbf{E}(\mathbf{r}) - k_1^2 \mathbf{E}(\mathbf{r}) = 0, \qquad \mathbf{r} \in \mathrm{V}_{ext} \tag{4.1}$$

$$\nabla \times \nabla \times \mathbf{E}(\mathbf{r}) - k_2^2 \mathbf{E}(\mathbf{r}) = 0, \qquad \mathbf{r} \in \mathrm{V}_{int}, . \tag{4.2}$$

The regions employed in the following discussion are shown in Figure 4.2, where $r_>$ defines the smallest circumscribing sphere of the scattering object centred at the origin and $r_<$ defines the largest concentric inscribed sphere. By considering the refractive index of the finite scattering region relative to the exterior, the two equations are combined into a single vector equation for the total electric field. If the

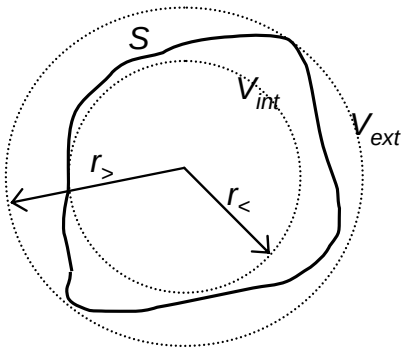

Figure 4.2: Cross section of arbitrarily shaped scattering object bounded by a surface S.

piecewise discontinuous refractive index

$$m(\mathbf{r}) = \begin{cases} 1, & \mathbf{r} \in \mathrm{V}_{ext} \\ \frac{k_2(\mathbf{r})}{k_1}, & \mathbf{r} \in \mathrm{V}_{int} \end{cases} \tag{4.3}$$

and the electric field inside the scattering object are made to constitute a forcing function,

$$\mathbf{j}(\mathbf{r}) = k_1^2[m^2(\mathbf{r}) - 1]\mathbf{E}(\mathbf{r}) = \begin{cases} 0, & \mathbf{r} \in \mathrm{V}_{ext} \\ [k_2^2(\mathbf{r}) - k_1^2]\,\mathbf{E}(\mathbf{r}), & \mathbf{r} \in \mathrm{V}_{int}, \end{cases} \tag{4.4}$$

then equations (4.2) and (4.1) are combined in a single inhomogeneous equation. The source function thus creates the equation for the total field,

$$\nabla \times \nabla \times \mathbf{E}(\mathbf{r}) - k_1^2\mathbf{E}(\mathbf{r}) = \mathbf{j}(\mathbf{r}), \qquad \mathbf{r} \in \mathrm{V}_{int} \cup \mathrm{V}_{ext}. \tag{4.5}$$

The total field must consist of a combination of a solution of the homogeneous problem and a particular solution of the inhomogeneous problem. The first solution

satisfies

$$\nabla \times \nabla \times \mathbf{E}^{inc}(\mathbf{r}) - k_1^2 \mathbf{E}^{inc}(\mathbf{r}) = 0, \qquad \mathbf{r} \in \mathrm{V}_{int} \cup \mathrm{V}_{ext}, \tag{4.6}$$

and describes the field that would exist in the absence of the scattering object, namely the incident field. The particular solution chosen for equation (4.5) must give the scattered field generated by $\mathbf{j}(\mathbf{r})$ and must vanish at large distances from the scattering object to ensure energy conservation.

The *dyadic Green's function*, a solution to the singular vector Helmholtz equation for the electric field

$$\nabla \times \nabla \times \overline{\overline{\mathsf{G}}}(\mathbf{r}, \mathbf{r}') - k_1^2 \overline{\overline{\mathsf{G}}}(\mathbf{r}, \mathbf{r}') = \bar{\bar{\mathsf{I}}} \delta(\mathbf{r} - \mathbf{r}'), \tag{4.7}$$

provides the framework for solving the boundary-value problem. The dyadic Green's function $\overline{\overline{\mathsf{G}}}(\mathbf{r}, \mathbf{r}')$ is found through applying a Lorentz gauge to the vector potential in the solution of the free-space Maxwell's equations, and is expressed (*Tai*, 1971) as

$$\overline{\overline{\mathsf{G}}}(\mathbf{r}, \mathbf{r}') = \left(\bar{\bar{\mathsf{I}}} + \frac{1}{k_1^2} \nabla \nabla \right) g(\mathbf{r}, \mathbf{r}'), \quad g(\mathbf{r}, \mathbf{r}') = \frac{e^{ik_1 |\mathbf{r} - \mathbf{r}'|}}{4\pi |\mathbf{r} - \mathbf{r}'|}, \tag{4.8}$$

where $g(\mathbf{r}, \mathbf{r}')$ is the Green's function for the scalar Helmholtz equation. From the dyadic property

$$\nabla \times [\overline{\overline{\mathsf{G}}}(\mathbf{r}, \mathbf{r}') \cdot \mathbf{j}(\mathbf{r}')] = [\nabla \times \overline{\overline{\mathsf{G}}}(\mathbf{r}, \mathbf{r}')] \cdot \mathbf{j}(\mathbf{r}'), \tag{4.9}$$

it follows that

$$\nabla \times \nabla \times [\overline{\overline{\mathsf{G}}}(\mathbf{r}, \mathbf{r}') \cdot \mathbf{j}(\mathbf{r}')] - k_1^2 [\overline{\overline{\mathsf{G}}}(\mathbf{r}, \mathbf{r}') \cdot \mathbf{j}(\mathbf{r}')] = \bar{\bar{\mathsf{I}}} \cdot \mathbf{j}(\mathbf{r}') \delta(\mathbf{r} - \mathbf{r}'). \tag{4.10}$$

Integrating both sides of equation (4.10) over the entire space, we obtain

$$\left(\nabla \times \nabla \times \bar{\bar{\mathsf{I}}} - k_1^2 \bar{\bar{\mathsf{I}}} \right) \cdot \int_{\mathrm{V}_{int} \cup \mathrm{V}_{ext}} \overline{\overline{\mathsf{G}}}(\mathbf{r}, \mathbf{r}') \cdot \mathbf{j}(\mathbf{r}') \, \mathrm{d}V' = \mathbf{j}(\mathbf{r}). \tag{4.11}$$

Comparison of (4.11) with (4.5) shows that

$$\mathbf{E}^{\text{sca}}(\mathbf{r}) = \int_{\mathrm{V}_{int}} \overline{\overline{\mathsf{G}}}(\mathbf{r},\mathbf{r}') \cdot \mathbf{j}(\mathbf{r}')\,\mathrm{d}V', \text{ for } \mathbf{r} \in \mathrm{V}_{int} \cup \mathrm{V}_{ext}, \tag{4.12}$$

having taken into account that $\mathbf{j}(\mathbf{r})$ vanishes everywhere outside V_{int}. This particular solution satisfies the necessary conditions, and the complete solution to (4.5) is

$$\mathbf{E}(\mathbf{r}) = \mathbf{E}^{\text{inc}}(\mathbf{r}) + \int_{\mathrm{V}_{int}} \overline{\overline{\mathsf{G}}}(\mathbf{r},\mathbf{r}') \cdot \mathbf{j}(\mathbf{r}')\,\mathrm{d}V', \text{ for } \mathbf{r} \in \mathrm{V}_{int} \cup \mathrm{V}_{ext}. \tag{4.13}$$

The total field is then expressed as

$$\begin{aligned}\mathbf{E}(\mathbf{r}) &= \mathbf{E}^{\text{inc}}(\mathbf{r}) + k_1^2 \int_{\mathrm{V}_{int}} \overline{\overline{\mathsf{G}}}(\mathbf{r},\mathbf{r}') \cdot \mathbf{E}(\mathbf{r}')[m^2(\mathbf{r}') - 1]\mathrm{d}V' \\ &= \mathbf{E}^{\text{inc}}(\mathbf{r}) + k_1^2 \left(\bar{\bar{\mathsf{I}}} + \frac{1}{k_1^2}\nabla\nabla\right) \cdot \int_{\mathrm{V}_{int}} [m^2(\mathbf{r}') - 1]\mathbf{E}(\mathbf{r}') \frac{e^{ik_1|\mathbf{r}-\mathbf{r}'|}}{4\pi|\mathbf{r}-\mathbf{r}'|}\mathrm{d}V', \\ &\text{for } \mathbf{r} \in \mathrm{V}_{int} \cup \mathrm{V}_{ext}.\end{aligned} \tag{4.14}$$

Here the total field at all locations of interest is expressed in terms of the incident field and the total field inside the scattering object. Equation (4.14) is typically solved numerically by first assuming the internal field is equal to the incident field, then computing the resulting total field. The resulting field is then substituted into the integral, and the process is repeated to convergence. The *dyadic transition operator*, $\overline{\overline{\mathsf{T}}}$, for the process of obtaining the internal field, gives the total field as

$$\mathbf{E}(\mathbf{r}) = \mathbf{E}^{\text{inc}}(\mathbf{r}) + \int_{\mathrm{V}_{int}} \overline{\overline{\mathsf{G}}}(\mathbf{r},\mathbf{r}') \cdot \left(\int_{\mathrm{V}_{int}} \overline{\overline{\mathsf{T}}}(\mathbf{r},\mathbf{r}') \cdot \mathbf{E}^{\text{inc}}(\mathbf{r}'')\mathrm{d}V''\right)\mathrm{d}V', \tag{4.15}$$

where $\overline{\overline{\mathsf{T}}}$ is defined in the integral equation

$$\overline{\overline{\mathsf{T}}}(\mathbf{r},\mathbf{r}') = k_1^2[m^2(\mathbf{r}) - 1]\delta(\mathbf{r}-\mathbf{r}')\bar{\bar{\mathsf{I}}} + k_1^2[m^2(\mathbf{r}) - 1] \int_{\mathrm{V}_{int}} \overline{\overline{\mathsf{G}}}(\mathbf{r},\mathbf{r}'') \cdot \overline{\overline{\mathsf{T}}}(\mathbf{r}'',\mathbf{r}')\,\mathrm{d}V''. \tag{4.16}$$

In the far-field zone, $|\mathbf{r}-\mathbf{r}'| \approx r - \mathbf{r}' \cdot \hat{\mathbf{r}}$, and

$$g(\mathbf{r}-\mathbf{r}') = \frac{e^{ik_1 r}}{r} e^{-ik_1 \mathbf{r}' \cdot \hat{\mathbf{r}}}. \tag{4.17}$$

Expressing ∇ in the spherical coordinate system,

$$\nabla = \hat{\mathbf{r}}\frac{\partial}{\partial r} + \hat{\theta}\frac{1}{r}\frac{\partial}{\partial \theta} + \hat{\phi}\frac{1}{r\sin\theta}\frac{\partial}{\partial \phi}. \tag{4.18}$$

The dyad product $\nabla\nabla$ is taken directly in the spherical coordinate system, according to the definition of a tensor, $T'^{ij} = \frac{\partial x'^i}{\partial x^k}\frac{\partial x'^j}{\partial x^l}T^{kl}$. All terms in the operation of the dyad product $\nabla\nabla$ on the far-field Green's function (4.17) contain terms r^{-n}. If all terms with $n > 1$ are neglected, the remaining dyad is

$$\nabla\nabla = \hat{\mathbf{r}}\hat{\mathbf{r}}\frac{\partial^2}{\partial r^2}, \tag{4.19}$$

which gives the dyadic Green's function as

$$\overline{\overline{\mathsf{G}}}(\mathbf{r},\mathbf{r}') = \left(\bar{\mathsf{I}} - \hat{\mathbf{r}}\hat{\mathbf{r}}\right)\frac{e^{-ik_1 r}}{r}e^{-ik_1\mathbf{r}'\cdot\hat{\mathbf{r}}}, \tag{4.20}$$

where the term $\propto r^{-3}$ has been neglected. Then from equation (4.15), the scattered electric field is expressed as

$$\mathbf{E}^{\mathrm{sca}}(\mathbf{r}) = \frac{e^{ik_1 r}}{r}\frac{k_1^2}{4\pi}\left(\bar{\mathsf{I}} - \hat{\mathbf{r}}\hat{\mathbf{r}}\right)\cdot\int_{\mathrm{V}_{int}}[m^2(\mathbf{r}') - 1]\mathbf{E}(\mathbf{r}')e^{-ik_1\mathbf{r}'\cdot\hat{\mathbf{r}}}\mathrm{d}V'. \tag{4.21}$$

The scattered field will be directly related to the incident field from this formulation.

Assuming the incident field is a plane wave,

$$\mathbf{E}^{\mathrm{inc}}(\mathbf{r}) = \mathbf{E}_0^{\mathrm{inc}}\exp\left(ik_1\hat{\mathbf{\Omega}}^{\mathrm{inc}}\cdot\mathbf{r}\right), \tag{4.22}$$

which is substituted into equation (4.15), and assuming that the field inside the scattering object is $\mathbf{E}^{\mathrm{inc}}$ to a first approximation, we have

$$\begin{aligned}\mathbf{E}^{\mathrm{sca}}(\mathbf{r}) = \frac{e^{ik_1 r}}{r}\frac{1}{4\pi}&\left(\bar{\mathsf{I}} - \hat{\mathbf{\Omega}}^{\mathrm{sca}}\,\hat{\mathbf{\Omega}}^{\mathrm{sca}}\right)\\ &\cdot\int_{\mathrm{V}_{int}}\exp(-ik_1\hat{\mathbf{\Omega}}^{\mathrm{sca}}\cdot\mathbf{r}')\left[\int_{\mathrm{V}_{int}}\overline{\overline{\mathsf{T}}}(\mathbf{r}',\mathbf{r}'')\exp(ik_1\hat{\mathbf{\Omega}}^{\mathrm{inc}}\cdot\mathbf{r})\cdot\mathbf{E}_0^{\mathrm{inc}}\,\mathrm{d}V''\right]\mathrm{d}V',\end{aligned} \tag{4.23}$$

with the observer point $\mathbf{r} = r\hat{\mathbf{\Omega}}^{\mathrm{sca}}$. The *scattering dyad*, $\overline{\overline{\mathsf{A}}}$, is expressed as

$$\overline{\overline{\mathsf{A}}} = \frac{1}{4\pi}\left(\bar{\mathsf{I}} - \hat{\mathbf{\Omega}}^{\mathrm{sca}}\,\hat{\mathbf{\Omega}}^{\mathrm{sca}}\right) \cdot \int_{\mathrm{V}_{int}} e^{-ik_1\hat{\mathbf{\Omega}}^{\mathrm{sca}}\cdot\mathbf{r}'}\left[\int_{\mathrm{V}_{int}} \overline{\overline{\mathsf{T}}}(\mathbf{r}',\mathbf{r}'')e^{ik_1\hat{\mathbf{\Omega}}^{\mathrm{inc}}\cdot\mathbf{r}''}\,\mathrm{d}V''\right]\mathrm{d}V', \quad (4.24)$$

such that the incident and scattered fields are linearly related,

$$\mathbf{E}^{\mathrm{sca}}(r\hat{\mathbf{\Omega}}^{\mathrm{sca}}) = \frac{e^{ik_1 r}}{k_1 r}\overline{\overline{\mathsf{A}}}(\hat{\mathbf{\Omega}}^{\mathrm{sca}},\hat{\mathbf{\Omega}}^{\mathrm{inc}}) \cdot \mathbf{E}_0^{\mathrm{inc}}. \quad (4.25)$$

Although this expression was derived for an incident plane wave, scattering of any plane-wave composed incident field can be computed by superposition from this expression. By ensuring that the scattered and incident fields are transverse,

$$\begin{aligned} \hat{\mathbf{\Omega}}^{\mathrm{sca}}\cdot\overline{\overline{\mathsf{A}}}(\hat{\mathbf{\Omega}}^{\mathrm{sca}},\hat{\mathbf{\Omega}}^{\mathrm{inc}}) = 0 \\ \overline{\overline{\mathsf{A}}}(\hat{\mathbf{\Omega}}^{\mathrm{sca}},\hat{\mathbf{\Omega}}^{\mathrm{inc}}) \cdot \hat{\mathbf{\Omega}}^{\mathrm{inc}} = 0, \end{aligned} \quad (4.26)$$

the number of independent components of $\overline{\overline{\mathsf{A}}}$ are reduced from nine to four. The *amplitude scattering matrix*, $\mathbf{S}$, which relates the orthogonal components of the fields as

$$\begin{bmatrix} \mathbf{E}^{\mathrm{sca}_\theta}(r\hat{\mathbf{\Omega}}^{\mathrm{sca}}) \\ \mathbf{E}^{\mathrm{sca}_\phi}(r\hat{\mathbf{\Omega}}^{\mathrm{sca}}) \end{bmatrix} = \frac{e^{ik_1 r}}{k_1 r}\mathbf{S}(\hat{\mathbf{\Omega}}^{\mathrm{sca}},\hat{\mathbf{\Omega}}^{\mathrm{inc}}) \begin{bmatrix} \mathbf{E}^{\mathrm{inc}_\theta}(r\hat{\mathbf{\Omega}}^{\mathrm{inc}}) \\ \mathbf{E}^{\mathrm{inc}_\phi}(r\hat{\mathbf{\Omega}}^{\mathrm{inc}}) \end{bmatrix}, \quad (4.27)$$

is dimensionless and relates the transverse components of the incident and scattered electric fields. In terms of the scattering dyad, its components are

$$\mathbf{S}(\hat{\mathbf{\Omega}}^{\mathrm{sca}},\hat{\mathbf{\Omega}}^{\mathrm{inc}}) = \begin{bmatrix} \mathsf{S}_2 & \mathsf{S}_3 \\ \mathsf{S}_4 & \mathsf{S}_1 \end{bmatrix} = \begin{bmatrix} \hat{\theta}^{sca}\cdot\overline{\overline{\mathsf{A}}}\cdot\hat{\theta}^{inc} & \hat{\theta}^{sca}\cdot\overline{\overline{\mathsf{A}}}\cdot\hat{\phi}^{inc} \\ \hat{\phi}^{sca}\cdot\overline{\overline{\mathsf{A}}}\cdot\hat{\theta}^{inc} & \hat{\phi}^{sca}\cdot\overline{\overline{\mathsf{A}}}\cdot\hat{\phi}^{inc} \end{bmatrix}. \quad (4.28)$$

When known, the amplitude matrix provides a complete description of the scattering pattern in the far-field zone. A key property of the amplitude matrix is the reciprocity relation for reversal of incident and scattered directions,

$$\mathbf{S}(-\hat{\mathbf{\Omega}}^{\mathrm{inc}},-\hat{\mathbf{\Omega}}^{\mathrm{sca}}) = \begin{bmatrix} \mathsf{S}_2(\hat{\mathbf{\Omega}}^{\mathrm{sca}},\hat{\mathbf{\Omega}}^{\mathrm{inc}}) & -\mathsf{S}_3(\hat{\mathbf{\Omega}}^{\mathrm{sca}},\hat{\mathbf{\Omega}}^{\mathrm{inc}}) \\ -\mathsf{S}_4(\hat{\mathbf{\Omega}}^{\mathrm{sca}},\hat{\mathbf{\Omega}}^{\mathrm{inc}}) & \mathsf{S}_1(\hat{\mathbf{\Omega}}^{\mathrm{sca}},\hat{\mathbf{\Omega}}^{\mathrm{inc}}). \end{bmatrix} \quad (4.29)$$

By substituting the scattered field expressions into the defining equation for the amplitude matrix, equation (4.27), the sixteen elements of the phase matrix, (3.32), are given as combinations of the amplitude matrix elements. The amplitude matrix consists of seven independent values: the magnitudes $\mathsf{S}_j,\ j = 1 \ldots 4$, and the three phases between them.

4.1.3 Optical Properties of Scattering Particles

The definitions invoked in equations (3.16) and (3.19) for the scattering and absorption cross sections are made more specific by describing the power measured by photosensitive detectors in the presence and absence of a scattering particle. Through a hypothetical extinction experiment, as illustrated in Figure 4.3, we can relate the optical cross sections to the change in the electromagnetic fields from interactions with the scattering particle.

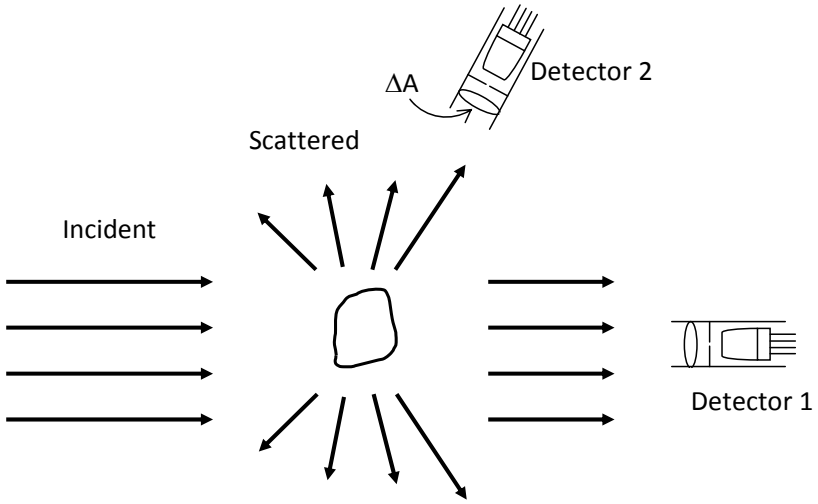

Figure 4.3: Extinction-measuring experiment.

The time-averaged Poynting vector of the total electromagnetic field at any point in the far-field region, which can be expressed as an irradiance, is

$$\begin{aligned}\langle \mathbf{S}(\mathbf{r}) \rangle &= \langle \mathbf{S}^{\mathrm{inc}}(\mathbf{r}) \rangle + \langle \mathbf{S}^{\mathrm{sca}}(\mathbf{r}) \rangle + \langle \mathbf{S}^{\mathrm{ext}}(\mathbf{r}) \rangle \\ &= \frac{1}{2} \mathrm{Re} \left\{ \mathbf{E}^{\mathrm{inc}} \times \mathbf{H}^{\mathrm{inc}*} + \mathbf{E}^{\mathrm{sca}} \times \mathbf{H}^{\mathrm{sca}*} + \mathbf{E}^{\mathrm{inc}} \times \mathbf{H}^{\mathrm{sca}*} + \mathbf{E}^{\mathrm{sca}} \times \mathbf{H}^{\mathrm{inc}*} \right\},\end{aligned} \tag{4.30}$$

where the terms on the right-hand side are, respectively, the incident and scattered irradiances, and two interaction terms between the incident and scattered fields. For an incident plane wave, the fields can be expressed in the far-field region as the sum of an outgoing and incoming spherical wave using the far-field form of the spherical Bessel functions, which gives

$$\begin{aligned}
\mathbf{E}^{\text{inc}}(\mathbf{r}) &= \mathbf{E}_0^{\text{inc}} \exp\left(ik_1 \hat{\mathbf{\Omega}}^{\text{inc}} \cdot \mathbf{r}\right) \\
&\approx \frac{2\pi i}{k_1}\left[\delta(\hat{\mathbf{\Omega}}^{\text{inc}} + \hat{\mathbf{r}})\frac{e^{-ik_1 r}}{r} - \delta(\hat{\mathbf{\Omega}}^{\text{inc}} - \hat{\mathbf{r}})\frac{e^{ik_1 r}}{r}\right]\mathbf{E}_0^{\text{inc}}, \qquad \mathbf{E}_0^{\text{inc}} \cdot \hat{\mathbf{\Omega}}^{\text{inc}} = 0, \\
\mathbf{H}^{\text{inc}}(\mathbf{r}) &= \sqrt{\frac{\epsilon_1}{\mu_0}} \exp\left(ik_1 \hat{\mathbf{\Omega}}^{\text{inc}} \cdot \mathbf{r}\right) \hat{\mathbf{\Omega}}^{\text{inc}} \times \mathbf{E}_0^{\text{inc}} \\
&\approx \frac{2\pi i}{k_1}\left[\delta(\hat{\mathbf{\Omega}}^{\text{inc}} + \hat{\mathbf{r}})\frac{e^{-ik_1 r}}{r} - \delta(\hat{\mathbf{\Omega}}^{\text{inc}} - \hat{\mathbf{r}})\frac{e^{ik_1 r}}{r}\right]\sqrt{\frac{\epsilon_1}{\mu_0}}\,\hat{\mathbf{\Omega}}^{\text{inc}} \times \mathbf{E}_0^{\text{inc}}.
\end{aligned} \tag{4.31}$$

In these expressions $\mathbf{r} = r\hat{\mathbf{r}}$ is the position vector of the observation point. Using the expressions for the scattered electric field derived in the previous section, the scattered fields in the far-field limit are expressed as

$$\begin{aligned}
\mathbf{E}^{\text{sca}}(\mathbf{r}) &= \frac{e^{-ik_1 r}}{k_1 r}\mathbf{E}_1^{\text{sca}}(\hat{\mathbf{r}}), \qquad\qquad \mathbf{E}_1^{\text{sca}}(\hat{\mathbf{r}}) \cdot \hat{\mathbf{r}} = 0 \\
\mathbf{H}^{\text{sca}}(\mathbf{r}) &= \sqrt{\frac{\epsilon_1}{\mu_0}}\frac{e^{-ik_1 r}}{k_1 r}\hat{\mathbf{\Omega}}^{\text{sca}} \times \mathbf{E}_1^{\text{sca}}(\hat{\mathbf{r}}).
\end{aligned} \tag{4.32}$$

Consider detector 2 in Figure 4.3, which lies at a distance r from the particle in the far-field zone and has its surface aligned normal to $\hat{\mathbf{r}}$. The detector surface is assumed to be sufficiently large that the scattered fields do not change significantly over the detector area. The time-averaged power measured by this detector is found by substituting the expressions for the incident and scattered fields into equation (4.30). The measured power at this location is simply

$$W_{sca,\Delta A}(\hat{\mathbf{r}} \neq \hat{\mathbf{\Omega}}^{\text{inc}}) = \int_{\Delta A} \langle \mathbf{S}(\mathbf{r}) \rangle \cdot \hat{\mathbf{r}}\, \mathrm{d}A = \frac{1}{2}\sqrt{\frac{\epsilon_1}{\mu_0}}\,\frac{|\mathbf{E}_1^{\text{sca}}(\hat{\mathbf{r}})|^2}{k_1^2}\,\Delta\Omega, \tag{4.33}$$

where $\Delta\Omega = \frac{\Delta A}{r^2}$ is the solid angle subtended by the detector area as seen by the particle.

In a similar manner, the power measured by detector 1, which lies at a distance z from the particle in the forward-scattering direction, $\hat{\mathbf{r}} = \hat{\mathbf{\Omega}}^{\mathrm{inc}}$, is

$$\begin{aligned} W(\hat{\mathbf{r}} = \hat{\mathbf{\Omega}}^{\mathrm{inc}}) &= \int_{\Delta A} \langle \mathbf{S}(\mathbf{r}) \rangle \cdot \hat{\mathbf{r}} \, \mathrm{d}A \\ &= \frac{1}{2}\sqrt{\frac{\epsilon_1}{\mu_0}} \left[|\mathbf{E}_0^{\mathrm{inc}}|^2 \Delta A + \frac{|\mathbf{E}_1^{\mathrm{sca}}|^2}{k_1^2} \Delta\Omega - \frac{4\pi}{k_1^2} \mathrm{Im} \left\{ \mathbf{E}_1^{\mathrm{sca}}(\hat{\mathbf{\Omega}}^{\mathrm{inc}}) \cdot \mathbf{E}_0^{\mathrm{inc}*} \right\} \right] \\ &= F_0 \left[\Delta A + \frac{|\mathbf{E}_1^{\mathrm{sca}}|^2}{k_1^2 |\mathbf{E}_0^{\mathrm{inc}}|^2} \Delta\Omega - \frac{4\pi}{k_1^2 |\mathbf{E}_0^{\mathrm{inc}}|^2} \mathrm{Im} \left\{ \mathbf{E}_1^{\mathrm{sca}}(\hat{\mathbf{\Omega}}^{\mathrm{inc}}) \cdot \mathbf{E}_0^{\mathrm{inc}*} \right\} \right]. \end{aligned} \tag{4.34}$$

The incident irradiance,

$$F_0 = \frac{1}{2}\sqrt{\frac{\epsilon_1}{\mu_0}} |\mathbf{E}_0^{\mathrm{inc}}|^2, \tag{4.35}$$

has been substituted for simplicity. The first term on the right-hand side of (4.34) corresponds to the incident field power captured by the detector, and is independent of the distance of the detector from the scattering particle. This component of the power also remains unchanged if the scattering particle is removed.

The second term in equation (4.34) corresponds to the power scattered into a solid angle $\Delta\Omega$ centred about the forward direction. If this solid angle is made sufficiently small, consistent with the requirement that $k_1 R^2/z \gg 4\pi$, where R is the maximum linear dimension of the detector surface, then the measured power is

$$W(\hat{\mathbf{r}} = \hat{\mathbf{\Omega}}^{\mathrm{inc}}) = F_0 \left(\Delta A - \sigma_{ext} \right). \tag{4.36}$$

In this expression the term that expresses the maximum reduction in measured power due to the presence of the scattering particle is the extinction cross section, σ_{ext}, defined as the ratio of the power removed from the beam to the incident irradiance,

$$\begin{aligned} \sigma_{ext} = \frac{W_{ext}}{F_0} &= \frac{4\pi}{k_1^2} \frac{\mathrm{Im} \left\{ \mathbf{E}_1^{\mathrm{sca}}(\hat{\mathbf{\Omega}}^{\mathrm{inc}}) \cdot \mathbf{E}_0^{\mathrm{inc}*} \right\}}{|\mathbf{E}_0^{\mathrm{inc}}|^2} \\ &= \frac{4\pi}{k_1^2} \mathrm{Im} \left\{ \mathbf{S}(\hat{\mathbf{\Omega}}^{\mathrm{inc}}, \hat{\mathbf{\Omega}}^{\mathrm{inc}}) \cdot \mathbf{e}^* \right\}, \end{aligned} \tag{4.37}$$

which has dimensions of area. In this expression, $\mathbf{e}$ is the complex polarization vector

of the incident electric field. Note that in this expression the extinction cross section depends on the value of the scattering amplitude, $\mathbf{S}$, in the forward direction only.

From equation (4.36), the extinction cross section is then a directly observable physical quantity. When the measurement of the scattered-field power is made sufficiently small, then the reduction in measured power due to the presence of the intervening particle yields the value σ_{ext}.

In analogy with the measurement from detector 2 in Figure 4.3, the scattering cross section is defined by the integral of the scattered field over the surface of a far-field sphere that encloses the scattering particle, again as a power removed from the beam relative to the incident radiance,

$$\sigma_{sca} = \frac{W_{sca}}{F_0} = \int_{4\pi} \frac{|\mathbf{E}_1^{\mathrm{sca}}|^2}{k_1^2 |\mathbf{E}_0^{\mathrm{inc}}|^2} \, \mathrm{d}\Omega. \tag{4.38}$$

Similarly, the absorption cross section is evaluated as a ratio of power to the incident irradiance. In this case, the power is that absorbed by a particle as computed by integrating the total Poynting vector over the surface of a sphere,

$$\sigma_{abs} = \frac{W_{abs}}{F_0} = \frac{1}{F_0} \int_{4\pi} \langle \mathbf{S}(\mathbf{r}) \rangle \cdot \hat{\mathbf{r}} \, \mathrm{d}A. \tag{4.39}$$

When equations (4.30), (4.37), and (4.38) are evaluated for a non-absorbing medium, we obtain the relation

$$\sigma_{ext} = \sigma_{sca} + \sigma_{abs}. \tag{4.40}$$

We note that the definition of the extinction cross section in equation (4.37) is a statement of the optical theorem (**?**, *Newton* (1976)). This theorem states that for a process in which the scattering amplitude is S, such that the total field is $\psi(r) = e^{ikz} + \frac{e^{ikr}}{kr} S(\theta)$, the extinction cross section is

$$\sigma_{ext} = \frac{4\pi}{k_1^2} \mathrm{Im} \left\{ S(0) \right\}. \tag{4.41}$$

This is a fundamental result that states that the extinction depends only on the

scattering amplitude in the forward direction and that describes scattering properties for a wide range of physical processes from acoustic and electromagnetic waves to operations involving elementary particles.

4.1.4 Particle Size Distributions

The optical properties described thus far have been those for a single particle. In any measurements of the optical properties of real particles there is always an underlying distribution in particle size due to ongoing particle formation, growth, and removal processes.

Various particle size distributions (PSDs) are used to parameterize the microphysical distribution of the scattering or absorbing particles, where optical properties are calculated as expectation values from the distribution. For a given PSD, the number of particles of size between L and $L + \mathrm{d}L$ is $n(L)\mathrm{d}L$. The *gamma distribution*,

$$n(L) = N_{0\Gamma} L^{\mu}\, e^{-\lambda_{\Gamma} L}, \tag{4.42}$$

where both λ_{Γ} and $L > 0$, and $-1 \geq \mu \geq +1$, is typically used to describe the size distribution of cirrus cloud ice crystals and has also been used to model blowing snow particles (*Pomeroy and Male*, 1988). This distribution is used at several points within this work. The *lognormal distribution*, which describes a quantity whose natural logarithm is distributed according to the normal distribution, is expressed as

$$n(L) = \frac{1}{\ln s_g \sqrt{2\pi}} \frac{1}{L} e^{-\frac{(\ln L - \ln L_0)^2}{2(\ln s_g)^2}}. \tag{4.43}$$

The lognormal distribution is typically used to describe the size distribution of stratospheric sulphate aerosols, where L and $L_0 \geq 0$ and $s_g > 1$. Ice cloud size distributions are typically expressed as a function of the maximum dimension of detected particles, denoted by L, since this is the most readily measurable linear dimension of irregularly-shaped particles.

The *effective size*, D_e, is a characteristic dimension used to describe the scattering

properties of a cirrus cloud in a way that is representative of the bulk behaviour of constituent ice crystals. There is some variety in the definitions of an effective size of cirrus ice crystals due to the varying crystal shapes encountered (*McFarquhar and Heymsfield*, 1998).

A common definition comes from *Hansen* (1971), who found that the optical properties of liquid water clouds composed of spherical droplets with large size parameter depended mainly on the effective radius for scattering, defined as

$$r_e = \frac{1}{\langle G \rangle} \int_0^\infty \pi r^2 \, n(r) \, r \, \mathrm{d}r. \tag{4.44}$$

In this expression, $\langle G \rangle$ is the average geometric cross-sectional area of water drops per unit volume, and the size parameter for the particles studied were sufficiently large that Q_{ext} was taken to have a value of two. An alternate definition of the effective size is in terms of the ratio of the total volume to the total projected area normal to an imaging beam,

$$D_e = \frac{3}{2} \frac{\int_{L_{min}}^{L_{max}} V(L) n(L) \, \mathrm{d}L}{\int_{L_{min}}^{L_{max}} A(L) n(L) \, \mathrm{d}L}. \tag{4.45}$$

In this definition, L_{min} and L_{max} are the sizing instrumentation detection limits.

These definitions are made explicit since later chapters will describe the effective size that best describes scattering by a detected cloud. The width of a size distribution is typically expressed in cloud microphysics in terms of the *effective width*,

$$w_e = \frac{1}{\langle G \rangle} \int_0^\infty \pi r^2 \, n(r) \, (r - r_e)^2 \, \mathrm{d}r. \tag{4.46}$$

The terminology used in this work describes cloud particles in terms of their effective size expressed as a diameter, $D_e = 2r_e$, to correspond to the maximum particle dimension, L. It is worth noting at this point that many cirrus clouds parameterizations within climate models use as inputs the properties τ_c, D_e, and cloudiness fraction in a geographical area to represent clouds within a given grid cell.

4.2 Sources for Optical Properties of Ice Crystals

The development of numerical techniques for computing the optical properties σ_{ext}, σ_{scat}, and $P(\Theta)$ of non-spherical particles is a large and complex field, and in this work we only briefly summarize the approaches used to obtain these properties. The T-matrix technique (*Mishchenko et al.*, 1996) expands the incident, internal, and scattered fields in vector spherical wave function representations, and enforces continuity at the particle surface. The Discrete Dipole Approximation (DDA, *Yurkin and Hoekstra* (2007)) models the scattering body as a collection of interacting point dipoles. For larger particles, a database of optical properties generated by a geometric ray-tracing technique is used in this work. A summary of these sources follows.

4.2.1 T-Matrix Technique

The T-matrix method is based on expanding the incident and scattered electromagnetic fields in vector spherical basis functions $\mathbf{M}_{mn}$ and $\mathbf{N}_{mn}$ similar to those used in Mie theory,

$$\begin{aligned}\mathbf{E}^{\text{inc}}(\mathbf{r}) &= \sum_{n=1}^{\infty}\sum_{m=-n}^{n}\left[a_{mn}\,\text{Rg}\,\mathbf{M}_{mn}(k_1\mathbf{r}) + b_{mn}\,\text{Rg}\,\mathbf{N}_{mn}(k_1\mathbf{r})\right] \\ \mathbf{E}^{\text{sca}}(\mathbf{r}) &= \sum_{n=1}^{\infty}\sum_{m=-n}^{n}\left[p_{mn}\,\mathbf{M}_{mn}(k_1\mathbf{r}) + q_{mn}\,\mathbf{N}_{mn}(k_1\mathbf{r})\right],\end{aligned} \tag{4.47}$$

where $\mathbf{M}_{mn}$ is purely transverse. The functions Rg $\mathbf{M}_{mn}$ and Rg $\mathbf{N}_{mn}$ are regular (finite) at the origin, with radial components given by spherical Bessel functions, while $\mathbf{M}_{mn}$ and $\mathbf{N}_{mn}$ contain spherical Hankel functions to ensure the radiation condition at infinity is satisfied. From the linearity of Maxwell's equations, the scattered- and incident-field coefficients are related in matrix form as

$$\begin{bmatrix}\mathbf{p}\\ \mathbf{q}\end{bmatrix} = \begin{bmatrix}\mathbf{T}^{11} & \mathbf{T}^{12}\\ \mathbf{T}^{21} & \mathbf{T}^{22}\end{bmatrix}\begin{bmatrix}\mathbf{a}\\ \mathbf{b}\end{bmatrix} = \mathbf{T}\begin{bmatrix}\mathbf{a}\\ \mathbf{b}\end{bmatrix}, \tag{4.48}$$

and the **T**-matrix relates the incident and scattered field coefficients. The extended boundary condition method (EBCM, *Waterman* (1971)) on which the T-matrix method is based, uses the vector Green's theorem to solve for the electric and magnetic fields in the scattering volume in terms of their behavior on the particle surface. The vector Huygens' principle, based on applying Green's theorem to the electric field in the region V_{ext} outside the scattering particle, relates the incident, scattered, and total fields (*Mishchenko et al.*, 2002) as

$$\mathbf{E}^{\mathrm{inc}}(\mathbf{r}') + \int_S \hat{\mathbf{n}} \cdot \Big([\nabla \times \mathbf{E}(\mathbf{r})] \times \overline{\overline{\mathsf{G}}}(\mathbf{r}, \mathbf{r}') + \mathbf{E}(\mathbf{r}) \times [\nabla \times \overline{\overline{\mathsf{G}}}(\mathbf{r}, \mathbf{r}')] \Big) \, \mathrm{d}S = \begin{cases} \mathbf{E}(\mathbf{r}'), & \mathbf{r}' \in \mathrm{V}_{ext} \\ 0, & \mathbf{r}' \in \mathrm{V}_{int}, \end{cases} \tag{4.49}$$

where $\hat{\mathbf{n}}$ is a unit vector normal to surface element $\mathrm{d}S$. The scattered field outside the particle is expressed in terms of the components of the fields on the exterior of the particle surface (denoted by the '+' superscript) as

$$\mathbf{E}^{\mathrm{sca}}(\mathbf{r}') = \int_S \Big(i\omega\mu_0 [\hat{\mathbf{n}} \times \mathbf{H}^+(\mathbf{r})] \cdot \overline{\overline{\mathsf{G}}}(\mathbf{r}, \mathbf{r}') + [\hat{\mathbf{n}} \times \mathbf{E}^+(\mathbf{r})] \cdot [\nabla \times \overline{\overline{\mathsf{G}}}(\mathbf{r}, \mathbf{r}')] \Big) \, \mathrm{d}S. \tag{4.50}$$

The boundary condition separating the regions in equation (4.49) is 'extended' by moving $\mathbf{r}'$ inside the particle. In this scheme, the incident field is then also expressed as a function of the surface fields,

$$\mathbf{E}^{\mathrm{inc}}(\mathbf{r}') = -\int_S \Big(i\omega\mu_0 \left[\hat{\mathbf{n}} \times \mathbf{H}^+(\mathbf{r})\right] \cdot \overline{\overline{\mathsf{G}}}(\mathbf{r}, \mathbf{r}') + \left[\hat{\mathbf{n}} \times \mathbf{E}^+(\mathbf{r})\right] \cdot [\nabla \times \overline{\overline{\mathsf{G}}}(\mathbf{r}, \mathbf{r}')] \Big) \, \mathrm{d}S. \tag{4.51}$$

Numerically, the incident field series coefficients **a** and **b** are precalculated with reference to the incident field orientation. Equation (4.51) thus reinterprets the incident field $\mathbf{E}^{\mathrm{inc}}$ as equivalent electric and magnetic currents $\mathbf{J} = \hat{\mathbf{n}} \times \mathbf{H}^+$ and $\mathbf{M} = \mathbf{E}^+ \times \hat{\mathbf{n}}$ on the particle surface according to Schelkunoff's equivalence theorem (*Barber and Yeh*, 1975). By expressing the free space dyadic Green's function in vector spherical

wave functions (*Morse and Feshbach*, 1953),

$$\overline{\overline{\mathsf{G}}}(\mathbf{r},\mathbf{r}') = ik_1 \sum_{n=1}^{\infty}\sum_{m=-n}^{n}(-1)^m \begin{cases} \mathbf{M}_{-mn}(k_1\, r,\theta,\phi)\mathrm{Rg}\,\mathbf{M}_{mn}(k_1\, r',\theta',\phi') \\ +\mathbf{N}_{-mn}(k_1\, r,\theta,\phi)\mathrm{Rg}\,\mathbf{N}_{mn}(k_1\, r',\theta',\phi') & r > r' \\ \mathrm{Rg}\,\mathbf{M}_{-mn}(k_1\, r,\theta,\phi)\mathbf{M}_{mn}(k_1\, r',\theta',\phi') \\ +\mathrm{Rg}\,\mathbf{N}_{-mn}(k_1\, r,\theta,\phi)\mathbf{N}_{mn}(k_1\, r',\theta',\phi') & r' > r, \end{cases} \tag{4.52}$$

and substituting this form into equations (4.50) and (4.51), the scattered field series coefficients $\mathbf{p}$ and $\mathbf{q}$ are given in terms of the surface currents $\hat{\mathbf{n}}\times\mathbf{H}^+(\mathbf{r})$ and $\hat{\mathbf{n}}\times\mathbf{E}^+(\mathbf{r})$. The fundamental series expansions in equation (4.47) are found in this way, where the series coefficients $\mathbf{a}$, $\mathbf{b}$, $\mathbf{p}$, and $\mathbf{q}$ are the terms leading the desired basis functions. Then the coefficients are found as

$$\begin{aligned} a_{mn} &= (-1)^m k_1 \int_S \omega\mu_0 \big[\hat{\mathbf{n}}\times\mathbf{H}^+(\mathbf{r})\cdot\mathbf{M}_{-mn}(k_1\, r,\theta,\phi) \\ &\qquad - ik_1\hat{\mathbf{n}}\times\mathbf{E}^+(\mathbf{r})\cdot\mathbf{N}_{-mn}(k_1\, r,\theta,\phi)\big]\mathrm{d}S \\ b_{mn} &= (-1)^m k_1 \int_S [\omega\mu_0\big[\hat{\mathbf{n}}\times\mathbf{H}^+(\mathbf{r})]\cdot\mathbf{N}_{-mn}(k_1\, r,\theta,\phi) \\ &\qquad - ik_1[\hat{\mathbf{n}}\times\mathbf{E}^+(\mathbf{r})]\cdot\mathbf{M}_{-mn}(k_1\, r,\theta,\phi)\big]\mathrm{d}S \end{aligned} \tag{4.53}$$

and

$$\begin{aligned} p_{mn} &= -(-1)^m k_1 \int_S \big[\mu_0\omega[\hat{\mathbf{n}}\times\mathbf{H}^+(\mathbf{r})]\cdot\mathrm{Rg}\ \mathbf{M}_{-mn}(k_1\, r,\theta,\phi) \\ &\qquad - ik_1[\hat{\mathbf{n}}\times\mathbf{E}^+(\mathbf{r})]\cdot\mathrm{Rg}\ \mathbf{N}_{-mn}(k_1\, r,\theta,\phi)\big]\mathrm{d}S \\ q_{mn} &= -(-1)^m k_1 \int_S \big[\mu_0\omega[\hat{\mathbf{n}}\times\mathbf{H}^+(\mathbf{r})]\cdot\mathrm{Rg}\ \mathbf{N}_{-mn}(k_1\, r,\theta,\phi) \\ &\qquad - ik_1[\hat{\mathbf{n}}\times\mathbf{E}^+(\mathbf{r})]\cdot\mathrm{Rg}\ \mathbf{M}_{-mn}(k_1\, r,\theta,\phi)\big]\mathrm{d}S. \end{aligned} \tag{4.54}$$

These relations express the scattered fields in terms of surface currents generated by the incident and induced fields. To obtain the total surface current, surface fields due to the internal fields must be determined. The fields everywhere inside the scattering object are expanded in regular vector spherical wave functions of the *interior* wave

equation (4.2)

$$\begin{aligned}\mathbf{E}(\mathbf{r}) &= \sum_{n'=1}^{\infty}\sum_{m'=-n'}^{n'}\left[c_{m'n'}\,\mathrm{Rg}\,\mathbf{M}_{m'n'}(k_2\mathbf{r}) + d_{mn}\,\mathrm{Rg}\,\mathbf{N}_{m'n'}(k_2\mathbf{r})\right] \\ \mathbf{H}(\mathbf{r}) &= \frac{k_2}{i\omega\mu_0}\sum_{n'=1}^{\infty}\sum_{m'=-n'}^{n'}\left[d_{m'n'}\,\mathrm{Rg}\,\mathbf{M}_{m'n'}(k_2\mathbf{r}) + c_{mn}\,\mathrm{Rg}\,\mathbf{N}_{m'n'}(k_2\mathbf{r})\right]\end{aligned} \tag{4.55}$$

for $\mathbf{r} \in \mathrm{V}_{int}$. The boundary conditions for the solution of Maxwell's equations requires the continuity of the tangential electric and magnetic fields at all points on the surface,

$$\begin{aligned}\hat{\mathbf{n}} \times \mathbf{E}^{+}(\mathbf{r}) &= \hat{\mathbf{n}} \times \mathbf{E}^{-}(\mathbf{r}) \\ \hat{\mathbf{n}} \times \mathbf{H}^{+}(\mathbf{r}) &= \hat{\mathbf{n}} \times \mathbf{H}^{-}(\mathbf{r}).\end{aligned} \tag{4.56}$$

Substituting (4.55) through (4.56) into (4.53) and rearranging, the matrix equation

$$\begin{bmatrix}\mathbf{a} \\ \mathbf{b}\end{bmatrix} = \mathbf{Q}\begin{bmatrix}\mathbf{c} \\ \mathbf{d}\end{bmatrix} = \begin{bmatrix}\mathbf{Q}^{11} & \mathbf{Q}^{12} \\ \mathbf{Q}^{21} & \mathbf{Q}^{22}\end{bmatrix}\begin{bmatrix}\mathbf{c} \\ \mathbf{d}\end{bmatrix} \tag{4.57}$$

is obtained, where elements of $\mathbf{Q}$ are integrals of the vector spherical wave functions over the particle surface. Effectively, incident field coefficients $\mathbf{a}$ and $\mathbf{b}$ have been recast in terms of the resulting field inside the scattering object. Similarly, substituting (4.55) through (4.56) into (4.54) gives the scattered field coefficients $\mathbf{p}$ and $\mathbf{q}$,

$$\begin{bmatrix}\mathbf{p} \\ \mathbf{q}\end{bmatrix} = -\mathrm{Rg}\ \mathbf{Q}\begin{bmatrix}\mathbf{c} \\ \mathbf{d}\end{bmatrix} = -\begin{bmatrix}\mathrm{Rg}\ \mathbf{Q}^{11} & \mathrm{Rg}\ \mathbf{Q}^{12} \\ \mathrm{Rg}\ \mathbf{Q}^{21} & \mathrm{Rg}\ \mathbf{Q}^{22}\end{bmatrix}\begin{bmatrix}\mathbf{c} \\ \mathbf{d}\end{bmatrix}. \tag{4.58}$$

So the T-matrix – which relates the scattered field expansion coefficients to the incident field coefficients as in (4.48) – is given in the particle's reference frame, P, as

$$\mathbf{T}(P) = -(\mathrm{Rg}\mathbf{Q})\mathbf{Q}^{-1}. \tag{4.59}$$

Because the T-matrix depends only on the scattering particle size, shape, and refractive index, averaging may be performed over the particle orientation, and the results

of a computation are extensively cached. All scattering properties for the particle are expressed in terms of the T-matrix, for example

$$\begin{aligned}\sigma_{ext} &= -\frac{1}{k_1^2|\mathbf{E}_0^{\text{inc}}|^2}\text{Re}\sum_{n=1}^{\infty}\sum_{m=-n}^{n}\left[a_{mn}(p_{mn})^* + b_{mn}(q_{mn})^*\right] \\ \sigma_{sca} &= \frac{1}{k_1^2|\mathbf{E}_0^{\text{inc}}|^2}\sum_{n=1}^{\infty}\sum_{m=-n}^{n}\left[|p_{mn}|^2 + |q_{mn}|^2\right],\end{aligned} \tag{4.60}$$

and the amplitude matrix (4.27) and scattering matrix (3.33) elements are formed by linear combinations of angular eigenfunctions with T-matrix elements as coefficients. For the case of a spherical scattering problem, this method exactly recovers the results obtained from Lorenz-Mie computations.

A sample computation of the scattering phase function $P(\Theta)$ for prolate circular cylinders with axis ratio 2:1 is shown in Figure 4.4 for a range of effective sizes, x, on a logarithmic scale. For size parameters near zero, it is clear that the scattering phase

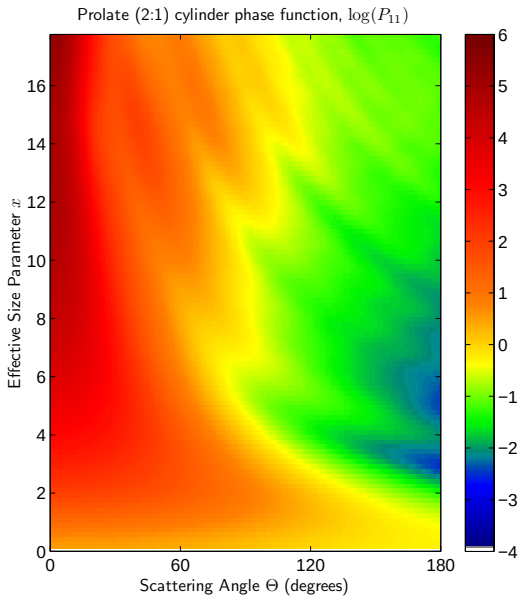

Figure 4.4: T-matrix phase functions for scattering of 750 nm light by varying particle sizes.

function appears quite close to the near-isotropic behaviour of Rayleigh scattering. As the size parameter increases, the scattering behaviour becomes increasingly dom-

inated by forward scattering. A number of 'halo' features are present as well in this figure for size parameters above $x = 4$ and for scattering angles $30 < \Theta < 150$.

The T-matrix code of *Mishchenko et al.* (1996), which is written in the FORTRAN programming language, has been incorporated into the SASKTRAN model as a dynamically-linked library (DLL) through the use of wrapper classes to calculate ice-scattering properties.

4.2.2 Discrete Dipole Approximation

The discrete dipole approximation begins by discretizing the integration volume V_{int} of equation (4.14) into N spherical subvolumes, each of which is modeled as a dipole. The total scattered field is computed from the bulk effect of the interaction of the dipoles with the incident field and with each other. From equation (4.14), the electric field at a point inside subvolume V_i that results from the incident field is

$$\mathbf{E}(\mathbf{r}) = \mathbf{E}^{\mathrm{inc}}(\mathbf{r}) + k_1^2 \sum_{j \neq i}^{N} \int_{V_j} \overline{\overline{\mathsf{G}}}(\mathbf{r}, \mathbf{r}') \cdot \mathbf{E}(\mathbf{r}') \chi(\mathbf{r}') \mathrm{d}V' + \mathbf{M}(V_i, \mathbf{r}) - \overline{\overline{\mathsf{L}}}(\Delta V_i, \mathbf{r}) \cdot \mathbf{E}(\mathbf{r}) \chi(\mathbf{r}), \tag{4.61}$$

where $\chi(\mathbf{r}) = [m^2(\mathbf{r}) - 1]$ is the material susceptibility. The vector

$$\mathbf{M}(V_i, \mathbf{r}) = \int_{V_i} \left(\overline{\overline{\mathsf{G}}}(\mathbf{r}, \mathbf{r}') \cdot \mathbf{E}(\mathbf{r}') \chi(\mathbf{r}') - \overline{\overline{\mathsf{G}}}^{s}(\mathbf{r}, \mathbf{r}') \cdot \mathbf{E}(\mathbf{r}) \chi(\mathbf{r}) \right) \mathrm{d}V' \tag{4.62}$$

accounts for the finiteness of volume V_i, and approaches zero as V_i decreases. Here $\overline{\overline{\mathsf{G}}}^{s}(\mathbf{r}, \mathbf{r}')$ is the static limit ($k \to 0$) of the higher-order Green's dyadic

$$\overline{\overline{\mathsf{G}}}^{s}(\mathbf{r}, \mathbf{r}') = \nabla\nabla \frac{1}{R} = -\frac{1}{R^3} \left(\bar{\bar{\mathsf{I}}} - 3 \frac{\hat{\mathbf{R}}\hat{\mathbf{R}}}{R^2} \right), \tag{4.63}$$

where $\mathbf{R} = \mathbf{r} - \mathbf{r}'$. The effect of subvolume V_i on itself is accounted for by the self-term dyadic

$$\overline{\overline{\mathsf{L}}}(\Delta V_i, \mathbf{r}) = - \oint_{\Delta V_i} \frac{\hat{\mathbf{n}}' \hat{\mathbf{R}}}{R^3} \mathrm{d}S'. \tag{4.64}$$

where surface ΔV_i has unit normal $\hat{\mathbf{n}}'$ at $\mathbf{r}'$. Assuming the dielectric properties are constant within each subvolume and that the representation of interacting dipoles captures well the effects of material polarization, a matrix formulation of the scattering problem follows (*Yurkin and Hoekstra*, 2007), which solves for the exciting electric fields at each dipole location

$$\mathbf{E}_i^{\text{exc}} = \left[\bar{\bar{\mathsf{I}}} + (\bar{\bar{\mathsf{L}}}_i - \bar{\bar{\bar{\mathsf{M}}}}_i)\chi_i\right] \cdot \mathbf{E}_i = \mathbf{E}_i - \mathbf{E}_i^{\text{self}} \tag{4.65}$$

$$\mathbf{E}_i^{\text{self}} = (\bar{\bar{\bar{\mathsf{M}}}}_i - \bar{\bar{\mathsf{L}}}_i)\chi_i \cdot \mathbf{E}_i. \tag{4.66}$$

Here $\chi_i = \chi(r_i)$ is the susceptibility of the i^{th} dipole and $\mathbf{E}_i^{\text{self}}$ is the field induced by the sub-volume on itself. In this expression the values of $\bar{\bar{\mathsf{L}}}_i$ and $\bar{\bar{\bar{\mathsf{M}}}}_i$ are evaluated using their equivalents at the 'dipole' sphere centres. With these assumptions, the total field in equation (4.14) through equation (4.61) is

$$\mathbf{E}_i^{\text{inc}} = \mathbf{E}_i^{\text{exc}} - \sum_{j \neq i} \bar{\bar{\bar{\mathsf{G}}}}_{ij} \bar{\bar{\alpha}}_j \mathbf{E}_j^{\text{exc}}, \tag{4.67}$$

where $\bar{\bar{\alpha}}_i$ is the polarizability tensor,

$$\bar{\bar{\alpha}}_i = V_i \chi_i \left[\bar{\bar{\mathsf{I}}} + (\bar{\bar{\mathsf{L}}}_i - \bar{\bar{\bar{\mathsf{M}}}}_i)\chi_i\right]^{-1}, \tag{4.68}$$

and the scattered-field solution requires solving only $3N$ linear equations. This method has received considerable attention due to its numerical simplicity and quite good accuracy.

The DDSCAT code of *Draine and Flatau* (1994), which is written in the FORTRAN programming language, has also been incorporated into the SASKTRAN model as a dynamically-linked library (DLL) through the use of wrapper classes to calculate ice-scattering properties.

Either of the T-matrix or DDA algorithm may be used in SASKTRAN to compute scattering of sunlight by small ice crystals, depending on the type of ice-scattering computations needed. The T-matrix approach has slightly faster computational times

that come at the expense of assuming axially-symmetric scattering particles. The DDA algorithm, by contrast, allows the user to specify arbitrary particle shape. For currently available computational resources, these algorithms work for particle sizes up to approximately 1 μm for the wavelengths of interest in this work.

4.3 Database of Cirrus Optical Properties

The characteristic sizes of ice crystals frequently encountered in cirrus clouds can vary over a very large range, depending on the thermodynamic conditions in the cloud region as well as on the available water vapour amount. Typical effective radii for cirrus range from 10 μm to 200 μm, with effective size parameter x between 1 and 1500. For any but the smallest of these size parameters, analytical computations become impractical. For this purpose, *Baum et al.* (2005a) and *Baum et al.* (2005b) have compiled a database of ice crystal scattering properties for a large variety of ice crystal habits based on in-situ collection of cloud particles.

From a series of experiments in which high-altitude aircraft with particle size spectrometer probes were taken through Lagrangian descents through clouds (*Heymsfield et al.*, 2002), 1117 measured particle size spectra from tropical and sub-tropical cloud observations were fit to gamma distributions (4.42). The measured size distributions, characterized by a median mass diameter D_m and cloud ice-water content (IWC), were supplemented by cloud-particle imager (CPI) and video ice particle sampler (VIPS) probe data taken concurrently, which also measured L, the maximum dimension of detected particles.

By using IWC and median mass diameter D_m as orthogonal fit parameters, ice optical property modeling was performed using combined DDA-geometric optics methods – for a range of assumed particle habits – for the measured PSDs to obtain habit-specific 'calculated' values IWC and D_m.

Relative amounts of each habit mixture were adjusted to obtain best-fit comparisons between the measured and 'calculated' D_m and IWC. Size-specific ice crystal habits were used: droxtals (*Yang et al.*, 2003) and plates for particles smaller than

$L = 60$ μm; plates, columns, and needles for crystals 60 μm $\leq L \leq$ 2000 μm; and aggregates for the largest crystals. The selected habit mixtures were consistent with CPI and VIPS images. The range of measured sizes is characterized by the effective size, D_e, using the definition of equation (4.45). The computed optical properties in the database are binned into 18 effective sizes: from $D_e = 10$ μm to 180 μm in 10 μm increments. The mean and standard deviation of computed properties from the 1117 measured PSDs are tabulated in the database for wavelengths between 400 nm and 2.2 μm.

A typical plot of the scattering phase function from this database, as a function of effective size parameter and scattering angle for scattering of 750 nm light, is shown in the left-hand panel of Figure 4.5. Note that the phase function values are shown on a logarithmic scale. The phase function for $D_e = 180$ μm from this figure is

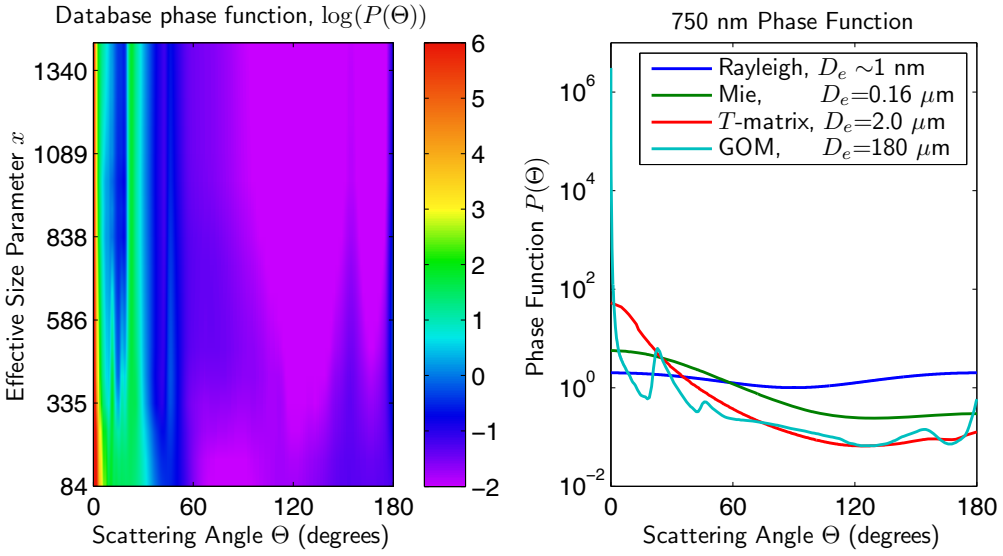

Figure 4.5: Phase function from in situ database optical properties (a) for all effective sizes, 10 to 180 μm. (b) Rayleigh- and Mie-scattering phase functions compared with T-matrix and $D_e = 180$ μm database phase functions.

shown at right along with phase functions for 750 nm light scattering by particles whose effective size span several orders of magnitude. Rayleigh scattered light from atmospheric molecules is nearly isotropic with preferential forward and backward scattering. Mie scattering from typical stratospheric aerosol particles in a lognormal

distribution from the code of *Wiscombe* (1980) has a clear forward peak. This peak increases by an order of magnitude for T-matrix computations of scattering by ice crystals with size $D_e = 2.0\ \mu$m and effective width $w_e = 0.113$. This diffraction peak becomes extremely large for scattering by large particles, as also seen in the left-hand figure, where for most particle sizes at this wavelength, the value of the phase function in the near-forward direction is on the order of 10^6. As well, there are several haloes present for all effective sizes in the left-hand plot. There is a distinct halo near 22° due to a single refraction between the opposing faces of a hexagonal crystal at 240° to one another; and a halo near 46° from refraction between the basal and prismatic faces.

The ice crystal optical properties from this database have been incorporated into the SASKTRAN model. However, the inclusion of such extremely sharply peaked phase functions requires several modifications to a standard successive-orders model, whose scattering integral evaluation was designed for Rayleigh- and Mie-scattering particles. These modifications, and the techniques developed to study their effectiveness, are discussed in the next chapter.

Chapter 5

Unit Sphere Integration

The scattering behaviour of ice crystals encountered in a typical subvisible cirrus cloud is preferentially peaked in the forward direction. For a typical ice crystal 50 μm in length, half of the incoming radiance at visible wavelengths is scattered into a small cone of angle 0.05° about the forward direction. This behaviour presents a challenge to the numerical evaluation of the source term in ray-tracing radiative transfer models. This chapter describes solutions that we have implemented for this problem and closely follows work published in *Wiensz et al.* (2012).

5.1 Multiple-Scattering Integral

The fundamental relation of the scattering of 'incoming' rays with radiance I to produce an 'outbound' source function J, is given by equation (3.30), shown here for reference,

$$J_{i+1}(s, \hat{\mathbf{\Omega}}) = \frac{k_{\text{scat}}(s)}{k(s)} \int_{4\pi} I_i(s, \hat{\mathbf{\Omega}}')\, \bar{P}(s, \hat{\mathbf{\Omega}}, \hat{\mathbf{\Omega}}')\, \mathrm{d}\Omega'. \tag{3.31}$$

In a typical successive-orders of scattering model concerned with molecular scattering, the incoming directions $\hat{\mathbf{\Omega}}'$ are distributed in a zenith-azimuth grid such that the general variation of the diffuse radiance is captured by the rays, as was shown in

Figure 3.13. With this assumption, equation (3.30) becomes

$$J_{i+1}(s,\hat{\mathbf{\Omega}}) \approx \frac{k_{\text{scat}}(s)}{k(s)} \sum_{\Delta\Omega'_j} \int_{\Delta\Omega'_j} I_i(s,\hat{\mathbf{\Omega}}')\, \bar{P}(s,\hat{\mathbf{\Omega}},\hat{\mathbf{\Omega}}')\, \mathrm{d}\Omega', \tag{5.1}$$

with incoming radiances specified at directions $\hat{\mathbf{\Omega}}'_j$ with associated solid angles $\Delta\Omega'_j$. Because the incoming radiances are assumed to be constant over their respective solid angles,

$$J_{i+1}(s,\hat{\mathbf{\Omega}}) \approx \frac{k_{\text{scat}}(s)}{k(s)} \sum_{\Delta\Omega'_j} I_i(s,\hat{\mathbf{\Omega}}'_j) \int_{\Delta\Omega'_j} \bar{P}(s,\hat{\mathbf{\Omega}},\hat{\mathbf{\Omega}}'')\, \mathrm{d}\Omega'', \tag{5.2}$$

and if Rayleigh and Mie scattering with $x \lesssim 1$ are primarily of interest, then it is quite sufficient to assume that the required mean value of the phase function over solid angle $\Delta\Omega_j$ is well approximated by

$$\bar{P}(s,\hat{\mathbf{\Omega}}_k,\hat{\mathbf{\Omega}}'_j) \approx \bar{P}(s,\hat{\mathbf{\Omega}}_k \cdot \hat{\mathbf{\Omega}}'_j), \tag{5.3}$$

where the scattering angle is $\Theta_j = \arccos(\hat{\mathbf{\Omega}} \cdot \hat{\mathbf{\Omega}}'_j)$, so that

$$J_{i+1}(s,\hat{\mathbf{\Omega}}) \approx \frac{k_{\text{scat}}(s)}{k(s)} \sum_{j=1}^{N_{inc}} I_i(s,\hat{\mathbf{\Omega}}'_j)\, \bar{P}(s,\Theta_j)\, \Delta\Omega'_j, \tag{5.4}$$

It will be shown that this approximation holds well for the molecular and Mie scattering, but fails quickly as the forward-scattering peak $P(\Theta = 0°)$ increases with size parameter x.

The numerical techniques developed in this work to handle highly asymmetric phase functions will be presented in Section 5.2. First, a brief survey of the treatment of this problem in other radiative transfer model families is presented.

5.1.1 Photon Conservation in Discrete Ordinates Models

Within discrete-ordinates or $2N$-stream models (*Stamnes et al.*, 1988), the integration over incoming radiances – which depends only on zenith angle due to the Fourier expansion in solar azimuth – is expressed as a Gaussian quadrature over $2N$ radiation

'streams', as in equation (3.36). The integral in (3.30) is a summation over the combined phase function and incoming radiance at discrete incoming streams.

The majority of models that incorporate highly asymmetric phase functions belong to the discrete-ordinates family of models, which employ plane-parallel geometry. In such models, photon conservation is analytically guaranteed through the Gaussian quadrature through which the multiple-scattering source term $J(\tau, \hat{\mathbf{\Omega}})$ is computed. In the standard formulation, this term reduces to a quadrature for the zenith angle integration

$$J^m(\tau, \mu_i) = \sum_{\substack{j=-N \\ j\neq 0}}^{N} w_j D^m(\tau, \mu_i, \mu_j)\, I^m(\tau, \mu_j),$$

that is used to solve for the Fourier cosine component $I^m(\tau, \mu_i)$ of the total radiance along the 'stream' μ_i, for $i = \pm 1, \ldots, \pm N$. The quadrature locations and weights for the radiances conform to the normalization condition from the Gaussian quadrature rule (*Stamnes et al.*, 1988),

$$\sum_{\substack{j=-N \\ j\neq 0}}^{N} w_j D^0(\tau, \mu_i, \mu_j) = \sum_{\substack{i=-N \\ i\neq 0}}^{N} w_i D^0(\tau, \mu_i, \mu_j) = \omega(\tau), \tag{5.5}$$

where the phase functions are internally expanded in terms of the modified Legendre functions as in equation (3.37). In this formulation, since the stream positions μ_i are distributed according to the zeros of the Legendre polynomials, equation (5.5) ensures photon conservation through the location of zeros in the Lagrangian interpolating polynomials.

Since the handling of very strongly-peaked phase functions within discrete-ordinates models requires the expansion of the phase function in increasingly high-order Legendre polynomials, the delta-Eddington (*Joseph et al.*, 1976) and delta-M (*Wiscombe*, 1977) methods were introduced, which approximated the forward-scattering peak by a Dirac delta function, and thereby reduced the number of expansion terms required for solution. The approximation of the forward-scattering peak by a delta function and truncation of the phase function was also done within a doubling-method model

by *Potter* (1970). The oscillation errors introduced by the delta-M method were quantified by *Nakajima and Tanaka* (1988), who also introduced a single-scattering correction to this method.

Iwabuchi and Suzuki (2009) have implemented a geometric phase function truncation technique within a Monte-Carlo model, where polynomial expansions are not needed. This work introduced different approximations of the phase function that are used for each order of scatter.

5.1.2 Photon Conservation Diagnostic

For any radiative transfer model in which the scattering integral is approximated numerically, photon conservation can be considered by checking the accuracy of the scattering numerical quadrature. One way this of doing this is through a photon-accounting technique in which the radiance value of a single incoming direction is compared before and after it undergoes scattering into all directions. Consider a single value of the incoming radiance, $I(s, \hat{\mathbf{\Omega}}')$. If this single value is scattered individually into all outbound directions, $\hat{\mathbf{\Omega}}$, then the integral over all resulting 'outbound' radiances should be exactly equal to the original incoming radiance. Due to the approximate nature of the numerical evaluation of the scattering integral, however, this is not the case. For this reason we develop a diagnostic technique to quantify and reduce this error.

Consider again the incoming radiance in a single direction, $I(s, \hat{\mathbf{\Omega}}')$. If this radiance is scattered into all outbound directions by multiplication with the phase function and the result is integrated over all outbound directions, then we obtain a function of incoming direction that we denote as

$$J(s, \hat{\mathbf{\Omega}}') = \int_{4\pi} J(s, \hat{\mathbf{\Omega}}, \hat{\mathbf{\Omega}}'_j)\, \mathrm{d}\Omega \tag{5.6}$$

$$= \int_{4\pi} \left[\tilde{\omega}\, I(s, \hat{\mathbf{\Omega}}') \bar{P}(s, \Omega, \Omega') \mathrm{d}\Omega' \right] \mathrm{d}\Omega \tag{5.7}$$

$$= \tilde{\omega}\, I(s, \hat{\mathbf{\Omega}}')\, \mathrm{d}\Omega' \int_{4\pi} \bar{P}(s, \Omega, \Omega') \mathrm{d}\Omega. \tag{5.8}$$

If the numerical evaluation of the scattering integral is performed accurately, then the value of this function – the $\hat{\mathbf{\Omega}}'$-specific integrated outbound radiance – should be identical to the incoming radiance, $I(s, \hat{\mathbf{\Omega}}')$, when divided by $\tilde{\omega}\,\mathrm{d}\Omega'$. We can measure the accuracy of the scattering integral evaluation when discrete incoming directions, $\hat{\mathbf{\Omega}}'_j$, are used by introducing a photon conservation *scaling factor*, κ (*Wiensz et al.*, 2012), as

$$\kappa(s, \hat{\mathbf{\Omega}}'_j) \cdot I(s, \hat{\mathbf{\Omega}}'_j)\,\tilde{\omega}\,\Delta\Omega'_j = \int_{4\pi} J(s, \hat{\mathbf{\Omega}}, \hat{\mathbf{\Omega}}'_j)\,\mathrm{d}\Omega. \tag{5.9}$$

In this expression, a value $\kappa(s, \hat{\mathbf{\Omega}}'_j)$ of unity would indicate that the incoming radiance $I(s, \hat{\mathbf{\Omega}}'_j)$ has been conserved through distribution into the outbound directions, and thus $\kappa(s, \hat{\mathbf{\Omega}}'_j) = 1$ for all j directions indicates ideal conservation of photons upon scattering. This factor provides a helpful diagnostic measure of the scattering integral uncertainty in practical numerical computations.

Since in SASKTRAN the set of outbound directions contain spherical cubature weights, w_k (*Sloan and Womersley*, 2004), the conservation condition of equation (5.9) can be expressed as

$$\kappa(s, \hat{\mathbf{\Omega}}'_j) = \frac{\displaystyle\sum_{k=1}^{N} w_k\, J(s, \hat{\mathbf{\Omega}}_k, \hat{\mathbf{\Omega}}'_j)}{I(s, \hat{\mathbf{\Omega}}'_j)\,\tilde{\omega} \cdot \Delta\Omega'_j}. \tag{5.10}$$

Since the incoming radiance is assumed constant over the solid angle $\Delta\Omega'_j$, equation (5.10) can be expressed using equation (5.4) in terms of the mean value of the phase function over the range of scattering angles defined by $\hat{\mathbf{\Omega}}_k$ and the incoming solid angle $\mathrm{d}\Omega'_j$,

$$\kappa(s, \hat{\mathbf{\Omega}}'_j) = \sum_{k=1}^{N} w_k\, \bar{P}(s, \hat{\mathbf{\Omega}}_k, \hat{\mathbf{\Omega}}'_j). \tag{5.11}$$

If the phase function is smoothly-varying, the scaling factors evaluate to

$$\kappa(\hat{\mathbf{\Omega}}'_j) = \sum_{k=1}^{N} w_k\, \bar{P}(s, \hat{\mathbf{\Omega}}_k \cdot \hat{\mathbf{\Omega}}'_j). \tag{5.12}$$

Within the SASKTRAN model, for each scattering event, the quantities $\kappa(s, \hat{\mathbf{\Omega}}'_j)$

are computed for each incoming direction using equation (5.12), and each outbound radiance is divided by the scaling factor $\kappa(s, \hat{\mathbf{\Omega}}'_j)$ appropriate to each incoming direction. For scattering by particles with highly asymmetric phase functions, these factors depart significantly from unity, and the scaling of outbound radiances introduces a false re-distribution of radiance. This problem is addressed in Section 5.3. In the following discussion, the spatial coordinate s is assumed and will be removed from all quantities.

The scaling factors, κ, constitute a set of values defined as a function of incoming direction $\hat{\mathbf{\Omega}}'_j$ that evaluate to unity when the integral (3.30) is well approximated by the summation (5.4). The departure of these factors from unity is illustrated in Figure 5.1 by modeling the scattering of 750 nm light by successively larger particles for a diffuse point at an altitude of 24.5 km. The phase functions that are combined for various atmospheric scattering operations in this figure are those that were shown on a logarithmic scale in Figure 4.5.

The set of scaling factors for a Rayleigh-scattering atmosphere is shown as a function of incoming radiance direction in Figure 5.1a. For molecular-only scattering, the scaling factors evaluate to unity to within eight decimal places of accuracy. The scaling factors for the same altitude, but when a sulphate aerosol layer is added to the molecular background, are shown in Figure 5.1b. The aerosol scattering used in this computation assumes lognormally distributed particles of background size ($r_g = 0.08$ μm, $s_g = 1.6$) and number density $n = 1$ cm^{-3}. From this figure, it is seen that the phase function quadrature for scattering by stratospheric aerosol is accurate to four decimal places.

When slightly larger particles with a lesser degree of symmetry, such as subvisual cirrus ice crystals, are added to the molecular background atmosphere, a more significant departure from unity is seen. The scaling factors computed for T-matrix (*Mishchenko et al.*, 1996) simulated ice cylinders (aspect ratio of unity) in a gamma distribution with volume-effective radius $r_e = 1.0$ μm, shape parameter 0.113, and number density $n = 1$ cm^{-3} are shown in Figure 5.1c. At this particle size, the inaccuracy in the phase function integration has become more significant, with accuracy

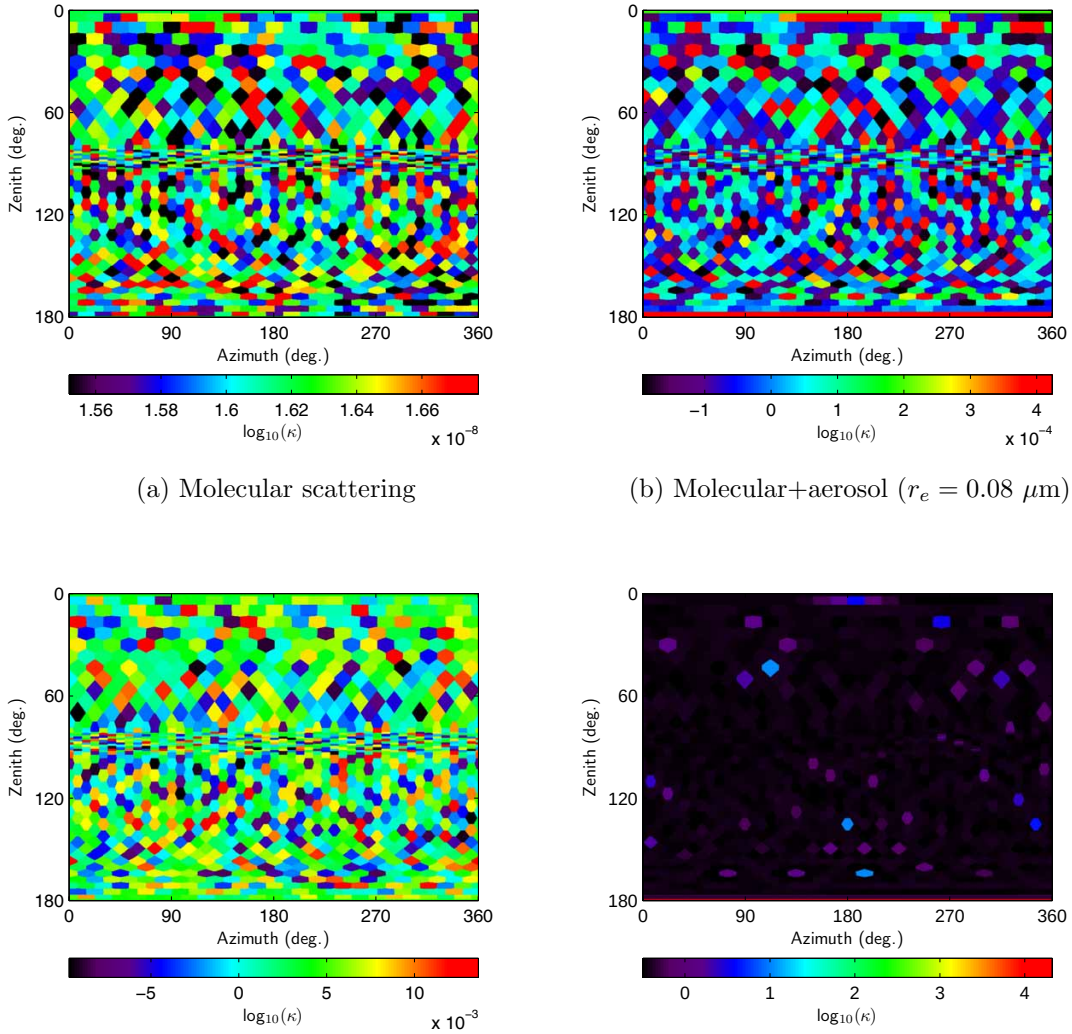

(a) Molecular scattering

(b) Molecular+aerosol ($r_e = 0.08$ μm)

(c) Molecular+small ice ($r_e = 1.0$ μm)

(d) Molecular+large ice ($D_e = 180$ μm)

Figure 5.1: Scaling factors $\kappa(\hat{\mathbf{\Omega}}'_j)$ as a function of incoming direction for increasing size of scattering particles.

now at two decimal places.

If particles with larger size parameters are involved in scattering, the scaling factors become very widely distributed, and the redistribution or 'smearing' effect involved in the scaling of radiances becomes very significant. The scattering properties from the in-situ database of *Baum et al.* (2005a) are used in SASKTRAN to simulate scattering by large ice crystals. As a worst-case example, the values κ for scattering of 750 nm light by ice crystals with an effective size of $D_e = 180$ μm and number

density of 10^{-4} cm^{-3} are shown in Figure 5.1d. The inadequacy of the assumptions underlying the sum in equation (5.4) is clear from this figure. Radiance computations involving such scattering parameters are quickly divergent. The majority of incoming directions in this case have $\kappa < 1$ since the combinations of scattering angles specified by $\hat{\mathbf{\Omega}}'_j \cdot \hat{\mathbf{\Omega}}_k$ do not sample the very narrow forward-scatter peak, and a few incoming directions have scattering angles sufficiently close to zero that their κ values are between 10^2 and 10^5.

5.2 Highly Asymmetric Phase Function Techniques

5.2.1 Mean Scattering Phase Function

A small improvement to this situation results if the mean value of the phase function over the incoming solid angle, $\Delta\Omega'_j$, is used instead of the value at $\hat{\mathbf{\Omega}}_k \cdot \hat{\mathbf{\Omega}}'_j$. If a set of points is distributed on the incoming unit sphere at very high resolution in both zenith and azimuth, then the mean value of the phase function can be taken for all scattering angles between $\hat{\mathbf{\Omega}}_k$ and each high-resolution point in $\Delta\Omega'_j$. This higher-resolution sampling of the phase function improves the quality of the numerical integration. Figure 5.2 shows the scaling factors that result if a set of points separated by 0.05° in zenith and azimuth are used.

At this resolution, the technique typically brings the values of κ to within an order of magnitude of unity for incoming directions except a narrow band about $\theta = 180°$ that samples the strong forward peak of an outbound direction positioned at $\theta = 0°$.

If the diffuse incoming radiance is well-represented by the incoming point distribution, this method presents a reasonable approach to reduce slightly the error introduced by the assumption in equation (5.11). This technique may be necessary for some conditions, but its usefulness is limited due to its computationally intensive nature. The evaluation of the mean phase function at angular separation of 0.05° requires distributing 26 million points on the surface of the unit sphere, and the required phase function interpolations slow the scattering computation by several

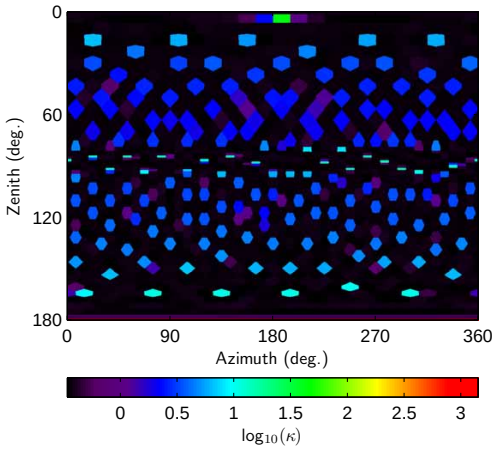

Figure 5.2: Scaling factors $\kappa(\hat{\mathbf{\Omega}}'_j)$ for ice crystal scattering with mean phase function computation over incoming solid angle, $\Delta\Omega_j$.

orders of magnitude.

5.2.2 δ-Function Approximation and Truncation

The scattering phase functions from the database of *Baum et al.* (2005a) display an extremely sharp forward-scattering peak, with half of the incident radiation being scattered into a cone of width less than approximately 1°. If these highly-asymmetric phase functions are expressed as a function of $\cos\Theta$, as shown in Figure 5.3a, the sharp forward-scattering peak increasingly resembles a Dirac delta function as the size parameter increases. In this plot, at scattering angles less than 5° (when $\cos\Theta \approx 1$), the value of the phase function can change by more than six orders of magnitude. When the same phase functions are shown with scattering angle on a logarithmic scale, as in Figure 5.3b, the large fraction of energy that increasingly scatters into the near-forward direction as x increases is more clearly seen. The very sharply-peaked nature of the phase function can be used as a simplifying assumption by expressing P as the sum of a sharply-peaked component and a smoothly-varying component, $P(\cos\Theta) = P_\delta(\cos\Theta) + P_s(\cos\Theta)$.

In an unpolarized model, light scattered according to $P_\delta(\cos\Theta) = 2\delta(1 - \cos\Theta)$ is effectively the same as light that is not scattered. The fraction f of incident light

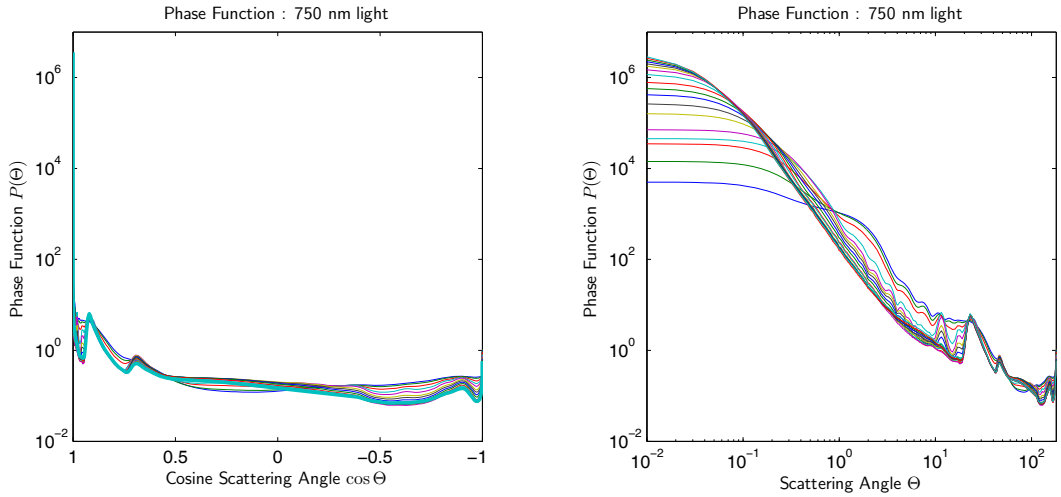

(a) $P(\cos\Theta)$ (b) $P(\log_{10}\Theta)$

Figure 5.3: Phase functions for 750 nm light scattering by cirrus ice crystals shown on two abscissae.

that scatters directly forward is expressed through the normalization condition for phase functions $\int_{4\pi} \frac{P}{4\pi} \mathrm{d}\Omega = 1$ as

$$f = \int_{\cos\Theta_c}^{1} \frac{P_\delta(\cos\Theta)}{2}\, \mathrm{d}(\cos\Theta). \tag{5.13}$$

In this expression Θ_c is a cutoff angle that defines the support for the numerical representation of $\delta(1-\cos\Theta)$. Given that the normalization criterion for the smoothly-varying component $P_s(\cos\Theta)$ is

$$\int_{4\pi} \frac{P_s(\hat{\mathbf{\Omega}}, \hat{\mathbf{\Omega}}')}{4\pi(1-f)}\, \mathrm{d}\Omega' = 1, \tag{5.14}$$

the combined phase function is substituted into the radiative transfer equation to give

$$\mathrm{d}I(s,\hat{\mathbf{\Omega}}) = -I(s,\hat{\mathbf{\Omega}})\tilde{k}(s)\,\mathrm{d}s + \tilde{\omega}\int_{4\pi} I(s,\hat{\mathbf{\Omega}}')\tilde{P}_s(\hat{\mathbf{\Omega}},\hat{\mathbf{\Omega}}')\,d\Omega'\,\mathrm{d}s.$$

The radiative transfer equation is now expressed with scaled parameters, as shown

by *McKellar and Box* (1981),

$$\tilde{k}(s) = (1 - \omega f)\, k(s) \qquad\qquad \tilde{\tilde{\omega}} = \left(\frac{1-f}{1-\omega f}\right) \tilde{\omega}.$$

These substitutions, together with the truncated and renormalized phase function $P_s(\Theta)$, now constitute a scaled RTE,

$$\frac{\mathrm{d}I(s,\hat{\mathbf{\Omega}})}{\mathrm{d}\tilde{\tau}(s)} = -I(s,\hat{\mathbf{\Omega}}) + J(s,\hat{\mathbf{\Omega}}), \tag{5.15}$$

where the source term is computed from the renormalized 'smooth' scattering component,

$$J_{i+1}(\hat{\mathbf{\Omega}}) = \tilde{\tilde{\omega}} \int_{4\pi} I_i(\hat{\mathbf{\Omega}}')\, \bar{P}_s(\hat{\mathbf{\Omega}}, \hat{\mathbf{\Omega}}')\, \mathrm{d}\Omega'. \tag{5.16}$$

This technique has been implemented in SASKTRAN by truncating the phase function at a cutoff angle Θ_c and using a constant-valued extrapolant for angles $\Theta \in [0, \Theta_c]$. Illustrations of phase function truncation for several ice crystal effective sizes are given in the following section. When this truncation and renormalization technique is applied to the diffuse point whose scaling factors κ were shown in Figure 5.1d, the resulting scaling factors are seen in Figure 5.4a to be significantly closer to unity. The phase function in this case has been truncated to a value of 10^2 for all angles less than 1.2°. Note that the scaling factors are displayed on a linear scale in this figure. The $\bar{P}$ averaging technique described above can further be applied to the scaling factors that result after truncation. This results in a small improvement in the range of scaling factors, as shown in Figure 5.4b.

5.3 Analysis

Key factors in the error analysis of the application of these techniques are the selection of an appropriate truncation method and a definition for what is a 'good' value for κ, that is, one that sets an upper limit on the acceptable amount of 'smearing' of source radiances when divided by κ. Since we are concerned in this work with very

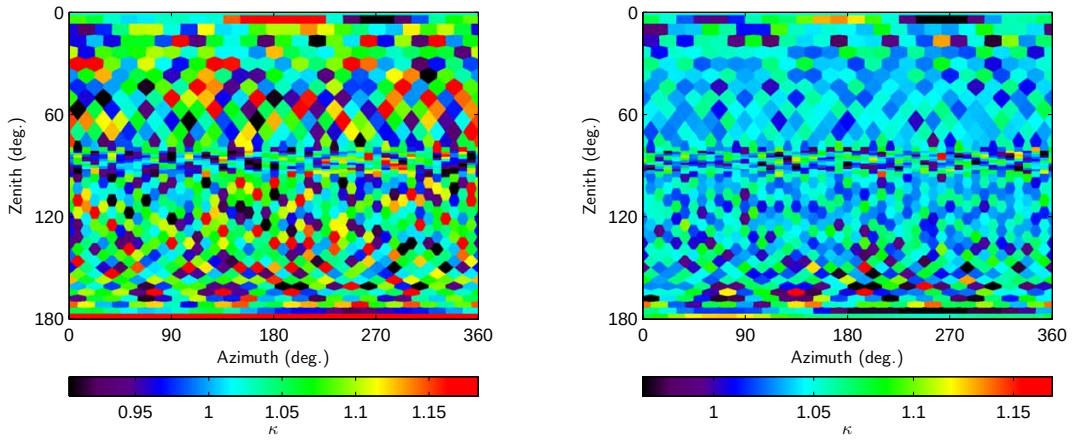

(a) Truncation only

(b) Truncation and $\bar{P}$

Figure 5.4: Effect of truncation and surface-mean value on scaling factors, $\kappa(\hat{\mathbf{\Omega}}'_j)$, for scattering by 180 μm ice crystals.

large size parameters, the following analysis will focus exclusively on phase functions from the database of *Baum et al.* (2005a) for optical wavelengths.

5.3.1 Phase Function Truncation Method

The phase function truncation scheme used in this analysis uses a 'smooth' phase function $P_s(\Theta)$ defined by

$$P_s(\Theta) = \begin{cases} P(\Theta_c), & \Theta \leq \Theta_c \\ P(\Theta), & \Theta > \Theta_c. \end{cases}$$

The selection of an appropriate truncation criterion thus amounts to finding the 'cutoff' angle Θ_c that minimizes the defined error criterion.

Other functional forms for $P_s(\Theta)$ in the peak region have been have been used in both others' previous work and in the current work on this problem. *Potter* (1970) used a power-law extrapolation in the narrow forward peak, which approximates well the functional form seen in Figure 5.3b for scattering angles just above 1°. *Iwabuchi and Suzuki* (2009) used a constant value P_0 out to an angle Θ_c that together

conserve the first and second Legendre moments of the phase function. Since neither of these approaches is qualitatively different to the one presented, but only modifies the resulting fraction f, and since the phase function derivative $\frac{\mathrm{d}P}{\mathrm{d}\cos\Theta}$ does not appear in radiative transfer calculations, it is quite sufficient to use the piecewise-continuous truncated phase functions P_s described above.

Analysis of the truncation methods used in a successive-orders model should consider the angular resolution of scattering used within the model. An angular width of 3° gives a reasonable upper bound on the width of the forward peak that can be truncated without distorting scattering into neighbouring directions.

It should be noted that although one could naïvely increase the numerical accuracy of the summation in equation (5.4) by using a finer-resolution grid of incoming zeniths and azimuths, this would quickly become prohibitive since memory usage and computational time in SASKTRAN increases rapidly with the number of incoming directions, N_{inc}. Geometries needed for ray-tracing and scattering computations are linked to the incoming rays, while outbound rays have little overhead to allow fast computations of many orders of scatter. Accordingly, the number of outbound directions N_{out} can be increased without a significant increase in computational time or memory usage. It is shown that this gives a slight improvement in the resolution of phase function sampling.

When investigating the effectiveness of phase function truncation, useful indicators for the distribution of κ values are

$$\overline{\kappa} = \exp\langle|\log\kappa_i|\rangle \tag{5.17}$$

and

$$\sigma_\kappa = \sqrt{\langle(|\log\kappa| - \log\overline{\kappa})^2\rangle}, \tag{5.18}$$

the absolute geometric mean and deviation of κ. The values of these two parameters for the scaling factors shown in Figures 5.1 and 5.4 are listed in Table 5.1.

If the phase function for scattering of 750 nm light by 180 μm particles is truncated below $\Theta_c = 2.0°$, then the scaling factors that were shown in Figure 5.1d are

Dominant Scattering Particles		$\overline{\kappa}$	σ_κ
Rayleigh		1.000000037	1.25×10^{-9}
Mie sulphate (0.08 μm)		1.00049	3.61×10^{-4}
T-matrix ice (1 μm)		1.0213	0.0162
Database ice (180 μm)	(do-nothing)	2.7385	0.2875
	($\bar{P}$)	2.7829	0.3313
	(truncated)	1.0654	0.0473
	(truncated+$\bar{P}$)	1.0452	0.0266

Table 5.1: Comparison of scaling factors for scattering of 750 nm light from several sources.

distributed much more favorably, as shown in Figure 5.5. The values of the statistical

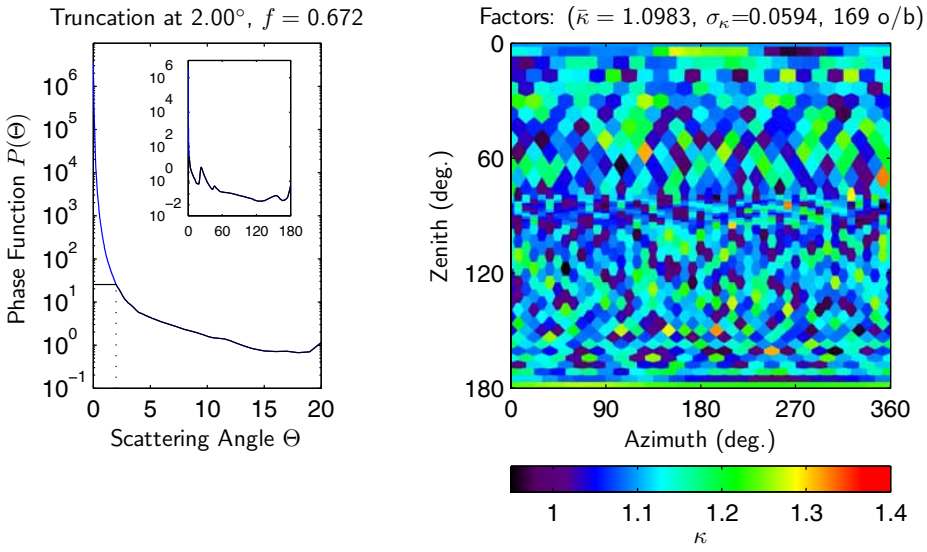

Figure 5.5: Truncated portion of phase function, with range of scaling factors shown as a function of incoming direction. The inset figure shows the phase function over the full range of scattering angles.

descriptors, $\bar{\kappa}$ and σ_κ, as well as the number of outbound directions (referred to by 'o/b') are indicated in the title of the right-hand plot. From this figure it is quite clear that a truncation angle near 2° will result in quite acceptable values of κ. It is noteworthy that the fraction f of incident light that is considered to have scattered directly forward in this configuration is significant – over two-thirds. The worst-case values of κ have been reduced from over 10^5 to 1.4, and the spread about $\kappa = 1$ is

very small: $\sigma_\kappa = 0.0594$. These values were computed for outbound rays distributed in 169 directions. The effect of changing the number of outbound directions can now be studied.

The values of $\bar{\kappa}$ and σ_κ that result from truncation at varying cutoff angles between 0.13° and 3°, and for varying numbers of outbound directions, are shown in Figure 5.6. Both $\bar{\kappa}$ and σ_κ drop significantly for cutoff angles $\Theta_c \geq 1°$, and larger cutoff angles

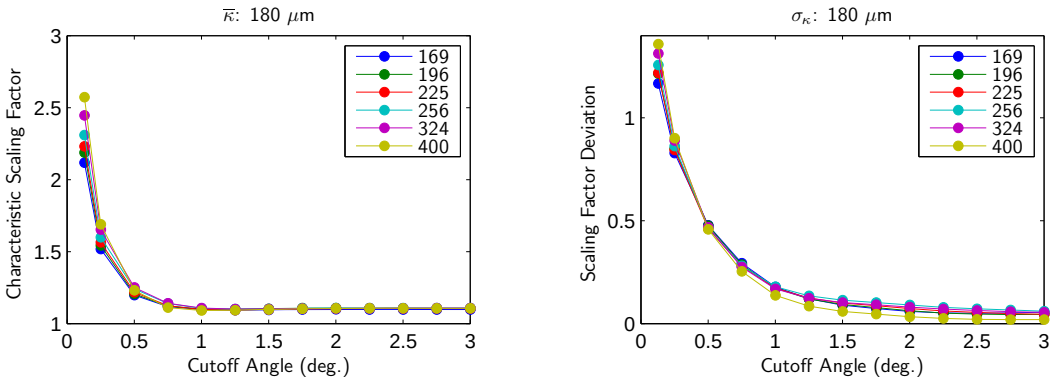

(a) $\bar{\kappa}$ (b) σ_κ

Figure 5.6: Change of (a) $\bar{\kappa}$ and (b) σ_κ with truncation angle Θ_c for varying numbers of outbound rays (from 169 to 400) for 180 μm particles.

will produce values of κ that are quite close to unity, since $\bar{\kappa} \leq 1.1$ and $\sigma_\kappa \leq 0.15$.

While this selection of cutoff criteria ensures that the overall behaviour of the scaling factors is favorable, it is necessary to consider also the exceptionally large and small scaling factors that remain after truncation has been applied. For treatment of these values, we consider the number of incoming directions that have large absolute values of the score

$$z_\kappa = \frac{\log \kappa - \log \bar{\kappa}}{\sigma_\kappa}. \tag{5.19}$$

The number of incoming directions that have values $|z_\kappa| > 3$ are shown, again as a function of cutoff angle and number of outbound directions, in Figure 5.7.

All outbound ray distributions show a significant drop in the number of directions with $|z_\kappa| > 3$ at angles between 1.5° and 2.0°. When outbound ray distributions with either 324 or 400 points are used, there are no directions that have scores $|z_\kappa| > 3$.

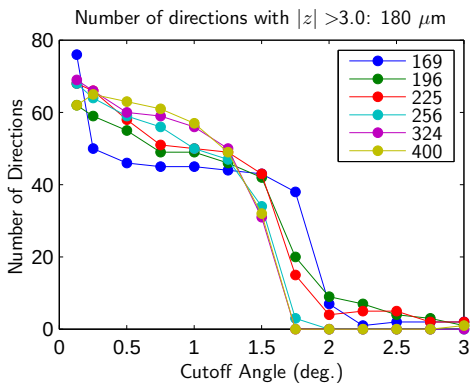

Figure 5.7: Number of scaling factors κ that have a score $|z_\kappa| > 3$. Total number of incoming directions for configuration shown is 1346.

This result is a significant improvement in the distribution of scaling factors, κ. From these considerations, it appears that using a distribution of 324 outbound points with a cutoff angle of 2° gives the best distribution of scaling factors. The distribution is shown in Figure 5.8a. The chosen selection of truncation angle and outbound ray distribution also works well for smaller particle sizes, as shown by the scaling factors for 60 μm scattering particles in Figure 5.8b.

5.3.2 Uniformity of Outbound Radiances

The scaling factors κ introduced in equation (5.11) assist successive-order models by numerically ensuring energy conservation to within the accuracy of the cubature weights of the outbound unit sphere. However, as with any normalization technique, this will introduce an amount of false scattering when the outbound radiances are divided by the scaling factors, $\kappa(\hat{\mathbf{\Omega}}'_j)$. As a measure of the effect of truncation and renormalization on computed radiances, it is instructive to consider an isotropic diffuse intensity field, which gives outbound radiances as

$$J_k = \sum_{j=1}^{N_{inc}} \frac{P(\hat{\mathbf{\Omega}}_k \cdot \hat{\mathbf{\Omega}}'_j)\,\Delta\Omega'_j}{\kappa_j}.$$

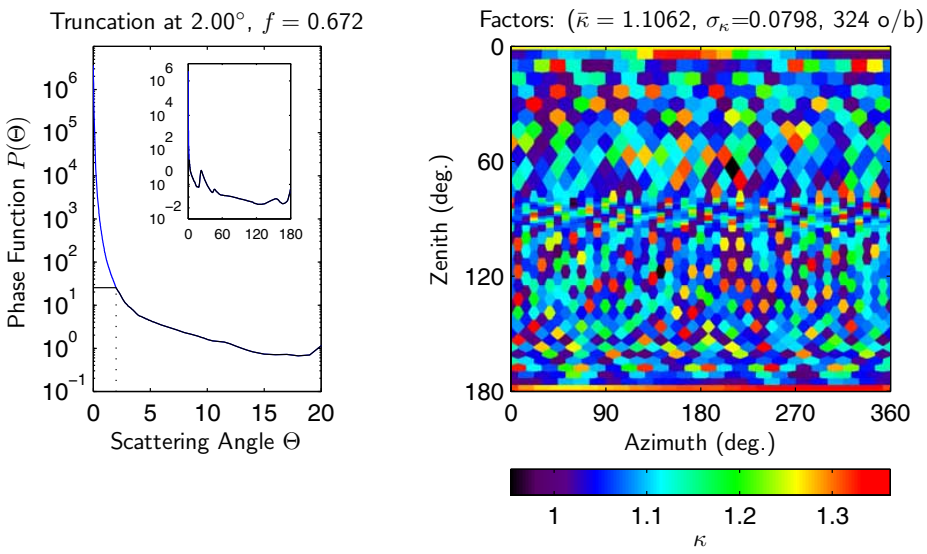

(a) 180 μm

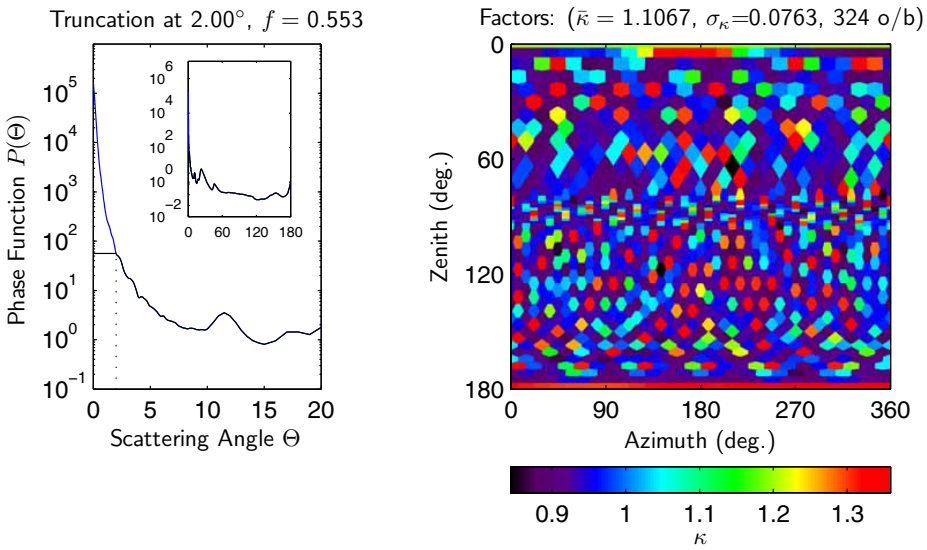

(b) 60 μm

Figure 5.8: Truncated phase function, with scaling factors for several ice crystal effective sizes.

The degree of nonuniformity of the outbound radiance for isotropic incoming radiance indicates the amount of false redistribution, or 'scaling' of radiance by scaling factors significantly far from unity.

To illustrate, consider again the non-truncated phase function for scattering of

750 nm light by 180 μm ice crystals, whose scaling factors were shown in Figure 5.1d. If an isotropic incoming radiance field is scattered into every outbound direction, the sets of outbound radiance that result – in the absence of scaling or phase function truncation – for 180 μm and 10 μm particles are shown in Figure 5.9. Note that

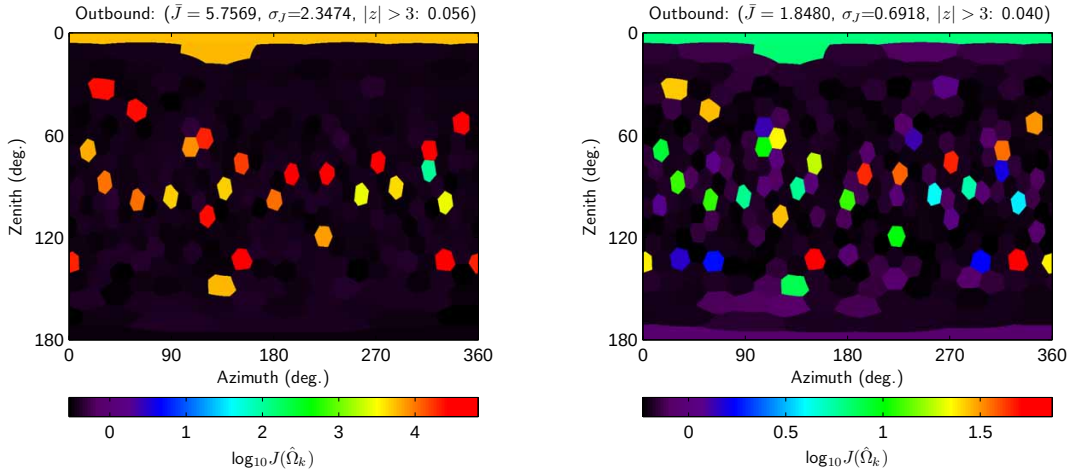

(a) 180 μm, no scaling

(b) 10 μm, no scaling

Figure 5.9: Outbound radiances for isotropic incoming radiance without scaling applied.

values in this figure are shown on a logarithmic scale. Clearly, when no phase function truncation is done, there are 'hot spots' where extremely large false outbound radiances result when the forward-scatter peak is sampled. This effect is somewhat reduced for smaller particles, as seen in the right-hand panel for 10 μm particles.

Outbound radiances that have been obtained by scaling without truncation are shown in Figure 5.10 for the same particle sizes. Here, there are regions that have large false radiances from contributing values with $\kappa < 1$, and some regions of too-low outbound radiance from directions with $\kappa > 1$.

The effect of truncation and renormalization, when combined with the scaling of outbound radiances, are shown in the outbound radiances in Figure 5.11. Here, the outbound radiances J are significantly more evenly distributed about unity. This is particularly true for smaller particles, as seen in the outbound radiances for 10 μm particles shown in the right-hand panel. If distribution parameters $\bar{J}$, σ_J, and z_J are

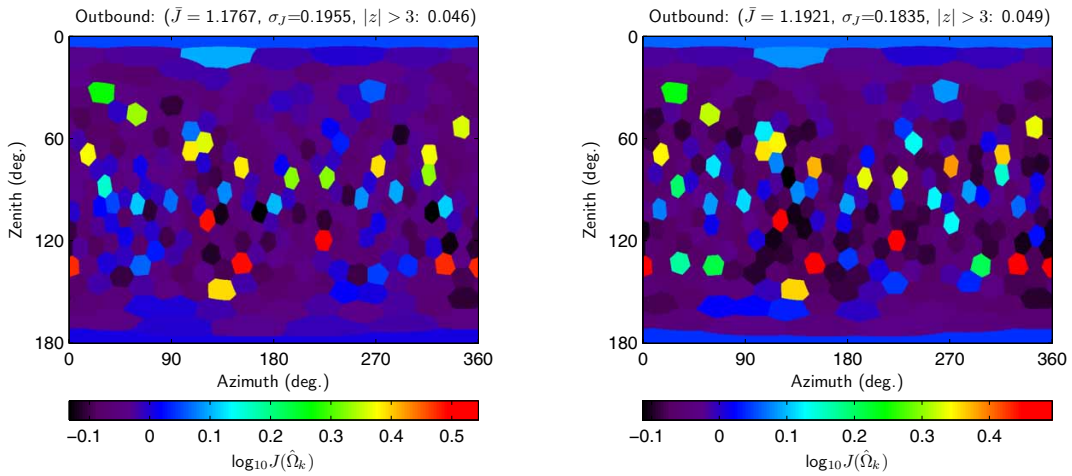

(a) 180 μm, scaled

(b) 10 μm, scaled

Figure 5.10: Outbound radiances for isotropic incoming radiance with scaling factors applied.

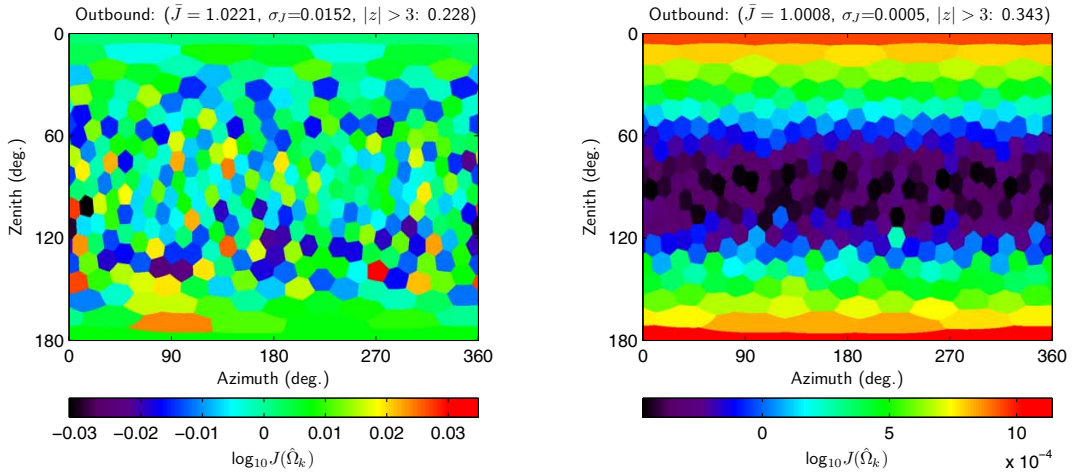

(a) 180 μm, truncated and scaled

(b) 10 μm, truncated and scaled

Figure 5.11: Outbound radiances for isotropic incoming radiance for ice crystals with varying effective size.

defined analogously to the parameters (5.17) and (5.18) for κ, the outbound radiance fields have characteristic values of $\bar{J}$ (σ_J) from 1.0221 (0.0152) for 180 μm, to 1.0008 (0.0005) for 10 μm.

In terms of the distribution parameters, truncation best shifts $\bar{J}$ toward unity, while photon conservation best reduces the number of directions with a large $|z_J|$

score while at the same time keeping the width, σ_J, small. The photon conservation operation eliminates spurious production or loss of photons, but will do so at the cost of re-distributing the radiance into other directions. Truncation alone effectively removes the sharp forward peaks, but does so with a loss of information on scattering behavior. A combination of photon conservation and phase function truncation is seen to produce the best approximation to the scattering integral.

The accuracy in modeled radiances for scattering by large ice crystals is significantly improved, with the errors being reduced by several orders of magnitude to now several percent. Treatment of this inaccuracy in the scattering integral allows for computations to be done for radiative transfer in subvisual cirrus clouds. This work continues in the next chapter, where changes to the line of sight integration in SASKTRAN necessary for computing in-cloud limb radiances are discussed.

Chapter 6

Modeling Cirrus Cloud Radiances

Retrieval of cloud optical properties requires modeling the in-cloud spectral radiance for a given set of bulk cloud parameters. In a spherical successive-orders model of limb measurements in clouds, two factors – the long path lengths near the tangent point and the high particle extinction – together act to violate a simplifying assumption of the technique. This chapter describes the methods that are used to solve this problem, and illustrates the variation of simulated in-cloud radiance with bulk cloud parameters.

6.1 Introduction

The optical thicknesses, τ_c, of typical opaque cirrus clouds range between 0.3 and 3.0 (*Lynch et al.*, 2002). For these larger optical depths, it often is necessary to use discrete-ordinates models for which the solution time is relatively independent of optical thickness. In addition, modeling of the radiation field within cirrus clouds must typically take into account the vertical and horizontal extents and inhomogeneities through the prescribed cloud property distributions and through appropriate selection of boundary conditions.

The limb-viewing geometry of OSIRIS is very well-suited to the detection of stratospheric aerosols and subvisual cirrus clouds but can only give limited information on cloud particle size from spectral measurements. The vertical field of view

of OSIRIS is 1 km at the tangent point and successive exposures are typically separated by 1.5-2 km. If a cloud thickness of 1 km is assumed, then for a typical OSIRIS exposure through a cirrus cloud when the cloud-top altitude is 14 km, the instrument line of sight will pass through the cloud region for a distance of approximately $\Delta s = 225$ km. An implication of limb-viewing geometry through clouds is that the microphysical properties of the cloud, which can vary significantly throughout the vertical extent of the cloud, will be obscured.

6.2 Radiative Transfer in Thin Cirrus

Since the size parameter, x, of the scattering particles for the wavelengths of interest is a key factor in selecting an appropriate source of scattering properties, the size range of ice crystals is a key consideration in cirrus cloud radiative transfer. The T-matrix (*Mishchenko et al.*, 1996) and Discrete Dipole Approximation (DDA) (*Yurkin and Hoekstra*, 2007) algorithms have been used in this work for scattering by small ice crystals, but as mentioned above are very limited by computational times for larger scattering particles.

We focus on scattering of solar irradiance by medium-large ice crystals, here defined as those with effective size greater than 5 μm. For these sizes, we use optical scattering properties from the *in-situ* cirrus database of *Baum et al.* (2005a) that uses measured size distributions of typical ice clouds to infer cirrus cloud scattering properties.

A ray-tracing model with spherical geometry such as SASKTRAN is well-suited to modeling limb-scattering observations, but requires a number of extensions to its configuration to model successfully the measured radiances in thin cirrus clouds.

6.2.1 Source Function Quadrature

The path integral in equation (3.43) is performed by taking the sum of individual integrals along each of the line of sight's path segments, Δs, through the homogeneous layers of the model atmosphere. The source functions, $J(s)$, that are integrated along

the path have been evaluated at the solar conditions particular to that path segment's location. Each individual path integral is evaluated using Gaussian quadrature.

Since path segments through spherical shells near the tangent point become quite long, each such path integral is subdivided into sub-integrals of maximum length 5 km over which Gaussian quadrature is done. The source function $J(s)$ is assumed to be constant within each such segment.

6.2.2 Optical Properties Specification

Since we assume constant atmospheric optical properties within spherical shells, scattering and extinction quantities along the observer line of sight are linearly interpolated as a function of height for computing the multiple scattering source term (3.30) and for attenuating radiances to the ground and to the observer, as in each of the attenuation terms in equation (3.43).

Simulated cloud layers in this work assume the optical properties from a single effective particle size D_e throughout the vertical extent of the cloud. The use of a single effective size is not a restrictive assumption since, for the thin clouds considered in this work, the true particle size distributions are typically well-described by a unimodal gamma distribution. The spatial distribution of cloud particle number density is characterized in this work by a Gaussian height profile, $n(h)$. The altitude of the cloud top, h_{ct}, as obtained from OS radiances, is assigned to the upper half-maximum point, and the cloud thickness is defined to be the full width at half-maximum of the distribution, as illustrated in Figure 6.1. The number density profile, $n(h)$, is scaled to produce a prescribed optical depth, τ_c. This formulation provides a simple characterization of a modeled cloud in terms of the parameters h_{ct}, Δh_{cld}, D_e, and τ_c.

6.2.3 Ray-Tracing Shell Specification

As discussed in Section 3.4.1, the fundamental unit of the SASKTRAN model is a ray that originates at a location $\mathbf{r}$ and which extends in the direction $\hat{\mathbf{\Omega}}$ with path

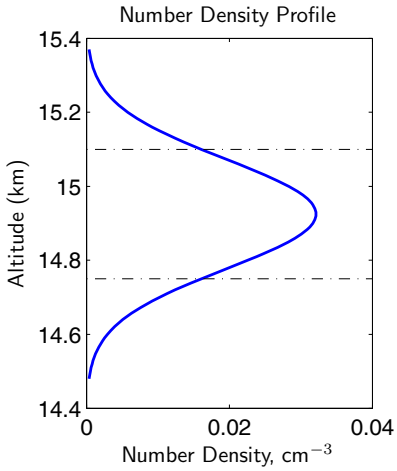

Figure 6.1: Cloud number density profile for h_{ctop}=15.1 km, Δh_{cld}=350 m, and D_e = 50 μm scaled to give $\tau_c = 0.04$.

coordinate s. An observer line of sight is one example of such a ray with the special condition that its origin is the instrument position. As mentioned in Chapter 3, the nomenclature used in discussing the model atmosphere is that concentric spherical *shells* define homogeneous *cells* that lie between them.

Each ray in SASKTRAN is traced from its origin through homogeneous spherical shells in the model atmosphere to its endpoint, which is either the top of the atmosphere or the surface of the earth. The ray-tracing operation is performed by finding all points of intersection of the ray with the set of spherical shells as it proceeds outward from the point $\mathbf{r}$ in the direction $\hat{\mathbf{\Omega}}$. The difference between successive intersection points is then the segment path length through that cell.

For satellite instruments that employ a limb-viewing geometry, the line of sight (LOS) along which the observation is made passes through a long segment of the atmosphere, up to thousands of kilometres for measurements at low tangent altitudes. When such a ray is traced through the equally-spaced spherical shells of the model atmosphere, the length of the path segments, Δs, between successive spherical shell intersections increases significantly at lower altitudes, and becomes very large when passing between spherical shells near the tangent point. This is illustrated in Figure 6.2. In this figure, it is clear that the longest path lengths, Δs, occur in those cells nearest the tangent point.

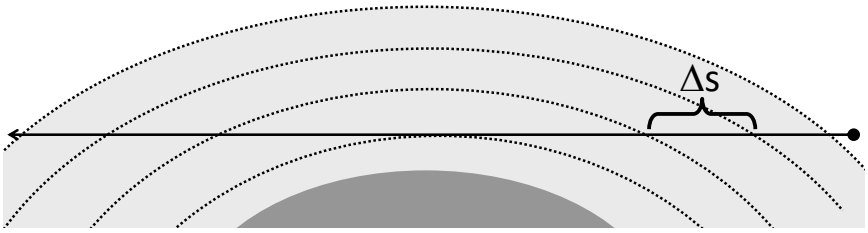

Figure 6.2: Varying length of path segments for a ray traced in a model atmosphere consisting of equally-spaced spherical shells.

The effect of long segment path lengths is further illustrated in Figure 6.3a, where a simulated OSIRIS line of sight that is tangent at exactly 13 km has been traced through the shells of the model atmosphere. For this line of sight, the mid-cell

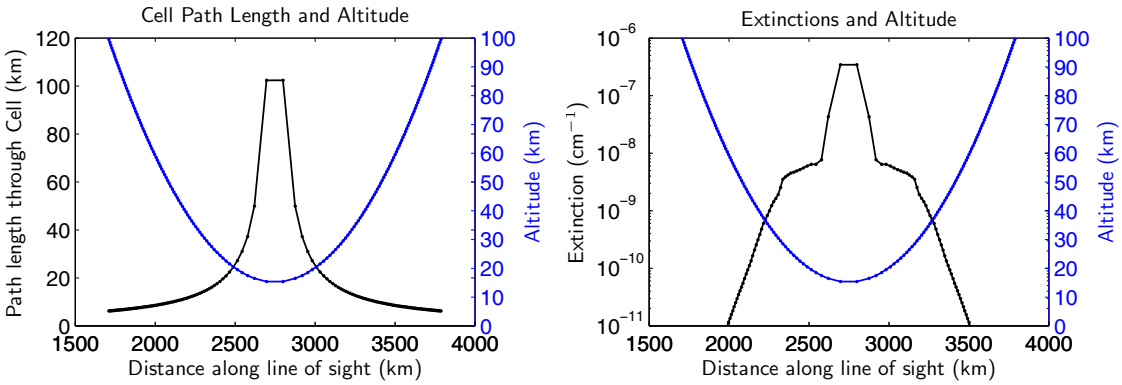

(a) Path lengths, Δs, through 1 km cells

(b) Extinction, $k(s)$, along line of sight

Figure 6.3: Observer geometry and cloud optical properties in the model coordinate system, shown as a function of distance s along observer line of sight (km).

altitude above the model earth, $z(s)$, and the path length per cell, $\Delta s(s)$, are shown as a function of distance from the observer along the line of sight. The ray-tracing path lengths in this plot are those obtained using the nominal 1 km spherical shell spacing. At the lowest altitudes along this line of sight, the path lengths become quite large and exceed 100 km per cell near the tangent point. A typical profile of total extinction, $k(s)$, as a function of distance along the observer line of sight is shown in Figure 6.3b for the case when a cloud surrounds the line of sight tangent point. The extinction within the cloud region – at the lowest altitudes – exceeds that of its surroundings by nearly two orders of magnitude. When the long path lengths coincide

with typical values of in-cloud extinction, the values of segment optical depth, $\Delta\tau_s$ – the optical depth along a path segment through a homogeneous layer – become quite large.

These high optical depths are illustrated in Figure 6.4a, in which the segment optical depths are shown as a function of distance along the observer LOS for the geometry and extinctions shown in Figure 6.3. It is clear that the segment optical

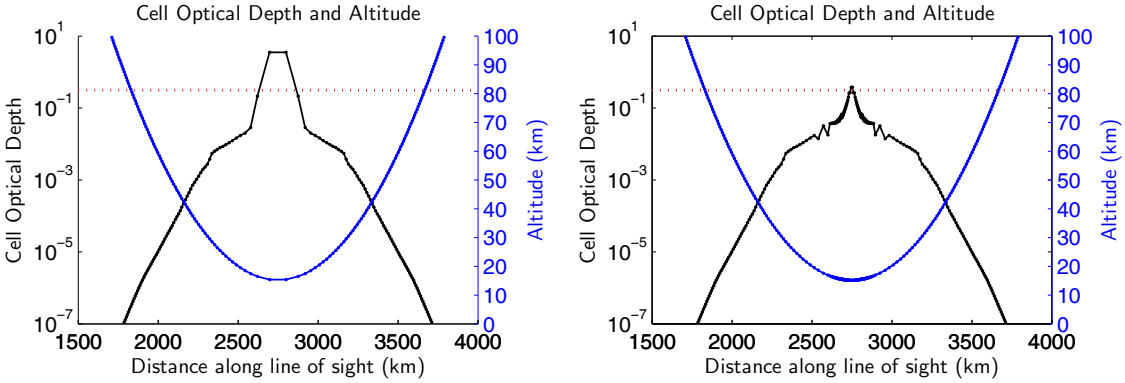

(a) $\Delta\tau_s$ for 1 km cells

(b) $\Delta\tau_s$, with tapered cell spacing

Figure 6.4: Cell optical depths, $\Delta\tau_s$, shown as a function of distance s along observer line of sight.

depths become extremely high within the cloud region. To avoid these high segment optical depths, we configure the ray-tracing shell spacings to the extinction profile for a given wavelength such that the segment optical depths, $\Delta\tau_s$, do not exceed an empirically-determined threshold of $\Delta\tau_s = 0.3$ due to scattering. The optical depths per cell, $\Delta\tau_s$, that result from this configuration are shown in Figure 6.4b.

The effect of these high optical depths on source function evaluations is best illustrated by considering the example of a thin cirrus cloud observed by OSIRIS that is 1 km-thick with optical thickness $\tau_c = 0.3$. If the cloud is assumed for the moment to be vertically homogeneous, the vertical extinction profile within the cloud has a value of $k(h) = 0.3$ km^{-1}, and the along-path optical depth, denoted by $\Delta\tau_s$, is near 70. Accordingly, there will be a very large number of scattering events along the observer line of sight in the cloud region, and the model must ensure that along-path optical depths remain sufficiently small to resolve these scattering events in its

solution.

Because the segment optical depth is necessarily a strong function of the cloud particle size, ray-tracing shell heights are configured according to the extinction value of the dominant scattering particles. The minimum height separation of ray-tracing shells, Δh_{rt}, is 10 m at the altitude of the maximum number density and is scaled to maintain a constant cell optical depth, $\Delta\tau_z = k_{sca}(h)\,\Delta h_{rt}$, along the vertical direction inside the cloud region.

The maximum cloud optical thickness that can be modeled for a specified vertical thickness with this configuration is shown in Figure 6.5. When the ray-tracing shells

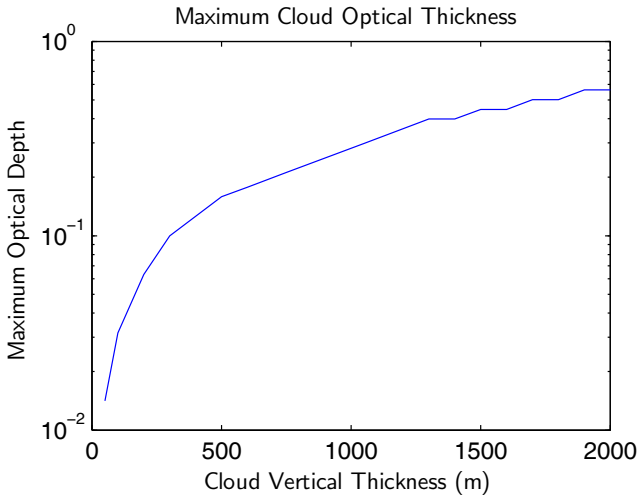

Figure 6.5: Maximum allowed cloud optical thickness for specified geometric thickness.

are configured in this way, individual scattering events within each layer are resolved and the linear interpolation of source functions can successfully capture the variation of the diffuse field within the ray-tracing geometry. Unless otherwise specified, the nominal ray-tracing shell separation outside the cloud region is 1000 m.

6.2.4 Diffuse Point Configuration

To compute the observed radiance $I(s, \hat{\mathbf{\Omega}})$ in equation (3.43), SASKTRAN solves the radiation field at discrete locations in altitude and solar zenith angle, then traces

the ray using linear interpolations of the radiance field in height, solar zenith angle, and discrete outbound direction coordinates. Put differently, the source functions $J(s, \hat{\mathbf{\Omega}})$ are evaluated at a set of discrete points distributed in altitude and in solar zenith angle. The discretizations used in each of these dimensions must be chosen in accordance with the desired accuracy of computations.

Outside cloud regions, diffuse points are separated in altitude by 1 km and are located midway between the spherical ray-tracing shells. In cloud regions, diffuse points are densely concentrated to capture the abrupt changes in the optical depth and the radiance field that results from the presence of cloud particles.

Since an appropriate discretization must exercise a tradeoff between numerical accuracy and computational effort, we monitor the percent change of the simulated in-cloud radiance with respect to a very high-resolution base case. For a base case we consider diffuse points separated by 10 m in altitude within the cloud region. Figure 6.6 shows the fractional change in the 750 nm in-cloud radiance as the diffuse point spacing is increased. A thin cirrus cloud layer with $D_e = 30$ μm and two vertical and

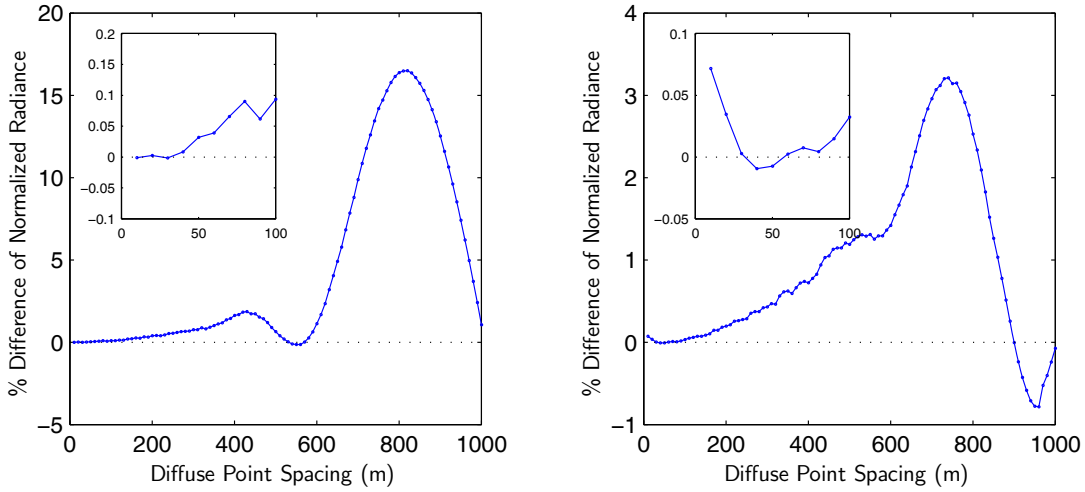

(a) $\Delta h_{cld} = 600$ m, $D_e = 30$ μm, $\tau_c = 0.075$ (b) $\Delta h_{cld} = 1000$ m, $D_e = 30$ μm, $\tau_c = 0.1$

Figure 6.6: Normalized modeled 750 nm limb radiance at 12.8 km tangent altitude as a function of diffuse point altitude spacing. The inset figures show the percent differences for diffuse point spacings between 10 and 100 m.

optical thicknesses were used for these computations. The ray-tracing shell locations were held fixed in the configuration described in the previous section. It is seen in these plots that the modeled radiance converges to a well-defined value for diffuse point spacings below 50 m. At wider spacings – from 100 m to spacings just narrower than the cloud thickness – the modeled radiance overshoots the converged value.

Within the thin cirrus cloud environments that are studied in this work, diffuse point spacing of 40 m in altitude is sufficient to ensure convergent solutions for cloud-sensitive wavelengths. To capture the change in radiance above and below the cloud layer, several bracketing diffuse points are placed above and below any region that contains cloud particles.

In a similar way, the discretization in solar zenith angle is studied by varying the spacing of diffuse profiles in solar zenith angle, $\Delta\theta_0$. Since the effect of this discretization on modeled radiances is most evident when the solar zenith angle, θ_0, is large, we model the in-cloud radiances for two OSIRIS scans in which the mean solar zenith angle is quite large, and for which the solar zenith angle varies over the line of sight by more than 5°. A cloud is placed in this study between altitudes of 16.2 km and 16.5 km with $\tau_c = 0.03$ and $D_e = 50$ μm. For the high-resolution base cases, the limb radiance is computed with diffuse profiles separated by $\Delta\theta_0 = 0.5°$, where each profile contains diffuse points separated by 40 m in the cloud region. The solar zenith angles at which the diffuse profiles are placed for the two scans are listed in Table 6.1.

The percent difference in modeled radiance is shown as a function of height in Figure 6.7 for a varying number of diffuse profile spacings for two extreme solar zenith angle cases. The percent difference in radiance from the base case are shown for diffuse profile spacings of approximately $\Delta\theta = 1°$, 3.16°, and 10°. For the radiances from scan 49644019 in Figure 6.7a, in which the mean solar zenith angle is 80.5°, the base case was computed with nine diffuse profiles, and it is clear that a single diffuse profile is sufficient to compute the radiance to a precision of better than 1%. For scan 53441016 in Figure 6.7b, in which mean solar zenith angle is $\theta_0 = 86.2°$, the percent difference from the benchmark case remains below 1.6% for all altitudes

Diffuse Profile Solar Zenith Angles			
Scan	$\overline{\theta_0}$	$\Delta\theta_0$	Profile Locations, θ_0 (°)
49644019	80.5°	1°	77.3, 78.4, 79.5, 80.6, 81.7
		3.2°	77.2, 81.7
		10°	80.5
53441016	86.2°	1°	82.0, 83.2, 84.3, 85.4, 86.6, 87.7
		3.2°	82.0, 87.7
		10°	86.2

Table 6.1: Diffuse profile locations for varying diffuse profile spacing.

above 10 km.

From these results, we find that one diffuse profile provides sufficient accuracy in modeled radiance since all clouds studied in this work have illumination conditions where the sun is, on average, higher in the sky than $\theta_0 = 73°$ at the measurement point.

6.2.5 OSIRIS Vertical Sampling Resolution

Before we investigate the effects of the various cloud optical properties on the simulated measurements, we briefly discuss the vertical sampling resolution of OSIRIS in relation to measurements of thin cirrus clouds. At typical OSIRIS exposure rates, successive exposures in a scan are separated by 1.5-2 km in tangent altitude. In this section we illustrate the effect of this somewhat coarse vertical sampling of thin cloud layers.

The simulated 750 nm radiance profiles for limb-scattering observations of a thin cloud layer, which are normalized to the radiance at 37.5 km, are shown in Figure 6.8 at several wavelengths and for several observation configurations. For all modeling computations shown in this chapter, the number densities of O_3, NO_2, and stratospheric aerosol from OSIRIS operational retrievals are used. In the top two figures, the altitude of the Gaussian-profile cloud layer 200 m thick (FWHM) that contains ice crystals with an effective size of $D_e = 160$ μm and optical depth $\tau_c = 0.02$ is shifted

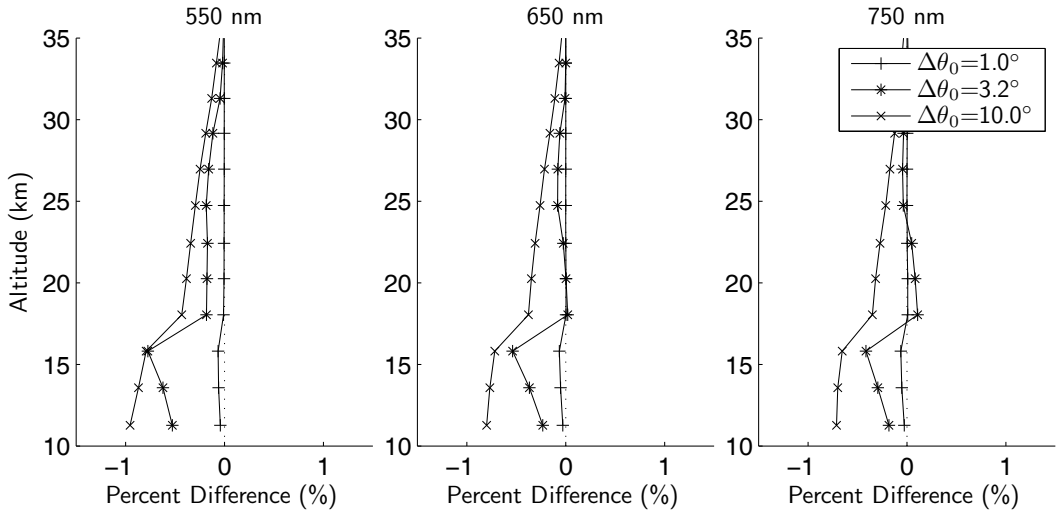

(a) OSIRIS scan 49644019: $\bar{\theta_0} = 80.5°$

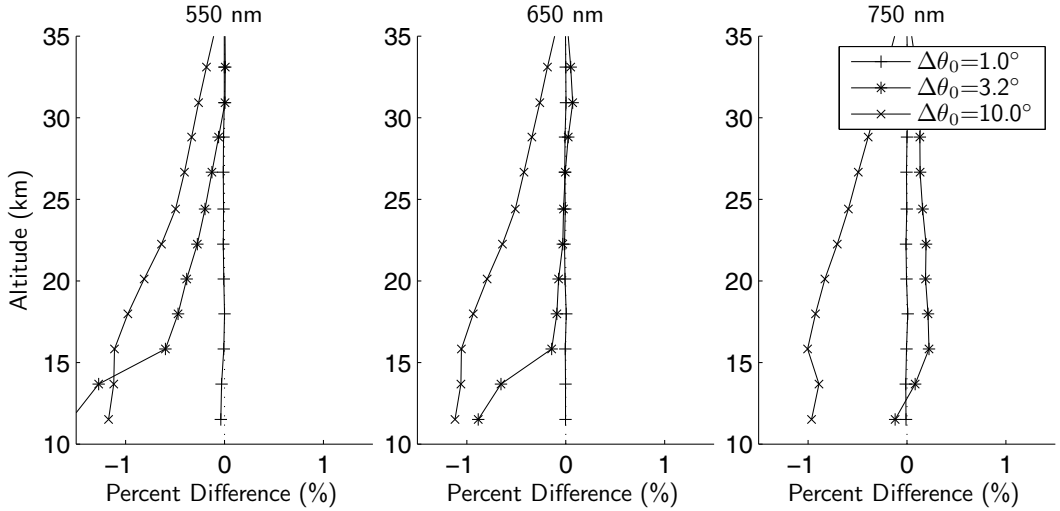

(b) OSIRIS scan 53441016: $\bar{\theta_0} = 86.2°$

Figure 6.7: Percent difference of modeled radiance for increasing coarseness of diffuse profile spacing.

upwards from 17 km to 19 km in 100 m steps to illustrate the simulated radiance profile for several viewing geometries. In a geophysical sense, this corresponds to limb measurement of a geometrically and optically thin cirrus cloud located slightly above the tropical tropopause. In the first two plots, the location and thickness of the cloud layer for its uppermost placement is shown as a shaded region for reference.

In Figure 6.8a, the limb radiance profiles for varying cloud height are shown

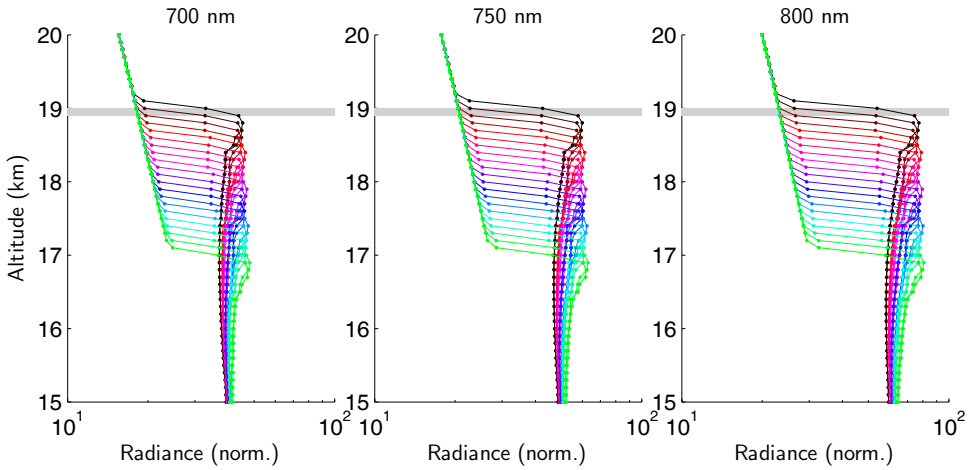

(a) Tangent points at shell boundaries (100 m).

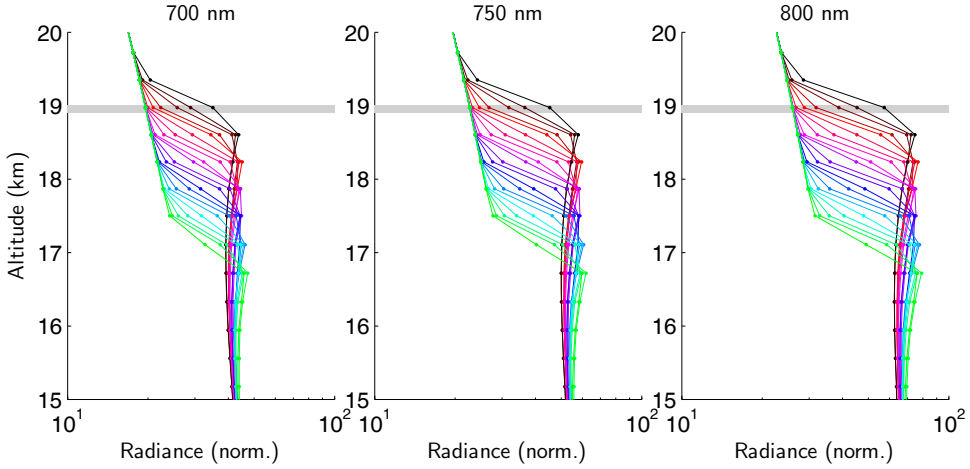

(b) Tangent points from high-resolution OSIRIS exposures (400 m)

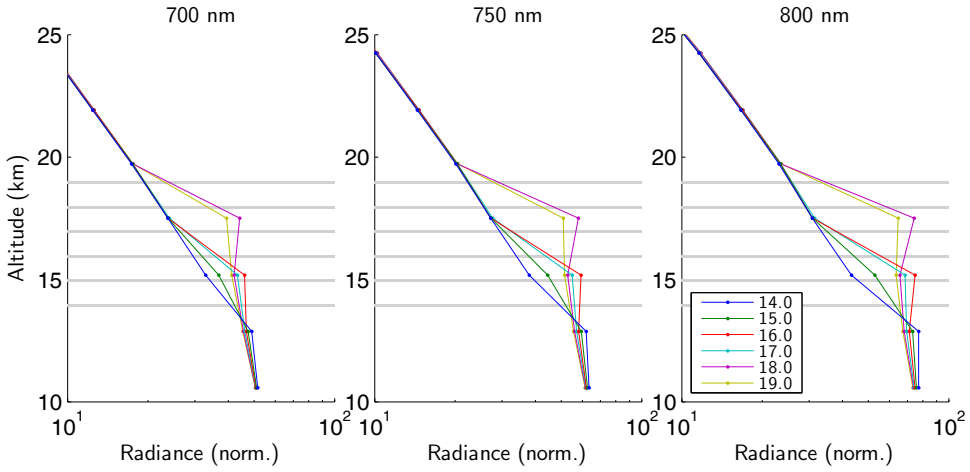

(c) Tangent points from actual OSIRIS exposures (2000 m)

Figure 6.8: Simulated shift in cloud-top altitude

for an observer with tangent altitudes separated by only $\Delta h_{tan} = 100$ m. This artificially-high resolution is used to capture accurately the limb radiance profile through a thin cloud layer. Due to its long path lengths through the highly-scattering region surrounding the tangent point, the modeled radiance reaches its peak value at a tangent height slightly below the cloud bottom. For tangent altitudes further below the cloud bottom, the enhancement to the radiance profile from a thin layer asymptotically approaches the radiance profile of the background signal.

This same shift in modeled cloud top altitude is shown in Figure 6.8b for a simulated OSIRIS scan that uses high-resolution sampling of at most $\Delta h_{tan} = 400$ m between successive exposures. The observer look directions to generate the radiances in this figure were found by using the measurement geometry for an actual OSIRIS scan, but the tangent altitudes of the OSIRIS exposures were interpolated to provide high-tangent altitude resolution. In addition, for this and subsequent modeling of OSIRIS cloud scans, 7 individual observer lines of sight were distributed within the OS vertical field of view, weighted binomially, and summed for each exposure in order to simulate more accurately the location of the cloud boundaries within the instrument field of view. For the figures in the middle row, there is no longer a clear relationship between the indicated cloud region and the radiance profile, but the radiance profile is dominated by the lower sampling resolution of the simulated geometry. The presence of a cloud is indicated primarily by an enhancement at several successive tangent altitudes below the cloud-top altitude.

A still more realistic view of the measured radiance profiles for the same 200 m-thick cloud is shown in Figure 6.8c. In these plots, the simulated radiance profile is shown when observed with the actual OSIRIS vertical sampling resolution. In this figure the cloud is moved upwards by 1 km for each model run, as indicated by the altitudes in the legend and by the shaded areas in the plots. From this figure one can see that there is limited information that can be gained about the cloud top and vertical thickness from consideration of the radiance profiles only for the OSIRIS vertical sampling resolution.

In Figure 6.8, it is noteworthy that the simulated radiance enhancements due

to the cloud are larger at longer wavelengths due to the decreasing value of the Rayleigh scattering cross section. As well, the measured enhancement is smaller at lower altitudes due to the reduction in solar irradiance for the current solar zenith angle, which is approximately 70°.

6.3 Modeled Limb Radiances

In this section, the dependence of the modeled limb radiances for a simulated OSIRIS scan are shown as functions of the four cloud parameters h_{ct}, Δh_{cld}, D_e, and τ_c. The OSIRIS measurement considered for this study, scan 47118030, is located over the western Pacific warm pool region.

Since the relative humidity, temperature, and vertical wind profiles are key parameters of interest in the formation of subvisual cirrus clouds, the height profiles of these parameters are shown in Figure 6.9 for this scan. In these profiles, the

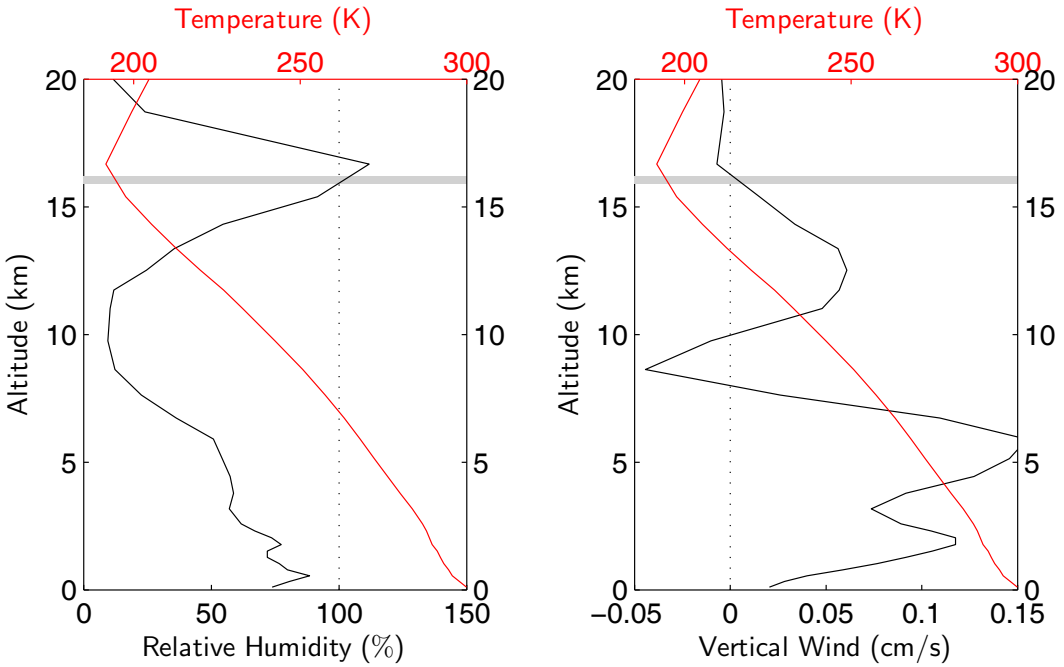

(a) Relative humidity profile (%)

(b) Vertical wind profile (cm/s)

Figure 6.9: ECMWF temperature, relative humidity, and vertical wind profiles for OSIRIS scan 47118030.

cloud-top altitude of 16.2 km for this scan, as determined from the criteria defined in Chapter 2, is shown with an estimated cloud thickness of 300 m as the shaded cloud region. At this altitude, which lies just below the cold point tropopause, the relative humidity is above 100% and the vertical wind is slightly upwards and decreasing with altitude, which microphysical modeling (*Luo et al.*, 2003) has shown to be an ideal stabilization condition for thin cirrus clouds.

In the sections that follow, we demonstrate the ability of the SASKTRAN model to simulate accurately the limb radiance observed by OSIRIS in the presence of thin cirrus clouds. This is demonstrated through comparisons of the modeled and measured in-cloud spectral radiance for those exposures which are placed directly through a thin cirrus cloud. In addition, the modeled and measured height profiles of the radiance at 750 m is shown for the simulated OSIRIS observations.

6.3.1 Albedo Configuration

Limb-scattered radiances are strong functions of surface albedo. As a result, accurate values for surface albedo values are essential for estimating cloud properties from OSIRIS limb scans. For the computations used in this study, the surface of the earth is assumed to be a Lambertian reflector.

The sensitivity of a modeled limb scan to surface albedo is shown in Figure 6.10. In this and subsequent figures the measured data are shown in the heavy black line. Note that the gap in the measured data near 500 nm is due to the spectral order sorter described in Section 2.3.2. The modeled radiance corresponds to the measurement shown in Figure 2.9a, with the measured and modeled spectra at 15.6 km tangent altitude shown. The modeled radiance is shown for a 500 m thick cloud layer with effective particle size 40 μm and optical depth 0.05, and where the wavelength-independent surface albedo is varied as indicated in the figure legend. It is clear that the modeled radiance across the spectrum is seen to vary approximately linearly with surface albedo. In addition, for this assumed wavelength-independent surface albedo, there is a distinct 'tilt' of the modeled spectrum relative to the measurement. Although a surface albedo of 0.2 provides a good spectral fit in our primary area of

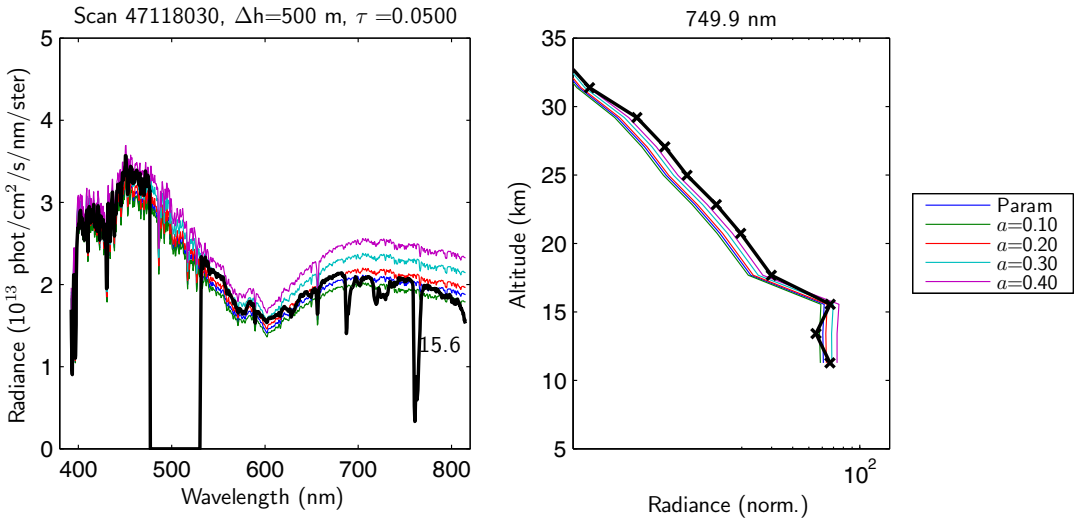

Figure 6.10: Modeled in-cloud spectra and radiance profile: varying surface albedo. Cloud thickness: 500 m, particle size 40 μm, optical depth 0.05.

interest – between 550 and 800 nm – this also significantly underestimates the measured signal at wavelengths below 550 nm. This illustrates the need for an accurate wavelength-dependent albedo.

Parameterized wavelength-dependent surface albedos for land cover (*Feister and Grewe*, 1995) and ocean surface (*Jin et al.*, 2004) are used with a land mask as *a priori* estimates for in-cloud radiance computations. The spectral variation of the selected surface albedos is shown in Figure 6.11. The modeled radiance using a parameterized surface albedo – in this case calculated for ocean surface albedo with typical wind speed, chlorophyll concentration, and aerosol optical depth – shown in Figure 6.10. It is seen that this wavelength-dependent albedo provides a better match across the measured spectrum. Later, the a priori wavelength-dependent albedo is scaled by the retrieved albedo at a reference wavelength, as described in Section 7.2.4.

6.3.2 Cloud Top and Vertical Thickness

The effect of cloud-top altitude and vertical thickness, as defined in Section 6.2.2, is not readily apparent from the in-cloud radiance nor from the radiance profile due to the vertical resolution of OSIRIS tangent altitude exposures. This is shown in Figure

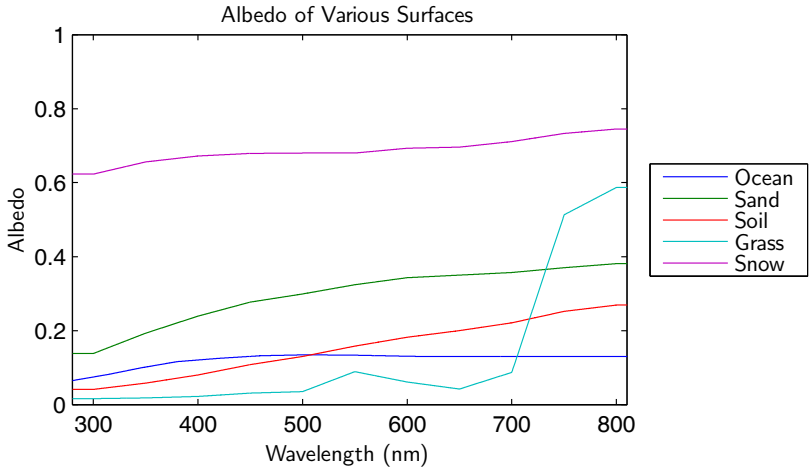

Figure 6.11: Wavelength-dependent values of land (*Feister and Grewe*, 1995) and ocean surface (*Jin et al.*, 2004) albedo.

6.12, where for a line of sight tangent at 15.6 km, the cloud thickness is increased successively by 200 m above a fixed cloud bottom altitude of 15.6 km. For this plot,

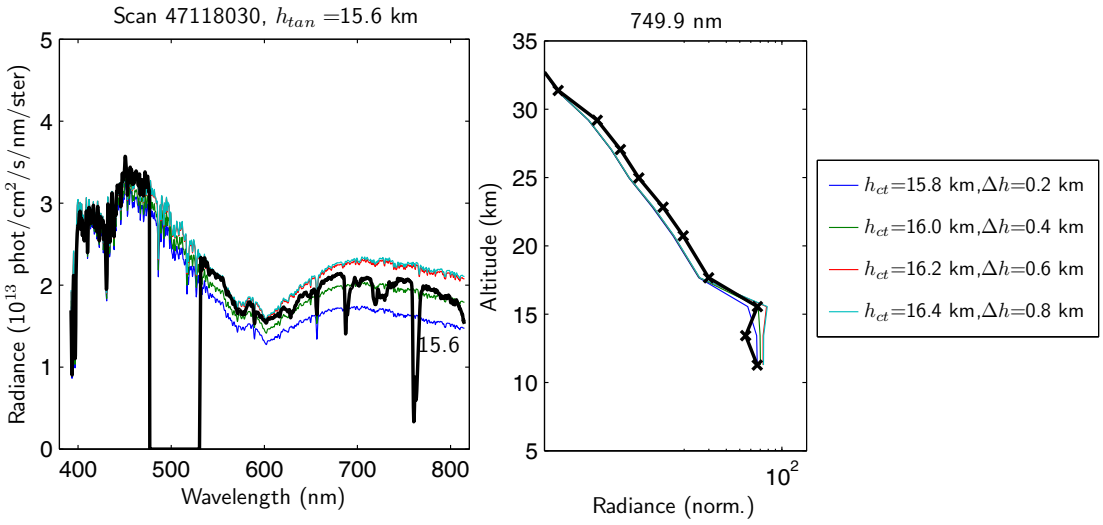

Figure 6.12: Modeled in-cloud spectra and radiance profile: varying cloud thickness and cloud top height.

the effective particle size is 50 μm and the cloud optical thickness is fixed at 0.049. The primary effect of a vertical thickening of the cloud layer is an increased radiance at longer wavelengths across the spectrum.

6.3.3 Cloud Optical Thickness

An increase in cloud optical thickness corresponds to an increase in the peak number density of the distribution. For a fixed cloud-top altitude of 16.2 km, vertical thickness of 300 m, and fixed effective size of 50 μm, the changing in-cloud radiance and radiance profile for varying optical depth are shown in Figure 6.13. The cloud optical thicknesses are indicated in the legend. In this figure, the limb radiance is seen to

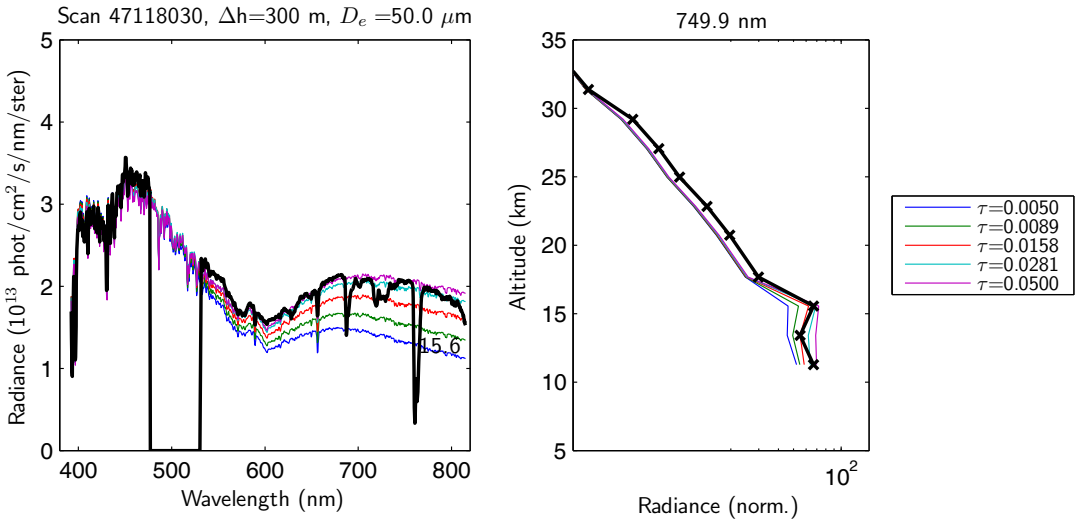

Figure 6.13: Modeled in-cloud spectra and radiance profile: varying cloud optical thickness.

increase quite uniformly for a uniform logarithmic increase in cloud optical depth. As well, the modeled spectrum at $\tau_c = 0.05$ is seen to match the measured spectrum very well between 550 and 800 nm. The notable decrease in measured radiance above 795 nm is likely due to the uncertainty in the preflight Woods anomaly calibration, which affects the absolute calibration of the spectrograph (*Lloyd*, 2011).

It is illustrative to view the change in the radiance profile due to an increase in cloud optical thickness for fixed cloud geometric size. The limb radiance profile for a simulated high-resolution scan is shown in Figure 6.14 for logarithmically-increasing cloud optical depth that spans the subvisual cirrus cloud threshold, $\tau_c = 0.03$. As the cloud becomes more optically thick the radiances of lines of sight below the first subcloud tangent altitude become approximately uniform in brightness since the cloud

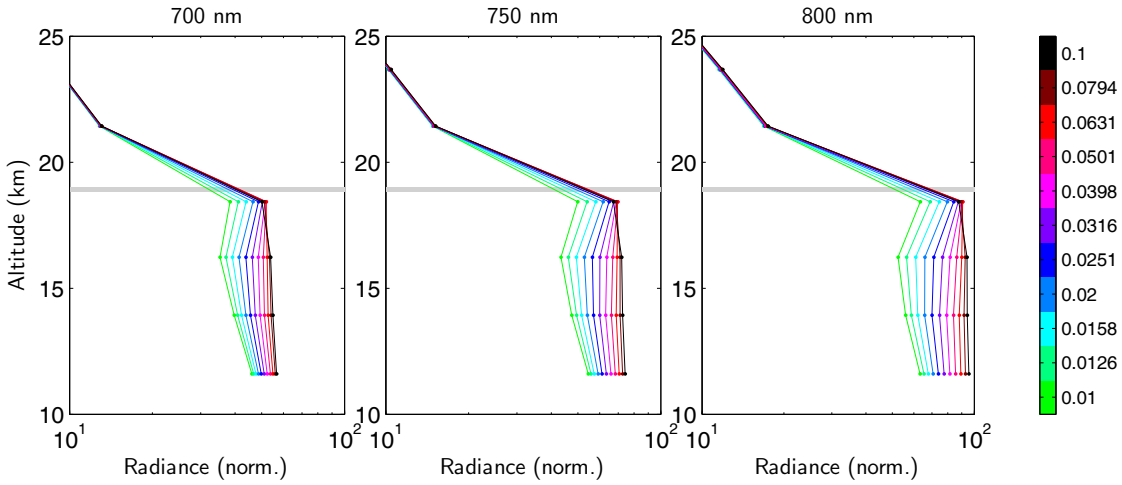

Figure 6.14: Modeled limb radiance profiles: varying cloud optical thickness.

top acts as a scattering surface of increasing reflectivity.

6.3.4 Cloud Effective Particle Size

Larger particle sizes tend to more strongly scatter light. This effect can be seen clearly when the modeled cloud top height and vertical and optical thicknesses are fixed while the effective size is varied, as shown in Figure 6.15. In this figure, the

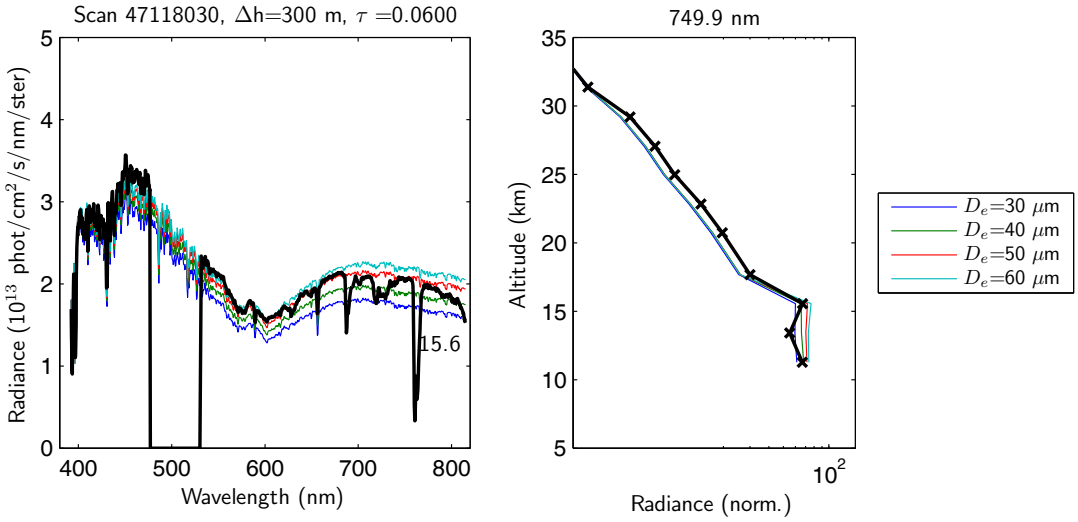

Figure 6.15: Modeled in-cloud spectra and radiance profile: varying cloud effective particle size.

in-cloud scattered radiance is seen to increase monotonically with effective size (4.45). The radiance profiles for changing effective particle size at selected wavelengths are shown in Figure 6.16. As seen in this figure, it is characteristic of scattering by

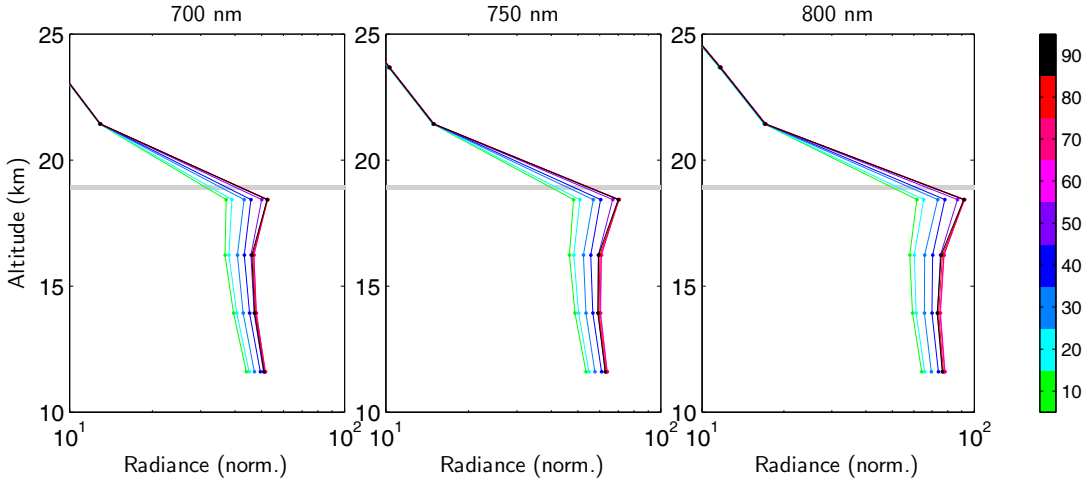

Figure 6.16: Modeled limb radiance profiles: varying cloud effective particle size.

larger particles that they form a more sharply-peaked radiance profile as the effective particle size increases.

For each effective particle size, the optical depth can be adjusted to best fit the in-cloud radiance over a given spectral range. Then a family of parameters are chosen that give a good spectral match to the observed in-cloud radiance, as shown in Figure 6.17. In the radiance profile, it can be seen that the $D_e = 50$ μm modeled profile displays a thicker scattering layer corresponding to its significantly larger assumed optical depth, despite its good agreement across the long-wavelength region of the in-cloud radiance. The dependence of the radiance profile on the cloud extinction profile and the assumed particle size is the primary source of information for retrieving cloud optical properties, as discussed in the next chapter.

The selection of optical properties shown in this section can be applied to many OSIRIS measurements in the presence of a strongly-scattering cloud layer. To illustrate, the modeled radiance for the scan immediately following the one studied thus far is shown in Figure 6.18. The measured radiance profile indicates a more optically thick cloud layer, as seen by comparison with the radiance profiles in Figure 6.14. It

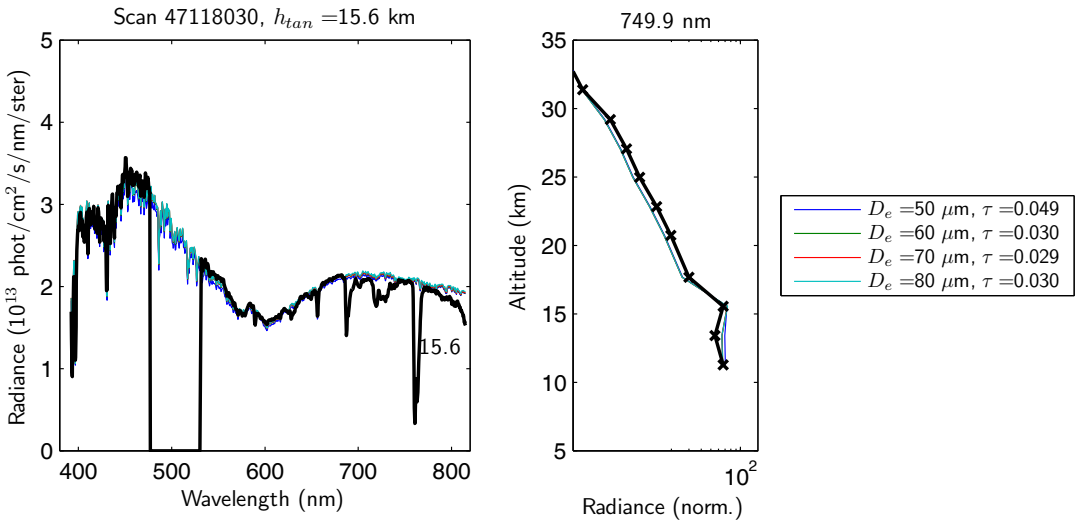

Figure 6.17: Modeled in-cloud spectra and radiance profile: selected particle sizes and cloud optical depths. Cloud thickness: 300 m.

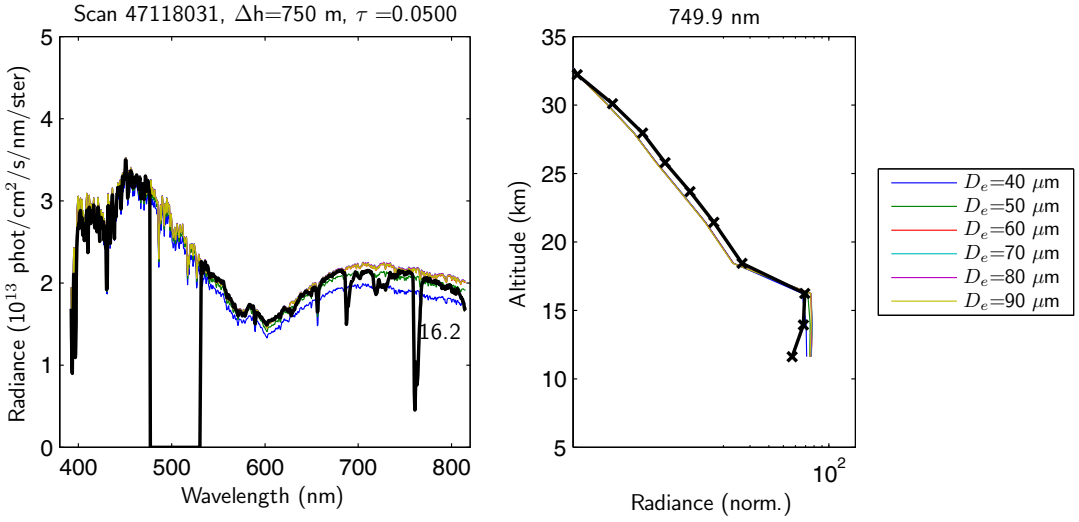

Figure 6.18: Modeled in-cloud spectra and radiance profile: varying particle sizes for cloud optical depth $\tau_c = 0.05$. Cloud thickness: 750 m.

is seen through preliminary modeling, as shown in this figure, that an optical depth of 0.05 matches the in-cloud spectrum very well for effective particle sizes between 50 and 90 μm across the measured spectrum. The effect of the assumed particle size on estimated cloud optical thickness is also investigated in the next chapter.

6.4 Summary

It has been shown that with the modifications and configurations discussed in this chapter and in the previous chapter, the SASKTRAN model is able to model accurately the in-cloud spectral radiance measured by OSIRIS. The in-cloud modeled spectral radiances for the two cloud scans investigated in this chapter are shown together with their percent difference from the measured in-cloud spectra in Figures 6.19 and 6.20 together with the modeled radiance if cloud properties are not included. For the percent differences, the modeled radiances are shown relative to the

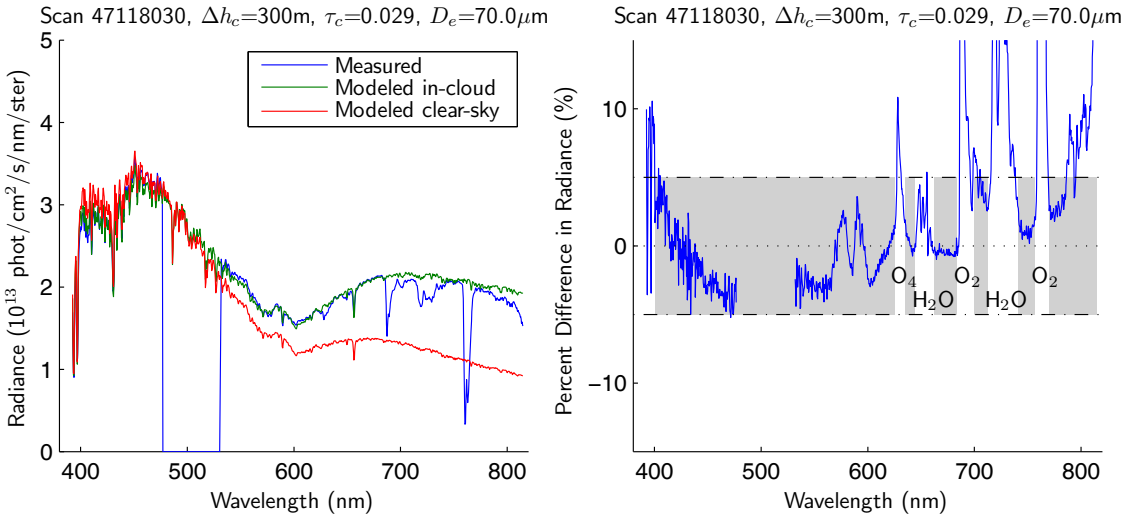

(a) Spectral radiances

(b) Radiance percent difference

Figure 6.19: Modeled and measured in-cloud radiances for OSIRIS scan 47118030.

measurements. It is seen that in the highlighted regions – outside of the indicated absorption bands and at wavelengths $\lambda > 400$ nm for which the cloud properties database is defined – the modeled spectra agree with the measurements to better than 5% across the spectrum. The only exception is due to the sharp decrease in the measured signal above 790 nm, which as mentioned previously is likely due to uncertainty in the preflight Woods anomaly calibration. These simulated in-cloud radiances demonstrate a significant improvement in the ability of the SASKTRAN model to simulate OSIRIS measurements in a variety of conditions.

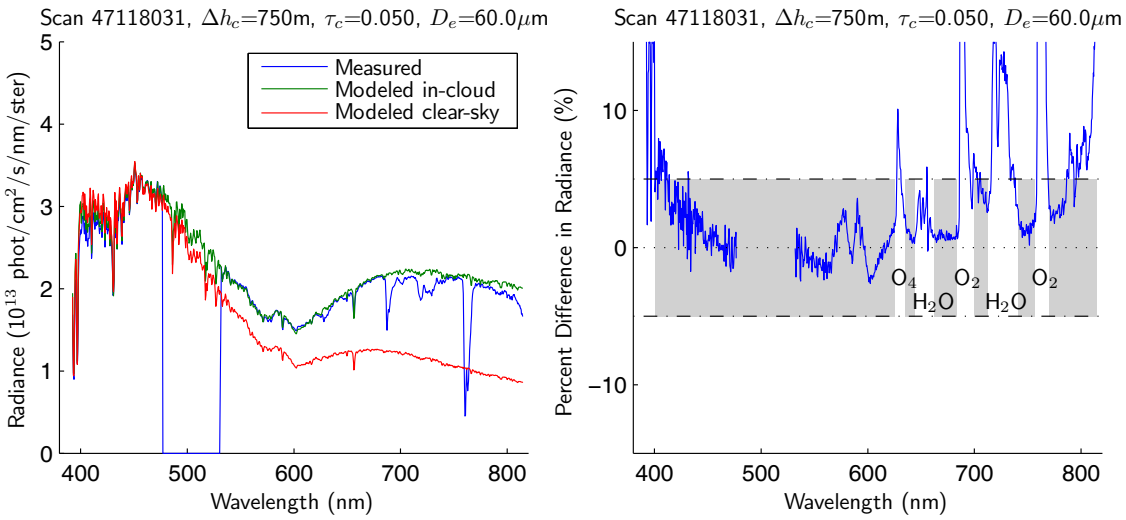

(a) Spectral radiances

(b) Radiance percent difference

Figure 6.20: Modeled and measured in-cloud radiances for OSIRIS scan 47118031.

The simulations of in-cloud radiance shown in this chapter have been done assuming suitable choices for the cloud top altitude, vertical and optical thickness, and effective particle size. Modeled spectral results agree very well with measurements in the wavelength range 550-800 nm, which is the region of primary interest in estimation of cloud optical properties. It is found that using an in-cloud diffuse point spacing of 40 m is sufficient to obtain a precise solution. Ray-tracing altitudes in the spherical geometry are configured to the altitude profile of the cloud extinction, down to a minimum shell spacing of 10 m.

Although a number of the modeled radiance profiles do not match the measurements to within the same accuracy as the in-cloud spectral radiance, determination of the cloud properties to improve this fit is done in an automated fashion in the next chapter. Clouds have been selected for this study to have the sun located at zeniths less than 72° at the measurement point, although these methods can easily be used for more general conditions with the use of additional diffuse profiles.

Chapter 7

Cloud Optical Property Retrieval

Estimating atmospheric properties from spectral measurements requires an accurate radiative transfer model that can run efficiently in an iterative way to infer the most probable parameters from the measurements. The inverse problem, or the process of inferring parameters from measurements, has devoted to it a significant body of literature and work. In this chapter we summarize several techniques relevant for retrievals of cirrus cloud optical properties from OSIRIS measurements. A technique is implemented to retrieve the optical thickness of cirrus clouds for an assumed particle size. The effects of the retrieval on retrieved amounts of other trace species from the same instrument, as well as the sensitivity to auxiliary model parameters, are investigated.

7.1 The Inverse Problem

Inversion of remote sensing measurements to obtain the most probable set of atmospheric parameters begins with specifying a *state vector*,

$$\mathbf{x} = \begin{bmatrix} x_1 \\ x_2 \\ \vdots \\ x_n \end{bmatrix}, \tag{7.1}$$

that consists of the n parameters that are to be inferred from the measurements. In general the measurements, $\mathbf{y}$, depend on the state vector through a physical process, f, and contain noise, ϵ, such that the relation between the measurement and the state is expressed mathematically as

$$\mathbf{y} = f(\mathbf{x}, b) + \epsilon. \tag{7.2}$$

The fact that the physical process depends upon the state of many parameters beyond the one of interest is indicated through the inclusion of the *auxiliary parameter*, b. The set of of m measurements that one defines to obtain information about the state is the *measurement vector*,

$$\mathbf{y} = \begin{bmatrix} y_1 \\ y_2 \\ \vdots \\ y_m \end{bmatrix}. \tag{7.3}$$

In general the number of measurements is not the same as the number of state parameters. Because a model, $\mathbf{F}(\mathbf{x}, \tilde{b})$, must be used to simulate measurements for a given state of the system it is assumed that the model approximates well the physical process, or

$$\mathbf{F}(\mathbf{x}, \tilde{b}) \approx f(\mathbf{x}, b). \tag{7.4}$$

The *forward model*, $\mathbf{F}(\mathbf{x}, \tilde{b})$, in the case of remote sensing of the atmosphere is a radiative transfer model that assumes a state vector, $\mathbf{x}$, for the parameters of interest in addition to the auxiliary parameters, $\tilde{b}$.

A typical method to quantify the suitability of a set of parameters is the least-squares method, in which the solution to the inverse problem is considered to be the state that minimizes the cost function

$$\chi^2 = \frac{1}{m} \sum_{i=1}^{m} \left(\frac{y_i - \mathrm{F}_i(\mathbf{x}, \tilde{b})}{\sigma_i} \right)^2, \tag{7.5}$$

where σ_i is the uncertainty in the measurement y_i. With this measure of error,

parameters are typically found through trial and error.

If changes in the measurements are linearly related to changes in the state vector, and if the measurements are noise-free, then the state that produced a given measurement can be found from an *a priori* estimate of the state, $\mathbf{x}_a$, by a linearization of the forward model about the a priori value of the state,

$$\mathbf{y} = \frac{\partial \mathbf{F}(\mathbf{x}, \tilde{b})}{\partial \mathbf{x}} (\mathbf{x} - \mathbf{x}_a) + \mathbf{F}(\mathbf{x}_a, \tilde{b}). \tag{7.6}$$

The $m \times n$ Jacobian matrix of forward-model derivatives with respect to the state vector elements is frequently called the *kernel matrix* in inversion theory and is expressed as

$$\mathbf{K} = \begin{bmatrix} \frac{\partial \mathrm{F}_1}{\partial x_1} & \cdots & \frac{\partial \mathrm{F}_1}{\partial x_n} \\ \vdots & \ddots & \vdots \\ \frac{\partial \mathrm{F}_m}{\partial x_1} & \cdots & \frac{\partial \mathrm{F}_m}{\partial x_n} \end{bmatrix}. \tag{7.7}$$

If there are the same number of measurements as state vector elements, then the Jacobian matrix in equation (7.6) can be inverted to solve directly for the desired state,

$$\tilde{\mathbf{x}} = \mathbf{x}_a + \mathbf{K}^{-1} \left(\mathbf{y} - \mathbf{F}(\mathbf{x}_a, \tilde{b}) \right). \tag{7.8}$$

For nonlinear problems, the solution can be found by trial and error by successive forward model computations, although this is prohibitive for all practical purposes. If the forward model is approximately linear for small changes to the state vector, then a direct solution can be attempted through Gauss-Newton iteration, in which the state can be moved forward from the a priori by stepwise application of equation (7.8), with the modification that the Jacobian, $\mathbf{K}^{(n)}$, is re-evaluated at each iteration using the iterated state value, $\mathbf{x}^{(n)}$. Inversion of the Jacobian matrix, $\mathbf{K}$, can introduce significant oscillation into the state solution, $\mathbf{x}$, if the measurement error is significant.

One of the most common algorithms used in nonlinear regression problems is the Levenberg-Marquardt technique (*Press et al.*, 1986), which uses a combination of steepest-descent and Gauss-Newton techniques to minimize the residual, χ^2. At each iteration the Jacobian matrix, $\mathbf{K}^{(n)}$, is calculated, and the update in the state vector

is computed as

$$\mathbf{x}^{(n+1)} = \mathbf{x}^{(n)} + \left(\mathbf{K}^{(n)}(\mathbf{K}^{(n)})^T + \gamma\mathbf{I}\right)^{-1}(\mathbf{K}^{(n)})^T\left[\mathbf{y} - \mathbf{F}(\mathbf{x}^{(n)})\right]. \tag{7.9}$$

The selection parameter, γ, determines the choice of minimization technique used: when χ^2 is large, the step-update matrix becomes diagonally dominant, and steepest-descent is used; when χ^2 decreases and the solution approaches the minimum, the diagonal elements no longer dominate, and a Gauss-Newton iteration performs the next step in parameter space.

7.1.1 Regularization Methods

The first solutions that were proposed for the inverse problem were based on *regularization*. In this method, a side constraint is added to the minimization of χ^2 such that the retrieved state is subject to a smoothness criterion. In this way, the minimization problem is restated as

$$\chi^2 = \frac{1}{m}\sum_{i=1}^{m}\left(\frac{y_i - \mathrm{F}_i(\mathbf{x}, \tilde{b})}{\sigma_i}\right)^2 + \gamma^2|\mathbf{L}\mathbf{x}|^2. \tag{7.10}$$

The additive term to the cost function seeks to minimize the effect of random noise in the measurements on the retrieved profile. The smoothest retrieved profile then will have a minimum value of the second term. The additional term thus sets up a balance between the fit of the forward model to the measurements and the variation in the retrieved state. A drawback to this method is that small-scale structure is not distinguished from noise. The main modifications to regularization methods consist in defining the smoothness of the state vector through the operator matrix, $\mathbf{L}$, and by smoothing the profile by using the difference between a retrieved state and the a priori state.

7.1.2 Optimal Estimation Technique

One of the most common methods used for retrievals of atmospheric states from remote sensing measurements is the *optimal estimation* technique (*Rodgers*, 1976), which is a regularization method based on statistical knowledge of the desired state parameter. This method is based on the Bayesian assumption that the probability density function (PDF) of a variable, rather than being a frequency distribution of various measurement trials, actually contains knowledge about the variable. Given a set of measurements with associated covariances and a linear forward model, Bayesian statistics are used to update the state PDF from an a priori estimate using information from the measurements according to the Bayesian relation between probabilities,

$$p(\mathbf{x}|\mathbf{y}) = \frac{p(\mathbf{y}|\mathbf{x})p(\mathbf{x})}{p(\mathbf{y})}. \tag{7.11}$$

In this expression, the probability distributions, p, of each of the variables is assumed to have a Gaussian form with associated covariance matrices, $\mathbf{S}$. The retrieved solution is then the peak of the Bayesian probability density function, $p(\mathbf{x}|\mathbf{y})$.

This method involves the assumption that the measurement error is random and that the PDF of the a priori state is a Gaussian distribution. The solution is sought by an iterative step derived by maximizing the value of $p(\mathbf{x}|\mathbf{y})$ with respect to $\mathbf{x}$. Since the PDF of the retrieved state is generally unknown, a climatological estimate is often used. The covariance of the retrieved state can be interpreted as a measure of the amount of information added to the PDF of the retrieved state by the measurements. The optimal estimation algorithm has the benefit of not requiring inversions of $\mathbf{K}$.

7.1.3 Relaxation Methods

Another family of solutions to the inverse problem falls under the category of *relaxation* methods. This general inversion method, as applied to retrievals of atmospheric parameters, was formalized by *Chahine* (1972) in which the state parameter is found

iteratively through

$$x_i^{(n+1)} = x_i^{(n)} \frac{y_i}{F_i(\mathbf{x}^{(n)}, \tilde{b})}. \tag{7.12}$$

Here the update to the state parameter x_i is the ratio of the measurement vector to the forward model prediction as evaluated at the current estimate.

This method requires that the measurement vector be constructed such that, if y_i is larger than the current model evaluation F_i, the change to the state parameter performed at this step must act to increase the value of F_i. This method requires a condition in which there is a nearly one-to-one relationship between the elements of $\mathbf{x}$ and $\mathbf{y}$. This often done by interpolation of the atmospheric state profile, which is assumed to be smooth.

An extension of (7.12) allows for the retrieval of a state vector at points between the measurement locations by using the Jacobian matrix to weight the ratio of actual to modeled measurement vectors,

$$x_i^{(n+1)} = x_i^{(n)} \frac{y_j}{F_j(\mathbf{x}^{(n)}, \tilde{b})} K_{ij} + x_i^{(n)}(1 - K_{ij}). \tag{7.13}$$

In any relaxation method, iteration is performed for each element of the state parameter and is repeated until convergence, that is, until a residual $R_i = y_i - F_i(\mathbf{x}^{(n)}, \tilde{b})$ approaches a predetermined threshold that is indicative of the measurement error. The use of the kernel matrix in equation (7.13) incorporates information from multiple measurements into the update for the state parameter $x_i^{(n)}$.

With the exception of the Chahine relaxation method, the techniques described thus far rely on computing the kernel matrix for each iteration of the state parameters. Since computing limb radiance profiles in the presence of a cloud is computationally expensive, and since computing $\mathbf{K}$ involves the greater of m or n forward model evaluations at each iteration, it is highly advantageous to avoid using any technique that requires evaluating the Jacobian matrix.

7.1.4 Multiplicative Algebraic Reconstruction Technique

A maximum-likelihood technique was applied by *Lloyd and Llewellyn* (1989) to deconvolve blurred images from a Fabry-Perot interferometer. An extension of this method was applied by *Degenstein et al.* (2003) to volume emission rate tomography for resolving small-scale horizontal structures of excited-state molecular oxygen emissions in the mesosphere. This technique was further developed and applied to retrievals of ozone from OSIRIS using the altitude-dependent absorption depths in the Hartley-Huggins and Chappuis bands.

In this scheme independent measurement sets, $\mathbf{y}_k$, which correspond to radiance profiles at different wavelengths and that have corresponding forward model computations, $\mathbf{F_k}(\mathbf{x}, \tilde{b})$, are applied to retrievals of the state parameter, $\mathbf{x}$. By allowing each independent wavelength to contribute to the update of the state parameter, the following relaxation iteration is obtained:

$$x_i^{(n+1)} = x_i^{(n)} \sum_k \sum_j \frac{y_{jk}}{F_{jk}(\mathbf{x}^{(n)}, \tilde{b})} W_{ijk}. \tag{7.14}$$

In this expression, the ratio of actual and modeled measurement vectors, $\frac{y_{jk}}{F_{jk}}$, for each independent measurement, k, is allowed to affect the iteration through its weight, W_{ijk}, where the weights are normalized such that $\sum_j W_{ijk} = \sum_k W_{ijk} = 1$ for each state element, i. This technique has been integrated with the SASKTRAN model to retrieve atmospheric profiles of of O_3 (*Degenstein et al.* (2009), *Roth et al.* (2007)); NO_2 (*Bourassa et al.*, 2011); and sulphate aerosols (*Bourassa et al.*, 2007); and is optimized for fast execution time.

7.2 MART Cloud Property Retrieval from OSIRIS

We apply the MART relaxation algorithm to cloud property retrievals from OSIRIS measurements. For this purpose the measurement vector, $\mathbf{y}$, is constructed from OSIRIS spectral radiances at tangent altitudes surrounding the cloud region. The state to be retrieved, $\mathbf{x}$, in this problem is characteristically the height profile of

the cloud particle number density for an assumed particle size distribution. The set of auxiliary parameters in the model that affect the accuracy of solution, $\tilde{b}$, consist primarily of the surface albedo and the aerosol and ozone number density profiles.

For scattering by cloud particles, the radiance of a single wavelength is used to estimate the cloud particle number density. In such a scheme, the cloud number density, $\mathbf{x}$, is updated at each iteration according to

$$x_i^{(n+1)} = x_i^{(n)} \sum_j \frac{y_j}{F_j(\mathbf{x}^{(n)}, \tilde{b})} W_{ij}. \tag{7.15}$$

Since in the cloud property retrieval we suspect a very direct relationship between the number density at altitudes near tangent point and the measured radiance, we use $W_{ij} = \delta_{ij}$. This is equivalent to the Chahine relaxation method, equation (7.12). The retrieval equation (7.15) is rewritten for diagnostic purposes as a matrix equation of the ratio between the next- and current-order state variable,

$$\alpha = \mathbf{W}\mathbf{m}, \tag{7.16}$$

where the vectors α and $\mathbf{m}$ are defined as

$$\alpha = \frac{\mathbf{x}^{(n+1)}}{\mathbf{x}^{(n)}}, \qquad \mathbf{m} = \frac{\mathbf{y}}{\mathbf{F}(\mathbf{x}^{(n)}, \tilde{b})}. \tag{7.17}$$

As iterations proceed, the progression of α values toward unity shows the convergence of the state toward a stable value. Convergence toward a solution is considered satisfied when the fractional change in the values of α fall within measurement uncertainty.

7.2.1 Measurement Vector Definition

The measurement vectors that are used to iterate towards a solution in the relaxation equation, (7.15), must be specified to increase together with the state parameter. Equivalently, the Jacobian matrix, equation 7.7, must be positive so that the

iterations do not diverge.

We select a measurement vector in a manner similar to that done for retrievals of stratospheric aerosol from OSIRIS by *Bourassa et al.* (2007). An element of the measurement vector, y_j, is constructed for each tangent altitude by taking the logarithmic ratio of a long-wavelength radiance and a short-wavelength radiance, then subtracting the same logarithmic ratio of the 'background' – that is, cloud- and aerosol-free – radiances,

$$\begin{aligned} r_j &= \log\left(\frac{I(h_j,\lambda_l)}{I(h_j,\lambda_s)}\right) - \log\left(\frac{I_{bg}(h_j,\lambda_l)}{I_{bg}(h_j,\lambda_s)}\right) \\ &= \log\left(\frac{I(h_j,\lambda_l)}{I_{bg}(h_j,\lambda_l)}\right) - \log\left(\frac{I(h_j,\lambda_s)}{I_{bg}(h_j,\lambda_s)}\right). \end{aligned} \tag{7.18}$$

The wavelength ratio provides sensitivity to the spectral signature of cloud particle scattering, and the subtraction of the background radiance ratio enhances the non-Rayleigh scattering contributions to the limb radiance. The short wavelength is chosen to be 470 nm, which is the longest wavelength on the short-wavelength side of the spectrograph order sorter that was mentioned in Section 2.3.2, and is also outside of any significant ozone absorption bands. The long wavelength is chosen to be 750 nm in order to maximize the wavelength separation while at the same time avoiding the O_2 A-band absorption feature near 762 nm, the diffraction grating Woods anomalies above 780 nm, and the O_3 Chappuis absorption band.

For limb radiance measurements, it is common to normalize the radiance profile of a given wavelength to a higher reference altitude, which provides a measure of insensitivity to the instrument absolute calibration and also to the surface albedo. We employ a modification of this technique, in which instead of normalizing the profile to the radiance at one tangent altitude, we normalize the vector r_j in equation (7.18) by subtracting from it the average value of r_j over a finite reference altitude range,

$$y_j = r_j - \langle r_{\mathrm{ref}} \rangle. \tag{7.19}$$

By using as a reference the average value of r over a more broad reference altitude

range, the measurement vector is better able to characterize and remove the background signal. The minimum reference altitude used in this work is chosen to be 37 km, which is above any significant amount of stratospheric aerosol and is below altitudes where light scattered from the instrument primary mirror becomes significant.

Examples of measurement vectors constructed by (7.19) are shown for two OSIRIS scans in Figure 7.1. The measurement vectors are shown for OSIRIS scan 47626029,

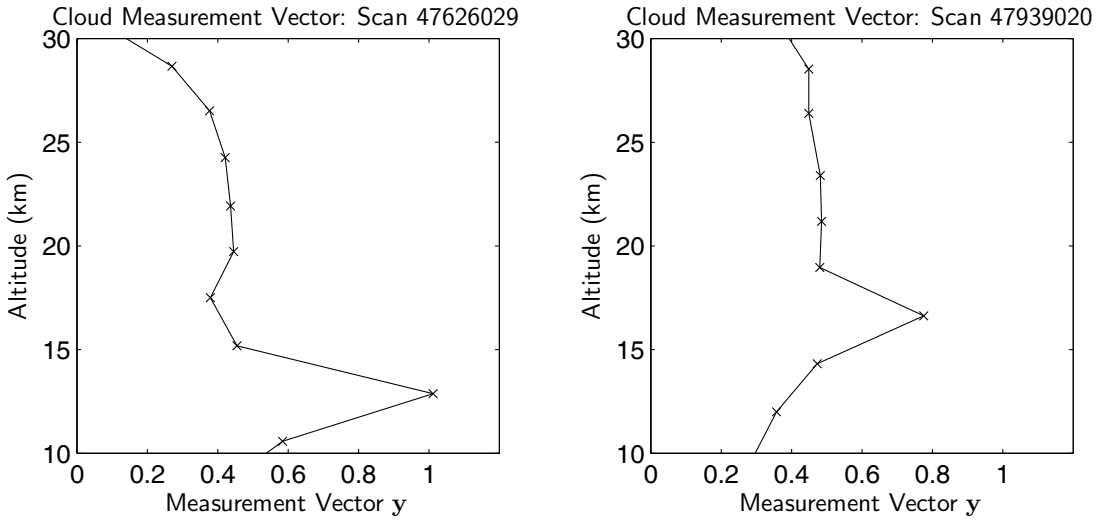

(a) Scan 47626029

(b) Scan 47939020

Figure 7.1: Measurement vector, $\mathbf{y}$, for selected scans.

which has a cloud-top altitude of 14.6 km; and for scan 47939020, with cloud-top altitude 18.6 km. It is seen in these figures that the measurement vector shows two distinct regions. First, the sharp peak at lower altitudes indicates a large amount of scattering in the presence of a cloud. Second, at higher altitudes the profile more smooth with a consistent value near 0.4 from scattering by stratospheric aerosols in the Junge layer.

7.2.2 State Vector Specification

Retrieval of cloud optical properties from a limb-scattering geometry is complicated by the numerous ways that solar radiation can reach the instrument, as illustrated

in Figure 3.1. To further illustrate by comparison, for occultation measurements the extinction profile, $k(h)$, of the intervening medium is measured directly through the decreased transmission as measurements are made through increasing depths of the atmosphere. Accordingly, for occultation measurements no knowledge of the scattering behaviour of the particles for non-forward directions is needed, and the phase function of the assumed particles plays a minor role in the retrieval process. By contrast, in limb-scattering geometry, the phase function is a key element of the retrievals since the primary measured signal is the single- or multiply-scattered radiance from near the tangent point. As such the particle extinction and phase function are equally important to retrievals of cloud properties from measurements in limb-viewing geometry.

Both the scattering cross section and the phase function depend on the ice crystal size distribution, which makes the retrieval of cloud particle number density sensitive to the assumed particle size. Some of the sensitivity to the assumed particle size distribution can be removed by using the cloud extinction profile, $k(h)$, as the retrieved state parameter. Although the phase function still depends on the size distribution, the phase functions used in this work to model cloud particle scattering vary smoothly with effective size and scattering angle in the OSIRIS solar scattering range, between 60° and 120°, as shown in Figure 4.5.

Retrievals are performed with the state vector defined as the cloud extinction profile, $x_i = k_{cloud}(h_i)$, at heights corresponding to the tangent altitudes within the troposphere. The sensitivity of the retrievals to the assumed particle size is investigated later in this chapter.

7.2.3 Cloud Scattering Radiance Signature

The sensitivity of the measurement vector to small perturbations to the cloud extinction profile is illustrated in Figure 7.2, in which the Jacobian matrix, equation (7.7), is shown for several wavelengths across the OSIRIS spectral range. Each curve in these figures is constituted by a column of $\mathbf{K}$, and corresponds to the change in the measurement vector $\mathbf{y}$ that results from a small perturbation to the state vector

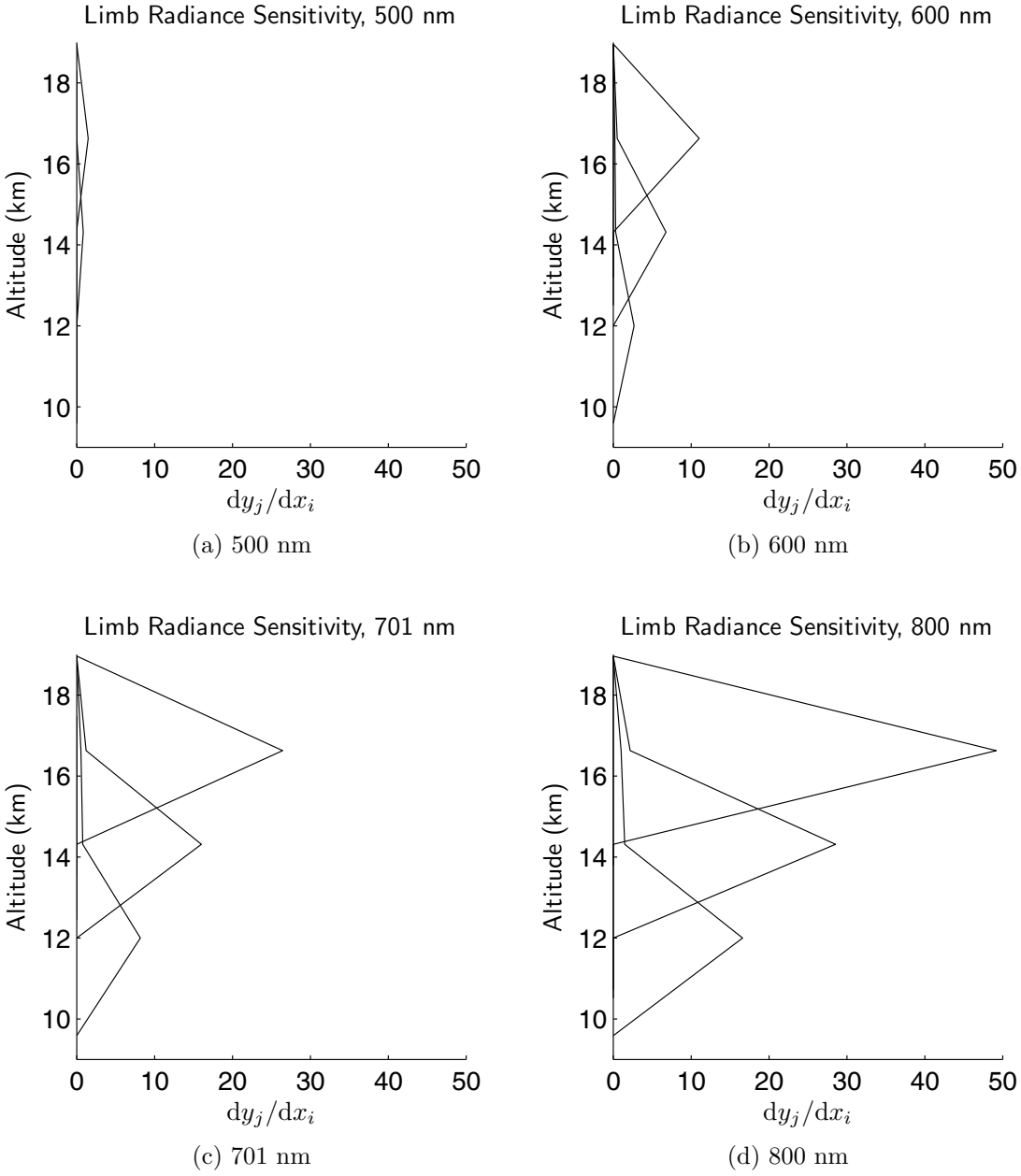

(a) 500 nm

(b) 600 nm

(c) 701 nm

(d) 800 nm

Figure 7.2: Kernel matrix for selected wavelengths for scattering by 50 μm particles.

element x_i. To produce these Jacobian elements, cirrus cloud properties with effective size $D_e = 50$ μm were distributed at heights between 9 and 19 km at very low number densities such that the cloud optical thickness was $\tau_c = 0.03$. The elements of $\mathbf{K}$ were computed by successively perturbing the elements of the state vector at altitudes corresponding to the measurement tangent heights by 2% and taking

a forward-difference derivative using the perturbed and unperturbed measurement vectors.

As expected for limb measurements, each modeled radiance shows the greatest sensitivity to the cloud particle number density near the tangent point. This results primarily from the long path lengths through a region that contains highly-scattering particles near the tangent point. It is evident that the tangent-point sensitivity decreases at lower altitudes due to increased attenuation of solar irradiance for this quite horizontally-oriented solar zenith angle, $\theta_0 = 71°$. In addition to the peak tangent-altitude sensitivity, there is a small contribution of the state element x_i to measurements at higher tangent altitudes. This contribution results from scattering into the observer line of sight from a path segment through a higher-altitude shell that is located between the tangent point and the observer.

We see that the measurement vector shows good sensitivity to the specified state vector. Also, the spectral dependence of the limb radiance cloud sensitivity is consistent with the measured in-cloud and clear-sky spectra that were shown in Figures 2.9 and 2.10, where the in-cloud radiances increase with wavelength across the measured spectrum.

Due to the sensitivity of simulated limb radiances to the assumed surface albedo, the retrieved cloud extinction is also closely coupled to this value. As a result, the surface albedo must be retrieved concurrently to the ice cloud extinction profile. The technique used to estimate the albedo is now discussed.

7.2.4 Surface Albedo Retrieval

Surface albedo retrievals for OSIRIS scans are performed in a simple manner in both the presence and absence of cloud light-scattering properties. Since the Wood's anomalies in the OS absolute calibration are extremely small near 675 nm, and since this wavelength is sufficiently far from the centre of the Chappuis O_3 absorption band, radiances at this wavelength give a highly-sensitive measure of surface albedo from high-altitude exposures.

The surface albedo is estimated by modeling the 675 nm radiance at a cloud- and aerosol-free reference altitude of 40 km for several values of surface albedo that span the range between $a = 0$ and $a = 1$. If the measured radiance falls within this range of values, then the albedo is found by linearly interpolation to the observed radiance. Once the albedo at 675 nm is calculated, this reference value is used to scale the wavelength-dependent albedo across the spectrum.

This procedure is used in the following discussion to retrieve the values of effective surface albedo before and after the retrieval of cloud optical properties.

7.2.5 Cloud extinction retrievals from OSIRIS scans

Since the radiance from OSIRIS at wavelengths near 750 nm is coupled to the surface albedo, the stratospheric aerosol amount, and to any cloud scattering properties, an iterative solution that adjusts each of these parameters to changes in the others is required to retrieve these properties.

The retrieval process proceeds as follows. First, the surface albedo is estimated using the technique just described when only the a priori estimates of cloud and aerosol extinction are in place. Next, the stratospheric aerosol extinction profile is retrieved. Following this, the cloud extinction profile is retrieved, and further the surface albedo is again retrieved, with the model having fixed the cloud and aerosol extinction profiles to their retrieved values.

To retrieve the tropospheric cirrus cloud extinction profile, we retrieve sulphate aerosol extinction only within the stratosphere. Since the measurements of interest for SVC predominantly occur in the tropics, we use as a demarcation between the two regions the *potential temperature tropopause*, $\Theta_{380\ K}$, that is, the altitude at which a potential temperature of $\Theta(h) = 380$ K occurs. This contour provides a useful division between the characteristics of stratospheric and tropospheric air (*Holton et al.*, 1995). Below this altitude the aerosol number density is held fixed to a representative value of 1 cm^{-3}, and is tapered slightly toward lower altitudes. With the aerosol profile thus fixed in the tropopause, cirrus cloud scattering properties for a specified effective size, D_e, are assumed and retrievals of cloud extinction are performed. The retrieval

algorithm is applied to the radiances from OSIRIS scans in which clouds were detected using the criteria defined in equation (2.4). For these retrievals, the a priori cloud extinction profile is fixed to be a cloud distributed from 10 km up to the potential temperature tropopause with total optical thickness $\tau = 0.03$.

The profiles of retrieved extinctions and measurement vectors for both the stratosphere (sulphate aerosols) and UTLS (cirrus cloud) regions for a very thin cloud are shown in Figure 7.3. It should be noted that for the figures in this chapter the extinction, k, is expressed in units of km^{-1} rather than cm^{-1} due to the measurement length scale. As well, the $\Theta_{380\ K}$ tropopause is shown for reference in subsequent figures.

In the extinction profiles shown in Figures 7.3a and 7.3c, the a priori estimates are shown as dashed lines together with the light blue lines that indicate successive iterations toward the retrieved profile. For the retrieval vectors in Figures 7.3b and 7.3d, it can be seen that the final modeled vectors, $\mathbf{F}(\mathbf{x}^{(n)}, \tilde{b})$, which are shown as heavy blue lines, match the measured vectors very well. In the cloud measurement vector, there is a small overestimation of $\mathbf{y}$ at 14.5 km for which the cloud extinction is not sufficiently low that is typical for tangent altitudes below a strongly-scattering region. The extinction profile gives a layer approximately 2 km thick, which when integrated yields a cloud optical thickness of $\tau_c = 0.0075$, which corresponds to a subvisual cirrus cloud according to the standard definition of $\tau_c \leq 0.03$.

The retrieved surface albedo varies according to the state of the model atmosphere as shown in Table 7.1 for the various stages of the processing chain. With no cloud

Processing State	Estimated Surface Albedo, a
Clear-sky (aerosol only)	0.288
With a priori cloud profile	0.292
With retrieved cloud profile	0.278

Table 7.1: Retrieved surface albedo throughout cloud property retrieval processing chain.

properties in the model, the increased upwelling radiation that is actually due to the

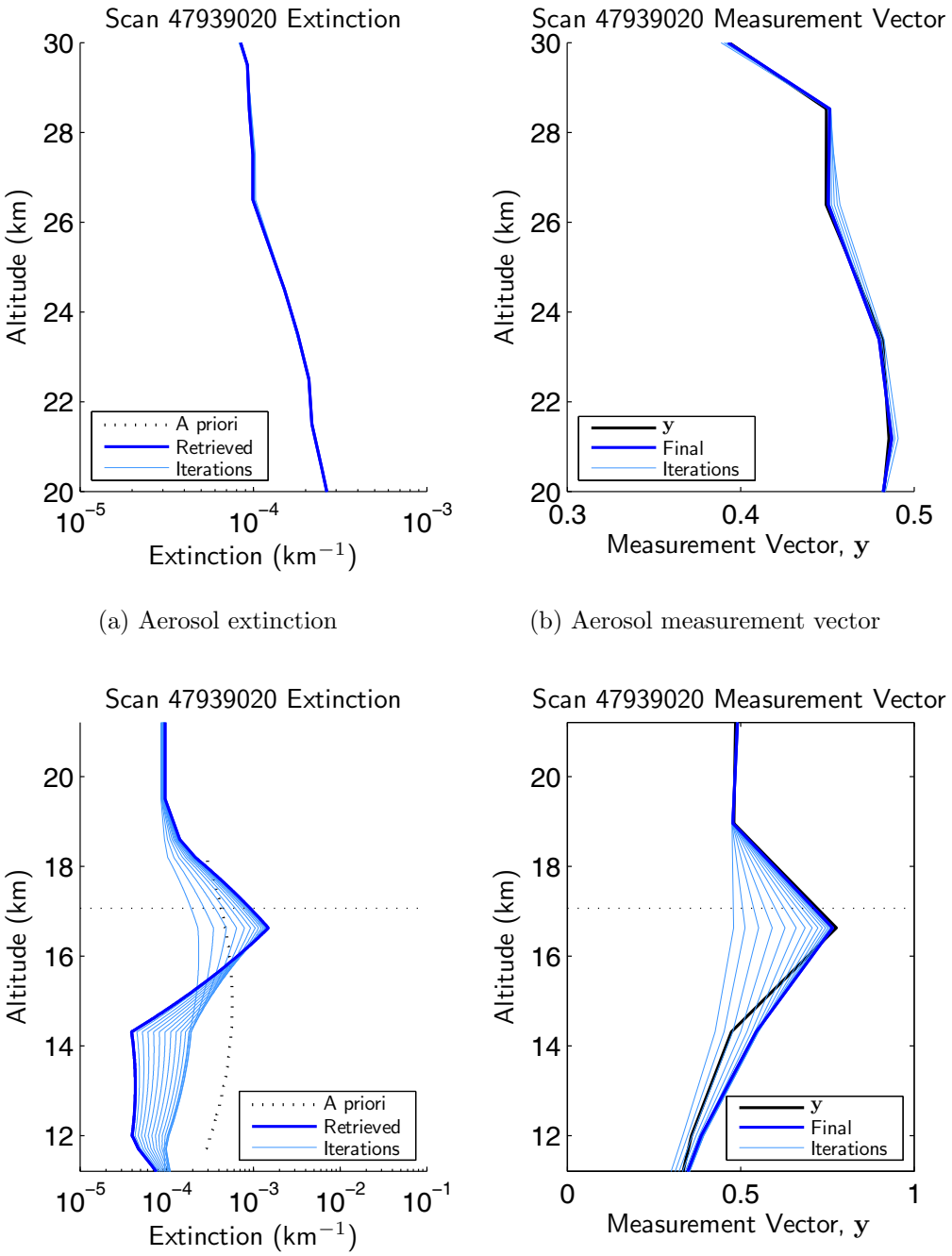

(a) Aerosol extinction

(b) Aerosol measurement vector

(c) Cloud extinction

(d) Cloud measurement vector

Figure 7.3: Stratospheric and UTLS profiles of retrieved extinction and measurement vectors for OSIRIS scan 47939020.

presence of a cloud is falsely attributed to increased surface albedo. Accordingly, the presence of a cloud layer in the retrieval decreases the retrieved surface albedo.

7.2.6 Retrieval Performance

In the MART retrieval of the cloud extinction profile, it is found that fifteen iterations of the relaxation step, equation (7.15), are sufficient to obtain convergence and to obtain a reasonable estimate of the cloud extinction profile. In total, the processing chain with six aerosol iterations and fifteen cloud-particle iterations currently takes approximately 30 minutes for one OSIRIS scan on a desktop computer with a 2.5 GHz processor and 16 GB of RAM. While these retrievals are quite computationally intensive, they are very beneficial in quantifying the cloud properties and their effect on trace gas retrievals, which we now discuss.

7.3 Trace Gas Retrieval Sensitivity

One motivating factor for cloud optical property retrievals is the need to quantify the uncertainty in other trace gas retrievals due to thin clouds that affect the measured radiances. Since a full statistical analysis of this sensitivity is beyond the scope of this thesis, we investigate the effect on the retrieved aerosol and ozone profiles for an OSIRIS scan that contains a subvisual cirrus cloud.

7.3.1 Aerosol Extinction Sensitivity

Stratospheric sulphate aerosols are retrieved from OSIRIS measurements using the same retrieval vector that is used to retrieve cirrus cloud properties. Since the radiances at these wavelengths are coupled to scattering by clouds at low altitudes, the OSIRIS aerosol extinction profile is sensitive to the presence of cloud properties in the retrieval algorithm.

We illustrate the difference in retrieved extinctions in Figure 7.4. When cloud properties are absent from the model, the retrieval attempts to fit the cloud-scattering region with aerosol properties, which is seen at altitudes below 19 km in Figure 7.4a. When cloud properties are used in the model, the aerosol profile within the cloud region is held fixed as described in Section 7.2.5, which is indicated by the dotted

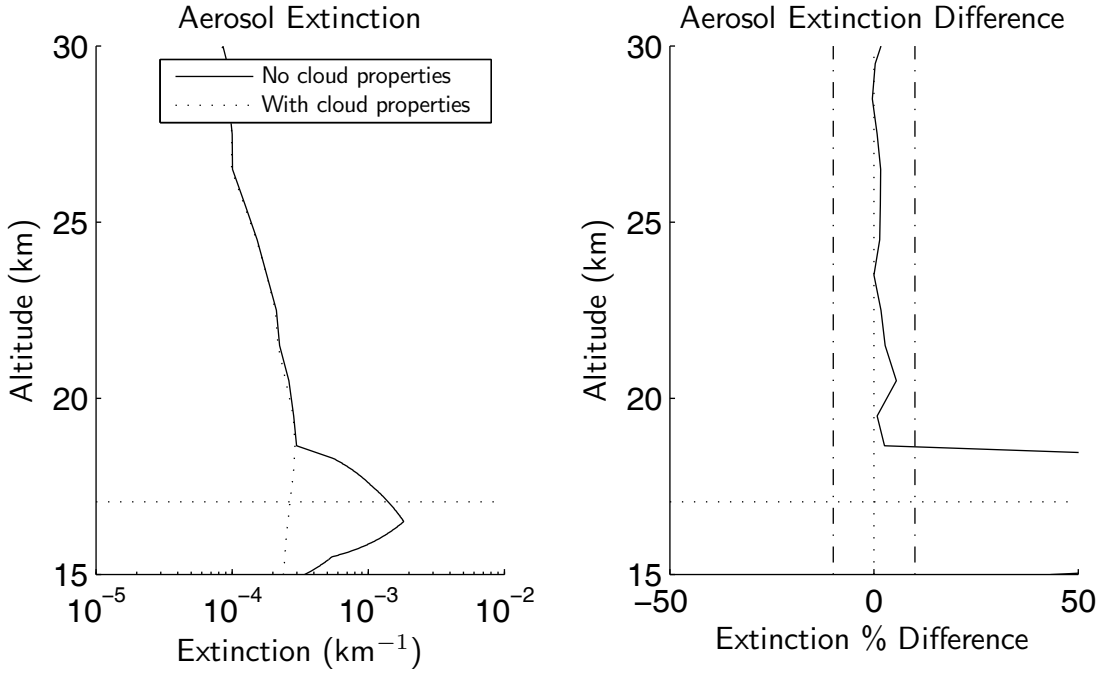

(a) Aerosol extinction

(b) Aerosol extinction difference

Figure 7.4: Difference in retrieved aerosol extinction, scan 47939020. Vertical bars indicate 10% error range.

line in the cloud region in Figure 7.4a. The extinction percent difference in Figure 7.4b, shown with respect to the profile that is retrieved together with cloud properties, shows that the retrieved stratospheric aerosol profile is typically biased to high values by several percent throughout its peak concentration. When cloud properties are absent from the model, the additional radiance signal that is actually due to cloud scattering at lower altitudes is falsely attributed to stratospheric aerosols, which has the effect of slightly raising the retrieved number density.

Since the scan that was shown in this example contains a very optically thin cloud, with retrieved cloud optical thickness $\tau_c \sim 0.01$, the aerosol extinction is only biased by approximately 2%. We expect that this is a typical offset when subvisual cirrus clouds are present. For more optically thick clouds, we expect that this error will increase by several percent throughout the peak concentration of the aerosol layer.

7.3.2 Ozone Retrieval Sensitivity

The presence of cirrus optical properties in the radiative transfer model will affect retrievals of ozone in a similar fashion due to enhanced radiance at longer wavelengths. The enhanced long-wavelength radiances that is attributable to cloud scattering affects the single ozone measurement vector that is most significant to retrievals below 25 km (*Degenstein et al.*, 2009). The effect of upper-tropospheric clouds on the determination of the ozone amount is the primary focus of this section, rather than retrieval of the in-cloud ozone amount. Thus we focus primarily on the effects of retrieved ozone at altitudes above the cloud top.

Retrievals of ozone from OSIRIS radiances at altitudes above approximately 27 km are performed using ultraviolet wavelengths and are not significantly affected by this work, however the measurement vector for lower-altitude ozone retrievals uses the amount of absorption within the Chappuis band between 540 nm and 680 nm. A measurement vector called a *Chappuis triplet* is used that has the form

$$y_{jk} = \log\left(\frac{\sqrt{\tilde{I}(h_j, \lambda_{\mathrm{ref}_1})\,\tilde{I}(h_j, \lambda_{\mathrm{ref}_2})}}{\tilde{I}(h_j, \lambda_{\mathrm{abs}})}\right), \tag{7.20}$$

where the radiances, $\tilde{I}$, are each normalized at an altitude of approximately 40 km. The reference wavelengths, $\lambda_{\mathrm{ref}_1} = 544$ nm and $\lambda_{\mathrm{ref}_2} = 679$ nm, are chosen to lie on the outer limits of the Chappuis absorption band, and $\lambda_{\mathrm{abs}} = 602$ nm lies near the peak absorption of the band. The construction of the Chappuis triplet from normalized radiances at several tangent altitudes is illustrated in Figure 7.5a. Since the measured radiance at the peak absorption wavelength λ_{abs} becomes small relative to the reference wavelengths as the ozone number density increases, the Chappuis vector is composed such that the value of the vector – which corresponds roughly to the length of the vertical lines in the figure – increases with ozone number density. This is shown in Figure 7.5a where the size of y_{jk} is the greatest near 24 km, which lies near the peak ozone number density. In Figure 7.5b the height variation of the Chappuis triplet is shown together with the ultraviolet O_3 measurement vectors.

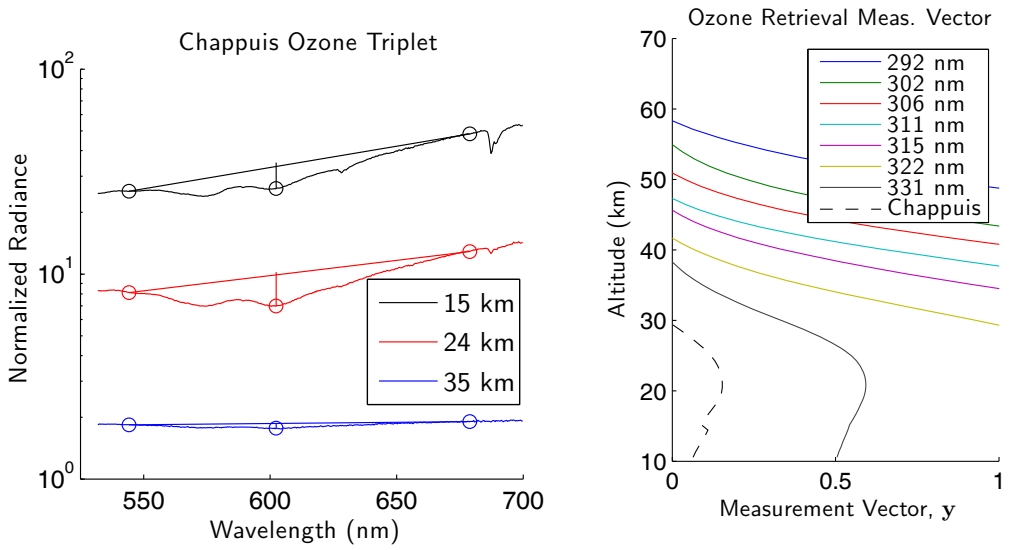

(a) O_3 Chappuis triplet illustration

(b) O_3 measurement vector profiles

Figure 7.5: Measurement vectors used for retrievals of ozone from OSIRIS measurements.

The effect of very thin cirrus clouds on retrieved ozone concentrations is shown in Figure 7.6, where the retrieved ozone profile is shown both for the operational OSIRIS O_3 retrieval, for which no cloud properties are included in the forward model, and when cloud scattering with assumed particle size $D_e = 50$ μm is implemented.

In general, lower-altitude clouds increase the limb radiance at higher altitudes due to their nature as a partially-reflecting surface. Even for thin clouds an increase in upwelling radiance all wavelengths – including at λ_{abs} at the center of the Chappuis band – occurs that can affect the retrieved ozone amounts. In the absence of cloud-scattering properties in the radiative transfer model, this increased radiance is attributed to a slightly lower amount of ozone, which biases the retrieved ozone to low values, as seen at the altitudes below the tropopause in Figure 7.6a. The positive differences between 18 km and 22 km are likely due to differences in the radiative transfer model configuration between the two retrievals and are likely not significant, however a small positive bias on the order of 1 % has been seen in previous studies of thin cloud effects on lower-stratospheric ozone from limb observations (*Sonkaew et al.*, 2009). The differences in ozone for the measurement shown in Figure 7.6b

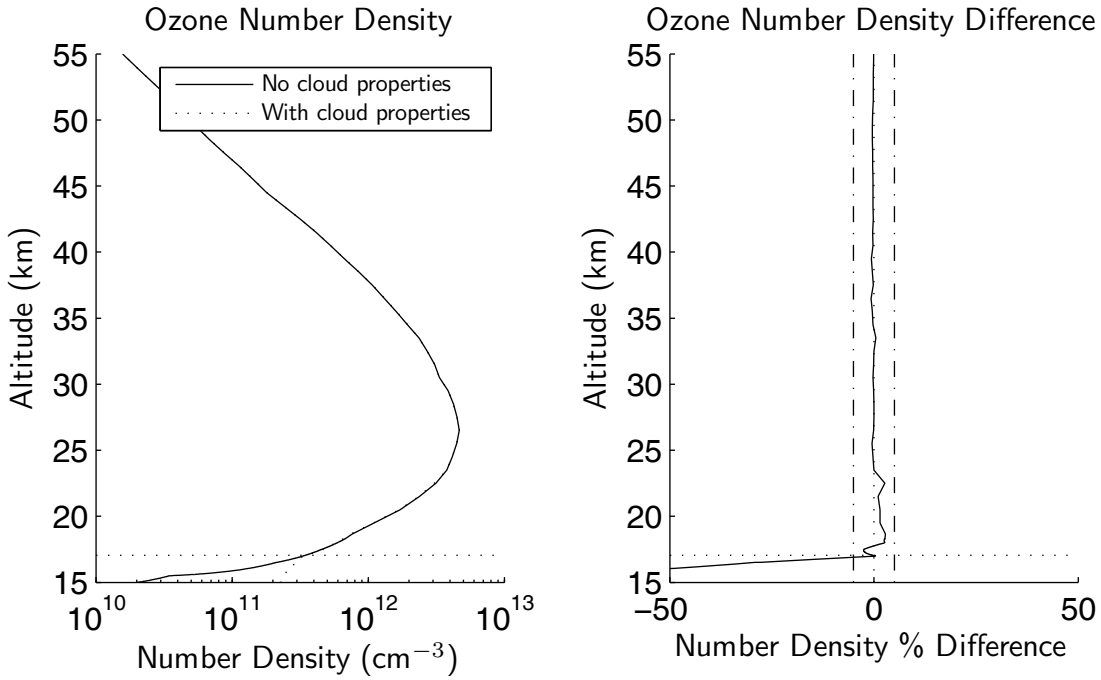

(a) Retrieved O_3 number densities

(b) Difference in retrieved O_3

Figure 7.6: Difference in retrieved ozone number density. Vertical bars indicate 5% error range.

are consistent with the work just cited, in which a much more in-depth study of the cloud sensitivity of ozone retrieved from a limb-viewing platform is performed.

Thus when ozone profiles are retrieved in the presence of thin cirrus clouds with no account of cloud scattering properties, the retrieved ozone at low altitudes is biased to low values. For subvisual cirrus clouds this bias is in the range of several percent and increases with cloud optical thickness.

7.4 Sensitivity Analysis

We now investigate the sensitivity of the retrieved cirrus cloud extinction profile to several auxiliary model parameters. For these sensitivity studies, we consider the variation to the cloud extinction profile that was retrieved in Section 7.2.5. Since both the surface albedo and the assumed effective particle size have the effect of shifting the limb radiance at long wavelengths, we study their effect on the accuracy

of cloud extinction retrievals.

7.4.1 Sensitivity to Surface Albedo

To investigate the sensitivity of retrieved cloud extinction to surface albedo, we consider the change in the retrieved extinction profile for varying values of surface albedo. For this sensitivity study, we consider a wavelength-independent albedo, which is a reasonable assumption since the parameterized albedos used in this work vary slowly with wavelength between 470 nm and 750 nm, as shown in Figure 6.11.

As a base case, the extinction profile is retrieved using the average planetary albedo of $a = 0.3$. To test the sensitivity, the assumed surface albedo in the retrieval is then set alternately to $a = 0.2$ and to $a = 0.4$ for separate retrievals. This variability of surface albedo gives a range of uncertainty in surface albedo that is quite large for measurements that occur above a well-defined surface type with variable cloud loading at lower altitudes.

The retrieved extinction profiles and percent differences in the retrieved extinction are shown in Figure 7.7. When a smaller value of surface albedo is used, the extinction profile throughout the cloud region is higher by a factor of approximately 15%, as shown in Figure 7.7b. In this case, because the assumed surface albedo is lower, the additional radiance is attributed to a slightly increased amount of cloud scattering. When a larger value of surface albedo is used, the opposite effect occurs, and the retrieved extinction is lower by a factor of approximately 10%. This sensitivity is shown in Table 7.2 in terms of the retrieved cloud optical thickness.

Assumed a	Retrieved $\tau_{c,\mathrm{ret}}$
0.2	0.0084
0.3	0.0075
0.4	0.0067

Table 7.2: Change in retrieved cloud optical thickness for varying surface albedo.

From these results, we expect that the retrieved cloud optical thickness varies by at most 25% depending on the accuracy of the surface albedo, although the uncertainty

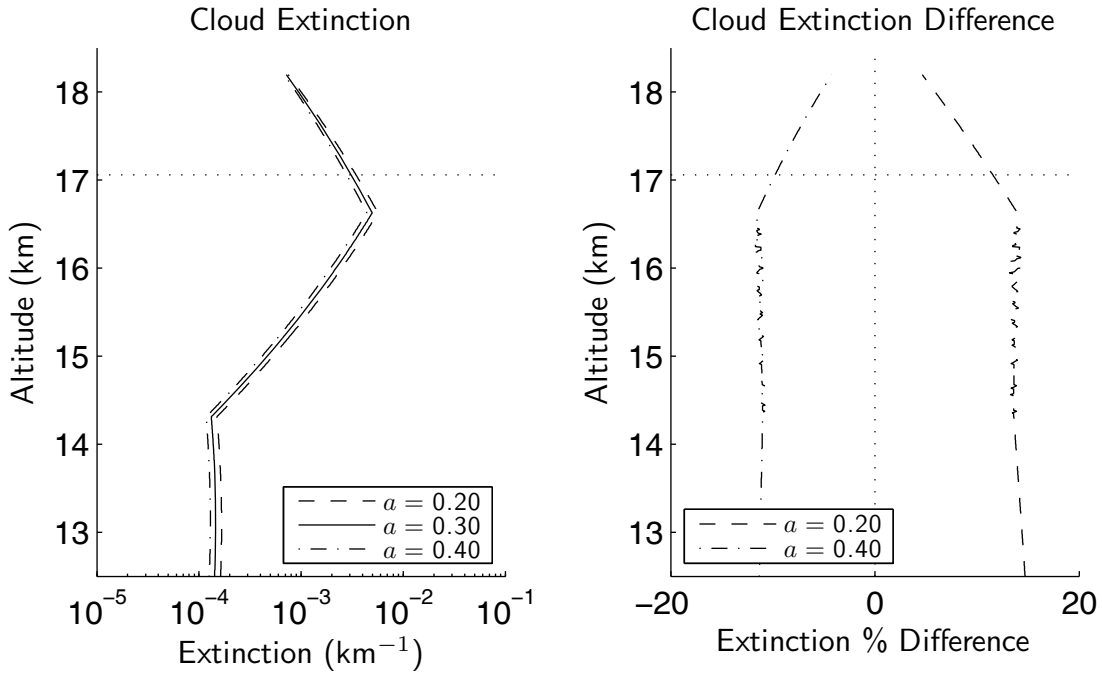

(a) Retrieved cirrus extinctions

(b) Difference in retrieved extinctions

Figure 7.7: Retrieved cirrus extinction for varying surface albedo, scan 47939020.

in the assumed surface albedo used for this study is larger than that obtained from the retrieval technique described in Section 7.2.4.

7.4.2 Sensitivity to Cloud Effective Particle Size

Since retrievals of the cloud extinction profile done in this work first assume an effective particle size, the sensitivity to the particle size is investigated similarly to the albedo sensitivity by studying the change in the retrieved extinction when different effective particle sizes are assumed.

Since the retrieved extinction depends on the scattering cross section of the assumed effective particle size, we show for reference the variation of scattering cross section with effective particle size from the database of *Baum et al.* (2005a) in Figure 7.8. The scattering cross sections are shown for the two wavelengths used in the measurement vector. The primary variation in scattering cross section occurs across effective size, with no significant difference between the two wavelengths. The

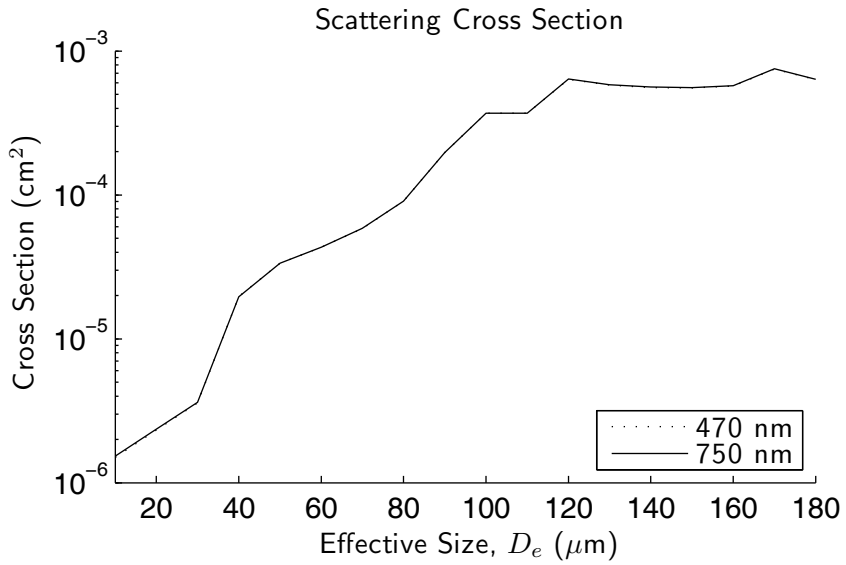

Figure 7.8: Cirrus database scattering cross section variation with ice crystal effective size.

structure superposed on the increasing trend in this curve is primarily due to the change in crystal habit distributions with crystal size as described in Section 4.3. Since the cross sections change quite rapidly below 40 μm, only effective sizes greater than $D_e > 30$ μm are used for retrievals in order to lower the sensitivity to effective particle size.

To study the effect of assumed particle size on the retrieved extinction, we retrieve the extinction profile from the same OSIRIS scan, but we assume effective particle sizes of 40 μm and 60 μm to perform the retrievals. The relative difference in the retrieved profile when these sizes are used, when compared to the retrieved profile obtained when using the $D_e = 50$ μm is used, gives an indication of the sensitivity to the assumed particle size.

The retrieved cloud extinctions and relative differences in extinction are shown in Figure 7.9. When a smaller effective particle size is assumed, the scattering cross section is smaller, and a larger number of cloud particles are used within the model to obtain the same modeled radiance. In this case, the retrieved extinction profile is higher by a factor of up to 10%. When a larger particle size is assumed, the larger scattering cross section results in a smaller retrieved cloud particle number density

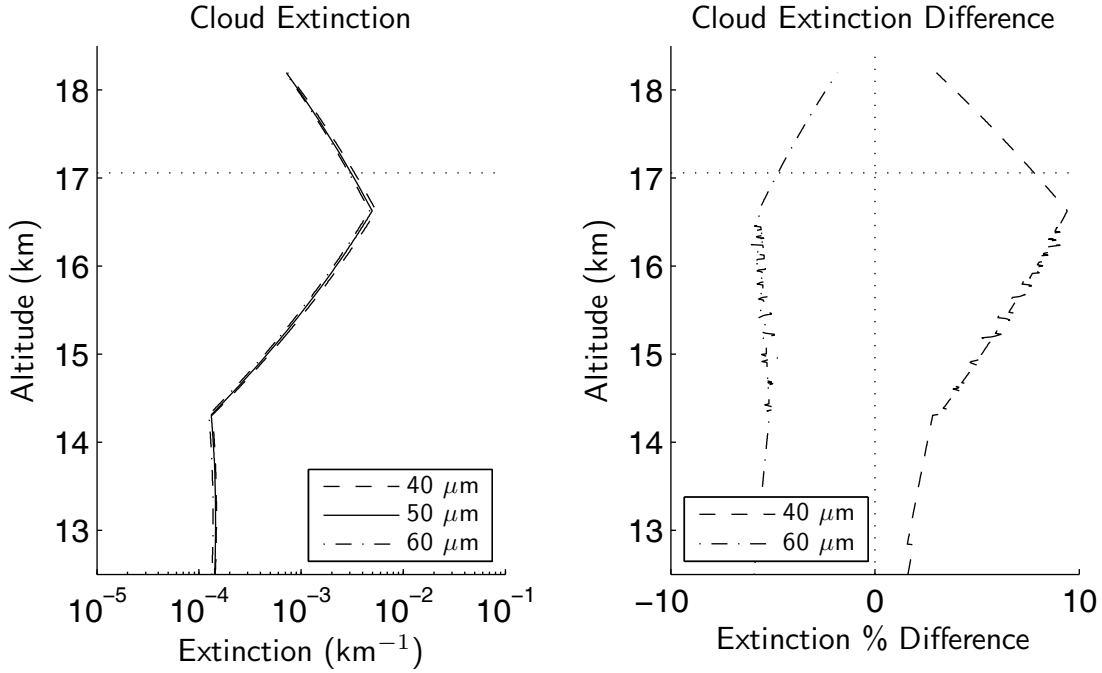

(a) Retrieved cirrus extinctions

(b) Difference in retrieved extinctions

Figure 7.9: Retrieved cirrus extinction for varying assumed particle size, scan 47626029.

such that the extinction profile is smaller by at most 5%. The corresponding retrieved optical thicknesses are listed in Table 7.3.

Assumed D_e	Retrieved $\tau_{c,\mathrm{ret}}$
40 μm	0.0080
50 μm	0.0075
60 μm	0.0071

Table 7.3: Change in retrieved cloud optical thickness for varying effective cloud particle size.

Since the extinction retrieval is somewhat sensitive to the assumed effective size, comparisons between the measured and modeled spectra are done to obtain an estimate of the best-fit effective size. The spectra modeled with the retrieved extinction profiles for each of the three assumed particle sizes are shown in Figure 7.10 together with the percent difference in modeled radiance with respect to the measured

spectrum. In this figure, the retrieved extinction profile with $D_e = 40$ μm gives an

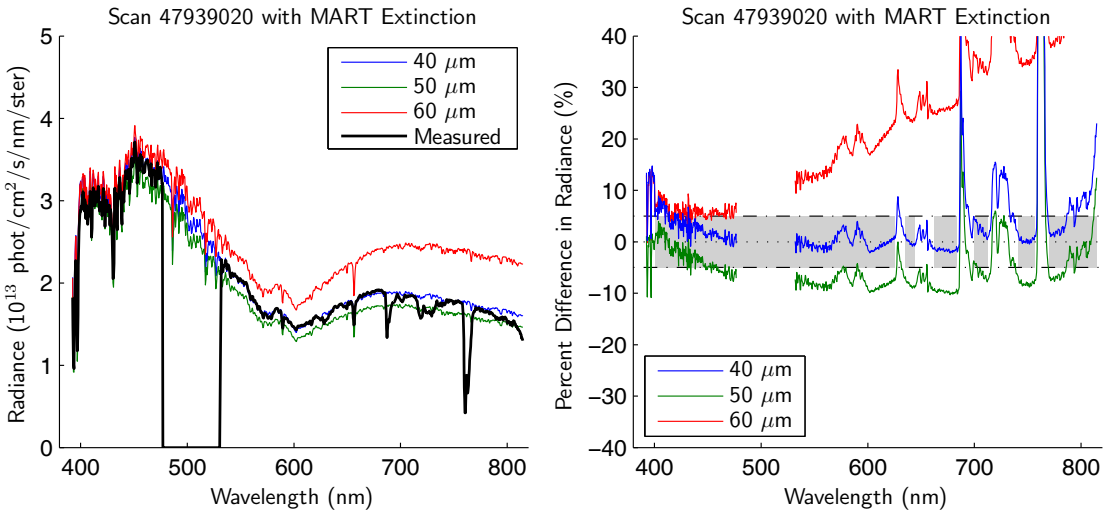

(a) Spectral radiances

(b) Radiance percent difference

Figure 7.10: In-cloud radiances modeled with retrieved extinction profile for several assumed particle sizes.

excellent match across the spectrum with percent difference in radiance of less than 3%. It is also seen that the radiances from the retrieved extinction with $D_e = 60$ μm overestimate the measured radiances, and the radiances for $D_e = 50$ μm slightly underestimate the in-cloud radiance.

For each of these effective sizes the computed vector, $\mathbf{F}(\mathbf{x}^{(n)}, \tilde{b})$, agrees very well with the measured vector, $\mathbf{y}$, throughout the region of interest, as shown in Figure 7.11, where the final computed vectors for each effective size is shown together with $\mathbf{y}$. It is seen in this figure that the simulated measurement vectors for the three effective sizes all overlie each other, but that the extinction profiles that generate them produce significantly different agreement with the measured in-cloud spectrum. Due to the differing scattering behaviours of the three particle sizes, only the $D_e = 40$ μm extinction profile is able to model accurately the measured spectrum.

From this study, it is clear that re-modeling the measured radiances across the spectrum is a key element in the optical property retrieval process. For the scan that we have been studying, it has been shown that modeling the observed cloud with

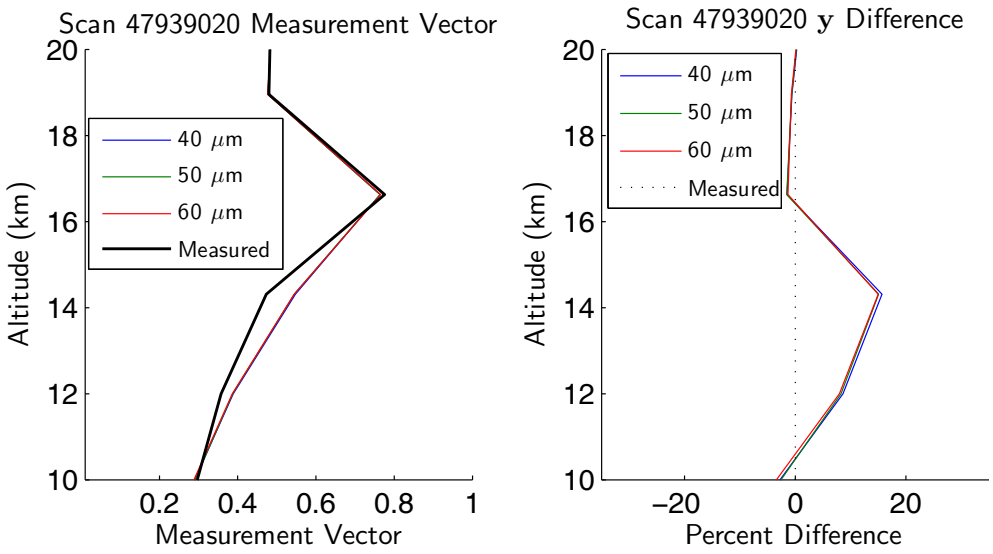

(a) Simulated measurement vectors (b) Differences from measuremed vector

Figure 7.11: Measurement vectors for the assumed effective particle sizes.

effective size $D_e = 40$ μm and optical thickness $\tau_c = 0.008$ gives excellent agreement with the measured in-cloud spectrum. We now perform comparisons of the retrieved cloud extinction profiles from OSIRIS with coincident measurements from another remote-sensing instrument.

7.5 SAGE II Comparisons

Coincident measurements of SVC that have been made with the SAGE II solar occultation instrument are identified through selecting appropriate coincidence criteria that allow for comparison of the retrieved extinction profiles. For this study, measurements are considered to be coincident if the measurements occurred within a distance of at most 250 km and 5° latitude, and if they were made within 3 hours of each other. These coincidence criteria are well within the typical lifetime and horizontal extents of subvisual cirrus clouds.

Thirty OSIRIS scans between 2002 and 2005 have been identified as coincident with SAGE II measurements by these criteria. The geographic locations and solar

illumination conditions of two typical coincident measurements are shown in Table 7.4.

Coincident Measurements				
Scan	Instrument	Time	Lat, Lon	Mean SZA & SSA
10413057	OSIRIS	16:03 Jan 21, 2003	-17.9°, 33.2°	85.0°, 101.1°
	SAGE II	16:30 Jan 21, 2003	-18.7°, 32.5°	
10424058	OSIRIS	09:46 Jan 22, 2003	-15.0°, 127.0°	85.6°, 101.1°
	SAGE II	09:59 Jan 22, 2003	-15.0°, 129.0°	

Table 7.4: Location and solar conditions for SAGE II-OSIRIS coincident measurement locations.

SAGE II detections of SVC are derived from the measured extinction profile at 1020 nm (*Wang et al.*, 1996), so extinction comparisons are best done at this wavelength. Since the measurement vector used in this work uses 750 nm radiances, the retrieved cloud extinction profile is scaled by assuming a constant number density to provide an equivalent extinction at 1020 nm. OSIRIS extinctions are compared with SAGE II extinctions by taking the sum of the retrieved cloud and aerosol extinctions at 750 nm and converting the sum to 1020 nm extinction.

The total OSIRIS extinction is shown together with the SAGE II extinction for two coincident scans in Figure 7.12. In this figure the operational OSIRIS aerosol extinction profiles, which are retrieved by assuming only stratospheric aerosol properties, are shown for reference. It is clear from the extinction values below 20 km that including cloud scattering properties in the OSIRIS retrieval gives much better agreement with the SAGE II extinction product.

The retrieved ozone from these scans is shown in the same comparative way in Figures 7.13 and 7.14. In these figures, it is seen that the inclusion of cloud properties in the OSIRIS retrieval improves the comparison of the retrieved ozone profile with the SAGE II measurement. There is, however, a significant decrease in the SAGE II profile that occurs near the tropopause in both coincident scans. Although the SAGE II aerosol retrieval uses a much more direct measurement of the extinction profile

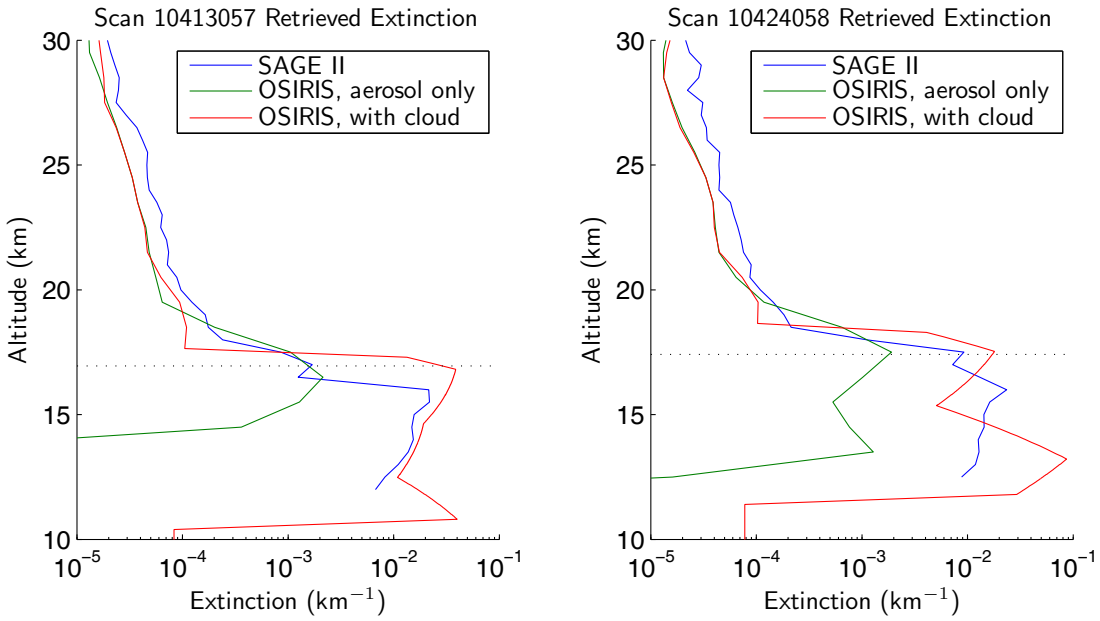

(a) OSIRIS scan 10413057

(b) OSIRIS scan 10424058

Figure 7.12: Retrieved cloud and aerosol extinction at 1020 nm for coincident SAGE II measurements.

than OSIRIS, the optical properties used to derive the particulate extinction assumes aerosol-like particles and does not account for cloud light-scattering properties. We suspect that this decrease in the SAGE II profile, consistent with the findings of Section 7.3.2 and with other studies, is a falsely negative-biased value that results from the presence of a high-altitude ice cloud.

It should be noted that, in the operational OSIRIS ozone retrievals, the presence of a tropospheric cloud is automatically flagged by a criterion similar to equation (2.4). The cloud-top altitude is used to indicate the lower bound beyond which the retrieved ozone profile is invalid so that the biases in retrieved ozone that have been shown in this section are not included in the operational data product.

7.6 Conclusion

The purpose of this chapter was to demonstrate the possibility of retrieving the optical properties of subvisual and thin cirrus clouds from OSIRIS. We have shown

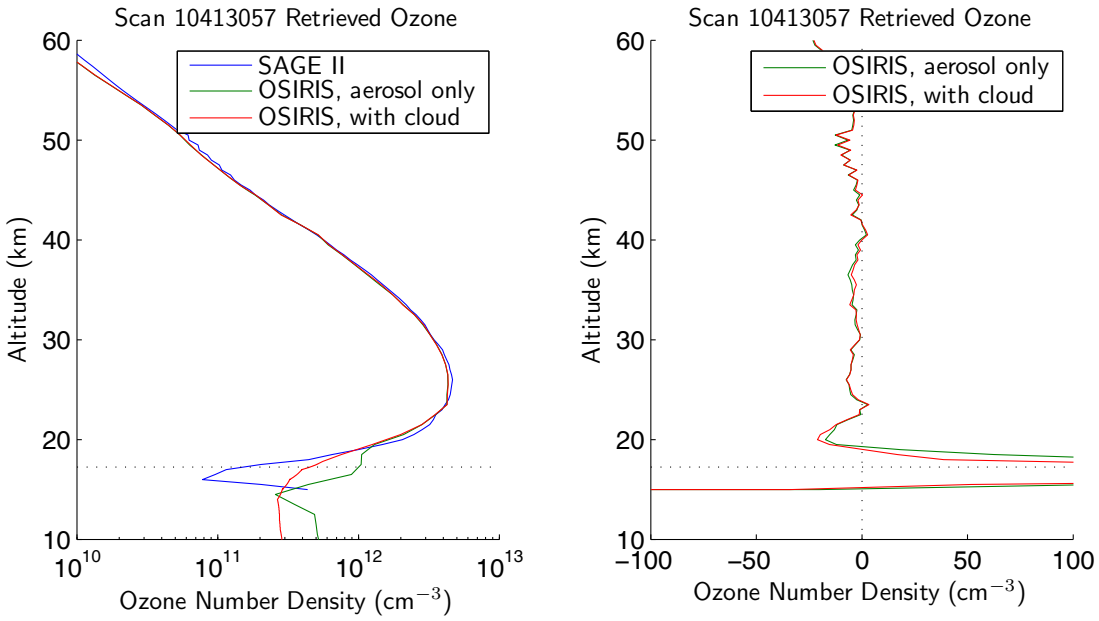

(a) O_3 number density

(b) Number density difference

Figure 7.13: Retrieved ozone number density for OSIRIS scan 10413057 and coincident SAGE II measurements.

that we are able to estimate cloud optical properties when the MART algorithm uses the SASKTRAN model with ice crystal scattering properties.

Comparisons of the retrieved extinction profile with coincident measurements by SAGE II show very good agreement. It is also clear that the retrieved profiles of both aerosol extinction and ozone concentration from OSIRIS agree much better with the SAGE II profiles when ice cloud scattering properties are included in the MART retrieval.

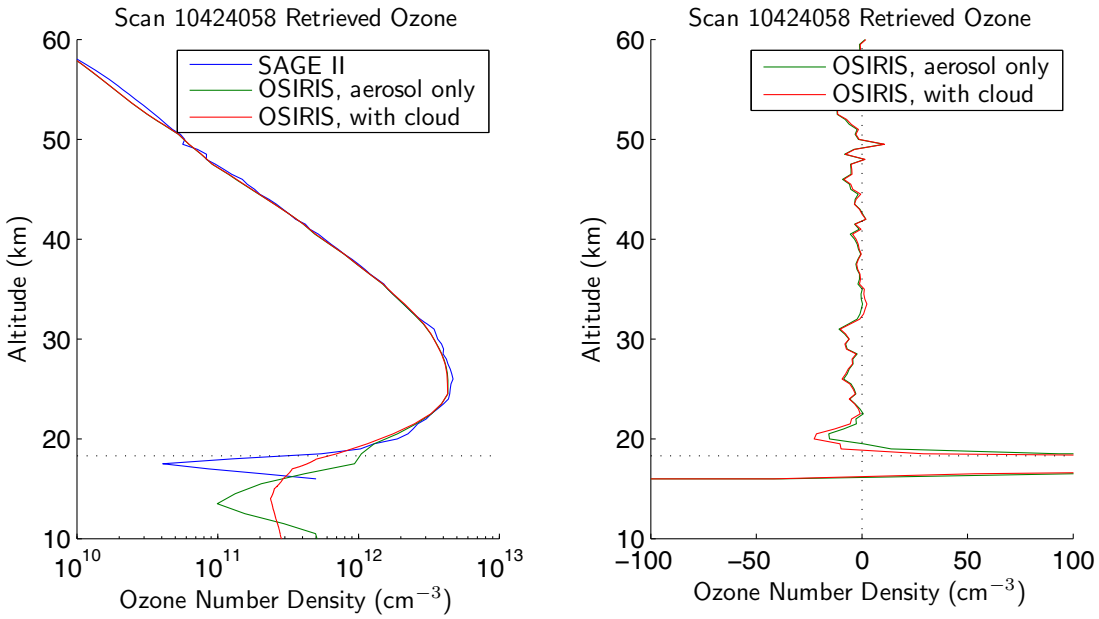

(a) O_3 number density

(b) Number density difference

Figure 7.14: Retrieved ozone number density for OSIRIS scan 10424058 and coincident SAGE II measurements.

Chapter 8

Summary and Outlook

The purpose of this work was to demonstrate the ability to retrieve thin cirrus optical properties from a limb-viewing satellite instrument. This was achieved in part by extending the capabilities of a radiative transfer model to model accurately the observations of scattered sunlight made by a limb-viewing instrument in the presence of thin cirrus clouds.

Since the OSIRIS instrument frequently displays upper-tropospheric radiance enhancements that appear to be caused by cirrus clouds, based both on location of occurrence and on light-scattering characteristics, a database of cloud detections was compiled. The resulting geographical distributions agree very well with cirrus cloud frequency distributions from other instruments.

In order to model and estimate the properties of these clouds, it was necessary to incorporate the scattering properties of ice crystals over visible and near-infrared wavelengths into a suitable radiative transfer model. For this purpose, dynamically-linked libraries (DLLs) from two first-principles light-scattering algorithms were built and incorporated into the SASKTRAN radiative transfer model. Scattering properties from the T-matrix and discrete dipole approximation techniques were incorporated into SASKTRAN and are used for computing the light scattering from clouds containing ice crystals with effective size up to 1 μm. Since it becomes numerically prohibitive to perform these computations for larger particles, a database of ice-crystal scattering properties from in-situ measurements was built into SASKTRAN.

These scattering properties allow for scattering computations over a large range of particle sizes – from 10 μm to 180 μm – for all OSIRIS wavelengths above 400 nm.

It was found that the scattering properties for ice crystals in the database required several modifications to the SASKTRAN radiative transfer model. First, since for scattering particles that are much larger than the wavelength of light there is a very large diffraction peak, the numerical scattering integral in SASKTRAN required modification. This was accomplished partly through the development of a novel photon conservation technique that quantifies the degree of inaccuracy in the scattering integral. In addition to this, the transport approximation – in which light scattered through a very small angle about the forward direction is treated as effectively unscattered – was implemented in SASKTRAN. It was found that the errors in the scattering integral evaluation were significantly reduced by using these techniques.

Modifications were also required to the solution space over which the diffuse radiance field is computed in SASKTRAN. In a limb-scattering geometry, the radiance measurements are dominated by the properties of the atmosphere near the tangent point due to the very long path lengths of the observer line of sight through this region. When cirrus clouds exist near the tangent point of the measurement, the tangent-point effect is compounded by the presence of scattering particles with cross sections several orders of magnitude larger than the surrounding molecular and aerosol constituents. The result is that the spherical layers of the model atmosphere, which nominally are spaced by 1 km, are too coarse to capture the large optical depths in these segments due to scattering. While this would not present a problem with large absorption optical depths, scattering operations require that the scattering events be resolved within the solution layers of the model atmosphere.

The necessary tradeoff between numerical accuracy and computational effort was achieved by configuring the ray-tracing shell spacing according to the extinction profile down to a minimum shell spacing of 10 m. It was found that an in-cloud diffuse point height spacing of 40 m was sufficient to ensure precision in modeled in-cloud radiances to better than 0.1%, and that the use of one diffuse profile was sufficient to compute in-cloud modeled radiances to within 1% precision for solar zenith angles less

than 80°. With these modifications, the SASKTRAN model is able to model scattering by clouds with optical thicknesses up to $\tau_c = 0.6$. In addition to these configurations, the surface albedo within SASKTRAN was made to vary with wavelength by incorporating a land-sea mask with automated selection of the wavelength-dependent albedo for the appropriate surface type. It was demonstrated that SASKTRAN can now model the observed in-cloud radiance from OSIRIS to better than 3% accuracy at all wavelengths across the spectrum.

The SASKTRAN model was used with a multiplicative algebraic reconstruction technique to retrieve the optical properties of cirrus clouds detected with OSIRIS. When an effective cloud particle size is assumed, this technique retrieves the extinction profile for the radiances from an OSIRIS limb scan. It was demonstrated that the retrieval technique is able to obtain an extinction profile that gives agreement with the measured in-cloud radiance to better than 5% at all wavelengths across the measured spectrum.

The sensitivity of this retrieval to the cloud particle size and the assumed surface albedo was briefly investigated. It was found that the retrieved cloud optical thickness is sensitive by approximately 15% to the assumed particle size, and by at most 25% to uncertainty in the assumed surface albedo. While determination of cloud effective particle size is beyond the scope of this work, it has been seen that the use of forward modeling with the retrieved extinctions from several particle sizes is useful in identifying particle sizes that accurately replicate the measurements.

The effect of including cloud properties in OSIRIS retrievals of ozone and stratospheric aerosol were investigated. It was found that, for very thin cirrus clouds, neglecting cloud optical properties in aerosol retrievals biases the retrieved number density in the stratosphere to positive values by several percent. Since the values of aerosol extinction below the tropopause are not of interest to most aerosol studies, this bias is the dominant effect of cloud properties on the operational OSIRIS aerosol product. For ozone retrievals, it was found that neglecting cloud properties in the retrieval biases the number density by several percent to smaller values below 25 km due to increased upwelling radiance that is falsely attributed to low ozone number

densities.

Some preliminary comparisons were done between extinction profiles retrieved from OSIRIS and coincident measurements from the SAGE II solar occultation instrument. It was found that both the retrieved extinction and ozone profiles from OSIRIS agree better with SAGE II when cloud properties are included.

There are several directions that could be taken with this work in the future. The first would be to apply the extinction retrieval that has been developed in this work to all cirrus clouds detected by OSIRIS. This would provide an eleven-year database of SVC detections, which would be of significant use to the remote-sensing community in quantifying retrieval errors due to these clouds. As well, a database of subvisual cirrus cloud occurrences and optical properties is of high value for current cloud parameterizations in GCMs.

With available resources, it would be highly advantageous to incorporate the cloud property retrieval into operational OSIRIS retrievals of ozone and stratospheric aerosols. Although a full inclusion of cloud scattering properties at the current stage is computationally prohibitive, it is possible to improve OSIRIS aerosol extinction and ozone number density products by accounting for cloud optical properties through parameterizations of cloud effects on the respective retrieval vectors.

It would be beneficial for OSIRIS retrievals in general, but especially for the study of cloud effects on OSIRIS measurements, to implement three-dimensional spatial solutions in SASKTRAN. Not only would this allow for better computation of the radiance field for near-terminator orbits in which there are sharp gradients in photochemically-active trace gases, but also the effects of horizontal non-homogeneity of cloud number densities could be studied with such a capability.

Finally, due to the computational limits involved in a successive-orders model in which the resource demands depend heavily on the number of layers in the model atmosphere, it would be highly advantageous to embed an adding-doubling radiative transfer model into SASKTRAN to simulate the effects of more optically thick cloud layers. Work of this type has been done by *van Diedenhoven et al.* (2006) in a plane parallel radiative transfer model, but to the author's knowledge this work has not

been done in a fully-spherical geometry.

It is the author's opinion that the work presented in this thesis gives a useful technique for estimating cloud properties from measurements of limb-scattered sunlight. Further, this work forms a foundation for full cloud property retrievals from limb-scattering measurements and for accurate estimation of errors in retrieved trace gas profiles that result from the presence of clouds.

Bibliography

Alley, R., T. Berntsen, N. Bindoff, Z. Chen, A. Chidthaisong, P. Friedlingstein, J. Gregory, G. Hegerl, M. Heimann, B. Hewitson, et al. (2007), IPCC 2007: Summary for Policymakers, *Climate Change*, *446*, 1–18.

Barber, P., and C. Yeh (1975), Scattering of electromagnetic waves by arbitrarily shaped dielectric bodies, *Appl. Opt.*, *14*, 2864–2872, doi:10.1364/AO.14.002864.

Barth, C., D. Rusch, R. Thomas, G. Mount, G. Rottman, G. Thomas, R. Sanders, and G. Lawrence (1983), Solar Mesosphere Explorer: scientific objectives and results, *Geophys Res Lett*, *10*, 237–240, doi:doi:10.1029/GL010i004p00237.

Baum, B., A. Heymsfield, P. Yang, and S. Bedka (2005a), Bulk scattering properties for the remote sensing of ice clouds. Part I: Microphysical data and models, *J. Appl. Met.*, *44*, 1885–1895, doi:10.1175/JAM2308.1.

Baum, B., P. Yang, A. Heymsfield, S. Platnick, M. King, Y. Hu, and S. Bedka (2005b), Bulk scattering properties for the remote sensing of ice clouds. Part II: Narrowband models, *J. Appl. Met.*, *44*, 1896–1911, doi:10.1175/JAM2309.1.

Bohren, C., and D. Huffman (1983), *Absorption and Scattering of Light by Small Particles*, Wiley Online Library.

Bourassa, A., D. Degenstein, R. Gattinger, and E. Llewellyn (2007), Stratospheric aerosol retrieval with Optical Spectrograph and InfraRed Imaging System limb scatter measurements, *J. Geophys. Res*, *112*, D10,217, doi:10.1029/2006JD008079.

Bourassa, A., D. Degenstein, and E. Llewellyn (2008), SASKTRAN: A spherical geometry radiative transfer code for efficient estimation of limb scattered sunlight, *J. Quant. Spectr. & Rad. Trans.*, *109*, 52–73, doi:10.1016/j.jqsrt.2007.07.007.

Bourassa, A., C. McLinden, C. Sioris, S. Brohede, A. Bathgate, E. Llewellyn, and D. Degenstein (2011), Fast NO2 retrievals from Odin-OSIRIS limb scatter measurements, *Atmos. Meas. Tech.*, *4*, 965–972, doi:10.5194/amtd-3-5499-2010.

Bovensmann, H., J. Burrows, M. Buchwitz, J. Frerick, S. Noël, V. Rozanov, K. Chance, and A. Goede (1999), SCIAMACHY: Mission objectives and measurement modes, *J. Atmos. Sci.*, *56*, 127–150, doi:10.1175/1520-0469(1999)056⟨0127:SMOAMM⟩2.0.CO;2.

Chahine, M. (1972), A general relaxation method for inverse solution of the full radiative transfer equation, *J. Atmos. Sci*, *29*, 741–747, doi:10.1175/1520-0469(1972)029⟨0741:AGRMFI⟩2.0.CO;2.

Chandrasekhar, S. (1960), *Radiative Transfer*, Dover Publications, Inc.

Cziczo, D., D. Murphy, P. Hudson, and D. Thomson (2004), Single particle measurements of the chemical composition of cirrus ice residue during CRYSTAL-FACE, *J. Geophys. Res*, *109*, D04,201, doi:10.1029/2003JD004032.

Degenstein, D., E. Llewellyn, and N. Lloyd (2003), Volume emission rate tomography from a satellite platform, *Appl. Opt.*, *42*, 1441–1450, doi:10.1364/AO.42.001441.

Degenstein, D., A. Bourassa, C. Roth, and E. Llewellyn (2009), Limb scatter ozone retrieval from 10 to 60 km using a Multiplicative Algebraic Reconstruction Technique, *Atmos. Chem. Phys*, *9*, 6521–6529, doi:10.5194/acp-9-6521-2009.

DeMott, P., D. Rogers, S. Kreidenweis, Y. Chen, C. Twohy, D. Baumgardner, A. Heymsfield, and K. Chan (1998), The role of heterogeneous freezing nucleation in upper tropospheric clouds: Inferences from SUCCESS, *Geophys. Res. Lett.*, *25*, 1387–1390, doi:10.1029/97GL03779.

Draine, B., and P. Flatau (1994), Discrete-dipole approximation for scattering calculations, *J. Opt Soc. Amer. A*, *11*, 1491–1499, doi:10.1364/JOSAA.11.001491.

Feister, U., and R. Grewe (1995), Spectral albedo measurements in the UV and visible region over different types of surfaces, *Photochem. Photobio.*, *62*, 736–744.

Flittner, D., P. Bhartia, and B. Herman (2000), O3 profiles retrieved from limb scatter measurements: Theory, *Geophys Res Lett*, *27*, 2601–2604, doi:10.1029/1999GL011343.

Froyd, K., D. Murphy, P. Lawson, D. Baumgardner, and R. Herman (2010), Aerosols that form subvisible cirrus at the tropical tropopause, *Atmos. Chem. Phys*, *10*, 209–218, doi:10.5194/acp-10-209-2010.

Fu, Q., Y. Hu, and Q. Yang (2007), Identifying the top of the tropical tropopause layer from vertical mass flux analysis and calipso lidar cloud observations, *Geophys. Res. Lett*, *34*, L14,813, doi:10.1029/2007GL030099.

Fueglistaler, S., A. Dessler, T. Dunkerton, I. Folkins, Q. Fu, and P. Mote (2009), Tropical tropopause layer, *Rev. Geophys*, *47*, RG1004, doi:10.1029/2008RG000267.

Haley, C., S. Brohede, C. Sioris, E. Griffioen, D. Murtagh, I. McDade, P. Eriksson, E. Llewellyn, A. Bazureau, and F. Goutail (2004), Retrieval of stratospheric O3 and NO2 profiles from Odin Optical Spectrograph and Infrared Imager System (OSIRIS) limb-scattered sunlight measurements, *J. Geophys. Res*, *109*, D16,303, doi:10.1029/2004JD004588.

Hansen, J. (1971), Multiple scattering of polarized light in planetary atmospheres. Part II. Sunlight reflected by terrestrial water clouds, *J. Atmos. Sci*, *28*, 1400–1426, doi:10.1175/1520-0469(1971)028⟨1400:MSOPLI⟩2.0.CO;2.

Herman, B., A. Ben-David, and K. Thome (1994), Numerical technique for solving the radiative transfer equation for a spherical shell atmosphere, *Appl. Opt.*, *33*, 1760–1770, doi:10.1364/AO.33.001760.

Heymsfield, A. (1986), Ice particles observed in a cirriform cloud at -83° C and implications for polar strotospheric clouds, *J. Atmos. Sci.*, *43*, 851–855, doi:10.1175/1520-0469(1986)043⟨0851:IPOIAC⟩2.0.CO;2.

Heymsfield, A., A. Bansemer, P. Field, S. Durden, J. Stith, J. Dye, W. Hall, and C. Grainger (2002), Observations and parameterizations of particle size distributions in deep tropical cirrus and stratiform precipitating clouds: Results from in situ observations in TRMM field campaigns, *J. Atmos. Sci.*, *59*, 3457–3491, doi:10.1175/1520-0469(2002)059⟨3457:OAPOPS⟩2.0.CO;2.

Holton, J., P. Haynes, M. McIntyre, A. Douglass, R. Rood, and L. Pfister (1995), Stratosphere-troposphere exchange, *Rev. Geophys*, *33*, 403–439, doi:10.1029/95RG02097.

Iwabuchi, H., and T. Suzuki (2009), Fast and accurate radiance calculations using truncation approximation for anisotropic scattering phase functions, *J. Quant. Spectr. & Rad. Trans.*, *110*, 1926–1939, doi:10.1016/j.jqsrt.2009.04.006.

Jensen, E., O. Toon, and D. Westphal (1994), Microphysical modeling of cirrus 1. Comparison with 1986 FIRE IFO measurements, *J. Geophys. Res.*, *99*, 10,421–10,442, doi:10.1029/93JD02334.

Jensen, E., L. Pfister, T. Bui, P. Lawson, B. Baker, Q. Mo, D. Baumgardner, E. Weinstock, J. Smith, E. Moyer, et al. (2008), Formation of large ($\sim$ 100 μm) ice crystals near the tropical tropopause, *Atmos. Chem. Phys.*, *8*, 1621–1633, doi:10.5194/acp-8-1621-2008.

Jin, Z., T. Charlock, W. Smith Jr, and K. Rutledge (2004), A parameterization of ocean surface albedo, *Geophys. Res. Lett*, *31*, L22,301, doi:10.1029/2004GL021180.

Joseph, J., W. Wiscombe, and J. A. Weinman (1976), The Delta-Eddington Approximation for Radiative Flux Transfer, *J. Atmos. Sci.*, *33*, 2452–2459, doi:10.1175/1520-0469(1976)033⟨2452:TDEAFR⟩2.0.CO;2.

Kärcher, B. (2002), Properties of subvisible cirrus clouds formed by homogeneous freezing, *Atmos. Chem. Phys.*, *2*, 357–383, doi:10.5194/acp-2-161-2002.

Kärcher, B. (2004), Cirrus clouds in the tropical tropopause layer: Role of heterogeneous ice nuclei, *Geophys. Res. Lett*, *31*, L12,101, doi:doi:10.1029/2004GL019774.

Kirkby, J., J. Curtius, J. Almeida, E. Dunne, J. Duplissy, S. Ehrhart, A. Franchin, S. Gagné, L. Ickes, et al. (2011), Role of sulphuric acid, ammonia and galactic cosmic rays in atmospheric aerosol nucleation, *Nature*, *476*, 429–433, doi:10.1038/nature10343.

Koelemeijer, R., and P. Stammes (1999), Effects of clouds on ozone column retrieval from GOME UV measurements, *J. Geophys. Res.*, *104*, 8281–8294, doi:doi:10.1029/1999JD900012.

Lawson, R., B. Baker, B. Pilson, and Q. Mo (2006), In situ observations of the microphysical properties of wave, cirrus, and anvil clouds. Part II: Cirrus clouds, *J. Atmos. Sci.*, *63*, 3186–3203, doi:10.1175/JAS3802.1.

Lawson, R., B. Pilson, B. Baker, Q. Mo, E. Jensen, L. Pfister, P. Bui, et al. (2008), Aircraft measurements of microphysical properties of subvisible cirrus in the tropical tropopause layer, *Atmos. Chem. Phys.*, *8*, 1609–1620, doi:10.5194/acp-8-1609-2008.

Liou, K. (2002), *An Introduction to Atmospheric Radiation*, Academic Press.

Llewellyn, E., N. Lloyd, D. Degenstein, R. Gattinger, S. Petelina, A. Bourassa, J. Wiensz, E. Ivanov, I. McDade, B. Solheim, J. C. McConnell, C. S. Haley, C. von Savigny, C. E. Sioris, C. A. McLinden, E. Griffioen, J. Kaminski, W. F. Evans, E. Puckrin, K. Strong, V. Wehrle, R. H. Hum, D. J. Kendall, J. Matsushita, D. P. Murtagh, S. Brohede, J. Stegman, G. Witt, G. Barnes, W. F. Payne, L. Piché, K. Smith, G. Warshaw, D. L. Deslauniers, P. Marchand, E. H. Richardson, R. A. King, I. Wevers, W. McCreath, E. Kyrölä, L. Oikarinen, G. W. Leppelmeier, H. Auvinen, G. Mégie, A. Hauchecorne, F. Lefèvre, J. de La Nöe, P. Ricaud, U. Frisk, F. Sjoberg, F. von Schéele, and L. Nordh (2004), The OSIRIS instrument on the Odin spacecraft, *Can. J. Phys*, *82*, 411–422, doi:10.1139/p04-005.

Lloyd, N. (2011), Private communication.

Lloyd, N., and E. Llewellyn (1989), Deconvolution of blurred images using photon counting statistics and maximum probability, *Can. J. Phys.*, *67*, 89–94, doi:10.1139/p89-013.

Luo, B., T. Peter, H. Wernli, S. Fueglistaler, M. Wirth, C. Kiemle, H. Flentje, V. Yushkov, V. Khattatov, V. Rudakov, et al. (2003), Ultrathin tropical tropopause clouds (UTTCs): II. Stabilization mechanisms, *Atmos. Chem. Phys.*, *3*, 1579–1597, doi:10.5194/acp-3-1093-2003.

Lynch, D., K. Sassen, D. Starr, and G. Stephens (2002), *Cirrus*, Oxford University Press, USA.

Martins, E., V. Noel, and H. Chepfer (2011), Properties of cirrus and subvisible cirrus from nighttime Cloud-Aerosol Lidar with Orthogonal Polarization (CALIOP), related to atmospheric dynamics and water vapor, *J. Geophys. Res.*, *116*, D02,208, doi:10.1029/2010JD014519.

McCartney, E. (1976), *Optics of the Atmosphere: Scattering by molecules and particles*, John Wiley and Sons.

McCormick, M. (1987), SAGE II: an overview, *Advances in space research*, *7*, 219–226.

McFarquhar, G., and A. Heymsfield (1998), The definition and significance of an effective radius for ice clouds, *J. Atmos. Sci.*, *55*, 2039–2052, doi:10.1175/1520-0469(1998)055⟨2039:TDASOA⟩2.0.CO;2.

McKellar, B., and M. Box (1981), The scaling group of the radiative transfer equation, *J. Atmos. Sci.*, *38*, 1063–1068, doi:10.1175/1520-0469(1981)038⟨1063:TSGOTR⟩2.0.CO;2.

McLinden, C., J. McConnell, E. Griffioen, and C. McElroy (2002), A vector radiative-transfer model for the Odin/OSIRIS project, *Can. J. Phys.*, *80*, 375–393, doi:10.1139/p01-156.

McPeters, R., S. Janz, E. Hilsenrath, T. Brown, D. Flittner, and D. Heath (2000), The retrieval of O3 profiles from limb scatter measurements: Results from the Shuttle Ozone Limb Sounding Experiment, *Geophys. Res. Lett.*, *27*, 2597–2600, doi:10.1029/1999GL011342.

Mishchenko, M., L. Travis, and D. Mackowski (1996), T-Matrix computations of Light Scattering by Nonspherical Particles: A Review, *J. Quant. Spectr. & Rad. Trans.*, *55*, 535–575, doi:10.1016/0022-4073(96)00002-7.

Mishchenko, M., L. Travis, and A. Lacis (2002), *Scattering, Absorption, and Emission of Light by Small Particles*, Cambridge University Press.

Morse, P., and H. Feshbach (1953), *Methods of Theoretical Physics*, McGraw-Hill Book Company, Inc.

Mote, P., K. Rosenlof, M. McIntyre, E. Carr, J. Gille, J. Holton, J. Kinnersley, H. Pumphrey, J. Russell, and J. Waters (1996), An atmospheric tape recorder: The imprint of tropical tropopause temperatures on stratospheric water vapor, *J. Geophys. Res.*, *101*, 3989–4006, doi:doi:10.1029/95JD03422.

Murray, B., T. Wilson, S. Dobbie, Z. Cui, S. Al-Jumur, O. Möhler, M. Schnaiter, R. Wagner, S. Benz, M. Niemand, et al. (2010), Heterogeneous nucleation of ice particles on glassy aerosols under cirrus conditions, *Nature Geosci.*, *3*, 233–237, doi:10.1038/ngeo817.

Murtagh, D., U. Frisk, F. Merino, M. Ridal, A. Jonsson, J. Stegman, G. Witt, P. Eriksson, C. Jiménez, G. Megie, et al. (2002), An overview of the Odin atmospheric mission, *Can. J. Phys.*, *80*, 309–319, doi:10.1139/p01-157.

Nakajima, T., and M. Tanaka (1988), Algorithms for radiative intensity calculations in moderately thick atmospheres using a truncation approximation, *J. Quant. Spectr. & Rad. Trans.*, *40*, 51–69, doi:10.1016/0022-4073(88)90031-3.

Newton, R. (1976), Optical theorem and beyond, *Am. J. Phys.*, *44*, 639–642, doi:10.1119/1.10324.

Pierce, J. (2011), Atmospheric chemistry: Particulars of particle formation, *Nature Geosci.*, *4*, 665–666, doi:10.1038/ngeo1267.

Pomeroy, J., and D. Male (1988), Optical properties of blowing snow, *Journal of Glaciology*, *34*, 3–10.

Potter, J. (1970), The delta function approximation in radiative transfer theory, *J. Atmos. Sci.*, *27*, 943–949, doi:10.1175/1520-0469(1970)027⟨0943:TDFAIR⟩2.0.CO;2.

Press, W., B. Flannery, S. Teukolsky, W. Vetterling, et al. (1986), *Numerical Recipes*, Cambridge Univ Press.

Pruppacher, H., and J. Klett (1997), *Microphysics of Clouds and Precipitation*, Kluwer Academic Publishers.

Rault, D. (2005), Ozone profile retrieval from Stratospheric Aerosol and Gas Experiment (SAGE III) limb scatter measurements, *J. Geophys. Res.*, *110*, D09,309, doi:10.1029/2004JD004970.

Rodgers, C. (1976), Retrieval of atmospheric temperature and composition from remote measurements of thermal radiation, *Rev. Geophys.*, *14*, 609–624, doi:10.1029/RG014i004p00609.

Roth, C., D. Degenstein, A. Bourassa, and E. Llewellyn (2007), The retrieval of vertical profiles of the ozone number density using Chappuis band absorption information and a multiplicative algebraic reconstruction technique, *Can. J. Phys.*, *85*, 1225–1243, doi:10.1139/p07-130.

Sassen, K., and B. Cho (1992), Subvisual-thin sirrus lidar dataset for satellite verification and climatological research, *J. Appl. Meteor.*, *31*, 1275–1285, doi:10.1175/1520-0450(1992)031⟨1275:STCLDF⟩2.0.CO;2.

Sassen, K., Z. Wang, and D. Liu (2008), Global distribution of cirrus clouds from CloudSat/Cloud-Aerosol Lidar and Infrared Pathfinder Satellite Observations (CALIPSO) measurements, *J. Geophys. Res*, *113*, D00A12, doi:doi:10.1029/2008JD009972.

Sloan, I., and R. Womersley (2004), Extremal systems of points and numerical integration on the sphere, *Adv. Comp. Math.*, *21*, 107–125, doi:10.1023/B:ACOM.0000016428.25905.da.

Solomon, S., K. Rosenlof, R. Portmann, J. Daniel, S. Davis, T. Sanford, and G. Plattner (2010), Contributions of stratospheric water vapor to decadal changes in the rate of global warming, *Science*, *327*, 1219, doi:10.1126/science.1182488.

Sonkaew, T., V. Rozanov, C. Von Savigny, A. Rozanov, H. Bovensmann, and J. Burrows (2009), Cloud sensitivity studies for stratospheric and lower mesospheric ozone profile retrievals from measurements of limb-scattered solar radiation, *Atmos. Meas. Tech*, *2*, 653–678, doi:10.5194/amt-2-653-2009.

Stamnes, K., S. Tsay, K. Jayaweera, and W. Wiscombe (1988), Numerically stable algorithm for discrete-ordinate-method radiative transfer in multiple scattering and emitting layered media, *Appl. Opt.*, *27*, 2502–2509, doi:10.1364/AO.27.002502.

Starr, D., and S. Cox (1985), Cirrus Clouds. Part II: Numerical Experiments on the Formation and Maintenance of Cirrus, *J. Atmos. Sci.*, *42*, 2682–2694, doi:10.1175/1520-0469(1985)042⟨2682:CCPINE⟩2.0.CO;2.

Tai, C.-T. (1971), *Dyadic Green's functions in Electromagnetic Theory*, Intext Educational Publishers.

Tao, W.-K., and M. Moncrieff (2009), Multiscale cloud system modeling, *Rev. Geophys.*, *47*, RG4002, doi:10.1029/2008RG000276.

van Diedenhoven, B., O. Hasekamp, and J. Landgraf (2006), Efficient vector radiative transfer calculations in vertically inhomogeneous cloudy atmospheres, *Appl. Opt.*, *45*, 5993–6006, doi:10.1364/AO.45.005993.

Von Savigny, C., C. Haley, C. Sioris, I. McDade, E. Llewellyn, D. Degenstein, W. Evans, R. Gattinger, E. Griffioen, E. Kyrölä, et al. (2003), Stratospheric ozone profiles retrieved from limb scattered sunlight radiance spectra measured by the OSIRIS instrument on the Odin satellite, *Geophys. Res. Lett*, *30*, 1755, doi:10.1029/2002GL016401.

Wang, P., P. Minnis, M. McCormick, G. Kent, and K. Skeens (1996), A 6-year climatology of cloud occurrence frequency from Stratospheric Aerosol and Gas Experiment II observations (1985–1990), *J. Geophys. Res*, *101*, 407–29, doi:10.1029/96JD01780.

Waterman, P. (1971), Symmetry, Unitarity, and Geometry in Electromagnetic Scattering, *Phys. Rev. D*, *3*, 825–839, doi:10.1103/PhysRevD.3.825.

Wiensz, J., A. Bourassa, N. Lloyd, A. Wiacek, R. Martin, and D. Degenstein (2012), Photon Conservation in Scattering by Large Ice Crystals with the SASKTRAN Radiative Transfer Model, *J. Quant. Spectr. & Rad. Trans.*, *113*, 582–593, doi:10.1016/j.jqsrt.2012.02.007.

Winker, D., and C. Trepte (1998), Laminar cirrus observed near the tropical tropopause by LITE, *Geophys. Res. Lett.*, *25*, 3351–3354, doi:10.1029/98GL01292.

Wiscombe, W. (1977), The Delta-M method: Rapid Yet Accurate Radiative Flux Calculations for Strongly Asymmetric Phase Functions, *J. Atmos. Sci.*, *34*, 1408–1422, doi:10.1175/1520-0469(1977)034⟨1408:TDMRYA⟩2.0.CO;2.

Wiscombe, W. (1980), Improved Mie scattering algorithms, *Appl. Opt.*, *19*, 1505–1509, doi:10.1364/AO.19.001505.

Wu, D., J. Jiang, and C. Davis (2006), EOS MLS cloud ice measurements and cloudy-sky radiative transfer model, *IEEE Trans. Geosci. Rem. Sens.*, *44*, 1156–1165, doi:10.1109/TGRS.2006.869994.

Yang, P., B. Baum, A. Heymsfield, Y. Hu, H. Huang, S. Tsay, and S. Ackerman (2003), Single-scattering properties of droxtals, *J. Quant. Spectr. & Rad. Trans.*, *79*, 1159–1169, doi:10.1016/S0022-4073(02)00347-3.

Yurkin, M., and A. Hoekstra (2007), The discrete dipole approximation: An overview and recent developments, *J. Quant. Spectr. & Rad. Trans.*, *106*, 558–589, doi:10.1016/j.jqsrt.2007.01.034.